Constitutive Modeling of the Thermomechanical and Cyclic Behavior of Shape Memory Alloys in Finite Deformations

Jun Wang

▶ **To cite this version:**

Jun Wang. Constitutive Modeling of the Thermomechanical and Cyclic Behavior of Shape Memory Alloys in Finite Deformations. Mechanics of materials [physics.class-ph]. Université Paris Saclay (COmUE), 2017. English. NNT : 2017SACLY013 . tel-01617607

HAL Id: tel-01617607
https://pastel.hal.science/tel-01617607

Submitted on 16 Oct 2017

HAL is a multi-disciplinary open access archive for the deposit and dissemination of scientific research documents, whether they are published or not. The documents may come from teaching and research institutions in France or abroad, or from public or private research centers.

L'archive ouverte pluridisciplinaire **HAL**, est destinée au dépôt et à la diffusion de documents scientifiques de niveau recherche, publiés ou non, émanant des établissements d'enseignement et de recherche français ou étrangers, des laboratoires publics ou privés.

NNT : 2017SACLY013

THÈSE DE DOCTORAT

DE L'UNIVERSITÉ PARIS-SACLAY

PRÉPARÉE A L'ENSTA ParisTech

ÉCOLE DOCTORALE N°579

Sciences mécaniques et énergétiques, matériaux et géosciences

Spécialité de doctorat : Mécanique des matériaux

par

M. WANG Jun

Constitutive Modeling of the Thermomechanical and Cyclic Behavior of Shape Memory Alloys in Finite Deformations

Thèse présentée et soutenue à Palaiseau, le 22 septembre 2017.

Composition du Jury :

M.	Jean-Baptiste LEBLOND	Professeur, Université Pierre et Marie Curie	Président
M.	Günay ANLAS	Professeur, Boğaziçi University	Rapporteur
M.	Tarak BEN-ZINEB	Professeur, Université de Lorraine	Rapporteur
Mme	Karine LAVERNHE-TAILLARD	Maître de conférences, ENS-Cachan	Examinateur
M.	Claude STOLZ	Directeur de recherche, Centrale Nantes	Examinateur
M.	ZHANG Weihong	Professeur, Northwestern Polytechnical University	Examinateur
M.	Ziad MOUMNI	Professeur, ENSTA-ParisTech	Directeur de thèse

致祖母，父母与爱人

Acknowledgements

The work reported in this dissertation was carried out in the Mechanics Unit of ENSTA-ParisTech/Université PARIS-SACLAY from October 2014 to September 2017. I sincerely appreciate everyone who helped me during this work period.

First of all, I would like to thank my PhD supervisor Prof. Ziad MOUMNI for his guidance and support during the course of my PhD studies. He taught me the knowledge of thermodynamics, mathematics and continuum mechanics, and constantly encouraged and helped me in both work and life.

I would also like to thank Prof. ZHANG Weihong, who was the first one to open my eyes to scientific research, and inspired me to pursue a PhD degree.

I am grateful to Dr. Wael ZAKI and Prof. XU Yingjie for their assistance when this dissertation was prepared. They taught me how to write and publish scientific papers.

I am thankful and fortunate enough to have Prof. Jean-Baptiste LEBLOND, Prof. Günay ANLAS, Prof. Tarak BEN-ZINEB, Dr. Karine LAVERNHE-TAILLARD and Prof. Claude STOLZ as my jury members. Their remarks and suggestions helped me a lot to improve my dissertation.

Many thanks to Profs. Habibou MAITOURNAM and HE Yongjun for their kindness and enthusiasm. I would also like to express my gratitude to my fellow research colleagues, Alain Van HERPEN, Lahcène CHERFA, Oana-Zenaida PASCAN, ZHENG Lin, GU Xiaojun, Quentin PIERRON, Nicolas THURIEAU, YIN Hao, ZHANG Yahui, and ZHANG Shaobin. It is a great pleasure to share the last wonderful three years with you.

I would like to acknowledge financial support from China Scholarship Council.

I owe a great deal to my parents, WANG Wenping and MA Xiaoming. They gave me life and taught me to explore this beautiful world. I owe special thanks to my grandmother, WANG Fengxia, who passed away during my PhD studies but her love last forever in my heart. Finally, my most sincere thanks go to my dear wife, LIU Yanan, for her love and accompany in both good and hard times.

Publications

Journals

Wang, J., Moumni, Z., & Zhang, W. (2017a). A thermomechanically coupled finite-strain constitutive model for cyclic pseudoelasticity of polycrystalline shape memory alloys. *International Journal of Plasticity*, *97*, 194-221.

Wang, J., Moumni, Z., Zhang, W., Xu, Y., & Zaki, W. (2017b). A 3D finite-strain-based constitutive model for shape memory alloys accounting for thermomechanical coupling and martensite reorientation. *Smart Materials and Structures*, *26*, 65006.

Wang, J., Moumni, Z., Zhang, W., & Zaki, W. (2017c). A thermomechanically coupled finite deformation constitutive model for shape memory alloys based on Hencky strain. *International Journal of Engineering Science*, *117*, 51–77.

Proceedings

Wang, J., Moumni, Z., & Zhang, W. (2016). A thermomechanical constitutive model of shape memory alloys in finite deformation. In *European Congress on Computational Methods in Applied Sciences and Engineering*. Crete, Greece.

Abstract

Shape Memory Alloys (SMAs) are a class of smart materials that possess two salient features known as pseudoelasticity (PE) and shape memory effect(SME). In industrial applications, SMA structures are typically subjected to complex service conditions, such as large deformations, thermomechanically coupled boundaries and loadings, and cyclic loadings. The reliability and durability analysis of these SMA structures requires a good understanding of constitutive behavior in SMAs. To this end, this work develops a comprehensive constitutive modeling approach to investigate thermomechanical and cyclic behavior of SMAs in finite deformations. The work is generally divided into three steps. First, to improve accuracy of SMA model in finite deformation regime, the ZM model proposed by Zaki and Moumni (2007b) is extended within a finite-strain thermodynamic framework. Moreover, the transformation strain is decomposed into phase transformation and martensite reorientation components to capture multi-axial non-proportional response. Secondly, in addition to the finite deformation, thermomechanical coupling effect is taken into account by developing a new finite-strain thermomechanical constitutive model. A more straightforward approach is obtained by using the finite Hencky strain. This model incorporates three important thermomechanical characteristics, namely the coexistence effect between austenite and two distinct martensite variants, the variation with temperature of hysteresis size, and the smooth transition at initiation and completion of phase transformation. Finally, with a view to studying SMA behavior under cyclic loading, the model developed in the second step is generalized to describe cyclic pseudoelasticity of polycrystalline SMAs. The generalized model captures four fundamental characteristics related to the cyclic behavior of SMAs: large accumulated residual strain, degeneration of pseudoelasticity and hysteresis loop, rate dependence, and evolution of phase transformation from abrupt to smooth transition. Numerical implementation of these models are realized by introducing proper integration algorithms. Finite element simulations, including orthodontic archwire, helical and torsion spring actuators, are carried out using the proposed models. The future directions of this work mainly involve plasticity and fatigue analysis of SMA structures.

Keywords: Shape Memory Alloy; Constitutive model; Finite deformation; Thermomechanical coupling; Cyclic loading; Numerical simulation.

Contents

List of Figures

List of Tables

Nomenclature

A_f^0	Austenite finish temperature at zero stress
A_f^σ	Austenite finish temperature at stress level of σ
$A_i, \boldsymbol{n}_i$	Eigenvalues and eigenvectors of the symmetric tensor $\boldsymbol{A}$
A_s^0	Austenite start temperature at zero stress
A_s^σ	Austenite start temperature at stress level of σ
$C(\theta)$	Heat density associated with phase transformation
$I_1^{\boldsymbol{A}}$	First invariant of the tensor $\boldsymbol{A}$
J	Determinant of the deformation gradient $\boldsymbol{F}$
M_f^0	Martensite finish temperature at zero stress
M_f^σ	Martensite finish temperature at stress level of σ
M_s^0	Martensite start temperature at zero stress
M_s^σ	Martensite start temperature at stress level of σ
R^{sat}	Saturated residual strain
$\Delta\eta_t$	Entropy difference between austenite and martensite
α_θ	Thermal expansion coefficient
$\bar{\boldsymbol{F}}$	Isochoric component of the deformation gradient $\boldsymbol{F}$
$\bar{\boldsymbol{h}}_e$	Deviatoric component of the elastic Eulerian Hencky strain tensor
$\mathbf{1}$	Second-order identity tensor
$\boldsymbol{C}$	Right Cauchy-Green deformation tensor
$\boldsymbol{D}$	Stretching tensor

$\boldsymbol{D}_e$	Elastic stretching tensor
$\boldsymbol{D}_r$	Residual stretching tensor
$\boldsymbol{D}_t$	Transformation stretching tensor
$\boldsymbol{D}_N$	Reorientation stretching tensor
$\boldsymbol{D}_*$	Inelastic stretching tensor
$\boldsymbol{F}$	Total deformation gradient tensor
$\boldsymbol{F}_e$	Elastic deformation gradient tensor
$\boldsymbol{F}_r$	Residual deformation gradient tensor
$\boldsymbol{F}_t$	Transformation deformation gradient tensor
$\boldsymbol{F}_*$	Total inelastic deformation gradient tensor
$\boldsymbol{F}_\theta$	Thermal deformation gradient tensor
$\boldsymbol{F}_{tr}$	Reorientation deformation gradient tensor
$\boldsymbol{H}$	Lagrangian Hencky strain tensor
$\boldsymbol{L}$	Velocity gradient tensor
$\boldsymbol{M}_e$	Mandel stress tensor
$\boldsymbol{R}$	Rotation tensor
$\boldsymbol{U}$	Right stretch tensor
$\boldsymbol{V}$	Left stretch tensor
$\boldsymbol{W}$	Spin tensor
$\boldsymbol{\sigma}$	Cauchy stress tensor
$\boldsymbol{\tau}$	Kirchhoff stress tensor
$\boldsymbol{\varepsilon}$	Green-Lagrange strain tensor
$\boldsymbol{\varepsilon}_A$	Local strain tensor in austenite
$\boldsymbol{\varepsilon}_M$	Local strain tensor in martensite
$\boldsymbol{\varepsilon}_t$	Transformation strain tensor

$\boldsymbol{\varepsilon}_{tr}$	Martensite orientation strain tensor
$\boldsymbol{b}$	Left Cauchy-Green deformation tensor
$\boldsymbol{h}$	Eulerian Hencky strain tensor
$\boldsymbol{h}_r$	Residual Eulerian Hencky strain tensor
$\boldsymbol{h}_t$	Transformation Eulerian Hencky strain tensor
$\boldsymbol{n}$	Outward unit vector normal to $\partial\mathcal{B}$
$\boldsymbol{q}$	Heat flux vector per unit area
$\boldsymbol{s}$	Deviatoric component of the Kirchhoff stress $\boldsymbol{\tau}$
χ	Volume fraction of martensite
χ^M	Multi-variant martensite volume fraction
χ^S	Single-variant martensite volume fraction
χ_c	Cumulated martensite volume fraction
δ	Trace of the Hencky strain $\boldsymbol{H}$
η_0	Reference entropy density
η_v	Entropy density per unit volume
$\mathbb{C}$	Spatial tangent operator
$\mathbb{D}$	Material tangent operator
$\mathcal{B}$	Homogeneous body occupied by the thermodynamic system
$\mathcal{H}$	Maximum orientation strain of martensite variants
$\partial\mathcal{B}$	Boundary of the homogeneous body $\mathcal{B}$
π	Circular constant
ψ	Helmholtz free energy density
ψ^e	Hyperelastic energy
ψ^θ	Thermal energy
ψ^{cst}	Energy due to the internal constraints

ψ^{int}	Interaction energy between austenite and martensite phases
σ_f	Detwinning finish stress
σ_f^A	Austenite finish stress
σ_f^M	Martensite finish stress
σ_s	Detwinning start stress
σ_s^A	Austenite start stress
σ_s^M	Martensite start stress
skew($\boldsymbol{A}$)	Skew part of the tensor $\boldsymbol{A}$
sym($\boldsymbol{A}$)	Symmetric part of the tensor $\boldsymbol{A}$
tr($\boldsymbol{A}$)	Trace of the tensor $\boldsymbol{A}$
θ	Temperature
θ_0	Reference temperature
θ_a	Ambient temperature
c_v	Specific heat capacity
e_0	Reference internal energy density
e_v	Internal energy density per unit volume
h	Heat convection coefficient
h_v	Heat source per unit volume
k	Thermal conductivity
p	Hydrostatic component of the Kirchhoff stress $\boldsymbol{\tau}$

Chapter 1

Introduction

1.1 Introduction and motivation

In the last few decades, smart materials have been one of the most important subjects in materials science and technology. These materials, due to their unique properties, attracted the attention towards potential innovative applications in various industrial fields. Shape memory alloys (SMAs) are a typical class of smart materials capable of undergoing severe but recoverable inelastic deformation under the influence of appropriate thermomechanical loadings. The most salient features in SMA behavior are undoubtedly their pseudoelasticity (PE) and shape memory effect (SME), which take place at the crystalline scale by means of a first-order diffusionless transformation between austenite and martensite solid phases. These unusual properties promoted the use of SMAs in various industrial applications including aerospace, biomedical, automotive and robotic domains.

In industrial applications, SMA structures are subjected to a variety of service conditions. For some complex loading cases, such as large deformation, thermomechanical coupling, and cyclic loading, complexities of the thermomechanical analysis of these SMA structures increase greatly. First, SMA wires, films and spring actuators typically undergo very large rotations and strains, which will bring about both geometric and material nonlinearities in SMA-based boundary value problems. Second, since the deformation and shape recovery processes of SMAs can be either thermal or stressed induced, SMA structures are typically subjected to thermomechanically coupled boundary and loading conditions. For example, the thermally-activated SMA actuator is subjected to repetitive cooling and heating cycles accompanied with a preloaded force. Third, some SMA structures are typically subjected to cyclic thermomechanical loadings that may induce fatigue failure of the structures after a certain number of cycles. Thermomechanical characteristics related to the cyclic behavior of SMAs, such as the accumulation of residual strain during cycling, as well as the degeneration of pseudoelasticity and hysteresis loop with the number of cycles, are worthy of study for fatigue analysis of the SMA structures. To be able to accurately predict the thermomechanical response of SMA structures under arbitrary complex loading conditions, an in-depth and comprehensive understanding of the constitutive behavior

of SMAs is indispensable. Thereby, the development of a reliable constitutive model becomes one of the most challenging subjects for current state of the art on SMAs.

This thesis aims to develop a comprehensive constitutive modeling approach to describe the thermomechanical and cyclic behavior of SMAs in finite-strain framework. The aforementioned three characteristics, *i.e.*, finite deformation, thermomechanical coupling, and cyclic effect, are integrally addressed in this work. Meanwhile, another objective of this work is to numerically implement the constitutive model into finite element software so that it can be used as a computational tool in engineering analysis, design and optimization. The whole work is accomplished by the following three steps.

The first step deals with finite deformations in SMAs. To this end, the small-strain ZM model (Zaki and Moumni, 2007b; Moumni et al., 2008) is extended, within a finite-strain framework, to describe large strains and rotations in SMAs. Before the finite-strain formulation, a summary of the ZM model is first presented. The development of the finite-strain model consists of the description of kinematics, the establishment of a finite strain thermomechanical framework, and the derivation of constitutive equations. Numerical implementation of the finite-strain model includes the time-discrete formulation of the constitutive equations, the symmetrization of the reorientation evolution equation, and material and spatial tangent operators.

The second step takes into account thermomechanical coupling in addition to finite deformations. To this end, a new 3D thermomechanically coupled, finite-strain constitutive model is developed. Hencky strain is used in the formulation, due to its remarkable properties in finite deformations, leading to a more straightforward modeling approach. The proposed model incorporates three important SMA characteristics: the effect of coexistence between austenite, single-variant and multi-variant martensites; the variation with temperature of the hysteresis size; and the smooth transition at the initiation and completion of phase transformation.

The third step addresses cyclic behavior of SMAs, by generalizing the model developed in the second step. The generalized model captures several fundamental characteristics related to the cyclic behavior of SMA, *i.e.*, large accumulated residual strain, degeneration of pseudoelasticity and hysteresis loop, rate dependence, and evolution of phase transformation from abrupt to smooth transition.

These proposed SMA models are well validated against experimental data under various thermomechanical loading cases. Finite element simulations of SMA structures, such as archwire, helical and torsion spring actuators, are also carried out. The future work mainly involves irreversible plasticity of SMAs undergoing severe mechanical loading, and fatigue analysis of SMA structures.

1.2 Overview of shape memory alloys

Shape memory alloys (SMAs) are a class of smart materials that can undergo severe but recoverable inelastic deformation under the influence of appropriate thermomechanical loadings. They have been the focus of intense research effort by the scientific community in the last decades (Müller and Bruhns, 2006; Moumni et al., 2008; Christ and Reese, 2008; Lagoudas et al., 2012; Xiao, 2014; Auricchio et al., 2014; Saleeb et al., 2015; Machado et al., 2015; Chatziathanasiou et al., 2016; Cisse et al., 2016a).

The first discovery of shape memory effect was reported by Ölander (1932) in Au-Cd alloy in 1932. This alloy could not survive large stresses or strains and therefore was not utilized as actuators. The formation and disappearance of the martensite was observed by Greninger and Troiano (1938) by decreasing and increasing the temperature of a Cu-Zn alloy. The crystallography and thermodynamics of martensite transformation were later investigated by Grange and Stewart (1946), Greninger and Troiano (1949) and Bowles and Mackenzie (1954). In 1963, the nickel-titanium (NiTi) alloys were first observed having shape memory effect by the United States Naval Ordnance Laboratory (Kauffman and Mayo, 1993). Afterwards, several other alloys, such as Ag-Cd, Au-Cd, Cu-Sn, In-Ti, Ni-Al, Ni-Ti, Mn-Cu, were found that exhibit shape memory tendencies. Now, there are three main types of SMAs: Fe-Mn-Si, Cu-Al-Ni and NiTi alloys. Fe-Mn-Si alloys are called as ferromagnetic shape memory alloy (FSMA), which change shape under magnetic fields. Although Fe-Mn-Si and Cu-Al-Ni alloys are commercially available and less expensive, NiTi alloys are regarded as the most promising SMAs for various applications due to their stability and practicability (Saadat et al., 2002; Machado and Savi, 2003; Hartl and Lagoudas, 2007). The most salient features in SMA behavior are undoubtedly their pseudoelasticity (PE) and shape memory effect (SME), which take place at the crystalline scale by means of a first-order diffusionless transformation between austenite (A) and martensite (M) solid phases. This unusual behavior attracted the attention towards potential innovative applications of SMAs in engineering, examples of which are orthodontic archwires, endovascular stents, smart circuit breakers, robotic muscles, shape morphing actuators, etc. (Williams and Elahinia, 2008; Auricchio et al., 2010; Gu et al., 2015). Recently, Lexcellent (2013) gave a detailed analysis, both physical and mechanical, properties of SMA materials. Mohd Jani et al. (2014) provided a review of SMA research, applications and opportunities. Hartl et al. (2015) introduced a specification and standardization effort of SMAs as employed as actuators for commercial and military aviation applications.

1.2.1 Martensitic transformation

The martensitic transformation (MT) is a first-order diffusionless solid-solid phase transformation occurring at lattice scale from a parent austenite phase, stable at high temperature and low stress, to a product martensite phase, metastable at low temperature and high stress (Otsuka and Wayman, 1999; Cisse et al., 2016a). The crystal structure of austenite is generally a perfect cube and thereby has the higher crystallography symmetry, as shown in Fig. 1.1. In contrast, martensite has tetragonal, orthorhombic or monoclinic crystal structure and thereby lower crystallography symmetry (Arghavani, 2010). The lower symmetry of this phase enables the existence of several martensite variants characterized by their orientation with respect to the interface with austenite called “habit plane”. The assembly of martensite variants may exist in two forms: multi-variant (twinned) martensite, in which variants with different orientations are “self-accommodated”, and single-variant (detwinned) martensite, in which a specific variant is dominant. More crystallographic theories for MT are available in the literature (Bowles and Mackenzie, 1954; Otsuka and Wayman, 1999; Sadjadpour and Bhattacharya, 2007; Lexcellent et al., 2008).

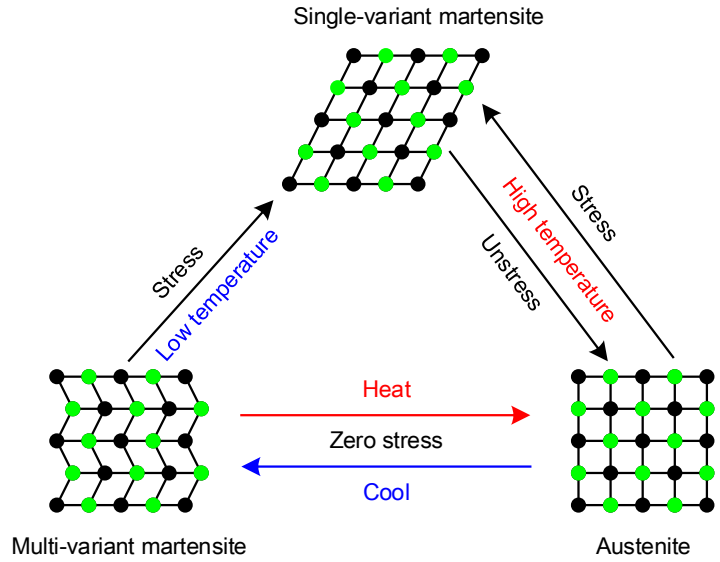

Figure 1.1 The crystal structures and phase transformations of austenite, single-variant and multi-variant martensites.

This inherent phase transformation (PT) can be either thermally-induced or stress-induced. Fig. 1.2 shows a phase diagram with control variables of stress and temperature, in which MT can occur under different thermomechanical loading paths. Upon cooling at zero stress (path 1), austenite transforms to multi-variant martensite, termed the forward transformation (A→M). This phase transformation is initiated at the "martensite start temperature" M_s^0, and completed at the "martensite finish temperature" M_f^0. During heating, the multi-variant martensite transforms back to the austenite, termed the reverse transformation (M→A), which is characterized by the "austenite start temperature" A_s^0 and the "austenite finish temperature" A_f^0. If a mechanical load is applied to the multi-variant martensite material at low temperature (path 2), the martensite will be detwinned by reorienting the variants in a certain direction depending on the applied stress. The "detwinning start stress" σ_s and the "detwinning finish stress" σ_f correspond to the stress levels at the initiation and the completion of the detwinning process. This martensite reorientation process results in a macroscopic deformation. A large part of this deformation remains after unloading. When the material is cooled with a constant applied stress σ, the austenite phase will transform directly to the single-variant martensite, producing a macroscopic deformation. Reheating the material will result in reverse transformation and thereby shape recovery. The loading path is shown in Fig. 1.2 (path 3). The characteristic temperatures M_f^σ, M_s^σ, A_s^σ, and A_f^σ represent, respectively, martensite finish, martensite start, austenite start, and austenite finish temperatures, which strongly depend on the applied stress level σ. Phase transformation from austenite to single-variant martensite can be also stress-induced by applying a sufficiently high mechanical load on the material in austenite phase (path 4). This phase transformation is initiated at the "martensite start stress" σ_s^M and completed at the "martensite finish stress" σ_f^M. When the load is released, the single-variant martensite

will transform back to austenite. σ_s^A and σ_f^A represent the "austenite start stress" and "austenite finish stress". These characteristic stresses significantly depend on the temperature.

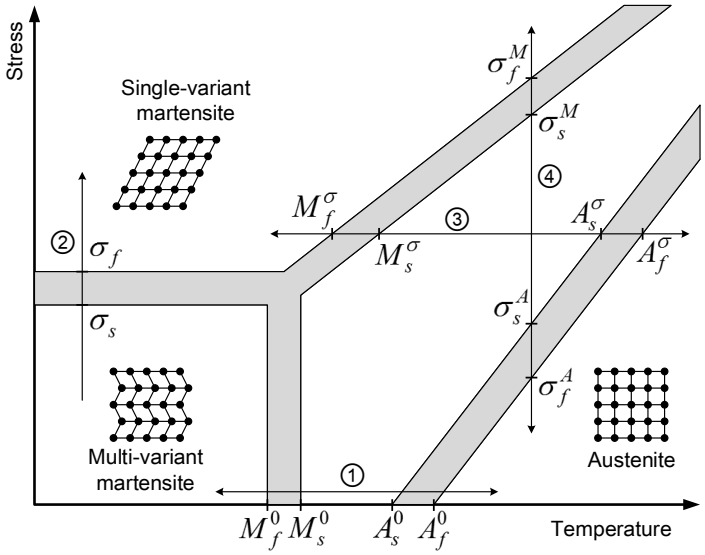

Figure 1.2 A phase diagram and the phase transformations between austenite, multi-variant and single-variant martensites.

1.2.2 Shape memory effect

Shape memory effect (SME) is probably the most well-known property of SMA. It consists in the ability of the SMA to recover its original shape upon heating. This phenomenon is illustrated in the stress-strain-temperature diagram, as shown in Fig. 1.3. Starting from the parent phase (austenite), the stress-free material is cooled below the forward transformation temperatures (M_s^0 and M_f^0), resulting in the formation of multi-variant martensite. When subjected to an applied stress, the product multi-variant martensite is reoriented to single-variant martensite. The reorientation process is initiated at the detwinning start stress σ_s, and completed at the detwinning finish stress σ_f, which is characterized by a transformation plateau in the stress-strain curve. It should be noted that the stress level for reorientation of the martensite variants is far lower than the permanent plastic yield stress of martensite. The applied stress is then released and the single-variant martensite is retained. Upon heating in the absence of stress, the reverse transformation is initiated at A_s^0 and completed at A_f^0. Finally, the single-variant martensite completely transforms to the parent austenite phase, and the material recover its original shape. The shape memory cycle can be repeated if the material is again cooled to multi-variant martensite.

In addition to the above one-way shape memory effect (OWSME), the two-way shape memory effect (TWSME) is the ability of the material to remember its shape at both low and high temperatures. It is not an intrinsic property in SMAs, but is rather acquired by "training". Early work on the TWSME was reported by Perkins (1974), Miyazaki et al. (1981) and Liu and McCormick (1990). Generally, the TWSME can be induced by thermomechanical cyclic loadings. The physical mechanism for the

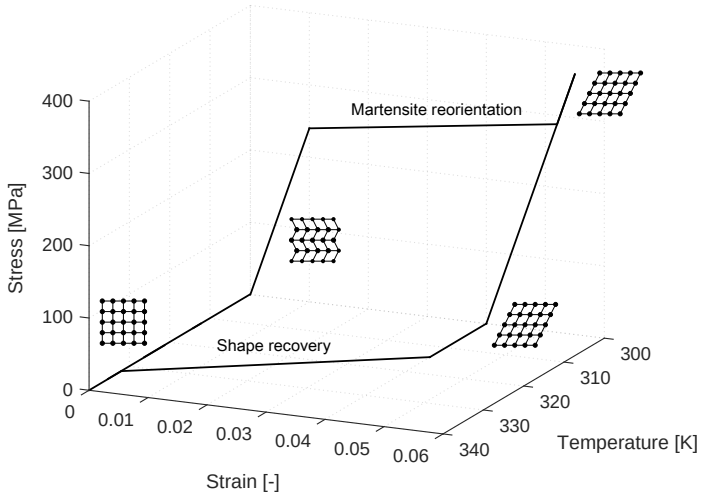

Figure 1.3 Schematic of the shape memory effect for a typical NiTi SMA.

development of TWSME in trained SMAs was explained by Perkins and Sponholz (1984), Tadaki et al. (1988) and Lovey et al. (1995) as follows: unrecoverable strain at the end of each loading cycle accumulates during training until saturation. The resulting permanent dislocations, defects and the residual internal stress stabilize a fraction of the martensite plates which are then identically recreated during subsequent transformations, thus producing macroscopic strain. This allows a trained SMA to switch configurations between stable austenite and oriented martensite phases by heating or cooling in the absence of external mechanical load. Due to the training requirements and to the fact that it averagely produces only half of the recovery strain compared to the OWSMA for the same material and its strain tends to deteriorate quickly, TWSMA is less applied commercially (Schroeder and Wayman, 1977; Huang and Toh, 2000; Ma et al., 2010).

1.2.3 Pseudoelasticity

Pseudoelasticity (PE), sometimes referred to as superelasticity, is associated with the stress-induced phase transformation between austenite and single-variant martensite in SMAs. Fig. 1.4 shows a typical pseudoelastic stress-strain response of polycrystalline SMAs. It is featured with large reversible strain and hysteresis loop. The thermomechanical loading path for such an example is shown as path 4 in Fig. 1.2. At temperature above A_f^0, the material in austenite phase undergoes elastic deformation when a mechanical load is applied. The phase transformation from austenite to single-variant martensite is initiated at stress level of σ_s^M and completed at σ_f^M. This stress-induced transformation is accompanied by the generation of large transformation strains, as shown in the stress-strain curve of Fig. 1.4. A subsequent increase in the stress produces no further transformation but only the elastic deformation of the product single-variant martensite. Upon unloading, the reverse transformation is initiated at stress level of σ_s^A and completed at σ_f^A, accompanied by the recovery of the transformation strain. SMA reverts to its original shape when the mechanical load is completely released. It is noteworthy that the

transformation stresses and the size of the hysteresis loop are significantly influenced by the testing temperature, as shown by path 4 in Fig. 1.2.

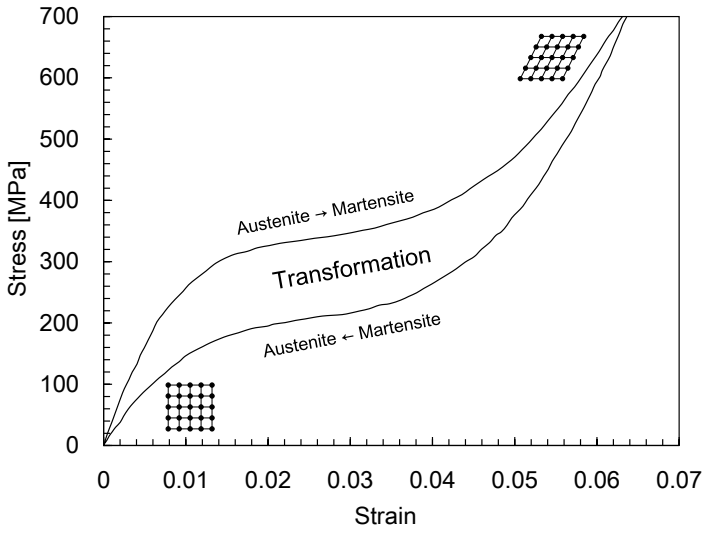

Figure 1.4 Schematic of the pseudoelasticity for a polycrystalline NiTi SMA.

1.3 Application of SMAs

Since the 1960s, SMAs attracted great attention of scientists and engineers worldwide. Many SMA-based structures and systems were designed for various industrial applications. According to the primary function of the shape memory element, these applications can be classified into the following five categories:

- Free recovery. The one way or two way shape memory effects can be used for free recovery applications. The sole function of the SMA element is to cause motion or shape change without any externally applied stress.
- Constrained recovery. The constrained SMA element is prevented from changing shape and therefore generates a stress or force on the applications. This recovery stress can be used for clamping and coupling devices.
- Actuation. Since the SMA element can generate motion against the externally applied stress, it exhibits work production and thermal energy is directly converted into mechanical energy.
- Pseudoelasticity. This characteristic is mostly used in biomedical applications wherein the SMA element undergoes large reversible strains with high stress plateaus.
- Damping. The high damping capacity of the stress-induced martensite transformation is interesting for passive damping. The pseudoelastic hysteresis can be used for energy absorption uses.

In the last three decades, SMAs have found many applications in industrial activities. The relevant SMA applications are presented in this section, particularly from the aerospace, biomedical, automotive and robotic domains.

1.3.1 Aerospace applications

The first and most well-known SMA application in aerospace domain was the hydraulic tube coupling used on the F-14 fighter jets in 1970s Otsuka and Wayman (1999). Since then the unique characteristics of SMAs were exploited in aerospace applications, which are mostly subjected to high dynamic loads and geometric space constraints (Mohd Jani et al., 2014). These applications include actuators (Giacomel, 1998; Hartl and Lagoudas, 2007), couplings and fasteners (Otsuka and Wayman, 1999), release or deployment mechanisms (Huett and Willey, 2000; Cleveland, 2008), vibration dampers, and manipulators (Birman, 1997; Prahlad and Chopra, 2001).

Since the 1990s, aerospace communities mainly focused on the active and adaptive structures toward morphing capability and system-level optimization under various flight conditions. The most well-known examples are the Smart Wings program from Defense Advanced Research Projects Agency (DARPA) (Kudva, 2004), and the Smart Aircraft and Marine Propulsion System Demonstration (SAMPSON) program (Pitt et al., 2001). To reduce the engine noise during take off and landing, designers from Boeing developed an active serrated aerodynamic device, known as a Variable Geometry Chevron (VGC), and installed on a GE90-115B jet engine for the Boeing 777-300 ER commercial aircraft (Hartl et al., 2009b,a; Oehler et al., 2012). Afterwards, different VGC solutions were proposed by Boeing, DARPA, NASA and other relevant research agencies, which were reviewed by Calkins and Mabe (2010). Sofla et al. (2010) also provided a review of aircraft morphing wing technologies, and proposed a shape morphing wing design for small aircraft. In rotorcraft applications, SMA-based technologies have been used in rotor blade twisting (Prahlad and Chopra, 2001; Caldwell et al., 2007), rotor blade tracking tab (Singh and Chopra, 2002; Kennedy et al., 2004), rotor control (Loewy, 1997), and rotor blade trip morphing (Testa et al., 2005). Meanwhile, SMAs have been used in spacecraft applications to address problems related to actuation and low-shock release mechanisms in zero atmosphere environment (Johnson, 1992; Birman, 1997; Carpenter and Lyons, 2001), as well as vibration dampers and isolators during spacecraft launch (Saadat et al., 2002). In addition, considerable SMA applications for aerospace, such as telescopic wing system (Knowles and Bird, 2004), retractable landing gear (Kutlucinar, 2005), jet engine components (Song and Ma, 2009), and flap edge fence (Larssen and Calkins, 2013), have been developed to exploit SMA advantages.

1.3.2 Biomedical applications

The shape memory and pseudoelastic characteristics, coupled with the biocompatibility, make NiTi alloys the most promising candidates for biomedical applications, such as orthodontic wires and drills (Auricchio, 2001; Lagoudas, 2008), filters (Poletti et al., 1998), stents (Dotter et al., 1983; Itzhak'Vinograd et al., 1994), intervertebral spacer (Duerig et al., 1997), orthopedic staples (Laster et al.,

2001), and surgical instruments (Sanders et al., 1994). According to the different uses, they are classified into four categories: orthodontic, cardiovascular, orthopedic, and surgical instruments applications.

Since the 1970s, NiTi orthodontic archwires have been successfully used in a variety of dental applications. They were proven to be more effective than other alternative materials because of their pseudoelastic plateau, during which a nearly constant and moderate force was provided over a larger deformation and thereby a longer period of time compared with stainless steel (Andreasen and Hilleman, 1971). Another key dental application involves the use of NiTi drills in root canal surgery (Cheung and Darvell, 2007; Lagoudas, 2008). The advantage of the NiTi drills is that they can with stand the high cyclic rotations with large bending and strains. The most common cardiovascular application is the self-expanding NiTi stent (Cwikiel et al., 1993; Yanagihara et al., 1997; Pelton et al., 2008). This device is used to support the inner circumference of tubular passages in the body such as blood vessels. Compared to conventional balloon inflated stainless steel stents, NiTi stents can gently expand the blood vessels to the appropriate diameter. Another cardiovascular SMA devices are the Simon filters for trapping clots traveling in the blood stream (Engmann and Asch, 1998), and the atrial septal occlusion for sealing the atrial hole located on the surface dividing the upper heart chambers (Thanopoulos et al., 1998; Chan et al., 1999). For orthopedic applications, the SMA devices are mostly used to support injured, weakened or fractured bones. These applications include intervertebral spacer used to provide local reinforcement to the vertebra (Duerig et al., 1997), porous SMAs used as artificial bone implants (Lagoudas and Vandygriff, 2002), orthopedic staples used to provide a compressive force at the interface of the separated bones (Krone et al., 2005), and shape memory plates to hold the fractured joints together (Tawfik et al., 2002). Moreover, many SMA-based surgical instruments, including SMA baskets and pseudoelastic guide wires, have been introduced in Minimally Invasive Surgery (MIS), in which the instruments are inserted through small openings and subsequently expanded to a desired size (Lim et al., 1996; Duerig et al., 1997; Song, 2010).

1.3.3 Automotive applications

In modern automotive industry, SMAs have been extensively used for applications ranging from sensors and actuators to vibration dampers and impact absorption uses, due to the demand of safer, more comfortable vehicles with better performance. The drive-by-wire technology offers a wide range of opportunities for SMA actuators as an alternative to conventional electromagnetic actuators in automotive applications. The mechanical simplicity and compactness of SMA actuators significantly reduce the scale, weight and cost of automotive components and provide substantial performance benefits, as demonstrated by Neugebauer et al. (2010). General Motors (GM) claimed that their 2014 Chevrolet Corvette became the first vehicle to incorporate SMA actuators to actuate the hatch vent that releases air from the trunk for easier closing of the trunk lid (Mohd Jani et al., 2014). SMAs can also be used for sensor and actuator purposes simultaneously as the SMA spring for continuous variable transmission system, wherein the spring acts as a sensor that monitors the temperature and actuates a valve at a specific temperature to adjust the oil flow (Bhattacharyya et al., 1995). The pseudoelastic hysteresis

behavior provides an effective system to dissipate vibration and impact. Taken the advantage of this property, SMAs are used in vibration isolation and impact absorption applications (Paine and Rogers, 1995; Barnes et al., 2006). Several other SMA applications in automotive industry are the automatic pedestrian protection system to minimize pedestrian injuries during impact collisions (Strittmatter et al., 2009), the micro-scanner system for optical sensing of objects distance and angle (Brugger et al., 2006), the SMA activated automotive tumble flaps (Bellini et al., 2009), and a cost effective side mirror actuator (Williams et al., 2010).

1.3.4 Robotic applications

With the increasing trends towards miniaturization of robotic system, SMAs have been exploited as micro-actuators and artificial muscles in a diverse range of commercial robotic systems. Kheirikhah et al. (2011) recently presented a review of SMA applications in robotics' different branches such as crawler robots, jumper robots, flower robots, fish robots, walker robots, medical robots, and biomimetic robotic hand. The ideology of these researches is to utilize SMA actuators to design and develop innovative, lightweight, powerful, compact, and dexterous robotic system. Nishida et al. (2006) proposed a lightweight micro biped walking robot incorporating multiple SMA-based Flexible Flat Plates (FFPs) that consist of polyethylene plates and SMAs. A new biomimetic tendon-driven actuation system for prosthetic and wearable robotic hand applications was presented by Bundhoo et al. (2009), based on the combination of compliant tendon cables and one-way SMA wires that form a set of artificial muscle pairs for the required flexion/extension or abduction/adduction of the finger joints. Later, a novel sensory system for robotics was developed by Tuna et al. (2012), they employed the pseudoelastic characteristic of a NiTi SMA to create an artificial rate whisker by utilizing the rat's sensing capabilities. Ali and Takahata (2010) also developed passive micro-grippers that can be actuated wirelessly with magnetic field. The opportunity to control multiple selections of micro-SMA actuators became possible by applying different resonant frequencies. In addition to these, several other SMA applications are in fish robots (Tao et al., 2006; Cho et al., 2008; Wang et al., 2008b), walker robots (Carlo and Metin, 2006; Nishida et al., 2006; Berry and Garcia, 2008), and flying robots (Furst et al., 2012; Colorado et al., 2012).

1.4 Research objectives

In industrial applications, SMA structures are typically subjected to complex thermomechanical boundary and loading conditions. Moreover, some of these SMA structures, such as SMA wires, films and spring actuators, typically undergo very large strains and rotations. A good understanding of constitutive relation of SMAs, especially in finite deformation regime, is indispensable to study the thermomechanical behavior of these SMA structures, and further to improve the reliability and durability of the SMA systems. To this end, the objectives of this research are: (i) to develop a comprehensive constitutive modeling approach capable of describing diverse SMA behavior under complex thermomechanical

boundary and loading conditions as well as large strains and rotations; (ii) to numerically implement the SMA models into finite element software so that it can be used as a computational tool in engineering analysis, design and optimization. The objectives are accomplished by the following three aspects:

- Theoretical modeling. The small-strain ZM model (Zaki and Moumni, 2007b) is extended, within a finite-strain framework, to account for large strains and rotations. Afterwards, to account for thermomechanical coupling effect, a new 3D finite-strain thermomechanical constitutive model is developed. The Hencky strain is used in the formulation for the straightforwardness of modeling approach. This model is then generalized to describe cyclic behavior of SMAs.
- Numerical implementation. With the introduction of the proper numerical integration algorithms, the proposed models are implemented into finite element software by means of user-defined material subroutines.
- Finite element simulation. The proposed SMA models are first validated against the experimental data under various thermomechanical boundary and loading conditions. Then, finite element simulations of SMA structures undergoing complex thermomechanical loadings as well as large strains and rotations, such as orthodontic archwire, helical and torsion spring actuators, are carried out using the proposed models.

1.5 Outline of dissertation

In this thesis, a comprehensive constitutive modeling approach is developed to investigate the thermomechanical and cyclic behavior of SMAs in finite deformations. After the motivation and introduction in Chapter 1 , the rest of the thesis is organized as follows:

- In Chapter 2, a literature review of constitutive modeling of SMAs is presented. Depending on the scale of the continuum, the existing SMA models are classified into microscopic, micro-macro and macroscopic models. The macroscopic models, also referred to as phenomenological models, are discussed in detail, respectively, with respect to finite deformation, thermomechanical coupling and cyclic behavior.
- In Chapter 3, a summary of the ZM model proposed by Zaki and Moumni (2007b) is first presented, which is then generalized, within a finite-strain thermodynamical framework, to account for large strains and rotations. The kinematics of the model features a two-tier decomposition of the deformation gradient. Constitutive equations are derived from a Helmholtz free energy and their time-discrete formulation is presented. Numerical algorithm of the model involves a logarithmic map integration, a symmetrization of the reorientation evolution equation, and material and spatial tangent operators. The integration algorithm is then implemented into Abaqus/Standard by means of a implicit user-defined material subroutine (UMAT). Model predictions are validated against

experimental data under various loading conditions. The model is also used to simulate a SMA archwire subjected to large strains and rotations.

- In Chapter 4, in order to take into account thermomechanical coupling, a new 3D thermomechanically coupled, finite-strain model is developed based on Hencky strain. The kinematics description of the model characterizes a decomposition of the Hencky strain into elastic, transformation and thermal parts, and a decomposition of the transformation stretching into phase transformation and martensite reorientation components. The model incorporates three important SMA characteristics: the effect of coexistence between austenite, single-variant and multi-variant martensites; the variation with temperature of the hysteresis size; and the smooth transition at the initiation and completion of phase transformation. Finite element simulation of a SMA helical spring actuator subjected to complex thermomechanical loading and boundary conditions is carried out using the proposed model.

- In Chapter 5, the model developed in Chapter 4 is generalized to describe cyclic behavior of polycrystalline SMAs in finite deformations. The model captures several fundamental characteristics related to the cyclic behavior of SMA, *i.e.*, large accumulated residual strain, degeneration of pseudoelasticity and hysteresis loop, rate dependence, and evolution of phase transformation from abrupt to smooth transition. The 3D model is reduced to a 1D version, and used to simulate the cyclic tensile experiments on NiTi wire at different loading rates under the assumption of uniform temperature field. Moreover, finite element simulation of a torsion spring undergoing large cyclic deformations is carried out, which shows the potential of the model for fatigue analysis of SMA structures.

Finally, in Chapter 6 a conclusion of our research as well as several future directions of the work are given.

Chapter 2

Literature review of the constitutive modeling of SMAs

2.1 Constitutive modeling approaches

Over the last three decades, substantial research was dedicated to developing constitutive models that can accurately describe the thermomechanical behavior of SMAs. Depending on the scale of the continuum, the existing models can be classified into microscopic, micro-macro and macroscopic models. Reviews of these models can be found in the literature of Lagoudas et al. (2006), Khandelwal and Buravalla (2009), Lexcellent (2013) and Cisse et al. (2016a,b).

2.1.1 Microscopic models

Microscopic models are developed at the lattice or grain-crystal levels to describe microstructural features in SMA behavior such as phase nucleation-completion, interface motion, martensite twin growth, etc. (Arghavani, 2010; Guthikonda and Elliott, 2013). They are mostly constructed by means of the Ginzburg-Landau (GL) theory or molecular dynamics (MD) Cisse et al. (2016a).

The microscopic models based on the GL theory are derived from a polynomial energy expression, usually written in terms of observable variables such as strain and temperature. Falk (1980, 1983) proposed the earliest polynomial potential models for SMAs. In his work, a Landau-Devonshire-like free energy based on similarity of the electromagnetic curves of ferromagnetic materials was used to describe phase transformation and shape memory effect. The GL theory was later used to explore a theoretical approach to fine phase mixtures (Ball and James, 1987), to describe the atomic lattice vibrations (Levitas and Preston, 2002), to solve the kinetic equations with FEM (Idesman et al., 2005; Zhong and Zhu, 2014) and to describe the mesoscale phase field (Wang and Melnik, 2007).

Molecular dynamics (MD) is a computer simulation method for studying the physical movements of atoms and molecules. It originated within the field of theoretical physics in the late of 1950s but now is mostly used in chemical physics and materials science (Alder and Wainwright, 1959; Rahman,

1964). Newton's equations are numerically solved to determine the motions of particles for a system consisting of a finite number of interacting particles. Depending the potential energy of interaction between particles considered, the MD models can be divided into the the embedded-atom-method (EAM) (Daw and Baskes, 1984; Lai and Liu, 2000; Uehara et al., 2009; Mutter and Nielaba, 2013) and Lennard-Jones (LJ) (Suzuki and Shimono, 2003; Deng et al., 2010; Zhong and Zhu, 2012) potentials.

These microscopic models are powerful and promising to understand the fundamental phenomena at the microscopic level. However, the use of these models for engineering applications remains impractical to-date because of the inconvenient scale-transition and the high computation cost.

2.1.2 Micro-macro models

Micro-macro models rely on micromechanics to describe the microscopic or mesoscopic material behavior. Macroscopic constitutive equations are derived by the method of scale transition (Sun and Hwang, 1993; Blanc and Lexcellent, 2004; Patoor et al., 2006; Levitas and Ozsoy, 2009; Khater et al., 2014). The development of these models requires the use of suitable observable variables (such as strain $\boldsymbol{\varepsilon}$, stress $\boldsymbol{\sigma}$ and temperature θ), and internal variables (such as the martensitic volume fraction χ and the mean transformation strain $\bar{\boldsymbol{\varepsilon}}_t$). Generally, the micro-macro models are developed by means of the micro-mechanical and micro-plane/micro-sphere approaches.

The essence of micro-mechanical approach lies in the modeling of a single grain and averaging the behavior of the grains using scale transition techniques to describe the macroscopic material response of polycrystalline SMAs. The scale transition can be accomplished using the Mori-Tanaka scheme (Mori and Tanaka, 1973; Sun and Hwang, 1994; Brassart et al., 2009), the self consistent scheme (Patoor et al., 1989; Gall and Sehitoglu, 1999; Guthikonda and Elliott, 2013), the uniform stress (Sachs) or uniform strain (Taylor) mix approaches (Šittner and Novák, 2000; Thamburaja and Anand, 2001; Hackl and Heinen, 2008), and the finite element technique (Lim and McDowell, 2002; Anand and Gurtin, 2003; Sengupta et al., 2009; Junker and Hackl, 2011). This approach was used to develop polycrystalline SMA models considering various features, such as plastic deformation (Kudoh et al., 1985; Wang et al., 2008a; Yu et al., 2012), grain-size effect (Stupkiewicz and Petryk, 2010), transformation degeneration and shakedown (Yu et al., 2013, 2015a) and so on.

The micro-plane theory was introduced by Taylor and Quinney (1932) to describe the multiaxial macroscopic behavior of polycrystalline SMAs as a superposition of uniaxial responses with several micro-planes of different orientations under the assumption of static constraints or kinematic constraints. Sometimes the static and kinematic constraints are combined to get a so-called double constrained model (Bažant et al., 2000). Meanwhile, micro-sphere models are based on the projection of the macroscopic strain or stress onto directions that are normal to a micro-sphere (Ostwald et al., 2010b,a). To obtain the evolution of the volume fractions of the different phases, statistical physics and the 1D constitutive model proposed by Govindjee and Hall (2000) were employed. This approach was subsequently used to simulate the pseudoelastic and pseudoplastic behavior (Ostwald et al., 2014) as well as the cyclic effect on SMAs (Ostwald et al., 2015).

Micro-macro models appear to allow accurate simulations, and in some cases they can successfully predict the reorientation and detwinning of martensite variants. However, they employ a large number of state variables and model parameters, which makes computation expense challenging and results in difficulty in engineering application.

2.1.3 Macroscopic models

Macroscopic models are based on simplified micro-macro thermodynamics, phenomenological thermodynamics or direct experimental data fitting. Suitable assumptions and approximations are commonly made to aim at capturing macroscopic SMA behavior such as pseudoelasticity, one-way or two-way shape memory effect, martensitic reorientation, tension-compression asymmetry and accumulation of residual strain. Plasticity models, thermodynamic potential models and hysteresis models are three main macroscopic modeling approaches (Khandelwal and Buravalla, 2009; Cisse et al., 2016a).

The plasticity models are developed by analogy with a well-established elastoplasticity approach. In these models, the thermodynamic processes such as phase transformation and detwinning of the martensite variants are governed by loading functions and flow rules. The evolution rules normally have a certain structure and obey consistency conditions with the loading functions. Souza et al. (1998) proposed a 3D phenomenological model that can describe the mechanical behavior of polycrystalline CuZnAlMn alloys undergoing stress-induced phase transformation. The model was built on the assumptions of an admissibility condition for thermodynamic forces and a locking constraint for phase transformations. This work was later improved by Auricchio and Petrini (2002) who proposed a robust algorithm to simulate the SME and PE under non-proportional loading. Boyd and Lagoudas (1996) proposed the first model that accounts for martensite reorientation by introducing an inelastic strain tensor, which is experimentally validated by Lagoudas et al. (1996). Recently, Lagoudas et al. (2012) proposed a model that accounts for smooth response of polycrystalline SMA using nonlinear hardening functions.

For the models derived from the thermodynamic potentials, a suitable form of free energy or potential that represents the state of the thermodynamic system is first constructed from either microscopic, phenomenological or physical considerations. Macroscopic constitutive equations are then derived in compliance with thermodynamic principles. Zaki and Moumni (2007b,a) and Moumni et al. (2008) developed a phenomenological model for NiTi SMAs within the framework of generalized standard materials with internal constraints (Halphen and quoc Son, 1974). The state variables used in the ZM model include the temperature θ, the martensite volume fraction χ, the local transformation strain tensors for austenite $\boldsymbol{\varepsilon}_A$ and martensite $\boldsymbol{\varepsilon}_M$, and the local martensite orientation strain tensor $\boldsymbol{\varepsilon}_{ori}$. The model was later extended to account for tension-compression asymmetry (Zaki, 2010), plastic deformation (Zaki et al., 2010b), thermomechanical coupling (Zaki et al., 2010a; Morin et al., 2011a) and cyclic loading effect (Zaki and Moumni, 2007a; Moumni et al., 2009; Morin et al., 2011b). Leclercq and Lexcellent (1996) generalized the R_L model proposed by Raniecki et al. (1992) to develop a general macroscopic model that explicitly takes into account the reorientation of martensite variants. To this end, they separated the martensite volume fraction into oriented and self-accommodation parts. The

authors later used the model to discuss the validity of the four criteria proposed by James and Zhang (2005) for hysteresis minimization in alloys exhibiting first-order transition (Lexcellent et al., 2008).

Hysteresis models describe the hysteresis thermodynamic response in SMAs without necessarily going into the underlying physics. In analogy to input-output models, a suitable transfer function is constructed to capture the observed hysteresis between the forcing function and the response variable. Such models are commonly used in modeling magnetic and ferroelectric materials (Smith, 2005). Depending on the nature of the hysteresis operator used, the modeling approaches can be generally classified into Preisach type and Duhem-Madelung models. Preisach models follow an integration of the response of individual relays that switch between two transformation type (Ortin, 1992; Ortin and Delaey, 2002). Unlike, Duhem-Madelung models capture the hysteresis using differential equations. Two different operators are used, respectively, for the loading segment and unloading segment of the load path to capture the incremental material response (Ivshin and Pence, 1994; Bekker and Brinson, 1998).

In the current state of art in constitutive modeling, the macroscopic models, of which the present work is an example, are widely considered the most convenient for structural analysis and engineering design applications because of their smaller number of parameters and less computation expense (Souza et al., 1998; Peultier et al., 2006; Lexcellent et al., 2006; Moumni et al., 2008; Arghavani et al., 2010; León Baldelli et al., 2015).

2.2 Phenomenological models of SMAs

Throughout the history of SMA modeling, a large number of macroscopic phenomenological models have been proposed in the literature. Recently, with the increasing sophistication, these phenomenological models were capable of accurately describing complex SMA material responses such as the tension-compression-torsion asymmetry (Zaki, 2010; Reedlunn et al., 2014; Mehrabi et al., 2014; Rizzoni and Marfia, 2015), the multi-variant phase transformation (Levitas and Preston, 2002; Idesman et al., 2005; Auricchio et al., 2014), the strain localization and softening (Idesman et al., 2005; León Baldelli et al., 2015; Bechle and Kyriakides, 2016), the variation of the transformation hysteresis (Lagoudas et al., 2012; Sedlák et al., 2012), the smooth transition in trained polycrystalline SMA (Sittner et al., 1995; Grabe and Bruhns, 2008; Lagoudas et al., 2012), the residual strain accumulation and the cyclic effect (Zaki and Moumni, 2007a; Song et al., 2014; Yu et al., 2014, 2015a; Kimiecik et al., 2016; Kan et al., 2016), the crack growth (Baxevanis et al., 2015; Hazar et al., 2015), the size-dependent pseudoelasticity (Qiao and Radovitzky, 2015), the plastic deformation (Zhou, 2012; Zhu et al., 2014), the rate dependence (Hartl et al., 2010; Andani and Elahinia, 2014; Yu et al., 2015b), and so on. The vast majority of these models were developed under the assumption of infinitesimal deformation, and disregarded thermomechanical coupling effect in SMAs, which greatly simplifies the modeling framework that can be effective in presence of small strain/rotation and simple thermomechanical loading conditions. However, these models lose accuracy with increasing strains and rotations or complex thermomechanical loading paths and heat transfer conditions (Christ and Reese, 2008; Andani and Elahinia, 2014).

2.2.1 Finite deformation

SMA models with finite strain formulation (FSF) are indispensable to accurately describe large rotations (Christ and Reese, 2008) and distortions (Ziolkowski, 2007). Early finite strain models, such as the work of Lubliner and Auricchio (1996), Auricchio and Taylor (1997) and Masud et al. (1997), were mostly built by generalizing small strain formulations (SSF) of elastoplastic materials. Following these pioneering work, many FSF models were developed using either hypoelastic-based additive or hyperelastic-based multiplicative approaches.

Hypoelastic FSF models are based on the additive split of the stretching tensor $\boldsymbol{D}$, wherein constitutive relations are expressed directly in rate form and the formulation is limited to small strains but finite rotations. In this approach, standard infinitesimal elastoplasticity models are extended to the finite strain range by recasting the original evolution equations in terms of suitably chosen objective stress rates. An example of an isotropic hypoelastic SMA model was proposed by Müller and Bruhns (2006) based on a self-consistent Eulerian theory of finite deformation using a logarithmic rate. The model is shown to be consistent with the definition of a Helmholtz free energy by fulfilling appropriate integrability conditions. Zaki (2012) proposed an efficient implementation for the finite deformation extension of the work of Zaki (2011) considering a hypoelastic framework. Teeriaho (2013) proposed an alternative modeling approach for isotropic deformation involving logarithmic strain definitions and internal variables with a Eulerian rate formulation. This approach was then utilized to derive SMA constitutive relations. Xiao (2014) proposed a finite J_2-flow elastoplastic model with nonlinear combined hardening that allows changes in the size and center of the elastic domain as the material deforms. This additive approach would be consistent with the multiplicative approach if appropriate integrability conditions are satisfied.

Hyperelastic FSF models are based on the multiplicative decomposition of the deformation gradient $\boldsymbol{F}$ into elastic and inelastic parts. Masud et al. (1997) presented a finite-deformation finite element model for pseudoelastic SMAs under stress-controlled loading conditions at constant temperature. Auricchio (2001) derived a finite-strain SMA model and presented an efficient and robust integration algorithms. Anand and Gurtin (2003) used the multiplicative decomposition to develop a FSF SMA model that successfully describes isothermal pseudoelasticity of an initially textured NiTi. Stupkiewicz and Petryk (2006) extended the SSF model of Stupkiewicz and Petryk (2002) to develop a micromechanical FSF model for SMAs with elastic anisotropy. Reese and Christ (2008) proposed a finite deformation constitutive model to describe the pseudoelasticity of SMAs and developed a new integration scheme to preserve the incompressibility of material during the phase transformation. Arghavani et al. (2011) presented a phenomenological finite-Hencky-strain formulation featuring kinematic hardening and non-associative flow rules integrated using a solution algorithm involving a nucleation-completion step. Panoskaltsis et al. (2014) introduced a general finite-strain model accounting for diffusionless phase transformations and discussed possible extensions to account for tension-compression asymmetry and the influence of loading rate. Paranjape et al. (2016) developed a finite element framework in which the constitutive formulation simultaneously accounts for phase transformations at the martensite correspondence variant (CV) scale and rate-dependent crystal plasticity in austenite.

However, a common drawback of these models is that the inelastic deformation of SMAs is accounted for by means of a single tensorial internal variable representing transformation strain. Therefore, they do not always guarantee complete recovery of transformation strain when SMAs undergo multiaxial non-proportional loading, wherein phase transformation and martensite reorientation may take place simultaneously.

2.2.2 Thermomechanical coupling

Extensive experimental investigations have shown that phase transformation of SMAs is a thermomechanically coupled process, with heat production due to latent heat and intrinsic dissipation (Shaw and Kyriakides, 1995; Müller and Bruhns, 2006). The resulting temperature variations can readily influence the mechanical behavior of SMAs. From the experimental point of view, Shaw and Kyriakides (1995) performed a series of experiments at different strain rates, temperatures and loading conditions. The results show stronger strain rate dependence in air than in water, indicating that the dependence is due to thermomechanical coupling. Peyroux et al. (1998) used infrared thermography to investigate heat exchange during phase transformation in SMAs and concluded that intrinsic dissipation can be neglected before latent heat. Grabe and Bruhns (2008) conducted biaxial tension/torsion experiments under both isothermal and non-isothermal conditions and found that the stress-strain responses for various strain rates coincide under isothermal conditions, proving that the dependence is due to temperature effect rather than strain rate.

Based on these experimental findings, a few models that take into account thermomechanical coupling were proposed. Müller and Bruhns (2006) proposed a thermodynamic finite-strain model describing the pseudoelastic response of SMAs based on a self-consistent Eulerian theory. The model was used to simulate the material response under isothermal and adiabatic conditions. Christ and Reese (2009) proposed a thermomechanically coupled SMA model and carried out finite element simulation involving a medical foot staple which interacts with a bone segment. Morin et al. (2011a) presented a generalized ZM model (Zaki and Moumni, 2007b) for SMAs accounting for thermomechanical coupling. The model showed that the mechanical hysteresis is mainly due to the intrinsic dissipation, whereas the thermal response is governed by latent heat. Andani and Elahinia (2014) modified the model originally developed by Lagoudas et al. (2012) to capture the multi-axial pseudoelastic behavior of SMAs under quasi-static isothermal and dynamic loading conditions. Chatziathanasiou et al. (2016) proposed a new 3D thermodynamic coupled model for SMAs to describe martensitic reorientation, forward and reverse phase transformation, dissipation and latent heat, wherein the strain mechanisms are associated with proper internal variables.

However, these models are either limited to small deformations (Andani and Elahinia, 2014; Morin et al., 2011a) or developed without considering thermal deformation (Christ and Reese, 2009; Müller and Bruhns, 2006). Indeed, at high temperature and large stress magnitude the martensite structures has a much lower Young's modulus and can be readily deformed by application of an external force or heat,

indicating that thermoelastic deformations can not be neglected (Mohd Jani et al., 2014; Chemisky et al., 2014).

2.2.3 Cyclic behavior

Over the last decades, extensive experiments were carried out to investigate thermomechanical behavior of SMAs undergoing cyclic deformations. The following four primary characteristics were deduced from the experimental observations:

1. Large accumulated residual strain during cycling. Fig. 2.1(a) represents a typical pseudoelastic response of SMA under the stress-controlled cyclic loading. It is seen that the starting point of the stress-strain curves deviates with the number of cycles. This residual strain grows speedy at the beginning and tends to saturate after a certain number of cycles. This accumulated residual strain can be physically attributed to residual martensite and dislocations slipping in austenite during the cyclic deformation (Kockar et al., 2008; Yu et al., 2015b). According to the literature (Kan and Kang, 2010), the maximum residual strain reaches more than 7%. Thus, the total strain during cycling commonly reaches 10%-15%, which enters the finite strain regime.

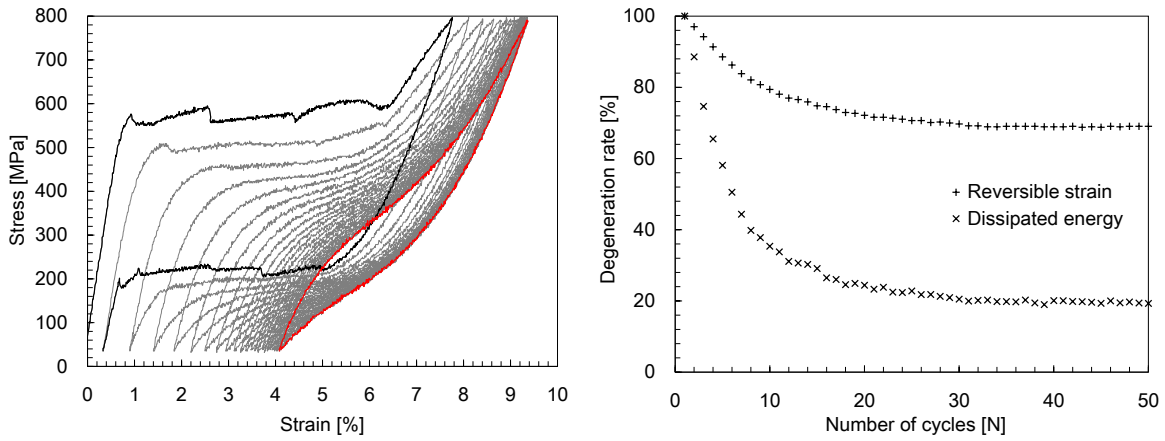

(a) (b)

Figure 2.1 Cyclic pseudoelastic response of the NiTi wire at strain rate of $1 \times 10^{-3} s^{-1}$ (Morin et al., 2011b): (a) stress-strain curves (black for first cycle and red for stabilized cycle), (b) evolutions of the dissipated energy and the reversible strain with the number of cycles.

2. Degeneration of pseudoelasticity and dissipated energy with the number of cycles. During the cyclic deformation, the hysteresis loop evolves progressively with the number of cycles as shown in Fig. 2.1(a), wherein the black curve represents the stress-strain response in the first cycle and the red curve represents the stabilized one. Fig. 2.1(b) shows the evolutions of the reversible strain and the dissipated energy with the number of cycles. It is seen that the reversible strain and the dissipated energy decrease, respectively, around 30% and 80% throughout the cyclic process. From a physical standpoint, the residual martensite and the dislocations slipping induce internal

stress that can assist the formation of stress-induced martensite (Zaki and Moumni, 2007a; Wang et al., 2014). As a consequence, the transformation stresses decrease with the number of cycles. Moreover, the increase of dislocation density obstructs the growth of martensite in a way similar to strain hardening in plasticity. Thus, the transformation hardening modulus increases gradually during cycling. Finally, the hysteresis loop stabilizes in a way comparable to plastic shakedown when the residual strain saturates.

3. Rate dependence. Fig. 2.2(a) shows the pseudoelastic stress-strain curves at different strain rates in the first cycle, and Fig. 2.2(b) the stabilized cycle. It is seen that the size of hysteresis loop, the reversible strain, the residual strain, the transformation stresses and hardening modulus are significantly influenced by the strain rate. The underlying cause for this rate dependence lies in four aspects: (i) phase transformation takes place with internal heat production due to the intrinsic dissipation and the latent heat; (ii) external heat transfer depends on the testing duration and therefore the loading rate; (iii) competition of the internal heat production against the external heat transfer determines the temperature in SMAs; (iv) pseudoelastic behavior of SMAs is strongly influenced by temperature. These experimental evidences can be found in the literature (Shaw and Kyriakides, 1995; Grabe and Bruhns, 2008; Thamburaja, 2010; Hartl et al., 2010; Morin et al., 2011b; Kan et al., 2016; Zhang et al., 2017). As a matter of fact, in the experiments of Shaw and Kyriakides (1995) and Grabe and Bruhns (2008), the stress-strain curves for different strain rates coincide under isothermal condition, which further evince that this rate dependence is due to thermomechanical coupling effect.

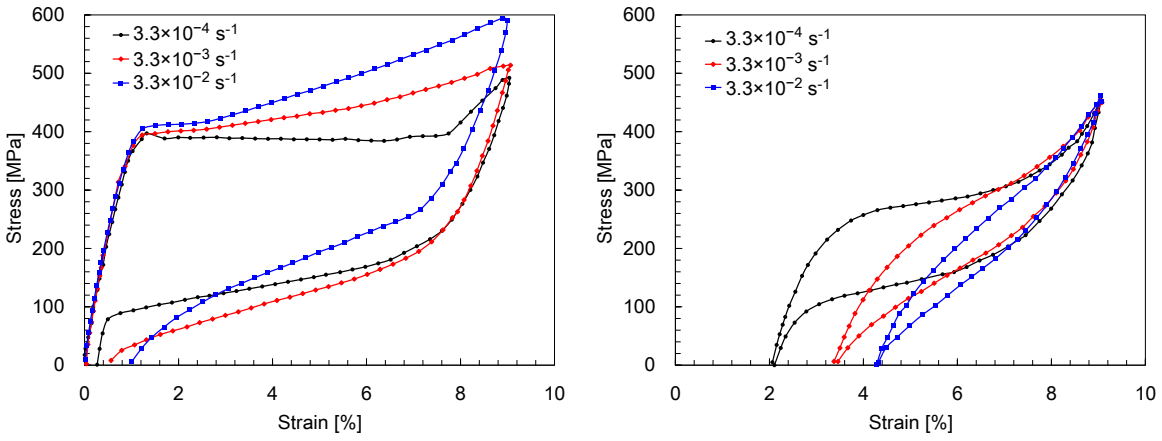

Figure 2.2 Strain rate dependent stress-strain curves in the cyclic experiments (Kan et al., 2016): (a) the first cycle, (b) the stabilized cycle.

4. Evolution of the phase transformation from abrupt to smooth transition. It is well known that the cyclic loading is usually used to “train” the polycrystalline SMA material. For “untrained” polycrystalline SMAs, a sharp transition between the elastic and the transformation regimes is

observed on the pseudoelastic stress-strain curves, as shown in Fig. 2.1(a) (black curve) and Fig. 2.2(a). This phenomenon is also commonly observed in single-crystalline SMAs. However, the phase transformation initiates and completes in a smooth manner in "trained" polycrystalline SMAs, as shown in Fig. 2.1(a) (red curve) and Fig. 2.2(b). This gradual phase transformation is due to the different crystallographic orientations of the grains, the strong heterogeneity of internal stresses and the presence of non-transforming precipitates during the cyclic deformation (Lagoudas et al., 2012). As a consequence, the pseudoelastic stress-strain curves evolve progressively from abrupt to smooth at the initiation and the completion of the phase transformation.

Based on these experimental findings, a few constitutive models that aim to describe the cyclic behavior of SMAs were proposed. Lexcellent and Bourbon (1996) introduced the concept of instantaneous residual martensite that evolves with the number of cycles to describe cyclic pseudoelasticity. Abeyaratne and Kim (1997) provided a 1D continuum model to qualitatively predict the cyclic behavior by capturing the idea that defects are precipitated during cycling and these defects tend to assist the nucleation of martensite. Subsequently, Bo and Lagoudas (1999) proposed a more complete model. Micromechanical analysis over a representative volume element (RVE) was employed to describe the evolution of internal state variables during cyclic phase transformation. Zaki and Moumni (2007a) proposed a 3D phenomenological model. The cyclic effects, *i.e.*, training and two-way shape memory are accounted for by introducing internal state variables such as internal back stress, residual strain and cumulated martensite volume fraction. The model was later improved by Morin et al. (2011b) by accounting for thermomechanical coupling. The improved model was used to determine the area of hysteresis loop in stabilized state and therefore the fatigue life of pseudoelastic SMAs. Auricchio et al. (2007) proposed a 3D model including permanent inelastic deformations, which was used to describe both pseudoelasticity and shape memory behavior under cyclic loading. Saint-Sulpice et al. (2009) performed a series of cyclic tests and developed a 3D macroscopic model to describe the pseudoelasticity and the evolution of permanent inelastic strain during cycles. Kan and Kang (2010) constructed a cyclic constitutive model in the framework of generalized plasticity. The dependence of transformation ratcheting on the applied stress level and the anisotropic transformation surface are considered in the model. Zhang et al. (2014) split the total cumulated martensite volume fraction into the forward transformation and the reverse transformation parts to construct a cyclic constitutive model. Yu et al. (2015b) proposed a 3D thermomechanically coupled and physical mechanism-based constitutive model to describe rate-dependent cyclic deformation of pseudoelastic NiTi SMA. The interactions between the martensite transformation and dislocations slipping in austenite phase are included in the model.

However, these models suffer from the following limitations: (i) all these models were developed under assumption of small strain, though most of the strain levels in cyclic experiments have entered finite strain regime; (ii) most of them are not able to capture the rate dependence; (iii) none of them considered the abrupt to smooth transition during training process.

Therefore, this work is dedicated to developing a comprehensive constitutive model that is able to capture the aforementioned thermomechanical and cyclic characteristics of SMAs in finite deformations.

Chapter 3

Finite-strain extension of the ZM model

3.1 Introduction

This chapter introduces the first step of the comprehensive constitutive modeling approach to investigate thermomechanical and cyclic behavior of SMAs in finite deformation. The chapter addresses the constitutive modeling of SMA using finite strain formulation. The model developed in this chapter is a finite-strain extension of the small-strain ZM model (Zaki and Moumni, 2007b; Moumni et al., 2008).

Before the development of the model, a summary of the ZM model is presented. The formulation of the model is based on a two-tier, multiplicative decomposition of the deformation gradient into elastic and transformation parts, where the transformation deformation is further split into phase transformation and martensite reorientation components. The finite-strain model is derived, within a thermodynamically consistent framework, from a Helmholtz free energy function. Numerical integration algorithm of the proposed model is presented featuring time-discrete formulation of the constitutive equations, proper symmetrization of the tensor variables, and explicit formulation of the material and spatial tangent operators involved. The algorithm is implemented into the finite element analysis (FEA) software Abaqus/Standard by means of a UMAT subroutine, to carry out simulations of SMAs subjected to various thermomechanical loading conditions. Simulation results of the proposed finite-strain model are compared against those of the small-strain ZM model. Moreover, the model is applied to simulate a SMA archwire undergoing large strains and rotations.

3.2 Summary of the small-strain ZM model

The ZM model for SMAs was proposed by Zaki and Moumni (2007b) based on the framework of generalized standard materials with internal constraints (Moumni, 1995). In this model, austenite is assumed to be elastic while martensite is inelastic. The assumption is physically motivated by the fact that reversible macroscopic inelastic deformation of SMAs is due to orientation of martensite variants. The Helmholtz free energy density ψ is constructed as the sum of free energy contributions

from austenite $\mathcal{W}_A$ and martensite $\mathcal{W}_M$ as well as an interaction energy term $\mathcal{I}$:

$$\begin{aligned}\psi = (1-\chi)\underbrace{\frac{1}{2}\boldsymbol{\varepsilon}_A : \boldsymbol{K}_A : \boldsymbol{\varepsilon}_A}_{\mathcal{W}_A} + \chi \underbrace{\left[\frac{1}{2}(\boldsymbol{\varepsilon}_M - \boldsymbol{\varepsilon}_{tr}) : \boldsymbol{K}_M : (\boldsymbol{\varepsilon}_M - \boldsymbol{\varepsilon}_{tr}) + C(\theta)\right]}_{\mathcal{W}_M} + \\ \underbrace{G\frac{\chi^2}{2} + \frac{\chi}{2}[\alpha\chi + \beta(1-\chi)]\left(\frac{2}{3}\boldsymbol{\varepsilon}_{tr} : \boldsymbol{\varepsilon}_{tr}\right)}_{\mathcal{I}},\end{aligned} \tag{3.1}$$

where $\mathcal{W}_A$ and $\mathcal{W}_M$ are, respectively, the local austenite and martensite strain energies. $\boldsymbol{\varepsilon}_A$ and $\boldsymbol{\varepsilon}_M$ are the local strain tensors in austenite and martensite. $\boldsymbol{K}_A$ and $\boldsymbol{K}_M$ are the elastic moduli of austenite and martensite. χ is the martensite volume fraction and $\boldsymbol{\varepsilon}_{tr}$ is the martensite orientation strain tensor. The interaction energy $\mathcal{I}$ consists of three components: $G\chi^2/2$ quantifies orientation-independent interaction between martensite variants, $\beta\chi(1-\chi)/2\left(\frac{2}{3}\boldsymbol{\varepsilon}_{tr} : \boldsymbol{\varepsilon}_{tr}\right)$ represents interaction between austenite and martensite and $\alpha\chi^2/2\left(\frac{2}{3}\boldsymbol{\varepsilon}_{tr} : \boldsymbol{\varepsilon}_{tr}\right)$ accounts for interaction increase due to orientation of martensite plates. G, α and β are model parameters. The heat density $C(\theta)$ associated with the thermal-induced phase transformation is given by

$$C(\theta) = \xi(\theta - A_f^0) + \mathcal{K}, \tag{3.2}$$

where ξ and $\mathcal{K}$ are model parameters, A_f^0 is the reverse phase transformation finish temperature at zero stress.

The state variables used for modeling obey the following physical constraints:

- Since the Reuss rheological model is adopted as rule of mixtures, the macroscopic strain tensor $\boldsymbol{\varepsilon}$ and the local strain tensor in austenite $\boldsymbol{\varepsilon}_A$ and martensite $\boldsymbol{\varepsilon}_M$ are subjected to

$$(1-\chi)\boldsymbol{\varepsilon}_A + \chi\boldsymbol{\varepsilon}_M - \boldsymbol{\varepsilon} = \mathbf{0}; \tag{3.3}$$

- The martensite volume fraction χ is restricted within the $[0, 1]$ interval,

$$0 \leq \chi \leq 1; \tag{3.4}$$

- The magnitude of martensite orientation strain $\boldsymbol{\varepsilon}_{tr}$ may not exceed a material-specific upper limit $\mathcal{H}$, *i.e.*

$$\mathcal{H} - \sqrt{\frac{2}{3}\boldsymbol{\varepsilon}_{tr} : \boldsymbol{\varepsilon}_{tr}} \geq 0. \tag{3.5}$$

The above physical constraints derive from the following potential:

$$\mathcal{W}_c = -\boldsymbol{\zeta}^p : [(1-\chi)\boldsymbol{\varepsilon}_A + \chi\boldsymbol{\varepsilon}_M - \boldsymbol{\varepsilon}] - \zeta^{tr}\left(\mathcal{H} - \sqrt{\frac{2}{3}\boldsymbol{\varepsilon}_{tr} : \boldsymbol{\varepsilon}_{tr}}\right) - \zeta^f(1-\chi) - \zeta^r\chi, \tag{3.6}$$

where $\boldsymbol{\zeta}^p$, ζ^{tr}, ζ^f and ζ^r are nonnegative Lagrangian multipliers. The potential (3.6) is complemented by the following Kuhn-Tucker conditions:

$$\begin{cases} \zeta^f \geq 0, & 1-\chi \geq 0, & \zeta^f\,(1-\chi) = 0; \\ \zeta^r \geq 0, & \chi \geq 0, & \zeta^r \chi = 0; \\ \zeta^{tr} \geq 0, & \mathcal{H} - \sqrt{\frac{2}{3}\boldsymbol{\varepsilon}_{tr} : \boldsymbol{\varepsilon}_{tr}} \geq 0, & \zeta^{tr}\left(\mathcal{H} - \sqrt{\frac{2}{3}\boldsymbol{\varepsilon}_{tr} : \boldsymbol{\varepsilon}_{tr}}\right) = 0. \end{cases} \tag{3.7}$$

The sum of the Helmholtz free energy (3.1) and the potential (3.6) gives the generalized Lagrangian free energy function,

$$\mathcal{L} = \psi + \mathcal{W}_c, \tag{3.8}$$

which is then used to derive the constitutive equations. With some algebra, the following elasticity constitutive equation is obtained:

$$\boldsymbol{\sigma} = \boldsymbol{K} : (\boldsymbol{\varepsilon} - \chi \boldsymbol{\varepsilon}_{tr}), \tag{3.9}$$

where $\boldsymbol{K} = \left[(1-\chi)\boldsymbol{K}_A^{-1} + \chi \boldsymbol{K}_M^{-1}\right]^{-1}$ is the equivalent elastic moduli of austenite and martensite mixtures. In equation (3.9), the product $\chi\boldsymbol{\varepsilon}_{tr}$ represents the inelastic part of the total strain. Therefore, $\boldsymbol{\varepsilon}$ is additively split into elastic and transformation parts, $\boldsymbol{\varepsilon} = \boldsymbol{\varepsilon}_e + \boldsymbol{\varepsilon}_t$, where $\boldsymbol{\varepsilon}_e$ and $\boldsymbol{\varepsilon}_t$ are given by

$$\boldsymbol{\varepsilon}_e = (1-\chi)\boldsymbol{\varepsilon}_A + \chi(\boldsymbol{\varepsilon}_M - \boldsymbol{\varepsilon}_{tr}) \quad \text{and} \quad \boldsymbol{\varepsilon}_t = \chi\boldsymbol{\varepsilon}_{tr}. \tag{3.10}$$

The thermodynamic forces associated with χ and $\boldsymbol{\varepsilon}_{tr}$ are taken as sub-gradients of a pseudo-potential of dissipation $\mathcal{D}$ defined as

$$\mathcal{D} = [a(1-\chi) + b\chi]\,|\dot{\chi}| + \chi^2 Y \sqrt{\frac{2}{3}\dot{\boldsymbol{\varepsilon}}_{tr} : \dot{\boldsymbol{\varepsilon}}_{tr}}, \tag{3.11}$$

where a, b and Y are positive model parameters. The evolution equations and yield functions associated with the forward phase transformation (A $\rightarrow$ M), the reverse phase transformation (M $\rightarrow$ A), and the martensite orientation are then derived from the Lagrangian $\mathcal{L}$ and the dissipation $\mathcal{D}$ in equations (3.8) and (3.11).

3.3 Development of the finite-strain model

The derivation of the finite-strain constitutive model for SMAs is based on the following two-tier decomposition: (i) a multiplicative decomposition of the deformation gradient into elastic and transformation parts; (ii) an additive split of the transformation deformation into phase transformation and martensite reorientation parts. Then, a thermodynamic framework and a Helmholtz free energy are introduced and used to derive the constitutive equations satisfying the requirement of thermodynamic consistency.

3.3.1 Kinematics

Let $\boldsymbol{p}$ be an arbitrary material point of a homogeneous body $\mathcal{B}$. The motion of $\mathcal{B}$ is described with a smooth one-to-one mapping $\boldsymbol{x} = \boldsymbol{\varphi}(\boldsymbol{p}, t)$. The deformation gradient $\boldsymbol{F}$, the velocity $\boldsymbol{v}$, and the velocity gradient $\boldsymbol{L}$ of the motion $\boldsymbol{\varphi}$ are defined by

$$\boldsymbol{F} = \nabla\boldsymbol{\varphi} = J^{\frac{1}{3}}\bar{\boldsymbol{F}}, \quad \boldsymbol{v} = \dot{\boldsymbol{\varphi}} \quad \text{and} \quad \boldsymbol{L} = \nabla_x \boldsymbol{v} = \dot{\boldsymbol{F}}\boldsymbol{F}^{-1}, \tag{3.12}$$

where ∇ and ∇_x denote, respectively, the material and spatial gradients of a general field; the dot denotes the material time derivative of a general field; $J = \det \boldsymbol{F}$ and $\bar{\boldsymbol{F}}$ denote, respectively, volumetric and isochoric components of $\boldsymbol{F}$.

Using polar decomposition, $\boldsymbol{F}$ is written as

$$\boldsymbol{F} = \boldsymbol{R}\boldsymbol{U} = \boldsymbol{V}\boldsymbol{R}, \tag{3.13}$$

where the symmetric positive definite tensors $\boldsymbol{U}$ and $\boldsymbol{V}$ are the right and left stretch tensors, the proper orthogonal tensor $\boldsymbol{R}$ is the local rotation tensor. Thereby, the right and left Cauchy-Green deformation tensors, $\boldsymbol{C}$ and $\boldsymbol{b}$, are defined by

$$\boldsymbol{C} = \boldsymbol{F}^T\boldsymbol{F} = \boldsymbol{U}^2 \quad \text{and} \quad \boldsymbol{b} = \boldsymbol{F}\boldsymbol{F}^T = \boldsymbol{V}^2. \tag{3.14}$$

The stretching and spin tensors, $\boldsymbol{D}$ and $\boldsymbol{W}$, are defined as the symmetric and the skew parts of $\boldsymbol{L}$:

$$\boldsymbol{D} = \operatorname{sym}(\boldsymbol{L}) = \frac{1}{2}(\boldsymbol{L} + \boldsymbol{L}^T) \quad \text{and} \quad \boldsymbol{W} = \operatorname{skew}(\boldsymbol{L}) = \frac{1}{2}(\boldsymbol{L} - \boldsymbol{L}^T). \tag{3.15}$$

In this work, the finite-strain response of SMAs is modeled by analogy with a well-established finite-strain elastoplasticity approach (Auricchio, 2001; Souza Neto et al., 2008; Reese and Christ, 2008; Arghavani et al., 2011; Dimitrienko, 2011), in which the deformation gradient $\boldsymbol{F}$ is multiplicatively decomposed into elastic and transformation parts, such that

$$\boldsymbol{F} = \boldsymbol{F}_e\boldsymbol{F}_t, \tag{3.16}$$

where $\boldsymbol{F}_e$ is defined with respect to an local unstressed intermediate configuration, while $\boldsymbol{F}_t$ is defined with respect to the reference configuration.

Using equation (3.13), $\boldsymbol{F}_e$ and $\boldsymbol{F}_t$ are decomposed as

$$\boldsymbol{F}_e = \boldsymbol{R}_e\boldsymbol{U}_e \quad \text{and} \quad \boldsymbol{F}_t = \boldsymbol{R}_t\boldsymbol{U}_t, \tag{3.17}$$

where $\boldsymbol{R}_e$ and $\boldsymbol{R}_t$ are elastic and transformation rotation tensors, $\boldsymbol{U}_e$ and $\boldsymbol{U}_t$ are right elastic and transformation stretch tensors. The corresponding right Cauchy-Green tensors for elastic and transformation

deformation are given by

$$\boldsymbol{C}_e = \boldsymbol{U}_e^2 = \boldsymbol{F}_e^T \boldsymbol{F}_e \quad \text{and} \quad \boldsymbol{C}_t = \boldsymbol{U}_t^2 = \boldsymbol{F}_t^T \boldsymbol{F}_t. \tag{3.18}$$

From equation $(3.10)_2$, it can be concluded that the transformation deformation of SMAs is the result of phase transformation and martensite reorientation. Thus, a deformation gradient $\boldsymbol{F}_{tr}$ associated with martensite orientation is defined with respect to the reference configuration, which will enhance the ability of the model to properly describe the martensite reorientation and the phase transformation simultaneously. The polar decomposition of $\boldsymbol{F}_{tr}$ is written as

$$\boldsymbol{F}_{tr} = \boldsymbol{R}_{tr} \boldsymbol{U}_{tr}, \tag{3.19}$$

where $\boldsymbol{R}_{tr}$ is rotation tensor and $\boldsymbol{U}_{tr}$ is right stretch tensor associated with martensite reorientation. The corresponding right Cauchy-Green strain tensor is then given by

$$\boldsymbol{C}_{tr} = \boldsymbol{U}_{tr}^2 = \boldsymbol{F}_{tr}^T \boldsymbol{F}_{tr}. \tag{3.20}$$

From equation $(3.10)_2$, the stretch tensors $\boldsymbol{U}_t$ and $\boldsymbol{U}_{tr}$ are coaxial, which is verified if the rotation tensor for martensite orientation equals to the rotation tensor for transformation deformation:

$$\boldsymbol{R}_t = \boldsymbol{R}_{tr}. \tag{3.21}$$

In small-strain formulation, the strain tensor conventionally adopted is an approximation of the Green-Lagrange strain tensor,

$$\boldsymbol{\varepsilon} = \frac{1}{2} \left[\nabla_p \boldsymbol{u} + (\nabla_p \boldsymbol{u})^T \right] \approx \frac{1}{2} (\boldsymbol{C} - \boldsymbol{1}), \tag{3.22}$$

where $\boldsymbol{u}$ is the displacement, $\boldsymbol{C}$ is the right Cauchy-Green strain tensor and $\boldsymbol{1}$ is the second-order identity tensor. Using equation $(3.10)_2$, $\boldsymbol{C}_t$ is expressed in terms of χ and $\boldsymbol{C}_{tr}$:

$$\boldsymbol{C}_t = \chi \boldsymbol{C}_{tr} + (1 - \chi) \boldsymbol{1}. \tag{3.23}$$

This additive split of the inelastic deformation will enhance the ability of the model to properly describe the martensite reorientation and the phase transformation simultaneously.

3.3.2 Thermodynamic framework

In order to satisfy the principle of material objectivity, the Helmholtz free energy of SMA is assumed to depend on the right Cauchy-Green deformation tensors $\boldsymbol{C}_e$ and $\boldsymbol{C}_{tr}$, the martensite volume fraction χ and the temperature θ as

$$\psi = \psi(\boldsymbol{C}_e, \boldsymbol{C}_{tr}, \chi, \theta) = \psi_e(\boldsymbol{C}_e, \chi) + \psi_t(\boldsymbol{C}_{tr}, \chi, \theta), \tag{3.24}$$

where ψ_e and ψ_t represent the hyperelastic strain energy and transformation hardening energy, respectively. The dependence of ψ_e on χ allows the definition of an equivalent elastic stiffness for the SMA that depends on its phase composition. This dependence is often neglected in SMA models (Auricchio, 2001; Helm and Haupt, 2003; Bouvet et al., 2004; Reese and Christ, 2008; Arghavani et al., 2010), in which austenite and martensite are considered to have the same elastic stiffness. Thermal expansion is disregarded, with θ appearing only in the expression of ψ_t. Both ψ_e and ψ_t are considered isotropic functions of $\boldsymbol{C}_e$ and $\boldsymbol{C}_{tr}$. Thus, the time derivative of ψ in equation (3.24) gives

$$\dot{\psi} = \frac{\partial \psi}{\partial \boldsymbol{C}_e} : \dot{\boldsymbol{C}}_e + \frac{\partial \psi}{\partial \boldsymbol{C}_{tr}} : \dot{\boldsymbol{C}}_{tr} + \frac{\partial \psi}{\partial \chi}\dot{\chi} + \frac{\partial \psi}{\partial \theta}\dot{\theta}. \tag{3.25}$$

The second law of thermodynamics, stated in the form of the Clausius-Duhem inequality, is written as

$$\boldsymbol{S} : \frac{1}{2}\dot{\boldsymbol{C}} - \left(\dot{\psi} + \eta\dot{\theta}\right) \geq 0, \tag{3.26}$$

where $\boldsymbol{S}$ is the second Piola-Kirchhoff stress and η is the entropy density. Substituting equation (3.25) into equation (3.26) gives

$$\boldsymbol{S} : \frac{1}{2}\dot{\boldsymbol{C}} - \left(\frac{\partial \psi}{\partial \boldsymbol{C}_e} : \dot{\boldsymbol{C}}_e + \frac{\partial \psi}{\partial \boldsymbol{C}_{tr}} : \dot{\boldsymbol{C}}_{tr} + \frac{\partial \psi}{\partial \chi}\dot{\chi} + \frac{\partial \psi}{\partial \theta}\dot{\theta}\right) - \eta\dot{\theta} \geq 0. \tag{3.27}$$

Equation $(3.17)_1$, written in rate form, gives the following expression of the rate of elastic deformation $\dot{\boldsymbol{C}}_e$:

$$\dot{\boldsymbol{C}}_e = \boldsymbol{F}_t^{-T}\dot{\boldsymbol{C}}\boldsymbol{F}_t^{-1} - \boldsymbol{C}_e\boldsymbol{L}_t - \boldsymbol{L}_t^T\boldsymbol{C}_e, \tag{3.28}$$

where $\boldsymbol{L}_t = \dot{\boldsymbol{F}}_t\boldsymbol{F}_t^{-1}$ is the transformation velocity gradient. Moreover, the coaxiality of $\partial\psi/\partial\boldsymbol{C}_e$ and $\boldsymbol{C}_e$, allows writing $\frac{\partial \psi}{\partial \boldsymbol{C}_e} : \dot{\boldsymbol{C}}_e$ in equation (3.26) as

$$\frac{\partial \psi}{\partial \boldsymbol{C}_e} : \dot{\boldsymbol{C}}_e = \boldsymbol{F}_t^{-1}\frac{\partial \psi}{\partial \boldsymbol{C}_e}\boldsymbol{F}_t^{-T} : \dot{\boldsymbol{C}} - 2\boldsymbol{C}_e\frac{\partial \psi}{\partial \boldsymbol{C}_e} : \boldsymbol{D}_t, \tag{3.29}$$

where $\boldsymbol{D}_t = \frac{1}{2}(\boldsymbol{L}_t + \boldsymbol{L}_t^T)$ is the transformation stretching tensor.

Substituting the equation (3.29) into the inequality (3.27), taking into account the relation $\boldsymbol{D}_t = \frac{1}{2}\boldsymbol{F}_t^{-T}\dot{\boldsymbol{C}}_t\boldsymbol{F}_t^{-1}$, gives

$$\left(\frac{1}{2}\boldsymbol{S} - \boldsymbol{F}_t^{-1}\frac{\partial \psi}{\partial \boldsymbol{C}_e}\boldsymbol{F}_t^{-T}\right) : \dot{\boldsymbol{C}} + \boldsymbol{F}_t^{-1}\boldsymbol{C}_e\frac{\partial \psi}{\partial \boldsymbol{C}_e}\boldsymbol{F}_t^{-T} : \dot{\boldsymbol{C}}_t - \frac{\partial \psi}{\partial \chi}\cdot\dot{\chi} - \frac{\partial \psi}{\partial \boldsymbol{C}_{tr}} : \dot{\boldsymbol{C}}_{tr} - \left(\eta + \frac{\partial \psi}{\partial \theta}\right)\cdot\dot{\theta} \geq 0. \tag{3.30}$$

Taking time derivative of equation (3.23) then gives

$$\dot{\boldsymbol{C}}_t = \dot{\chi}(\boldsymbol{C}_{tr} - \boldsymbol{1}) + \chi\dot{\boldsymbol{C}}_{tr}, \tag{3.31}$$

where the term $\dot{\chi}(\boldsymbol{C}_{tr} - \boldsymbol{1})$ corresponds to phase transformation at fixed martensite orientation, while $\chi\dot{\boldsymbol{C}}_{tr}$ corresponds to martensite reorientation.

Substituting equation (3.31) into inequality (3.30) then gives

$$\begin{aligned}&\left(\frac{1}{2}\boldsymbol{S}-\boldsymbol{F}_t^{-1}\frac{\partial\psi}{\partial\boldsymbol{C}_e}\boldsymbol{F}_t^{-T}\right):\dot{\boldsymbol{C}}+\left(\boldsymbol{F}_t^{-1}\boldsymbol{C}_e\frac{\partial\psi}{\partial\boldsymbol{C}_e}\boldsymbol{F}_t^{-T}:(\boldsymbol{C}_{tr}-\boldsymbol{1})-\frac{\partial\psi}{\partial\chi}\right)\cdot\dot{\chi}+\\&\left(\chi\boldsymbol{F}_t^{-1}\boldsymbol{C}_e\frac{\partial\psi}{\partial\boldsymbol{C}_e}\boldsymbol{F}_t^{-T}-\frac{\partial\psi}{\partial\boldsymbol{C}_{tr}}\right):\dot{\boldsymbol{C}}_{tr}-\left(\eta+\frac{\partial\psi}{\partial\theta}\right)\cdot\dot{\theta}\geq 0.\end{aligned}\tag{3.32}$$

For arbitrary thermodynamic processes, inequality (3.32) is guaranteed by the following choice of the constitutive laws with respect to $\boldsymbol{S}$ and η:

$$\boldsymbol{S}=2\boldsymbol{F}_t^{-1}\frac{\partial\psi}{\partial\boldsymbol{C}_e}\boldsymbol{F}_t^{-T}\quad\text{and}\quad\eta=-\frac{\partial\psi}{\partial\theta},\tag{3.33}$$

and by the following inequalities, which ensure nonnegative intrinsic dissipation in arbitrary evolutions of the internal state variables χ and $\boldsymbol{C}_{tr}$, so that

$$[\boldsymbol{M}_t:(\boldsymbol{C}_{tr}-\boldsymbol{1})-\mathcal{Z}]\cdot\dot{\chi}\geq 0\quad\text{and}\quad(\chi\boldsymbol{M}_t-\boldsymbol{X}_{tr}):\dot{\boldsymbol{C}}_{tr}\geq 0,\tag{3.34}$$

with

$$\boldsymbol{M}_t=\boldsymbol{F}_t^{-1}\boldsymbol{C}_e\frac{\partial\psi}{\partial\boldsymbol{C}_e}\boldsymbol{F}_t^{-T},\quad\mathcal{Z}=\frac{\partial\psi}{\partial\chi},\quad\boldsymbol{X}_{tr}=\frac{\partial\psi}{\partial\boldsymbol{C}_{tr}},\tag{3.35}$$

where $\boldsymbol{M}_t$ and $\boldsymbol{X}_{tr}$ are, respectively, the Mandel stress and the symmetric stress-like tensors defined with respect to the reference configuration, $\mathcal{Z}$ is a scalar state variable.

The nonnegative dissipation during phase transformation, as expressed in inequality $(3.34)_1$, is guaranteed by the following choice of the evolution equation for χ:

$$\dot{\chi}=\dot{\gamma}^{\chi}\mathcal{S}(A_{\chi}),\tag{3.36}$$

where $\dot{\gamma}^{\chi}$ is a nonnegative multiplier, the sign function $\mathcal{S}(\cdot)$ is used to extract the sign of A_{χ}. The thermodynamic force A_{χ} associated with phase transformation is then given by

$$A_{\chi}=\boldsymbol{M}_t:(\boldsymbol{C}_{tr}-\boldsymbol{1})-\mathcal{Z}.\tag{3.37}$$

The associated loading function for phase transformation is given by

$$\mathcal{F}_{\chi}=\left|A_{\chi}\right|-\mathcal{Y}_{\chi},\tag{3.38}$$

where $\mathcal{Y}_{\chi}$ controls the phase transformation threshold. $\dot{\gamma}^{\chi}$ and $\mathcal{F}_{\chi}$ are subjected to the Kuhn-Tucker consistency conditions:

$$\dot{\gamma}^{\chi}\geq 0,\quad\mathcal{F}_{\chi}\leq 0,\quad\dot{\gamma}^{\chi}\mathcal{F}_{\chi}=0.\tag{3.39}$$

Moreover, using the relation $\dot{\boldsymbol{C}}_{tr} = 2\boldsymbol{F}_{tr}^T \boldsymbol{D}_{tr} \boldsymbol{F}_{tr}$, a push-forward operation is carried out to rewrite the dissipation due to martensite reorientation $(3.34)_2$ in the unstressed intermediate configuration as

$$2\boldsymbol{F}_{tr}\left(\chi \boldsymbol{M}_t - \boldsymbol{X}_{tr}\right)\boldsymbol{F}_{tr}^T : \boldsymbol{D}_{tr} \geq 0. \tag{3.40}$$

Then, the following associative evolution equation for martensite reorientation is formulated by analogy with the principle of maximum dissipation in elastoplasticity (Simo and Hughes, 2008):

$$\boldsymbol{D}_{tr} = \frac{1}{2}\dot{\gamma}^{tr}\frac{\boldsymbol{A}_{tr}^{\mathrm{D}}}{\|\boldsymbol{A}_{tr}^{\mathrm{D}}\|}, \tag{3.41}$$

where $\dot{\gamma}^{tr}$ is a nonnegative multiplier, $(\cdot)^{\mathrm{D}} = (\cdot) - \frac{1}{3}\mathrm{tr}(\cdot)$ is used to extract the deviator of a tensor, the thermodynamic force $\boldsymbol{A}_{tr}$ associated with martensite reorientation is given by

$$\boldsymbol{A}_{tr} = \boldsymbol{F}_{tr}(\chi \boldsymbol{M}_t - \boldsymbol{X}_{tr})\boldsymbol{F}_{tr}^T. \tag{3.42}$$

Furthermore, in order to express the constitutive equations in a Lagrangian description, the evolution equation (3.41) is mapped into the reference configuration by means of a pull-back operation to get

$$\dot{\boldsymbol{C}}_{tr} = \dot{\gamma}^{tr}\boldsymbol{F}_{tr}^T\frac{\boldsymbol{A}_{tr}^{\mathrm{D}}}{\|\boldsymbol{A}_{tr}^{\mathrm{D}}\|}\boldsymbol{F}_{tr}. \tag{3.43}$$

With the help of the following three transformations:

$$\mathrm{tr}\left(\boldsymbol{A}_{tr}\right) = \mathrm{tr}\left[\boldsymbol{C}_{tr}(\chi \boldsymbol{M}_t - \boldsymbol{X}_{tr})\right] = \mathrm{tr}\left(\boldsymbol{B}_{tr}\right), \quad \boldsymbol{F}_{tr}^T\boldsymbol{A}_{tr}\boldsymbol{F}_{tr} = \boldsymbol{B}_{tr}\boldsymbol{C}_{tr}, \quad \|\boldsymbol{A}_{tr}^{\mathrm{D}}\| = \|\boldsymbol{B}_{tr}^{\mathrm{D}}\|, \tag{3.44}$$

equation (3.43) is rewritten as

$$\dot{\boldsymbol{C}}_{tr} = \dot{\gamma}^{tr}\frac{\boldsymbol{B}_{tr}^{\mathrm{D}}}{\|\boldsymbol{B}_{tr}^{\mathrm{D}}\|}\boldsymbol{C}_{tr}. \tag{3.45}$$

The associated loading function for martensite reorientation is given by

$$\mathcal{F}_{tr} = \|\boldsymbol{B}_{tr}^{\mathrm{D}}\| - \mathcal{Y}_{tr}, \tag{3.46}$$

where $\mathcal{Y}_{tr}$ defines the martensite reorientation threshold. $\dot{\gamma}^{tr}$ and $\mathcal{F}_{tr}$ are subjected to the Kuhn-Tucker conditions:

$$\dot{\gamma}^{tr} \geq 0, \quad \mathcal{F}_{tr} \leq 0, \quad \dot{\gamma}^{tr}\mathcal{F}_{tr} = 0. \tag{3.47}$$

3.3.3 Constitutive equations

The Helmholtz free energy function ψ in equation (3.24) is additively split in the following form:

$$\psi = \psi^{e} + \psi^{int} + \psi^{cst}, \tag{3.48}$$

where ψ^e is the hyperelastic strain energy, ψ^{int} is the interaction energy between martensite and austenite phases (Moumni et al., 2008), ψ^{cst} is the potential energy due to the internal physical constraints.

As aforementioned, ψ^e is assumed to be an isotropic function of $\boldsymbol{C}_e$, allowing it to be expressed in terms of the invariants of $\boldsymbol{C}_e$ as

$$\psi^e = \frac{\mu}{2}\left(I_1^{\boldsymbol{C}_e} - 3\right) - \mu \ln J + \frac{\lambda}{2}(\ln J)^2 + \chi C(\theta), \tag{3.49}$$

where $\mu = \left(\frac{1-\chi}{\mu^A} + \frac{\chi}{\mu^M}\right)^{-1}$ and $\lambda = \left(\frac{1-\chi}{\lambda^A} + \frac{\chi}{\lambda^M}\right)^{-1}$ are equivalent Lamé constants that depend on χ in the austenite and martensite composition, $I_1^{\boldsymbol{C}_e}$ is the first invariant of $\boldsymbol{C}_e$, J is the determinant of the deformation gradient $\boldsymbol{F}$.

The interaction energy ψ^{int} is often derived from micro-mechanical or crystallographic considerations and finally expressed as a function of the martensite volume fraction and the local martensite orientation strain (Zaki and Moumni, 2007b; Auricchio et al., 2014). Likewise, ψ^{int} is assumed to be an isotropic function of $\boldsymbol{C}_{tr}$. The following interaction energy is introduced in terms of χ and the invariants of $\boldsymbol{C}_{tr}$ as

$$\psi^{int} = G\frac{\chi^2}{2} + \frac{\chi}{2}[\alpha\chi + \beta(1-\chi)]\left(I_1^{\boldsymbol{C}_{tr}} - 3\right), \tag{3.50}$$

where $I_1^{\boldsymbol{C}_{tr}}$ is the first invariant of $\boldsymbol{C}_{tr}$, G, α and β are model parameters. The dependence of ψ^{int} on the volume fraction χ and the orientation strain $\boldsymbol{C}_{tr}$ allows the model to simultaneously capture the transformation deformation due to either phase transformation or martensite reorientation.

To satisfy the physical constraints on internal state variables χ and $\boldsymbol{C}_{tr}$, the following Lagrangian potential is defined as the constraint contribution ψ^{cst} to free energy in equation (3.48):

$$\psi^{cst} = -\zeta^{tr}\left(C - \|\boldsymbol{C}_{tr}\|\right) - \zeta^f(1-\chi) - \zeta^r\chi, \tag{3.51}$$

where C is the upper limit of martensite orientation deformation, ζ^{tr} is the Lagrange multiplier associated with the unilateral constraint $\|\boldsymbol{C}_{tr}\| \leq C$, ζ^f and ζ^r are the Lagrange multipliers associated with the bilateral constraints $0 \leq \chi \leq 1$.

In conclusion, the Helmholtz free energy function ψ is given by

$$\begin{aligned}\psi =& \frac{\mu}{2}\left(I_1^{\boldsymbol{C}_e} - 3\right) - \mu \ln J + \frac{\lambda}{2}(\ln J)^2 + G\frac{\chi^2}{2} + \frac{\chi}{2}[\alpha\chi + \beta(1-\chi)]\left(I_1^{\boldsymbol{C}_{tr}} - 3\right) - \\ & \left[\zeta^{tr}\left(C - \|\boldsymbol{C}_{tr}\|\right) + \zeta^f(1-\chi) + \zeta^r\chi\right].\end{aligned} \tag{3.52}$$

The constitutive equations derived from the free energy function (3.52) are finally summarized in Table 3.1.

In addition, the physical meaning of model parameters used in the model are given as

- a and b, respectively, control the width of the hysteresis loop for $\chi = 0$ and $\chi = 1$;

Table 3.1 Summary of the finite-strain model.

Constitutive equations:

$$\boldsymbol{S} = \mu \boldsymbol{C}_t^{-1} + (\lambda \ln J - \mu)\, \boldsymbol{C}^{-1}$$

$$\boldsymbol{C}_t = \chi \boldsymbol{C}_{tr} + (1-\chi)\mathbf{1}$$

$$\boldsymbol{M}_t = \tfrac{\mu}{2} \boldsymbol{C}_t^{-1} \boldsymbol{C} \boldsymbol{C}_t^{-1} + \tfrac{1}{2} (\lambda \ln J - \mu)\, \boldsymbol{C}_t^{-1}$$

$$\mathcal{Z} = G\chi + \left[(\alpha-\beta)\chi + \tfrac{\beta}{2}\right] \left(I_1^{\boldsymbol{C}_{tr}} - 3\right) + C(\theta) + \zeta^f - \zeta^r$$

$$\boldsymbol{X}_{tr} = \tfrac{\chi}{2} \left[\alpha\chi + \beta(1-\chi)\right] \mathbf{1} + \zeta^{tr} \tfrac{\boldsymbol{C}_{tr}}{\|\boldsymbol{C}_{tr}\|}$$

$$A_\chi = \boldsymbol{M}_t : (\boldsymbol{C}_{tr} - \mathbf{1}) - Z$$

$$\boldsymbol{B}_{tr} = \boldsymbol{C}_{tr}(\chi \boldsymbol{M}_t - \boldsymbol{X}_{tr})$$

Evolution equations:

$$\dot{\chi} = \dot{\gamma}^{\chi} \mathcal{S}(A_\chi) \quad \text{and} \quad \dot{\boldsymbol{C}}_{tr} = \dot{\gamma}^{tr} \tfrac{\boldsymbol{B}_{tr}^{\mathrm{D}}}{\|\boldsymbol{B}_{tr}^{\mathrm{D}}\|} \boldsymbol{C}_{tr}$$

Yield functions:

$$\mathcal{F}_\chi = \left|A_\chi\right| - [a(1-\chi) + b\chi] \quad \text{and} \quad \mathcal{F}_{tr} = \|\boldsymbol{B}_{tr}^{\mathrm{D}}\| - \chi^2 Y$$

Kuhn-Tucker conditions:

$$\begin{cases} \dot{\gamma}^{\chi} \geq 0, & \mathcal{F}_\chi \leq 0, & \dot{\gamma}^{\chi} \mathcal{F}_\chi = 0; \\ \dot{\gamma}^{tr} \geq 0, & \mathcal{F}_{tr} \leq 0, & \dot{\gamma}^{tr} \mathcal{F}_{tr} = 0. \end{cases}$$

- α and β, respectively, govern the evolution of the orientation strain $\boldsymbol{C}_{tr}$ with respect to stress for $\chi = 0$ and $\chi = 1$;
- G measures interaction between martensite plates, affects the stress-strain curve slope during phase transformation;
- Y represents the stress level associated with the beginning of martensite reorientation;
- C defines the fully oriented strain magnitude of martensite variants;
- ξ represents the slope of phase diagram boundaries for forward and reverse transformations, which quantifies the influence of temperature on transformation yield stress;
- $\mathcal{K}$ is the heat density at reverse phase transformation finish temperature.

3.4 Numerical implementation

In this section, numerical implementation of the proposed model in an finite element analysis (FEA) framework is carried out. An implicit time-discrete formulation of the model is presented and then numerically integrated using a form of the return mapping algorithm. The symmetrization of the time-discrete evolution equation as well as the determination of the material and spatial tangent operators are also discussed.

3.4.1 Time-discrete formulation

The analytical equations of the finite-strain model are rewritten as a set of time-discrete incremental equations to be solved over discrete time intervals $[t_n, t_{n+1}]$ covering the complete loading history, where n indicates the n-th kinematic time instant. The initial boundary value problem is stated as follows: given the deformation gradient $\boldsymbol{F}_n$ and the state variables $\boldsymbol{C}_n^{tr}$, χ_n and $\boldsymbol{S}_n$ at time t_n, for a given deformation gradient $\boldsymbol{F}$ at time t_{n+1}, determine the state variables at time t_{n+1} satisfying the time-discrete constitutive equations. For convenience, deformation is considered to be controlled by the right Cauchy-Green deformation tensor $\boldsymbol{C}$ instead of $\boldsymbol{F}$. Implicit integration is used to ensure the stability and accuracy of the time-integration algorithm.

The evolution equation (3.36) of χ is written using backward Euler approximation as

$$\chi = \chi_n + \Delta\gamma^{\chi}\mathcal{S}(A_{\chi}), \tag{3.53}$$

where $\Delta\gamma^{\chi}$ is the phase transformation multiplier at time t_{n+1}.

Since backward Euler integration does not preserve the incompressibility of martensite orientation, expressed as $\det(\boldsymbol{C}_{tr}) = 1$, exponential map integration is used instead. This integration method is well-established in computational plasticity (Reese and Christ, 2008). Using backward exponential map integration to approximate the evolution equation (3.45) gives

$$\boldsymbol{C}_{tr} = \exp\left(\Delta\gamma^{tr}\boldsymbol{N}_{tr}\right)\boldsymbol{C}_n^{tr}, \tag{3.54}$$

where $\boldsymbol{N}_{tr} = \boldsymbol{B}_{tr}^{\mathrm{D}}/\|\boldsymbol{B}_{tr}^{\mathrm{D}}\|$ is the flow vector of martensite orientation, $\Delta\gamma^{tr}$ is the martensite orientation multiplier at time t_{n+1}. Since the tensor $\boldsymbol{N}_{tr}$ is traceless, *i.e.*, $\mathrm{tr}(\Delta\gamma^{tr}\boldsymbol{N}_{tr}) = 0$, a property of the exponential tensor function gives in this case $\det[\exp(\Delta\gamma^{tr}\boldsymbol{N}_{tr})] = \exp[\mathrm{tr}(\Delta\gamma^{tr}\boldsymbol{N}_{tr})] = 1$. The incompressibility of $\boldsymbol{C}_{tr}$ is thereby guaranteed when the exponential integration scheme in (3.54) is used.

3.4.2 Symmetrization of tensors

Even though the exponential integration scheme (3.54) satisfies the incompressibility of deformation due to martensite orientation, it presents some disadvantages in numerical analysis. The first disadvantage is that due to the non-coaxiality of $\boldsymbol{C}_{tr}$ and $\boldsymbol{M}_t$, their product $\boldsymbol{B}_{tr}$ is generally not symmetric. This asymmetry causes the loss of an important property of exponential functions whereby the exponential of a symmetric tensor can be calculated in closed form by means of spectral decomposition. The closed form expression of $\exp(\boldsymbol{A})$ is given by

$$\exp(\boldsymbol{A}) = \sum_{i=1}^{3} \exp(A_i)\boldsymbol{n}_i \otimes \boldsymbol{n}_i, \tag{3.55}$$

where A_i and $\boldsymbol{n}_i$ are the eigenvalues and corresponding eigenvectors of the symmetric tensor $\boldsymbol{A}$.

Similarly, since $\exp(\Delta\gamma^{tr}\boldsymbol{N}_{tr})$ and $\boldsymbol{C}_n^{tr}$ are not coaxial, their product is not symmetric. This is expressed mathematically by the relation:

$$\exp\left(\Delta\gamma^{tr}\boldsymbol{N}_{tr}\right)\boldsymbol{C}_n^{tr} \neq \boldsymbol{C}_n^{tr}\exp\left(\Delta\gamma^{tr}\boldsymbol{N}_{tr}\right). \tag{3.56}$$

Hence, the second disadvantage of directly using exponential numerical integration (3.54) is the possible loss of symmetry in numerical calculation, which may result in immediate breakdown of the symmetry balance. In order to avoid these disadvantages, (3.54) must be symmetrized.

In order to address this issue, Reese and Christ (2008) proposed a exponential time-discrete scheme with guaranteed symmetry. This integration scheme was successfully used in subsequent work by Evangelista et al. (2010), Vladimirov et al. (2010) and others. The same approach applied to the time-discrete evolution equation (3.54), taking into account the equality $\boldsymbol{C}_{tr}\boldsymbol{C}_n^{tr\,-1}\boldsymbol{C}_{tr} = \exp(\Delta\gamma^{tr}\boldsymbol{N}_{tr})\boldsymbol{C}_{tr}$, gives

$$-\boldsymbol{C}_n^{tr\,-1} + \boldsymbol{U}_{tr}^{-1}\exp\left(\Delta\gamma^{tr}\boldsymbol{U}_{tr}^{-1}\boldsymbol{N}_{tr}\boldsymbol{U}_{tr}\right)\boldsymbol{U}_{tr}^{-1} = \boldsymbol{0}. \tag{3.57}$$

An alternative logarithmic time-integration procedure was proposed by Arghavani et al. (2011) and shown to provide improved robustness and efficiency compared to the work of Reese and Christ (2008). Thus, the exponential scheme in (3.57), taking into account the relations $[\exp(\Delta\gamma^{tr}\boldsymbol{U}_{tr}^{-1}\boldsymbol{N}_{tr}\boldsymbol{U}_{tr})]^{-1} = \exp(-\Delta\gamma^{tr}\boldsymbol{U}_{tr}^{-1}\boldsymbol{N}_{tr}\boldsymbol{U}_{tr})$, gives the following logarithmic time-discrete scheme:

$$\ln\left(\boldsymbol{U}_{tr}^{-1}\boldsymbol{C}_n^{tr}\boldsymbol{U}_{tr}^{-1}\right) + \Delta\gamma^{tr}\boldsymbol{G} = \boldsymbol{0}, \tag{3.58}$$

where $\boldsymbol{G} = \boldsymbol{U}_{tr}^{-1}\boldsymbol{N}_{tr}\boldsymbol{U}_{tr}$ is symmetric.

The time-discrete evolution equations (3.53) and (3.58), together with the loading functions (3.38) and (3.46), are used to construct the following system of nonlinear time-discrete constitutive equations

$$\begin{cases} r^{\chi} = \chi - \chi_n - \Delta\gamma^{\chi}\mathcal{S}(A_{\chi}) = 0, \\ \boldsymbol{r}^{tr} = \ln\left(\boldsymbol{U}_{tr}^{-1}\boldsymbol{C}_n^{tr}\boldsymbol{U}_{tr}^{-1}\right) + \Delta\gamma^{tr}\boldsymbol{G} = \boldsymbol{0}, \\ \mathcal{F}_{\chi} = |A_{\chi}| - \mathcal{Y}_{\chi} = 0, \\ \mathcal{F}_{tr} = \|\boldsymbol{B}_{tr}^{\mathrm{D}}\| - \mathcal{Y}_{tr} = 0, \end{cases} \tag{3.59}$$

which is solved using a Newton-Raphson method, taking into account the discrete Kuhn-Tucker conditions:

$$\begin{cases} \Delta\gamma^{\chi} \geq 0, \quad \mathcal{F}_{\chi} \leq 0, \quad \Delta\gamma^{\chi}\mathcal{F}_{\chi} = 0; \\ \Delta\gamma^{tr} \geq 0, \quad \mathcal{F}_{tr} \leq 0, \quad \Delta\gamma^{tr}\mathcal{F}_{tr} = 0. \end{cases} \tag{3.60}$$

For comparison with the implicit time-discrete formulation of the small-strain ZM model, the reader is referred to (Zaki, 2012; Gu et al., 2015).

3.4.3 Material and spatial tangent operators

Tangent operators used in the integration of the time-discrete equations are determined in two steps: a material tangent operator is first obtained by taking the material derivative of the constitutive relations in Lagrangian configuration; a spatial tangent is then obtained by a push-forward operation on the material tangent with the objective rates of Kirchhoff stress.

The material tangent is determined by differentiating the second Piola-Kirchhoff stress tensor to get

$$\mathrm{d}\boldsymbol{S} = \mathbb{D} : \mathrm{d}\boldsymbol{C}. \tag{3.61}$$

Using the definition of $\boldsymbol{S}$ in Table 3.1, $\mathrm{d}\boldsymbol{S}$ is then written in terms of $\boldsymbol{C}_t$, J and $\boldsymbol{C}$ as follows:

$$\mathrm{d}\boldsymbol{S} = \frac{\partial \boldsymbol{S}}{\partial J} \cdot \mathrm{d}J + \frac{\partial \boldsymbol{S}}{\partial \boldsymbol{C}_t} : \mathrm{d}\boldsymbol{C}_t + \frac{\partial \boldsymbol{S}}{\partial \boldsymbol{C}} : \mathrm{d}\boldsymbol{C}, \tag{3.62}$$

with

$$\frac{\partial \boldsymbol{S}}{\partial J} = \frac{\lambda}{J}\boldsymbol{C}^{-1}, \quad \frac{\partial \boldsymbol{S}}{\partial \boldsymbol{C}_t} = \mu\mathbb{S}, \quad \frac{\partial \boldsymbol{S}}{\partial \boldsymbol{C}} = (\lambda \ln J - \mu)\,\mathbb{T}. \tag{3.63}$$

In the above equations, $\mathbb{S} = \partial \boldsymbol{C}_t^{-1}/\partial \boldsymbol{C}_t$ and $\mathbb{T} = \partial \boldsymbol{C}^{-1}/\partial \boldsymbol{C}$ are fourth-order tensors, the components of which are given by

$$\mathbb{S}_{ijkl} = -{C_{ik}^t}^{-1}{C_{lj}^t}^{-1} \quad \text{and} \quad \mathbb{T}_{ijkl} = -C_{ik}^{-1}C_{lj}^{-1}. \tag{3.64}$$

Using the definition $J = \det\boldsymbol{F} = \sqrt{\det\boldsymbol{C}}$ as well as equations (3.31) and (3.45) leads to the following material derivatives of J, $\boldsymbol{C}_t$ and $\boldsymbol{C}_{tr}$:

$$\begin{cases} \mathrm{d}J = \frac{1}{2}J\boldsymbol{C}^{-1} : \mathrm{d}\boldsymbol{C}, \\ \mathrm{d}\boldsymbol{C}_t = (\boldsymbol{C}_{tr} - \boldsymbol{1}) \cdot \mathrm{d}\chi + \chi \cdot \mathrm{d}\boldsymbol{C}_{tr}, \\ \mathrm{d}\boldsymbol{C}_{tr} = \mathrm{d}\gamma^{tr}\boldsymbol{N}_{tr}\boldsymbol{C}_{tr}. \end{cases} \tag{3.65}$$

Substituting $(3.65)_3$ into $(3.65)_2$ gives

$$\mathrm{d}\boldsymbol{C}_t = (\boldsymbol{C}_{tr} - \boldsymbol{1}) \cdot \mathrm{d}\chi + \chi\boldsymbol{N}_{tr}\boldsymbol{C}_{tr} \cdot \mathrm{d}\gamma^{tr}. \tag{3.66}$$

The loading conditions for phase transformation and martensite orientation are differentiated as follows:

$$\begin{cases} \mathcal{F}^{\chi}_{,\chi} \cdot \mathrm{d}\chi + \mathcal{F}^{\chi}_{,\boldsymbol{C}_{tr}} : \mathrm{d}\boldsymbol{C}_{tr} + \mathcal{F}^{\chi}_{,\boldsymbol{C}} : \mathrm{d}\boldsymbol{C} = 0, \\ \mathcal{F}^{tr}_{,\chi} \cdot \mathrm{d}\chi + \mathcal{F}^{tr}_{,\boldsymbol{C}_{tr}} : \mathrm{d}\boldsymbol{C}_{tr} + \mathcal{F}^{tr}_{,\boldsymbol{C}} : \mathrm{d}\boldsymbol{C} = 0. \end{cases} \tag{3.67}$$

Substituting equation $(3.65)_3$ into the above equations gives

$$\begin{cases} \mathcal{F}^{\chi}_{,\chi} \cdot \mathrm{d}\chi + \mathcal{F}^{\chi}_{,\boldsymbol{C}_{tr}} : \boldsymbol{N}_{tr}\boldsymbol{C}_{tr} \cdot \mathrm{d}\gamma^{tr} + \mathcal{F}^{\chi}_{,\boldsymbol{C}} : \mathrm{d}\boldsymbol{C} = 0, \\ \mathcal{F}^{tr}_{,\chi} \cdot \mathrm{d}\chi + \mathcal{F}^{tr}_{,\boldsymbol{C}_{tr}} : \boldsymbol{N}_{tr}\boldsymbol{C}_{tr} \cdot \mathrm{d}\gamma^{tr} + \mathcal{F}^{tr}_{,\boldsymbol{C}} : \mathrm{d}\boldsymbol{C} = 0. \end{cases} \tag{3.68}$$

The following expressions of $\mathrm{d}\chi$ and $\mathrm{d}\gamma^{tr}$ are then obtained:

$$\mathrm{d}\chi = \frac{(\mathcal{F}^{\chi}_{,\boldsymbol{C}_{tr}} : \boldsymbol{N}_{tr}\boldsymbol{C}_{tr})(\mathcal{F}^{tr}_{,\boldsymbol{C}} : \mathrm{d}\boldsymbol{C}) - (\mathcal{F}^{tr}_{,\boldsymbol{C}_{tr}} : \boldsymbol{N}_{tr}\boldsymbol{C}_{tr})(\mathcal{F}^{\chi}_{,\boldsymbol{C}} : \mathrm{d}\boldsymbol{C})}{\mathcal{F}^{\chi}_{,\chi}(\mathcal{F}^{tr}_{,\boldsymbol{C}_{tr}} : \boldsymbol{N}_{tr}\boldsymbol{C}_{tr}) - \mathcal{F}^{tr}_{,\chi}(\mathcal{F}^{\chi}_{,\boldsymbol{C}_{tr}} : \boldsymbol{N}_{tr}\boldsymbol{C}_{tr})}, \tag{3.69}$$

$$\mathrm{d}\gamma^{tr} = \frac{\mathcal{F}^{tr}_{,\chi}(\mathcal{F}^{\chi}_{,\boldsymbol{C}} : \mathrm{d}\boldsymbol{C}) - \mathcal{F}^{\chi}_{,\chi}(\mathcal{F}^{tr}_{,\boldsymbol{C}} : \mathrm{d}\boldsymbol{C})}{\mathcal{F}^{\chi}_{,\chi}(\mathcal{F}^{tr}_{,\boldsymbol{C}_{tr}} : \boldsymbol{N}_{tr}\boldsymbol{C}_{tr}) - \mathcal{F}^{tr}_{,\chi}(\mathcal{F}^{\chi}_{,\boldsymbol{C}_{tr}} : \boldsymbol{N}_{tr}\boldsymbol{C}_{tr})}, \tag{3.70}$$

which can be equivalently written as

$$\mathrm{d}\chi = \boldsymbol{P} : \mathrm{d}\boldsymbol{C} \quad \text{and} \quad \mathrm{d}\gamma^{tr} = \boldsymbol{Q} : \mathrm{d}\boldsymbol{C}, \tag{3.71}$$

where $\boldsymbol{P}$ and $\boldsymbol{Q}$ are second-order tensors. With the help of these tensors, equation (3.66) can be expressed as

$$\mathrm{d}\boldsymbol{C}_t = ((\boldsymbol{C}_{tr} - \boldsymbol{1}) \otimes \boldsymbol{P}) : \mathrm{d}\boldsymbol{C} + \chi\,(\boldsymbol{N}_{tr}\boldsymbol{C}_{tr} \otimes \boldsymbol{Q}) : \mathrm{d}\boldsymbol{C}. \tag{3.72}$$

The material tangent $\mathbb{D}$ is then obtained by substituting $\mathrm{d}J$ and $\mathrm{d}\boldsymbol{C}_t$ into equation (3.62) to get

$$\begin{aligned} \mathrm{d}\boldsymbol{S} = &\frac{\lambda}{2}\boldsymbol{C}^{-1} \otimes \boldsymbol{C}^{-1} : \mathrm{d}\boldsymbol{C} - (\lambda \ln J - \mu)\,\boldsymbol{C}^{-1}[\mathrm{d}\boldsymbol{C}]\boldsymbol{C}^{-1} - \\ &\mu\boldsymbol{C}_t^{-1}\left\{[(\boldsymbol{C}_{tr} - \boldsymbol{1}) \otimes \boldsymbol{P} + \chi\,(\boldsymbol{N}_{tr}\boldsymbol{C}_{tr} \otimes \boldsymbol{Q})] : \mathrm{d}\boldsymbol{C}\right\}\boldsymbol{C}_t^{-1}, \end{aligned} \tag{3.73}$$

which gives

$$\mathbb{D} = \frac{\lambda}{2}\boldsymbol{C}^{-1} \otimes \boldsymbol{C}^{-1} + \mu\mathbb{S} : [(\boldsymbol{C}_{tr} - \boldsymbol{1}) \otimes \boldsymbol{P} + \chi\,(\boldsymbol{N}_{tr}\boldsymbol{C}_{tr} \otimes \boldsymbol{Q})] + (\lambda \ln J - \mu)\,\mathbb{T}. \tag{3.74}$$

The implicit integration of the finite-strain model in Abaqus/Standard requires the specification of a spatial tangent operator based on the objective Jaumann rate of the Kirchhoff stress:

$$\mathring{\boldsymbol{\tau}} = \dot{\boldsymbol{\tau}} - \boldsymbol{W}\boldsymbol{\tau} + \boldsymbol{\tau}\boldsymbol{W}, \tag{3.75}$$

where $\boldsymbol{\tau} = J\boldsymbol{\sigma}$ is the Kirchhoff stress tensor and $\boldsymbol{W} = \frac{1}{2}(\boldsymbol{L} - \boldsymbol{L}^T)$ is the spin tensor. In contrast, the following Green-Naghdi stress rate is used for structural elements:

$$\overset{\nabla}{\boldsymbol{\tau}} = \dot{\boldsymbol{\tau}} - \dot{\boldsymbol{R}}\boldsymbol{R}^T\boldsymbol{\tau} + \boldsymbol{\tau}\dot{\boldsymbol{R}}\boldsymbol{R}^T, \tag{3.76}$$

where $\boldsymbol{R}$ is the rotation tensor. Both $\mathring{\boldsymbol{\tau}}$ and $\overset{\triangledown}{\boldsymbol{\tau}}$ are special cases of the Oldroyd stress rate $\overset{\diamond}{\boldsymbol{\tau}}$ (Lie time derivative of the Kirchhoff stress), expressed as

$$\overset{\diamond}{\boldsymbol{\tau}} = \dot{\boldsymbol{\tau}} - \boldsymbol{L}\boldsymbol{\tau} - \boldsymbol{\tau}\boldsymbol{L}^T, \tag{3.77}$$

where $\boldsymbol{L} = \dot{\boldsymbol{F}}\boldsymbol{F}^{-1}$ is the velocity gradient. Indeed, $\mathring{\boldsymbol{\tau}}$ corresponds to $\overset{\diamond}{\boldsymbol{\tau}}$ with the rate of deformation tensor $\boldsymbol{D}$ set to be zero, while $\overset{\triangledown}{\boldsymbol{\tau}}$ corresponds to $\overset{\diamond}{\boldsymbol{\tau}}$ with deformation gradient $\boldsymbol{F}$ substituted with the rotation tensor $\boldsymbol{R}$.

Taking the time derivative of the relation $\boldsymbol{\tau} = \boldsymbol{F}\boldsymbol{S}\boldsymbol{F}^T$ and substituting into the expression of the Oldroyd stress rate (3.77), gives

$$\overset{\diamond}{\boldsymbol{\tau}} = \boldsymbol{F}\dot{\boldsymbol{S}}\boldsymbol{F}^T. \tag{3.78}$$

Moreover, equations $\dot{\boldsymbol{S}} = \mathbb{D} : \dot{\boldsymbol{C}}$ and $\dot{\boldsymbol{C}} = 2\boldsymbol{F}^T\boldsymbol{D}\boldsymbol{F}$ give

$$\boldsymbol{F}^{-1}\overset{\diamond}{\boldsymbol{\tau}}\boldsymbol{F}^{-T} = \mathbb{D} : 2\boldsymbol{F}^T\boldsymbol{D}\boldsymbol{F}. \tag{3.79}$$

The spatial tangent $\mathbb{C}$, such that

$$\overset{\diamond}{\boldsymbol{\tau}} = \mathbb{C} : \boldsymbol{D}, \tag{3.80}$$

is then given by the following expression:

$$\begin{aligned}\mathbb{C} =& 2(\mu - \lambda \ln J)\mathbb{I} + \lambda \mathbf{1} \otimes \mathbf{1} - 2\mu \boldsymbol{F}\boldsymbol{C}_t^{-1}(\boldsymbol{C}_{tr} - \mathbf{1})\boldsymbol{C}_t^{-1}\boldsymbol{F}^T \otimes \boldsymbol{F}\boldsymbol{P}\boldsymbol{F}^T - \\ & 2\chi\mu \boldsymbol{F}\boldsymbol{C}_t^{-1}\boldsymbol{N}_{tr}\boldsymbol{C}_{tr}\boldsymbol{C}_t^{-1}\boldsymbol{F}^T \otimes \boldsymbol{F}\boldsymbol{Q}\boldsymbol{F}^T.\end{aligned} \tag{3.81}$$

where $\mathbb{I}$ is the fourth-order identity tensor.

3.5 Numerical simulation

The numerical integration scheme presented in the previous section is implemented into Abaqus/Standard by means of a UMAT subroutine. Several numerical simulations are carried out and compared to experimental data in different loading cases. The following examples are considered: (i) a single mesh hexahedral element subjected to uniaxial and non-proportional loadings; (ii) comparisons between the finite-strain model and the original ZM model; (iii) shape memory effect of SMA subjected to a thermomechanical loading; (iv) simulation of a SMA orthodontic archwire undergoing extensive strains and rotations.

3.5.1 Uniaxial proportional loading

A single hexahedral element (1 mm×1 mm×1 mm) subjected to uniaxial tensile loading is simulated at temperatures 293 K and 333 K. The tensile loading consists of uniform negative pressure applied on the top surface of the element with symmetry conditions prescribed on the bottom surface as well as on the

two adjacent side surfaces. The pressure is increased in magnitude from zero to the maximum value then removed. The maximum pressure is set to 600 MPa at 293 K and 1000 MPa at 333 K. The model parameters used for the simulation are determined from the experimental data reported in (Moumni et al., 2008) and listed in Table 3.2.

Table 3.2 Model parameters used in the uniaxial proportional simulations.

Parameter	Value	Unit	Parameter	Value	Unit
μ^A	15923	MPa	λ^A	23885	MPa
μ^M	6500	MPa	λ^M	9750	MPa
α	588.24	MPa	β	3186.3	MPa
Y	265	MPa	C	1.75	-
a	28.21	MPa	b	27.62	MPa
G	37.3	MPa	ξ	0.4398	MPa/K
A_f^0	313	K	$\mathcal{K}$	12.63	MPa

The simulated stress-strain curves are reported in Fig. 3.1(a) at temperature 293 K and in Fig. 3.1(b) at temperature 333 K. In the first case, because the prescribed temperature is well below the austenite finish temperature A_f^0, the transformation strains are not recovered upon unloading. In the second case, however, in which $\theta > A_f^0$, the transformation strains are completely recovered by way of pseudoelasticity. In both cases, the simulation results are in good agreement with the experimental data.

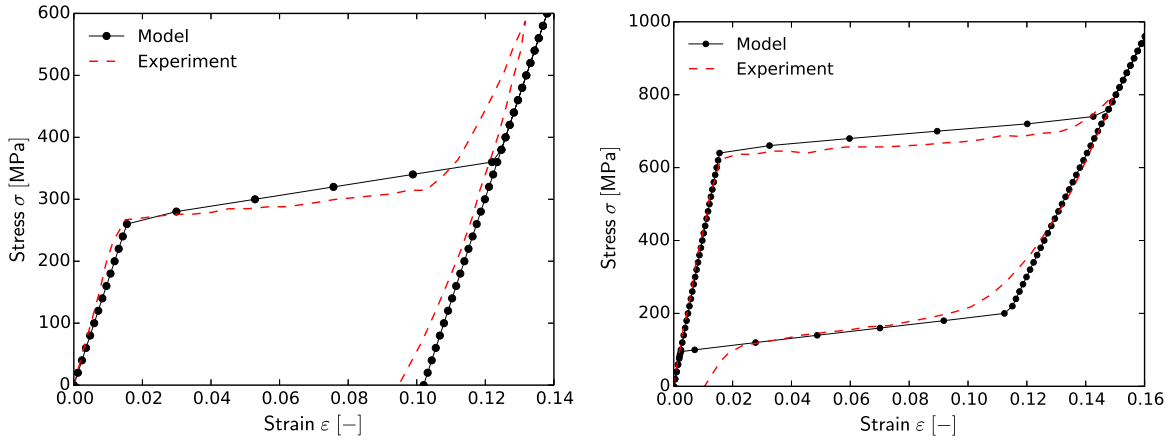

(a) (b)

Figure 3.1 Simulated results vs. experimental data under uniaxial loading: (a) martensite orientation at temperature 293 K, (b) pseudoelasticity at temperature 333 K.

3.5.2 Multiaxial non-proportional loading

Following Stebner and Brinson (2013) and Gu et al. (2015), the single hexahedral element is simulated considering multiaxial non-proportional loading consisting of combined axial and shear loadings. The model parameters used for the simulation are taken from Gu et al. (2015) and listed in Table 3.3. The

loading is strain-controlled, corresponding to the path in Fig. 3.2(a) where the maximum strain of 4% is achieved in tension/compression and in shear. Starting from an unloaded state, the hexahedral element undergoes tension, shear, compression, then reverse shear until all strain is recovered. The material response in this case shows pronounced nonlinearity, commonly reported for SMAs subjected to non-proportional loading. The simulation results in terms of shear vs. normal stress are reported in figure 3.2(b) and compared to the results of Stebner and Brinson (2013) and Gu et al. (2015). Overall, the results are in agreement, more so with those of Gu et al. (2015), which were obtained using the original small-strain ZM model. The most pronounced deviation is observed during shear strain reversal. This is mainly because the angle between the orientation direction of martensite variants and the driving force direction is neglected at high values of the volume fraction χ. Consequently, the orientation strain tensor becomes aligned with the thermodynamic driving force.

Table 3.3 Model parameters used in the multiaxial box-shaped simulation.

Parameter	Value	Unit	Parameter	Value	Unit
μ^A	31798	MPa	λ^A	47698	MPa
μ^M	13462	MPa	λ^M	20192	MPa
α	789.5	MPa	β	3421	MPa
Y	265	MPa	C	1.735	-
a	4.79	MPa	b	5.39	MPa
G	4.48	MPa	ξ	0.19	MPa/K
A_f^0	313	K	$\mathcal{K}$	2.32	MPa

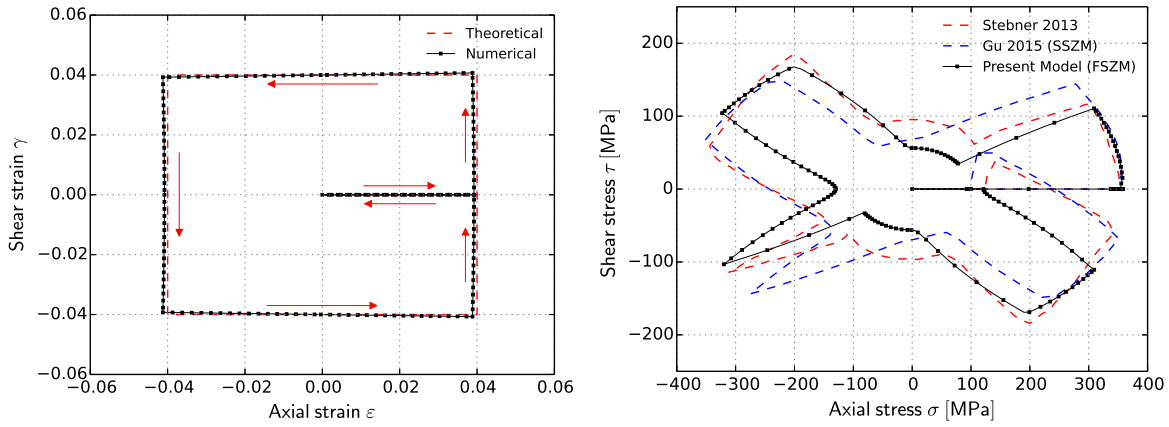

(a) (b)

Figure 3.2 Biaxial strain-controlled box-shaped loading test: (a) axial-shear loading path, (b) comparison of the simulated stress response with the results of Stebner and Brinson (2013) and Gu et al. (2015).

The evolution of the von Mises equivalent stress and the martensite volume fraction with time is plotted in Fig. 3.3. The results correlate well with those of Gu et al. (2015). Compared to the work of Stebner and Brinson (2013), however, lower values of the von Mises stress are obtained at approximate time instants 2–3, 5, and 6–7, and higher values of the martensite volume fraction at approximate time

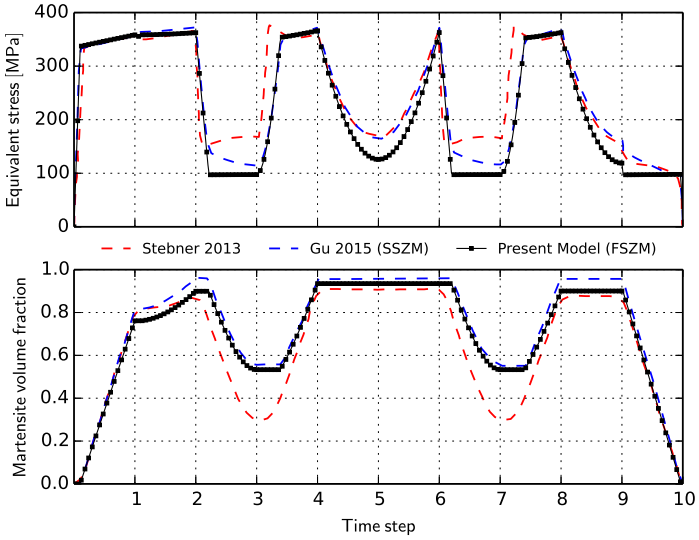

Figure 3.3 Evolution of the von Mises equivalent stress and the martensite volume fraction with time step.

instants 3 and 7. The deviation in this case is due to intrinsic differences in the formulation of the two models, including the expressions of the loading functions and interaction energies.

3.5.3 Comparison of the finite-strain model with the original ZM model

To illustrate the superiority of the present finite-strain model, simulation results involving large deformation and rotation are compared to those of the original ZM model. As a first example, the hexahedral element in section 3.5.1 is simulated using both models. The applied stress-displacement response in Fig. 3.4 shows increased deviation with increasing displacement as the validity of the small-strain assumption breaks down.

The observed deviation in the above example is mitigated by the absence of rotation. To illustrate the improved accuracy of the present model with increasing rotation as well as strain, an example of a SMA beam subjected to bending is considered. The dimensions of the beam are 200 mm×20 mm×10 mm. The boundary conditions are such that one end of the beam is fixed while the second is subjected to a downward acting force magnitude of 8 KN. Three sets of simulations are carried out using the two models: (a) original ZM model with NLGEOM OFF, (b) original ZM model with NLGEOM ON, (c) present finite-strain model. NLGEOM option is usually used in Abaqus to consider small strains but large rotations. The deformed beam and the contours of the volume fraction χ within are shown in Fig. 3.5. From the figures, the result obtained using the original ZM model with NLGEOM OFF shows exaggerated increase in element size and abnormal deformation in the transverse direction in the beam. The loading end is deflected downward with no horizontal displacement, which is in strong contrast with the results obtained using the ZM model with NLGEOM ON and the present finite strain model. Further deviation is observed when comparing the extent of phase transformation predicted by the two models,

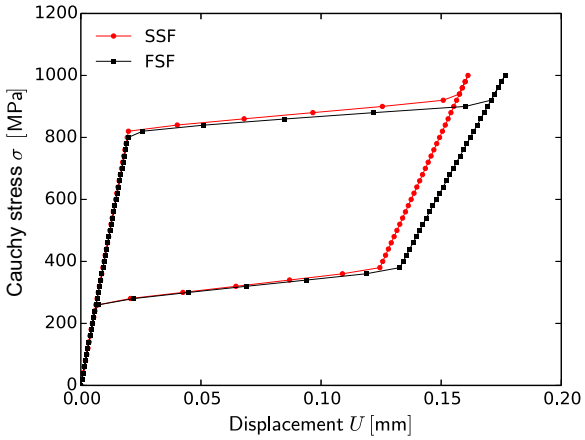

Figure 3.4 Simulation results using the present finite-strain formulation (FSF) model and the small-strain formulation (SSF) ZM model.

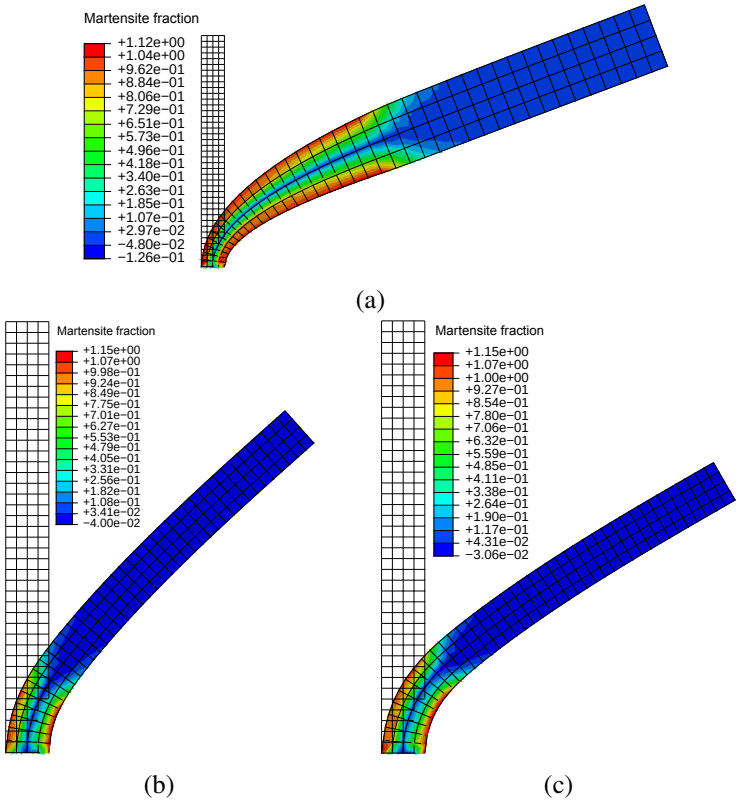

Figure 3.5 Deformation of the SMA beam in bending: (a) original ZM model with NLGEOM OFF, (b) original ZM model with NLGEOM ON, (c) present finite-strain model.

for which the simulated propagation of martensite into the volume of the beam is strongly exaggerated by the original ZM model with NLGEOM OFF. A possible explanation is that the absence of finite rotation makes for a less compliant beam that tends to deform inelastically in a more pronounced way to

accommodate the stress field generated by the applied loading. The result obtained using the original ZM model with NLGEOM ON shows more accuracy on both deformations and evolution of martensite volume fraction. However, it is still somewhat stiff compared to the result obtained by the present model.

3.5.4 Simulation of shape memory effect

In order to demonstrate the the model capability in predicting the shape memory effect of SMAs, the material subjected to a thermomechanical loading is simulated and the stress-strain-temperature response is shown in Fig. 3.6. At a temperature of 300 K, the material is loaded from zero to the maximum stress 360 MPa. The martensite variants are fully orientated in this magnitude of applied stress. A mechanically unrecoverable residual strain on the value of 4% is obtained by unloading the stress to zero and keeping the temperature constant. The unstressed material then is heated from the temperature of 300 K to 340 K. The strain starts recovery at the temperature of 314 K, which is the austenite start temperature A_s^0. Finally, the strain is fully recovered after heating the material above the austenite finish temperature $A_f^0 = 332$ K.

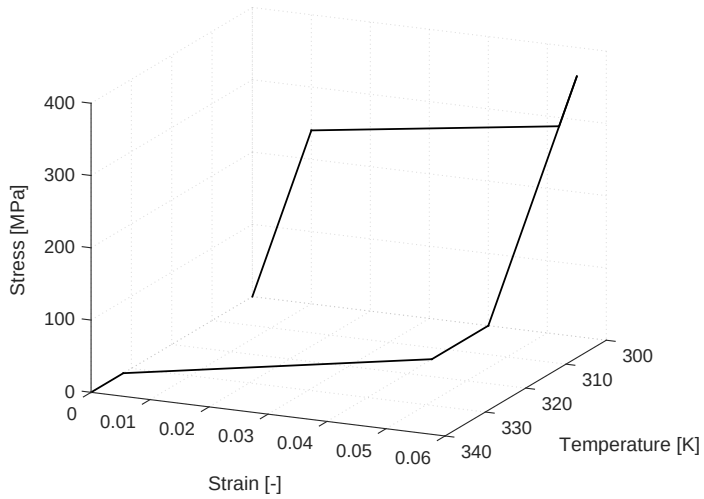

Figure 3.6 Model prediction of the shape memory effect.

3.5.5 Application to the simulation of an orthodontic archwire

The present model is used to simulate a SMA orthodontic archwire with the initial geometry shown in Fig. 3.7, with 1 mm×1 mm rectangular cross-section. The archwire is subjected to a force F that increases from zero to 45 N then decreases back to zero. Because of symmetry about the vertical centroidal axis, only one half of the structure is considered in the simulation. The results in Fig. 3.8(a) and (b) illustrate the contours of von Mises stress and martensite volume fraction in the structure at maximum deformation, at which large strain and rotation are observed. Maximum phase transformation is achieved, expectedly, at the location of the maximum von Mises stress. It is worth noting that values

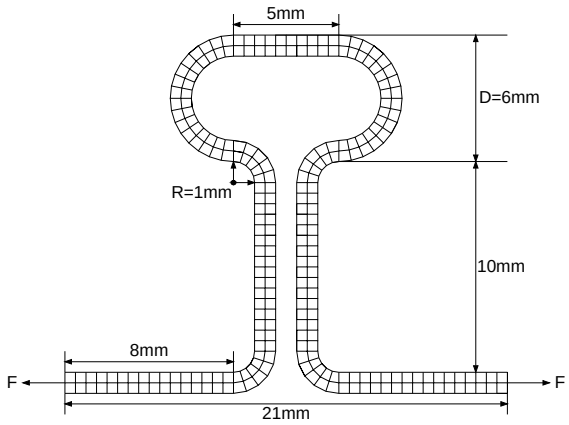

Figure 3.7 Initial geometry and dimension of the SMA orthodontic archwire.

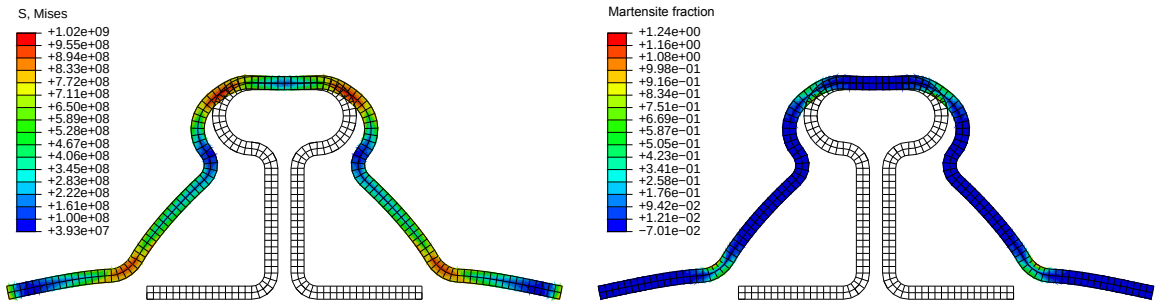

(a) (b)

Figure 3.8 Orthodontic archwire at maximum deformation: (a) von Mises stress contour plot, (b) martensite volume fraction χ contour plot.

of martensite volume fraction reported in Fig. 3.8(b) are outside interval [0,1], which is a result of data interpolation carried out by Abaqus for representing the volume fraction contours. The actual values at individual integration points are well within the interval [0,1]. Additionally, the force-displacement curve at the point of application of the load is reported in Fig. 3.9. The curve shows complete shape recovery upon unloading, even though the shape of the curve itself is quite different from that of the uniaxial force-displacement response.

3.6 Conclusion

In this chapter, a finite-strain constitutive model for SMAs is developed by generalizing the small-strain ZM model. The derivation of the finite-strain model is based on a multiplicative decomposition of the deformation gradient into elastic and transformation parts as well as a further decomposition of

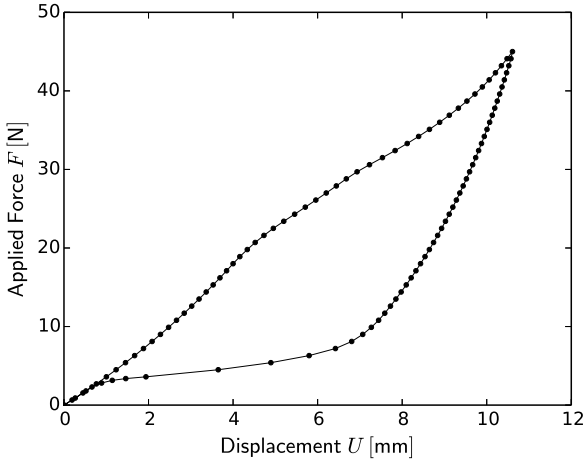

Figure 3.9 Pseudoelastic force vs. displacement response of the SMA archwire at the point of application of the load.

transformation deformation into phase transformation and martensite reorientation parts. Constitutive equations are derived within a thermodynamically consistent framework involving the Clausius-Duhem entropy inequality, the Helmholtz free energy density and the pseudo-potential of dissipation. Numerical implementation is performed including the logarithmic map integration, the symmetrization of tensors as well as the proper derivation of the material and spatial tangent operators. The numerical integration scheme then is implemented into the commercial FEA software Abaqus/Standard by using a UMAT subroutine. Finally, finite element simulations are carried out and discussed in comparison with the experimental data under different loading cases. An application example involving a SMA archwire subjected to large strains and rotations is also presented.

With this finite-strain extension of the ZM model, a more accurate prediction of the mechanical behavior of SMAs undergoing large strains and rotations is achieved. However, this prediction will be valid only for quasi-static isothermal loading cases. Indeed, experimental evidence suggests that phase transformation in SMAs is a thermomechanically coupled process, with internal heat production due to the latent heat and intrinsic dissipation. Meanwhile, the mechanical behavior of SMAs is strongly influenced by temperature. This thermomechanical coupling effect will be the topic of the next chapter.

Chapter 4

A thermomechanically coupled Hencky-strain model

4.1 Introduction

This chapter introduces the second step of the comprehensive constitutive modeling approach to investigate thermomechanical and cyclic behavior of SMAs in finite deformation. In order to take into account the strong thermomechanical coupling effect in SMAs, a new thermomechanically coupled, finite-strain model is developed based on Hencky strain in this chapter.

The Hencky strain measure, sometimes referred to as logarithmic or nature strain, has been used in constitutive modeling of solids due to its remarkable properties in large deformations (Arghavani et al., 2011). Among the usual finite strain measures, the Hencky strain has two important features: (i) only Hencky strain maps the volumetric and isochoric parts of the deformation gradient onto the pure spherical and deviatoric strain measures, which allows straightforward additive split of the total strain (Xiao et al., 2004) (ii) the logarithmic corotational rate of the Eulerian Hencky strain is the stretching tensor $\boldsymbol{D}$ (Reinhardt and Dubey, 1996), which makes it conjugate to the Cauchy stress in finite strain formulations. Hence, the kinematics description of the model characterizes a decomposition of the Hencky strain into elastic, transformation and thermal parts, and a decomposition of the transformation stretching into phase transformation and martensite reorientation components. The model incorporates three important characteristics of SMA behavior that have not been concurrently addressed in previous work.

First, the model accounts for the effect of coexistence between austenite, single-variant and multi-variant martensites, which is often neglected in the most SMA models (Zaki and Moumni, 2007b; Lagoudas et al., 2012; Paranjape et al., 2016). As a result, these models do not account properly for thermomechanical SMA behavior in situations involving coexistence of the three phases. At high stress level, phase transformation takes place only between austenite and single-variant martensite as temperature varies, whereas at low or moderate stress levels austenite transforms into both single-variant and multi-variant martensites and vice versa (Wu et al., 2003). The coexistence of these three

phases leads to the unsaturation of transformation strain, which could impact the utilization of SMA, *e.g.*, as actuators. Efforts to model this effect consisted in considering separate volume fractions for self-accommodated and reoriented martensite (Zaki and Moumni, 2007b; Auricchio et al., 2014), or relating the magnitude of the transformation strain to the applied stress level (Lagoudas et al., 2012). The modeling approach in this work consists in introducing two scalar variables to represent the volume fractions of multi-variant and single-variant martensites. The associated evolution rules and yield functions are derived separately and can be active simultaneously upon thermomechanical loading.

Secondly, the model considers the variation with temperature of the hysteresis size, which is also rarely addressed by current models despite experimental evidence (Shaw and Kyriakides, 1995). The hysteresis area can be physically interpreted as the amount of energy dissipated due to irreversible processes during phase transformation. In some models, the variation of this area with temperature is accounted for by introducing different temperature influence coefficients for the forward and reverse transformations (Saleeb et al., 2011; Sedlák et al., 2012; Lagoudas et al., 2012). However, the underlying thermodynamics of such variation have been largely left unaddressed. In this work, the hysteresis size is controlled by the entropy difference $\Delta\eta_t$ between different phases, which is related to latent heat and transformation temperatures. The forward entropy difference $\Delta\eta_f$ and the reverse entropy difference $\Delta\eta_r$ are determined, respectively, in terms of the forward transformation temperature θ_{AM} and reverse transformation temperature θ_{MA}.

Finally, the model can capture the smooth transition at the initiation and completion of phase transformation in polycrystalline SMAs. This smooth and gradual transition, compared to the abrupt transition in single-crystalline and untrained polycrystalline SMAs (Shaw and Kyriakides, 1995; Patoor et al., 2006), is experimentally observed in trained polycrystalline SMAs (Sittner et al., 1995; Grabe and Bruhns, 2008). To account for the smooth transition, several transformation hardening functions were proposed in the literature, including exponential (Tanaka et al., 1986), trigonometric (Liang and Rogers, 1990), power law functions (Lagoudas et al., 2012), etc. In many cases, however, the introduction of these functions result in significant increase in the number of model parameters without achieving the desired accuracy. In the present work, a unique tangential transformation hardening function g^t featuring only 5 parameters is introduced to describe smooth transformation in polycrystalline SMAs to a good degree of accuracy.

Incorporating these three characteristics, a thermodynamically consistent framework and a Helmholtz free energy including elastic, thermal, interaction and constraint components, are constructed to derive constitutive equations. Time-discrete formulation of the model and a Hencky-strain return-mapping integration algorithm are proposed. The algorithm is then implemented in FEA software Abaqus/Explicit by means of a explicit user-defined material subroutine (VUMAT). Simulation results using this model are validated against experimental data obtained under various thermomechanical loading conditions. The robustness and efficiency of the proposed framework are illustrated by simulating a SMA helical spring actuator subjected to complex thermomechanical loading and boundary conditions.

4.2 A thermomechanically coupled model based on Hencky strain

In this section, on the basis of a multiplicative decomposition of deformation gradient $\boldsymbol{F}$ into elastic $\boldsymbol{F}_e$, transformation $\boldsymbol{F}_t$ and thermal $\boldsymbol{F}_\theta$ parts, a thermodynamically consistent framework and a Helmholtz free energy function are introduced. Then, a thermomechanically coupled constitutive model in terms of Hencky strains is derived to describe SMA behavior in presence of complex thermomechanical loading and boundary conditions.

4.2.1 Kinematics

In most SMA models (Reese and Christ, 2008; Arghavani et al., 2011; Auricchio et al., 2014; Xiao, 2014; Chatziathanasiou et al., 2016), the deformation gradient $\boldsymbol{F}$ is simply decomposed into elastic and inelastic parts. However, extensive experimental investigations have shown that phase transformation in SMA is a thermomechanically coupled process, which involves heat production and transfer due to latent heat and intrinsic dissipation (Shaw and Kyriakides, 1995; Grabe and Bruhns, 2008). Therefore, an extended multiplicative decomposition of the deformation gradient $\boldsymbol{F}$ into elastic $\boldsymbol{F}_e$, transformation $\boldsymbol{F}_t$ and thermal $\boldsymbol{F}_\theta$ parts is assumed here, such that

$$\boldsymbol{F} = \boldsymbol{F}_e\boldsymbol{F}_t\boldsymbol{F}_\theta, \quad J = J_eJ_tJ_\theta, \quad \bar{\boldsymbol{F}} = \bar{\boldsymbol{F}}_e\bar{\boldsymbol{F}}_t\bar{\boldsymbol{F}}_\theta, \tag{4.1}$$

where $\boldsymbol{F}_e$ is defined with respect to a local unstressed intermediate configuration, $\boldsymbol{F}_t$ is defined with respect to a thermally expanded intermediate configuration, and $\boldsymbol{F}_\theta$ is defined with respect to the reference configuration. $J_e = \det\boldsymbol{F}_e$, $J_t = \det\boldsymbol{F}_t$ and $J_\theta = \det\boldsymbol{F}_\theta$ denote the volume-changing deformations, $\bar{\boldsymbol{F}}_e$, $\bar{\boldsymbol{F}}_t$ and $\bar{\boldsymbol{F}}_\theta$ denote the volume-preserving deformations and $\det\bar{\boldsymbol{F}}_e = \det\bar{\boldsymbol{F}}_t = \det\bar{\boldsymbol{F}}_\theta = 1$.

Substituting equation (4.1) into the definition of the velocity gradient $\boldsymbol{L}$ in equation (3.22) gives the following additive split:

$$\boldsymbol{L} = \bar{\boldsymbol{L}} + \frac{1}{3}\dot{\delta}\mathbf{1} = \bar{\boldsymbol{L}}_e + \bar{\boldsymbol{F}}_e\left(\bar{\boldsymbol{L}}_t + \bar{\boldsymbol{F}}_t\bar{\boldsymbol{L}}_\theta\bar{\boldsymbol{F}}_t^{-1}\right)\bar{\boldsymbol{F}}_e^{-1} + \frac{1}{3}\left(\dot{\delta}_e + \dot{\delta}_t + \dot{\delta}_\theta\right)\mathbf{1}, \tag{4.2}$$

with

$$\bar{\boldsymbol{L}}_e = \dot{\bar{\boldsymbol{F}}}_e\bar{\boldsymbol{F}}_e^{-1}, \quad \bar{\boldsymbol{L}}_t = \dot{\bar{\boldsymbol{F}}}_t\bar{\boldsymbol{F}}_t^{-1}, \quad \bar{\boldsymbol{L}}_\theta = \dot{\bar{\boldsymbol{F}}}_\theta\bar{\boldsymbol{F}}_\theta^{-1}, \quad \dot{\delta}_e = \frac{\dot{J}_e}{J_e}, \quad \dot{\delta}_t = \frac{\dot{J}_t}{J_t}, \quad \dot{\delta}_\theta = \frac{\dot{J}_\theta}{J_\theta}, \tag{4.3}$$

where $\bar{\boldsymbol{L}}_e$, $\bar{\boldsymbol{L}}_t$ and $\bar{\boldsymbol{L}}_\theta$ are isochoric elastic, transformation and thermal velocity gradients, δ_e, δ_t and δ_θ are respective rates of volumetric deformations. Thus, the corresponding elastic, transformation and

thermal stretching and spin tensors are given as

$$\begin{aligned}
\boldsymbol{D}_e &= \operatorname{sym}(\boldsymbol{L}_e) = \bar{\boldsymbol{D}}_e + \frac{1}{3}\dot{\delta}_e \mathbf{1} \quad \text{and} \quad \boldsymbol{W}_e = \operatorname{skew}(\boldsymbol{L}_e), \\
\boldsymbol{D}_t &= \operatorname{sym}(\boldsymbol{L}_t) = \bar{\boldsymbol{D}}_t + \frac{1}{3}\dot{\delta}_t \mathbf{1} \quad \text{and} \quad \boldsymbol{W}_t = \operatorname{skew}(\boldsymbol{L}_t), \\
\boldsymbol{D}_\theta &= \operatorname{sym}(\boldsymbol{L}_\theta) = \bar{\boldsymbol{D}}_\theta + \frac{1}{3}\dot{\delta}_\theta \mathbf{1} \quad \text{and} \quad \boldsymbol{W}_\theta = \operatorname{skew}(\boldsymbol{L}_\theta).
\end{aligned} \tag{4.4}$$

With regard to the thermal and the transformation deformations, the following three kinematic assumptions are made:

1. First, the thermal deformation is assumed to be an isotropic thermal expansion, so that

$$\boldsymbol{F}_\theta = J_\theta^{\frac{1}{3}} \mathbf{1}. \tag{4.5}$$

   Hence, using equations $(4.4)_3$,

$$\boldsymbol{D}_\theta = \frac{1}{3}\dot{\delta}_\theta \mathbf{1} \quad \text{and} \quad \boldsymbol{W}_\theta = \mathbf{0}. \tag{4.6}$$

2. Second, the transformation deformation is assumed incompressible, that is

$$J_t = \det \boldsymbol{F}_t = 1 \quad \text{and} \quad \boldsymbol{F}_t = \bar{\boldsymbol{F}}_t. \tag{4.7}$$

   Hence, using equations$(4.3)_5$ and $(4.4)_2$,

$$\dot{\delta}_t = 0 \quad \text{and} \quad \boldsymbol{D}_t = \bar{\boldsymbol{D}}_t. \tag{4.8}$$

3. Last, for isotropic materials, the assumption of the irrotationality of inelastic flow is widely used in modern elasto-viscoplastic constitutive theories (Dafalias, 1984; Gurtin and Anand, 2005; Anand et al., 2009). Therefore, the transformation flow is assumed irrotational (zero transformation spin)

$$\boldsymbol{W}_t = \mathbf{0}. \tag{4.9}$$

   Hence, the transformation stretching tensor

$$\boldsymbol{D}_t = \boldsymbol{L}_t = \dot{\boldsymbol{F}}_t \boldsymbol{F}_t^{-1} \quad \text{and} \quad \dot{\boldsymbol{F}}_t = \boldsymbol{D}_t \boldsymbol{F}_t. \tag{4.10}$$

Using the above three kinematic assumptions, the stretching and spin tensors, $\boldsymbol{D}$ and $\boldsymbol{W}$, are written as

$$\boldsymbol{D} = \bar{\boldsymbol{D}}_e + \operatorname{sym}\left(\bar{\boldsymbol{F}}_e \boldsymbol{D}_t \bar{\boldsymbol{F}}_e^{-1}\right) + \frac{1}{3}\left(\dot{\delta}_e + \dot{\delta}_\theta\right)\mathbf{1} \quad \text{and} \quad \boldsymbol{W} = \boldsymbol{W}_e + \operatorname{skew}\left(\bar{\boldsymbol{F}}_e \boldsymbol{D}_t \bar{\boldsymbol{F}}_e^{-1}\right). \tag{4.11}$$

Using equation (3.14), the elastic, transformation and thermal right and left Cauchy-Green deformation tensors are written as

$$\boldsymbol{C}_e = \boldsymbol{F}_e^T \boldsymbol{F}_e = J_e^{\frac{2}{3}} \bar{\boldsymbol{C}}_e, \quad \boldsymbol{b}_e = \boldsymbol{F}_e \boldsymbol{F}_e^T = J_e^{\frac{2}{3}} \bar{\boldsymbol{b}}_e, \quad \boldsymbol{C}_t = \boldsymbol{F}_t^T \boldsymbol{F}_t, \quad \boldsymbol{b}_t = \boldsymbol{F}_t \boldsymbol{F}_t^T, \quad \boldsymbol{C}_\theta = \boldsymbol{b}_\theta = J_\theta^{\frac{2}{3}} \mathbf{1}, \tag{4.12}$$

where $\det \bar{\boldsymbol{C}}_e = \det \bar{\boldsymbol{b}}_e = 1$ and $\det \boldsymbol{C}_t = \det \boldsymbol{b}_t = 1$.

The Lagrangian and Eulerian Hencky strain tensors are respectively defined as

$$\boldsymbol{H} = \ln \boldsymbol{U} = \frac{1}{2} \ln \boldsymbol{C} = \bar{\boldsymbol{H}} + \frac{1}{3}\delta \mathbf{1} \quad \text{and} \quad \boldsymbol{h} = \ln \boldsymbol{V} = \frac{1}{2} \ln \boldsymbol{b} = \bar{\boldsymbol{h}} + \frac{1}{3}\delta \mathbf{1}, \tag{4.13}$$

where $\bar{\boldsymbol{H}} = \ln \bar{\boldsymbol{U}}$ and $\bar{\boldsymbol{h}} = \ln \bar{\boldsymbol{V}}$ are the deviatoric components and $\delta = \ln J$ the volumetric component of the Hencky strain. Using equation (4.13), the elastic, transformation and thermal Lagrangian and Eulerian Hencky strain tensors are written as

$$\begin{aligned} &\boldsymbol{H}_e = \frac{1}{2} \ln \boldsymbol{C}_e = \bar{\boldsymbol{H}}_e + \frac{1}{3}\delta_e \mathbf{1}, \quad \boldsymbol{h}_e = \frac{1}{2} \ln \boldsymbol{b}_e = \bar{\boldsymbol{h}}_e + \frac{1}{3}\delta_e \mathbf{1}, \\ &\boldsymbol{H}_t = \frac{1}{2} \ln \boldsymbol{C}_t, \quad \boldsymbol{h}_t = \frac{1}{2} \ln \boldsymbol{b}_t, \quad \boldsymbol{H}_\theta = \boldsymbol{h}_\theta = \frac{1}{3}\delta_\theta \mathbf{1}, \end{aligned} \tag{4.14}$$

where

$$\bar{\boldsymbol{H}}_e = \frac{1}{2} \ln \bar{\boldsymbol{C}}_e, \quad \bar{\boldsymbol{h}}_e = \frac{1}{2} \ln \bar{\boldsymbol{b}}_e, \quad \delta_e = \ln J_e, \quad \delta_\theta = \ln J_\theta. \tag{4.15}$$

By making use of equation (A.11), the logarithmic tensor function maps the unimodular tensors $\bar{\boldsymbol{C}}_e$, $\bar{\boldsymbol{b}}_e$, $\boldsymbol{C}_t$ and $\boldsymbol{b}_t$ onto the traceless tensors $\bar{\boldsymbol{H}}_e$, $\bar{\boldsymbol{h}}_e$, $\boldsymbol{H}_t$ and $\boldsymbol{h}_t$, *i.e.* $\operatorname{tr}(\bar{\boldsymbol{H}}_e) = \operatorname{tr}(\bar{\boldsymbol{h}}_e) = \operatorname{tr}(\boldsymbol{H}_t) = \operatorname{tr}(\boldsymbol{h}_t) = 0$.

4.2.2 Thermodynamic framework

The model is derived based on the principle of virtual power (PVP) in compliance with the first (energy balance) and second (entropy inequality) laws of thermodynamics. A reduced form of the energy balance between internal energy $\mathcal{E}$, internal stress power $\mathcal{P}_i$ and heat supply $\mathcal{Q}$ is written

$$\underbrace{\dot{\int_{\mathcal{B}} e_v \, \mathrm{d}V}}_{\dot{\mathcal{E}}} - \underbrace{\int_{\mathcal{B}} J\boldsymbol{\sigma} : \boldsymbol{D} \, \mathrm{d}V}_{\mathcal{P}_i} + \underbrace{\int_{\partial\mathcal{B}} \boldsymbol{q} \cdot \boldsymbol{n} \, \mathrm{d}S - \int_{\mathcal{B}} h_v \, \mathrm{d}V}_{\dot{\mathcal{Q}}} = 0, \tag{4.16}$$

where e_v and h_v are, respectively, the internal energy and heat source per unit volume in spatial configuration, $\boldsymbol{q}$ is the heat flux vector per unit area and $\boldsymbol{n}$ is the outward unit vector normal to the boundary in the spatial configuration.

Substituting the additive split of $\boldsymbol{D}$ $(4.11)_1$ into the internal stress power in equation (4.16) gives

$$J\boldsymbol{\sigma} : \boldsymbol{D} = p\dot{\delta}_e + p\dot{\delta}_\theta + \boldsymbol{s} : \bar{\boldsymbol{D}}_e + \bar{\boldsymbol{F}}_e^T \boldsymbol{s} \bar{\boldsymbol{F}}_e^{-T} : \boldsymbol{D}_t, \tag{4.17}$$

where p and $\boldsymbol{s}$ are the hydrostatic and deviatoric components of the Kirchhoff stress tensor, *i.e.*, $\boldsymbol{\tau} = J\boldsymbol{\sigma} = p\mathbf{1} + \boldsymbol{s}$.

Substituting equation (4.17) into equation (4.16) and localizing the obtained integral equation gives the following local form of the energy balance:

$$\dot{e}_v - \left(p\dot{\delta}_e + p\dot{\delta}_\theta + \boldsymbol{s} : \bar{\boldsymbol{D}}_e + \bar{\boldsymbol{F}}_e^T \boldsymbol{s} \bar{\boldsymbol{F}}_e^{-T} : \boldsymbol{D}_t\right) - h_v + \nabla \cdot \boldsymbol{q} = 0. \tag{4.18}$$

The local form of the Clausius-Duhem entropy inequality is expressed as

$$\dot{\eta}_v \theta - h_v + \nabla \cdot \boldsymbol{q} - \frac{1}{\theta} \boldsymbol{q} \cdot \nabla\theta \geq 0, \tag{4.19}$$

where η_v is the entropy per unit volume in the spatial configuration.

The Helmholtz free energy ψ per unit volume and its time derivative $\dot{\psi}$ in the spatial configuration are given by

$$\psi = e_v - \eta_v \theta \quad \text{and} \quad \dot{\psi} = \dot{e}_v - \dot{\eta}_v \theta - \eta_v \dot{\theta}. \tag{4.20}$$

Combining the local energy balance in equation (4.18), the local entropy inequality in equation (4.19) and the free energy in equation $(4.20)_2$ gives the following entropy inequality:

$$p\left(\dot{\delta}_e + \dot{\delta}_\theta\right) + \boldsymbol{s} : \bar{\boldsymbol{D}}_e + \bar{\boldsymbol{F}}_e^T \boldsymbol{s} \bar{\boldsymbol{F}}_e^{-T} : \boldsymbol{D}_t - \left(\dot{\psi} + \eta_v \dot{\theta}\right) - \frac{1}{\theta} \boldsymbol{q} \cdot \nabla\theta \geq 0. \tag{4.21}$$

The Helmholtz free energy per unit volume is assumed here to depend on the elastic deformation gradient $\boldsymbol{F}_e$ through the elastic Lagrangian Hencky strain $\boldsymbol{H}_e$, on the transformation deformation gradient $\boldsymbol{F}_t$ through the transformation Lagrangian Hencky strain $\boldsymbol{H}_t$, on the thermal deformation gradient $\boldsymbol{F}_\theta$ through the thermal Lagrangian Hencky strain $\boldsymbol{H}_\theta$, on scalar internal variables χ^M, χ^S, and on temperature θ as

$$\psi = \psi\left(\boldsymbol{H}_e, \boldsymbol{H}_t, \boldsymbol{H}_\theta, \chi^M, \chi^S, \theta\right), \tag{4.22}$$

where χ^M and χ^S are, respectively, volume fractions of multi-variant and single-variant martensites. The free energy ψ is assumed to be an isotropic function of $\boldsymbol{H}_e$, $\boldsymbol{H}_t$ and $\boldsymbol{H}_\theta$, which allows ψ to be expressed as the function of their argument invariants. As the Lagrangian and Eulerian Hencky strains share the same invariants, the Helmholtz free energy ψ can be written in terms of Eulerian Hencky strains as

$$\psi\left(\boldsymbol{H}_e, \boldsymbol{H}_t, \boldsymbol{H}_\theta, \chi^M, \chi^S, \theta\right) = \psi\left(\delta_e, \bar{\boldsymbol{h}}_e, \boldsymbol{h}_t, \delta_\theta, \chi^M, \chi^S, \theta\right). \tag{4.23}$$

Hence, the time derivative of ψ gives

$$\dot{\psi} = \frac{\partial\psi}{\partial\delta_e}\dot{\delta}_e + \frac{\partial\psi}{\partial\bar{\boldsymbol{h}}_e} : \dot{\bar{\boldsymbol{h}}}_e + \frac{\partial\psi}{\partial\boldsymbol{h}_t} : \dot{\boldsymbol{h}}_t + \frac{\partial\psi}{\partial\delta_\theta}\dot{\delta}_\theta + \frac{\partial\psi}{\partial\chi^M}\dot{\chi}^M + \frac{\partial\psi}{\partial\chi^S}\dot{\chi}^S + \frac{\partial\psi}{\partial\theta}\dot{\theta}. \tag{4.24}$$

Because of isotropy, the derivatives of the isotropic functions $\frac{\partial\psi}{\partial\bar{\boldsymbol{h}}_e}$ and $\frac{\partial\psi}{\partial\boldsymbol{h}_t}$ are symmetric and coaxial with $\bar{\boldsymbol{h}}_e$ and $\boldsymbol{h}_t$. Using the definition of the logarithmic corotational rate of the Eulerian Hencky strain in

equation (A.4) and equation (A.8),

$$\frac{\partial \psi}{\partial \bar{\boldsymbol{h}}_e} : \dot{\bar{\boldsymbol{h}}}_e = \frac{\partial \psi}{\partial \bar{\boldsymbol{h}}_e} : \mathring{\bar{\boldsymbol{h}}}_e^L = \frac{\partial \psi}{\partial \bar{\boldsymbol{h}}_e} : \bar{\boldsymbol{D}}_e \quad \text{and} \quad \frac{\partial \psi}{\partial \boldsymbol{h}_t} : \dot{\boldsymbol{h}}_t = \frac{\partial \psi}{\partial \boldsymbol{h}_t} : \mathring{\boldsymbol{h}}_t^L = \frac{\partial \psi}{\partial \boldsymbol{h}_t} : \boldsymbol{D}_t, \tag{4.25}$$

where $\mathring{\bar{\boldsymbol{h}}}_e^L$ and $\mathring{\boldsymbol{h}}_t^L$ are, respectively, the logarithmic corotational rates of the elastic and transformation Eulerian Hencky strains.

Substituting equations (4.24) and (4.25) into the entropy inequality (4.21) gives

$$\begin{aligned} &\left(p - \frac{\partial \psi}{\partial \delta_e}\right)\dot{\delta}_e + \left(p - \frac{\partial \psi}{\partial \delta_\theta}\right)\dot{\delta}_\theta + \left(\boldsymbol{s} - \frac{\partial \psi}{\partial \bar{\boldsymbol{h}}_e}\right) : \bar{\boldsymbol{D}}_e + \left(\bar{\boldsymbol{F}}_e^T \boldsymbol{s} \bar{\boldsymbol{F}}_e^{-T} - \frac{\partial \psi}{\partial \boldsymbol{h}_t}\right) : \boldsymbol{D}_t - \\ &\frac{\partial \psi}{\partial \chi^M}\dot{\chi}^M - \frac{\partial \psi}{\partial \chi^S}\dot{\chi}^S - \left(\frac{\partial \psi}{\partial \theta} + \eta_v\right)\dot{\theta} - \frac{1}{\theta}\boldsymbol{q} \cdot \nabla\theta \geq 0. \end{aligned} \tag{4.26}$$

For arbitrary thermodynamic processes, inequality (4.26) is guaranteed by the following choice of the constitutive equations with respect to p, $\boldsymbol{s}$ and η_v:

$$p = \frac{\partial \psi}{\partial \delta_e} = \frac{\partial \psi}{\partial \delta_\theta}, \quad \boldsymbol{s} = \frac{\partial \psi}{\partial \bar{\boldsymbol{h}}_e}, \quad \eta_v = -\frac{\partial \psi}{\partial \theta}, \tag{4.27}$$

and by the following inequalities, which ensure nonnegative intrinsic dissipation in arbitrary evolutions of the internal state variables $\boldsymbol{D}_t$, χ^M and χ^S, so that

$$\left(\bar{\boldsymbol{F}}_e^T \boldsymbol{s} \bar{\boldsymbol{F}}_e^{-T} - \frac{\partial \psi}{\partial \boldsymbol{h}_t}\right) : \boldsymbol{D}_t - \frac{\partial \psi}{\partial \chi^M}\dot{\chi}^M - \frac{\partial \psi}{\partial \chi^S}\dot{\chi}^S \geq 0, \tag{4.28}$$

as well as nonnegative dissipation due to heat conduction, so that

$$-\frac{1}{\theta}\boldsymbol{q} \cdot \nabla\theta \geq 0. \tag{4.29}$$

The following deviatoric Mandel stress tensor is defined with respect to the intermediate unstressed configuration:

$$\bar{\boldsymbol{M}}_e = \bar{\boldsymbol{F}}_e^T \boldsymbol{s} \bar{\boldsymbol{F}}_e^{-T} = \bar{\boldsymbol{C}}_e \bar{\boldsymbol{S}}_e, \tag{4.30}$$

where $\bar{\boldsymbol{S}}_e = \bar{\boldsymbol{F}}_e^{-1} \boldsymbol{s} \bar{\boldsymbol{F}}_e^{-T}$ is a new second Piola-Kirchhoff stress tensor defined with respect to the intermediate unstressed configuration. As $\boldsymbol{s}$ and $\bar{\boldsymbol{V}}_e$ commute, $\bar{\boldsymbol{M}}_e$ can be written as

$$\bar{\boldsymbol{M}}_e = \boldsymbol{R}_e^T \bar{\boldsymbol{V}}_e^T \boldsymbol{s} \bar{\boldsymbol{V}}_e^{-1} \boldsymbol{R}_e^{-T} = \boldsymbol{R}_e^T \boldsymbol{s} \boldsymbol{R}_e, \tag{4.31}$$

which is a symmetric and traceless tensor by rotating the deviatoric Kirchhoff stress $\boldsymbol{s}$ back into the intermediate unstressed configuration. Substituting $\bar{\boldsymbol{M}}_e$ into inequality (4.28) gives

$$\left(\bar{\boldsymbol{M}}_e - \boldsymbol{X}_t\right) : \boldsymbol{D}_t - \mathcal{Z}^M \dot{\chi}^M - \mathcal{Z}^S \dot{\chi}^S \geq 0, \tag{4.32}$$

with

$$\boldsymbol{X}_t = \frac{\partial \psi}{\partial \boldsymbol{h}_t}, \quad \mathcal{Z}^M = \frac{\partial \psi}{\partial \chi^M} \quad \text{and} \quad \mathcal{Z}^S = \frac{\partial \psi}{\partial \chi^S}. \tag{4.33}$$

Substituting equation (4.27) into equation (4.24) gives the following first Gibbs relation between the free energy ψ and the temperature θ as

$$\dot{\psi} + \eta_v \dot{\theta} = p\left(\dot{\delta}_e + \dot{\delta}_\theta\right) + \boldsymbol{s} : \dot{\bar{\boldsymbol{h}}}_e + \boldsymbol{X}_t : \dot{\boldsymbol{h}}_t + \mathcal{Z}^M \dot{\chi}^M + \mathcal{Z}^S \dot{\chi}^S, \tag{4.34}$$

with equation $(4.20)_2$, which yields the following second Gibbs relation between the internal energy e_v and the entropy η_v:

$$\dot{e}_v - \theta \dot{\eta}_v = p\left(\dot{\delta}_e + \dot{\delta}_\theta\right) + \boldsymbol{s} : \dot{\bar{\boldsymbol{h}}}_e + \boldsymbol{X}_t : \dot{\boldsymbol{h}}_t + \mathcal{Z}^M \dot{\chi}^M + \mathcal{Z}^S \dot{\chi}^S. \tag{4.35}$$

Combining equations (4.35) and (4.18) gives the following entropy relation:

$$\theta \dot{\eta}_v = h_v - \nabla \cdot \boldsymbol{q} + \left(\bar{\boldsymbol{M}}_e - \boldsymbol{X}_t\right) : \boldsymbol{D}_t - \mathcal{Z}^M \dot{\chi}^M - \mathcal{Z}^S \dot{\chi}^S. \tag{4.36}$$

The internal energy and entropy densities are assumed to depend on the same state variables as the Helmholtz free energy:

$$e_v = e\left(\delta_e, \bar{\boldsymbol{h}}_e, \boldsymbol{h}_t, \delta_\theta, \chi^M, \chi^S, \theta\right) \quad \text{and} \quad \eta_v = \eta\left(\delta_e, \bar{\boldsymbol{h}}_e, \boldsymbol{h}_t, \delta_\theta, \chi^M, \chi^S, \theta\right). \tag{4.37}$$

The specific heat capacity is defined as

$$c_v \overset{\text{def}}{=} \frac{\partial e\left(\delta_e, \bar{\boldsymbol{h}}_e, \boldsymbol{h}_t, \delta_\theta, \chi^M, \chi^S, \theta\right)}{\partial \theta}, \tag{4.38}$$

with equations (4.20) and $(4.27)_3$, which can be written as

$$c_v = \theta \frac{\partial \eta\left(\delta_e, \bar{\boldsymbol{h}}_e, \boldsymbol{h}_t, \delta_\theta, \chi^M, \chi^S, \theta\right)}{\partial \theta} = -\theta \frac{\partial^2 \psi\left(\delta_e, \bar{\boldsymbol{h}}_e, \boldsymbol{h}_t, \delta_\theta, \chi^M, \chi^S, \theta\right)}{\partial \theta^2}. \tag{4.39}$$

Therefore, from equations (4.37), $(4.27)_3$ and (4.39),

$$\begin{aligned}
\theta \dot{\eta}_v &= \theta \left(\frac{\partial \eta}{\partial \delta_e} \dot{\delta}_e + \frac{\partial \eta}{\partial \bar{\boldsymbol{h}}_e} : \dot{\bar{\boldsymbol{h}}}_e + \frac{\partial \eta}{\partial \boldsymbol{h}_t} : \dot{\boldsymbol{h}}_t + \frac{\partial \eta}{\partial \delta_\theta} \dot{\delta}_\theta + \frac{\partial \eta}{\partial \chi^M} \dot{\chi}^M + \frac{\partial \eta}{\partial \chi^S} \dot{\chi}^S \right) + c_v \dot{\theta} \\
&= c_v \dot{\theta} - \theta \left(\frac{\partial^2 \psi}{\partial \theta \partial \delta_e} \dot{\delta}_e + \frac{\partial^2 \psi}{\partial \theta \partial \bar{\boldsymbol{h}}_e} : \dot{\bar{\boldsymbol{h}}}_e + \frac{\partial^2 \psi}{\partial \theta \partial \boldsymbol{h}_t} : \dot{\boldsymbol{h}}_t + \frac{\partial^2 \psi}{\partial \theta \partial \delta_\theta} \dot{\delta}_\theta + \frac{\partial^2 \psi}{\partial \theta \partial \chi^M} \dot{\chi}^M + \frac{\partial^2 \psi}{\partial \theta \partial \chi^S} \dot{\chi}^S \right).
\end{aligned} \tag{4.40}$$

Substituting equation (4.40) into equation (4.36) gives the following temperature evolution equation:

$$c_v\dot{\theta} = h_v - \nabla\cdot\boldsymbol{q} + \underbrace{\left(\bar{\boldsymbol{M}}_e - \boldsymbol{X}_t\right):\boldsymbol{D}_t - \mathcal{Z}^M\dot{\chi}^M - \mathcal{Z}^S\dot{\chi}^S}_{\mathcal{D}=\text{intrinsic dissipation}} + \underbrace{\theta\left(\frac{\partial^2\psi}{\partial\theta\partial\delta_e}\dot{\delta}_e + \frac{\partial^2\psi}{\partial\theta\partial\bar{\boldsymbol{h}}_e}:\bar{\boldsymbol{D}}_e + \frac{\partial^2\psi}{\partial\theta\partial\delta_\theta}\dot{\delta}_\theta\right)}_{\mathcal{X}=\text{thermoelastic coupling}} + \underbrace{\theta\left(\frac{\partial^2\psi}{\partial\theta\partial\boldsymbol{h}_t}:\boldsymbol{D}_t + \frac{\partial^2\psi}{\partial\theta\partial\chi^M}\dot{\chi}^M + \frac{\partial^2\psi}{\partial\theta\partial\chi^S}\dot{\chi}^S\right)}_{\mathcal{T}=\text{thermo-transformation coupling}}. \tag{4.41}$$

At this stage of the development of the theory and the experimental investigation, the thermoelastic coupling terms in equation (4.41) that give rise to a temperature variation due to variations in the state variables δ_e, δ_θ and $\bar{\boldsymbol{h}}_e$ are not well characterized (Ames et al., 2009; Bouvard et al., 2013). Hence, as approximations, the thermoelastic coupling is assumed to be neglected and instead a factor $\omega = (1 + \mathcal{X}/\mathcal{D})$ is introduced to represent the ratio of intrinsic dissipation converted into heat. Consequently, equation (4.41) reduces to

$$c_v\dot{\theta} = h_v - \nabla\cdot\boldsymbol{q} + \omega\mathcal{D} + \mathcal{T}, \tag{4.42}$$

where the thermo-transformation coupling term $\mathcal{T}$ is associated with the latent heat of phase transformation. The heat flux $\boldsymbol{q}$ is taken to be governed by Fourier's law

$$\boldsymbol{q} = -k\nabla\theta, \tag{4.43}$$

where k is the nonnegative thermal conductivity.

4.2.3 Helmholtz free energy

The Helmholtz free energy function ψ in equation (4.22) is additively split as

$$\psi = \psi^e + \psi^\theta + \psi^{int} + \psi^{cst}, \tag{4.44}$$

where ψ^e is the elastic energy, ψ^θ is the thermal contribution to free energy (Morin et al., 2011a; Lagoudas et al., 2012), ψ^{int} is the interaction energy between single-variant martensite, multi-variant martensite and austenite phases (Moumni et al., 2008), ψ^{cst} is the potential energy due to the internal constraints.

By applying the rule of mixtures (Lagoudas et al., 2006; Moumni et al., 2008; Auricchio et al., 2014), the elastic energy ψ^e and the thermal energy ψ^θ in equation (4.44) can be expressed in the following form:

$$\begin{cases} \psi^e = \left(1 - \chi^M - \chi^S\right)\psi^{e,A} + \chi^M\psi^{e,M} + \chi^S\psi^{e,S}, \\ \psi^\theta = \left(1 - \chi^M - \chi^S\right)\psi^{\theta,A} + \chi^M\psi^{\theta,M} + \chi^S\psi^{\theta,S}, \end{cases} \tag{4.45}$$

where $\psi^{*,A}$, $\psi^{*,M}$ and $\psi^{*,S}$ are the free energies of the austenite, multi-variant and single-variant martensites, respectively.

Considering a Reuss rheological model (Moumni et al., 2008; Auricchio et al., 2014), the elastic free energy of the mixture in equation $(4.45)_1$ is given by

$$\psi^e = \frac{1}{2}K\delta^2 + \mu\|\bar{\boldsymbol{h}}_e\|^2 - 3\alpha_\theta K\delta(\theta - \theta_0), \tag{4.46}$$

where $\delta = \delta_e + \delta_\theta$ is the volumetric part of the Hencky strain, θ_0 is the reference temperature, α_θ is the thermal expansion coefficient. The bulk modulus K is assumed to be equal for all phases and shear modulus μ are determined from the Reuss model (Wagner and Windl, 2008; Auricchio et al., 2014) using the relations:

$$K = K^A = K^M = K^S \quad \text{and} \quad \frac{1}{\mu} = \left(1 - \chi^S - \chi^M\right)\frac{1}{\mu^A} + \chi^M\frac{1}{\mu^M} + \chi^S\frac{1}{\mu^S}. \tag{4.47}$$

The thermal energy ψ^θ in equation (4.44), sometimes referred to as chemical energy (Sedlák et al., 2012; Auricchio et al., 2014), is related to changes in the internal energy and entropy. The thermal energies in equation $(4.45)_2$ for the different phases, $\psi^{\theta,*}$, are defined as

$$\psi^{\theta,*} = e_0^* - \eta_0^*\theta + c_v^*\left[(\theta - \theta_0) - \theta\ln\left(\frac{\theta}{\theta_0}\right)\right], \tag{4.48}$$

where $*$ denotes either of the phases A, M and S, e_0 and η_0 are reference internal energy and entropy at reference temperature θ_0, c_v is the specific heat capacity.

Substituting equation (4.48) into equation $(4.45)_2$ gives the following thermal energy ψ^θ:

$$\begin{aligned}\psi^\theta =& e_0^A - \eta_0^A\theta + c_v^A\left[(\theta - \theta_0) - \theta\ln\left(\frac{\theta}{\theta_0}\right)\right] - \left(\chi^M\Delta e^{AM} + \chi^S\Delta e^{AS}\right) + \\ & \left(\chi^M\Delta\eta^{AM} + \chi^S\Delta\eta^{AS}\right)\theta - \left(\chi^M\Delta c_v^{AM} + \chi^S\Delta c_v^{AS}\right)\left[(\theta - \theta_0) - \theta\ln\left(\frac{\theta}{\theta_0}\right)\right],\end{aligned} \tag{4.49}$$

where $\Delta e^{A*} = e_0^A - e_0^*$, $\Delta\eta^{A*} = \eta_0^A - \eta_0^*$ and $\Delta c_v^{A*} = c_v^A - c_v^*$ are the differences of internal energy, entropy and heat capacity between austenite and multi-/single-variant martensites.

Regarding the three different phases, the following assumptions are introduced to simplify the formulation of the model : (i) since many DSC experiments showed that the heat capacities of austenite and martensite are almost equal (Qidwai and Lagoudas, 2000), $c_v^A = c_v^M = c_v^S = c_v$ and $\Delta c_v^{AM} = \Delta c_v^{AS} = 0$; (ii) equal internal energy and entropy between multi- and single-variant martensites, i.e. $\Delta e^{AM} = \Delta e^{AS} = \mathcal{L}_h$ and $\Delta\eta^{AM} = \Delta\eta^{AS} = \Delta\eta_t = \mathcal{L}_h/\theta_t$, where $\mathcal{L}_h$ is the latent heat of phase transformation between austenite and martensite, the transformation temperature θ_t and the entropy

difference $\Delta\eta_t$ are given by

$$\theta_t = \begin{cases} \theta_{AM} & A \rightarrow M, S, \\ \theta_{MA} & M, S \rightarrow A, \end{cases} \quad \text{and} \quad \Delta\eta_t = \begin{cases} \Delta\eta_f = \mathcal{L}_h/\theta_{AM}, \\ \Delta\eta_r = \mathcal{L}_h/\theta_{MA}, \end{cases} \tag{4.50}$$

where θ_{AM} and θ_{MA} are forward and reverse phase transformation temperatures, $\Delta\eta_f$ and $\Delta\eta_r$ are forward and reverse entropy differences. With these assumptions, the thermal energy in equation (4.49) reduces to

$$\psi^{\theta} = e_0^A - \eta_0^A\theta + c_v\left[(\theta - \theta_0) - \theta\ln\left(\frac{\theta}{\theta_0}\right)\right] + \Delta\eta_t\left(\chi^M + \chi^S\right)(\theta - \theta_0). \tag{4.51}$$

The interaction energy ψ^{int} in equation (4.44) represents the crystal boundary energy between austenite, multi- and single-martensite phases, which is often derived from micro-mechanical or crystallographic considerations and finally expressed as a function of internal state variables (Zaki and Moumni, 2007b; Auricchio et al., 2014). In this work, the interaction energy ψ^{int} is assumed to depend on the multi-variant χ^M, single-variant χ^S martensite volume fractions and transformation strain $\boldsymbol{h}_t$ as

$$\psi^{int} = \psi^{int}\left(\chi^M, \chi^S, \boldsymbol{h}_t\right) = \mathcal{G}^t(\chi) + \frac{1}{2}\mu_t\|\boldsymbol{h}_t\|^2, \tag{4.52}$$

where $\chi = \chi^M + \chi^S$ is the volume fraction of total martensite. The first term $\mathcal{G}^t$ on the right-hand side of equation (4.52) represents the energy of interaction between austenite and martensite, while the second term $\frac{1}{2}\mu_t\|\boldsymbol{h}_t\|^2$ represents increase in interaction due to orientation/reorientation of martensite plates (multi-variant martensite to single-variant martensite). The difference between the two martensite variants is neglected with respect to interaction with austenite.

The internal state variables χ^M, χ^S and $\boldsymbol{h}_t$ used for modeling obey the following physical constraints:

- The volume fractions of multi-variant χ^M, single-variant χ^S and total $\chi^M + \chi^S$ martensites are restricted to the $[0, 1]$ interval,

$$0 \leq \chi^M, \chi^S, \chi^M + \chi^S \leq 1, \tag{4.53}$$

  which can be rewritten as the following three active constraints:

$$\chi^M \geq 0, \quad \chi^S \geq 0, \quad 1 - \left(\chi^M + \chi^S\right) \geq 0. \tag{4.54}$$

- The magnitude of transformation strain due to orientation of martensite variants must remain lower than a material-specific limit $\mathcal{H}$, *i.e.*

$$\mathcal{H} - \|\boldsymbol{h}_t\| \geq 0. \tag{4.55}$$

The above physical constraints on internal state variables are guaranteed by the following potential as the constraints contribution to free energy ψ^{cst} in equation (4.44):

$$\psi^{cst} = -\zeta^M \chi^M - \zeta^S \chi^S - \zeta^{MS}\left(1 - \chi^M - \chi^S\right) - \zeta^t\left(\mathcal{H} - \|\boldsymbol{h}_t\|\right), \tag{4.56}$$

where ζ^M, ζ^S, ζ^{MS} and ζ^t are nonnegative Lagrangian multipliers. The constraint energy (4.56) is complemented by the following classical Kuhn-Tucker conditions:

$$\begin{cases} \chi^M \geq 0, & \zeta^M \geq 0, & \zeta^M \chi^M = 0; \\ \chi^S \geq 0, & \zeta^S \geq 0, & \zeta^S \chi^S = 0; \\ 1 - \left(\chi^M + \chi^S\right) \geq 0, & \zeta^{MS} \geq 0, & \zeta^{MS}\left(1 - \chi^M - \chi^S\right) = 0; \\ \mathcal{H} - \|\boldsymbol{h}_t\| \geq 0, & \zeta^t \geq 0, & \zeta^t\left(\mathcal{H} - \|\boldsymbol{h}_t\|\right) = 0. \end{cases} \tag{4.57}$$

In conclusion, the Helmholtz free energy ψ is given by

$$\begin{aligned} \psi =& \frac{1}{2}K\delta^2 + \mu\|\bar{\boldsymbol{h}}_e\|^2 - 3\alpha_\theta K\delta(\theta - \theta_0) + e_0^A - \eta_0^A\theta + c_v\left[(\theta - \theta_0) - \theta\ln\left(\frac{\theta}{\theta_0}\right)\right] + \\ & \Delta\eta_t\left(\chi^M + \chi^S\right)(\theta - \theta_0) + g^t + \frac{1}{2}\mu_t\|\boldsymbol{h}_t\|^2 - \\ & \left[\zeta^M\chi^M + \zeta^S\chi^S + \zeta^{MS}\left(1 - \chi^M - \chi^S\right) + \zeta^t\left(\mathcal{H} - \|\boldsymbol{h}_t\|\right)\right]. \end{aligned} \tag{4.58}$$

4.2.4 Constitutive equations

Substituting the Helmholtz free energy function ψ (4.58) into the thermodynamic framework in section 4.2.2, the hydrostatic stress p, deviatoric stress $\boldsymbol{s}$ and entropy η_v are derived as

$$\begin{cases} p = \frac{\partial\psi}{\partial\delta} = K\left[\delta - 3\alpha_\theta(\theta - \theta_0)\right], \\ \boldsymbol{s} = \frac{\partial\psi}{\partial\bar{\boldsymbol{h}}_e} = 2\mu\bar{\boldsymbol{h}}_e, \\ \eta_v = -\frac{\partial\psi}{\partial\theta} = 3\alpha_\theta K\delta + \eta_0^A + c_v\ln\left(\frac{\theta}{\theta_0}\right) - \Delta\eta_t\left(\chi^M + \chi^S\right). \end{cases} \tag{4.59}$$

Using equations $(4.59)_2$ and (4.31), the Mandel stress $\bar{\boldsymbol{M}}_e$ in the intermediate unstressed configuration is written as

$$\bar{\boldsymbol{M}}_e = 2\mu\bar{\boldsymbol{H}}_e. \tag{4.60}$$

Moreover, the partial derivatives of ψ with respect to the internal state variables $\boldsymbol{h}_t$, χ^M and χ^S are given by

$$\begin{cases} \boldsymbol{X}_t = \frac{\partial\psi}{\partial\boldsymbol{h}_t} = \mu_t\boldsymbol{h}_t + \zeta^t\frac{\boldsymbol{h}_t}{\|\boldsymbol{h}_t\|}, \\ \mathcal{Z}^M = \frac{\partial\psi}{\partial\chi^M} = \Delta\eta_t(\theta - \theta_0) + g^t - \zeta^M + \zeta^{MS}, \\ \mathcal{Z}^S = \frac{\partial\psi}{\partial\chi^S} = \Delta\eta_t(\theta - \theta_0) + g^t - \zeta^S + \zeta^{MS}, \end{cases} \tag{4.61}$$

where $g^t = \partial \mathcal{G}^t / \partial \chi$ is the phase transformation hardening function. In order to capture the smooth phase transformation response, as experimentally demonstrated (Lagoudas et al., 2006; Hartl et al., 2010) and theoretically formulated (Lagoudas et al., 2012; Auricchio et al., 2014) in SMA literature, a tangential hardening function g^t is considered in the following form:

$$g^t = \kappa \tan^m \left[\frac{1}{2}(\xi_a \chi + \xi_b)\pi \right] + r, \tag{4.62}$$

where κ, m, ξ_a, ξ_b and r are model parameters obeying the following constraints:

$$\kappa > 0, \quad 0 < m < 1, \quad \xi_a > 0, \quad \xi_b > 0, \quad \xi_a + \xi_b < 1. \tag{4.63}$$

The single-variant martensite volume fraction χ^S, according to the literature (Reese and Christ, 2008; Moumni et al., 2008; Lagoudas et al., 2012), can be expressed in terms of the transformation strain as

$$\chi^S = \frac{\|\boldsymbol{h}_t\|}{\mathcal{H}}. \tag{4.64}$$

In addition, the transformation strain $\boldsymbol{h}_t$ can be equivalently expressed as

$$\boldsymbol{h}_t = \|\boldsymbol{h}_t\| \boldsymbol{N}_t, \tag{4.65}$$

where $\boldsymbol{N}_t$ is the direction of transformation strain. Using equations (4.64) and (4.65), the time derivative of $\boldsymbol{h}_t$ is given by

$$\dot{\boldsymbol{h}}_t = \mathcal{H} \boldsymbol{N}_t \dot{\chi}^S + \mathcal{H} \chi^S \dot{\boldsymbol{N}}_t, \tag{4.66}$$

where the first term represents the phase transformation between austenite and single-variant martensite, the second term represents the reorientation of single-variant martensite.

Substituting equation (4.66) into equation (A.4) gives the following split of logarithmic corotational rate of transformation Hencky strain:

$$\mathring{\boldsymbol{h}}_t^L = \mathcal{H} \boldsymbol{N}_t \dot{\chi}^S + \mathcal{H} \chi^S \left(\dot{\boldsymbol{N}}_t - \boldsymbol{\Omega}_t^L \boldsymbol{N}_t + \boldsymbol{N}_t \boldsymbol{\Omega}_t^L \right). \tag{4.67}$$

Considering the coaxiality of $\boldsymbol{h}_t$ and $\boldsymbol{N}_t$, the following corotational rate of $\boldsymbol{N}_t$ is introduced as

$$\boldsymbol{D}_N = \mathring{\boldsymbol{N}}_t^L = \dot{\boldsymbol{N}}_t - \boldsymbol{\Omega}_t^L \boldsymbol{N}_t + \boldsymbol{N}_t \boldsymbol{\Omega}_t^L. \tag{4.68}$$

Therefore, the transformation stretching tensor $\boldsymbol{D}_t$ is rewritten as

$$\boldsymbol{D}_t = \mathcal{H} \dot{\chi}^S \boldsymbol{N}_t + \mathcal{H} \chi^S \boldsymbol{D}_N. \tag{4.69}$$

Substituting equation (4.69) into inequality (4.32) gives

$$\underbrace{\mathcal{H}\chi^S\left(\bar{\boldsymbol{M}}_e-\boldsymbol{X}_t\right)}_{\boldsymbol{A}_N}:\boldsymbol{D}_N-\underbrace{\mathcal{Z}^M}_{A_M}\dot{\chi}^M+\underbrace{\left[\mathcal{H}\left(\bar{\boldsymbol{M}}_e-\boldsymbol{X}_t\right):\boldsymbol{N}_t-\mathcal{Z}^S\right]}_{A_S}\dot{\chi}^S\geq 0, \tag{4.70}$$

where the thermodynamic forces $\boldsymbol{A}_N$ associated to $\boldsymbol{D}_N$, A_M associated to $\dot{\chi}^M$, and A_S associated to $\dot{\chi}^S$ are given using equations (4.60) and (4.61) as

$$\begin{cases}\boldsymbol{A}_N=\mathcal{H}\chi^S\left(2\mu\bar{\boldsymbol{H}}_e-\mu_t\boldsymbol{h}_t-\zeta^t\boldsymbol{N}_t\right),\\ A_M=-\Delta\eta_t(\theta-\theta_0)-g^t+\zeta^M-\zeta^{MS},\\ A_S=2\mu\mathcal{H}\bar{\boldsymbol{H}}_e:\boldsymbol{N}_t-\mu_t\mathcal{H}^2\chi^S-\Delta\eta_t(\theta-\theta_0)-g^t-\mathcal{H}\zeta^t+\zeta^S-\zeta^{MS}.\end{cases} \tag{4.71}$$

The nonnegative dissipation of multi-variant and single-variant martensite phase transformations is guaranteed by the following choice of the evolution equations:

$$\dot{\chi}^M=\dot{\gamma}^M\mathcal{S}(A_M)\quad\text{and}\quad\dot{\chi}^S=\dot{\gamma}^S\mathcal{S}(A_S), \tag{4.72}$$

where $\dot{\gamma}^M$ and $\dot{\gamma}^S$ are nonnegative multipliers. The associated yield functions for the phase transformations are given by

$$\mathcal{F}_M=|A_M|-\mathcal{Y}_M\quad\text{and}\quad\mathcal{F}_S=|A_S|-\mathcal{Y}_S, \tag{4.73}$$

where $\mathcal{Y}_M$ and $\mathcal{Y}_S$ control the thresholds of the phase transformations. $\dot{\gamma}^M$, $\mathcal{F}_M$, $\dot{\gamma}^S$ and $\mathcal{F}_S$ are subjected to the following Kuhn-Tucker consistency conditions:

$$\begin{cases}\dot{\gamma}^M\geq 0,\quad\mathcal{F}_M\leq 0,\quad\dot{\gamma}^M\mathcal{F}_M=0;\\ \dot{\gamma}^S\geq 0,\quad\mathcal{F}_S\leq 0,\quad\dot{\gamma}^S\mathcal{F}_S=0.\end{cases} \tag{4.74}$$

The nonnegative dissipation of martensite reorientation is guaranteed by the following associative evolution equation:

$$\boldsymbol{D}_N=\dot{\gamma}^{tr}\frac{\boldsymbol{A}_N}{\|\boldsymbol{A}_N\|}, \tag{4.75}$$

where γ^{tr} is a nonnegative multiplier. The associated yield function for martensite reorientation is given by

$$\mathcal{F}_{tr}=\|\boldsymbol{A}_N\|-(\chi^S)^2Y_{tr}, \tag{4.76}$$

where Y_{tr} defines the martensite reorientation threshold. γ^{tr} and $\mathcal{F}_{tr}$ are subjected to the Kuhn-Tucker conditions:

$$\dot{\gamma}^{tr}\geq 0,\quad\mathcal{F}_{tr}\leq 0,\quad\dot{\gamma}^{tr}\mathcal{F}_{tr}=0. \tag{4.77}$$

Moreover, from the time derivative of $\|\boldsymbol{N}_t\|=1$ and the equation (A.8), one gets

$$\boldsymbol{N}_t:\dot{\boldsymbol{N}}_t=\boldsymbol{N}_t:\boldsymbol{D}_N=0. \tag{4.78}$$

Substituting equation (4.75) into equation (4.78) allows writing the Lagrangian multiplier ζ^t in equation (4.71) as

$$\zeta^t = \bar{\boldsymbol{M}}_e : \boldsymbol{N}_t - \mu_t \mathcal{H} \chi^S. \tag{4.79}$$

Then, the thermodynamic force $\boldsymbol{A}_N$ is written

$$\boldsymbol{A}_N = \mathcal{H}\chi^S \left[\bar{\boldsymbol{M}}_e - \left(\bar{\boldsymbol{M}}_e : \boldsymbol{N}_t\right) \boldsymbol{N}_t\right] = \mathcal{H}\chi^S \left(\mathbb{I} - \boldsymbol{N}_t \otimes \boldsymbol{N}_t\right) \bar{\boldsymbol{M}}_e, \tag{4.80}$$

where $\mathbb{I}$ is the fourth-order identity tensor. $\left(\mathbb{I} - \boldsymbol{N}_t \otimes \boldsymbol{N}_t\right) \bar{\boldsymbol{M}}_e$ represents the component normal to $\boldsymbol{N}_t$ of the Mandel stress $\bar{\boldsymbol{M}}_e$.

Substituting equations $(4.72)_2$ and (4.75) into equation (4.69) gives the following evolution equation for the transformation strain:

$$\boldsymbol{D}_t = \mathcal{H} \left[\dot{\gamma}^S \mathcal{S}(A_S) \boldsymbol{N}_t + \dot{\gamma}^{tr} \chi^S \frac{\boldsymbol{A}_N}{\|\boldsymbol{A}_N\|}\right]. \tag{4.81}$$

Using equations (4.41), (4.42), (4.72) and (4.75), the temperature evolution equation is written as

$$c_v \dot{\theta} = h_v - \nabla \cdot \boldsymbol{q} + \omega \left(\dot{\gamma}^{tr} \|\boldsymbol{A}_N\| + \dot{\gamma}^M |A_M| + \dot{\gamma}^S |A_S|\right) + \theta \Delta\eta_t \left[\dot{\gamma}^M \mathcal{S}(A_M) + \dot{\gamma}^S \mathcal{S}(A_S)\right]. \tag{4.82}$$

A review of the constitutive equations derived in this section is presented in Table 4.1.

4.3 Numerical implementation

In this section, numerical implementation of the constitutive model in an finite element analysis (FEA) framework is carried out. Time-discrete formulation of the proposed model is presented by using an exponential integrator for the transformation evolution equation. Then, a Hencky-strain return-mapping algorithm is introduced, which greatly increases the numerical simplicity and efficiency.

4.3.1 A time-discrete framework

The deformation-driven initial boundary value problem of the proposed thermomechanically coupled finite-strain model is described as: within the time interval $[t_n, t_{n+1}]$, given the deformation gradient $\boldsymbol{F}_n$, the internal state variables $\boldsymbol{N}_n^t$, χ_n^M, χ_n^S, the temperature θ_n at time t_n and the deformation gradient $\boldsymbol{F}$ at time t_{n+1}, determine the state variables and temperature change at time t_{n+1} satisfying the time-discrete constitutive equations.

The evolution equation $(4.72)_1$ of the multi-variant martensite phase fraction χ^M is written using a backward-Euler integration scheme as

$$\chi^M = \chi_n^M + \Delta\gamma^M \mathcal{S}(A_M), \tag{4.83}$$

where $\Delta\gamma^M$ is the multiplier at time t_{n+1}, the sign function $\mathcal{S}(\cdot)$ is used to extract the sign of A_M.

Table 4.1 Summary of the thermomechanically coupled, finite-Hencky-strain model.

State and internal variables: $\delta_e, \bar{\boldsymbol{h}}_e, \boldsymbol{h}_t, \delta_\theta, \chi^M, \chi^S, \theta$

Thermoelasticity:

$p = K\left[\delta_e + \delta_\theta - 3\alpha(\theta - \theta_0)\right]$ and $\boldsymbol{s} = 2\mu\bar{\boldsymbol{h}}_e$

Multi-variant martensite transformation:

$\dot{\chi}^M = \dot{\gamma}^M \mathcal{S}(A_M)$,

where

$A_M = -\Delta\eta_t(\theta - \theta_0) - g^t + \zeta^M - \zeta^{MS}$

Single-variant martensite transformation:

$\dot{\chi}^S = \dot{\gamma}^S \mathcal{S}(A_S)$,

where

$A_S = 2\mu\mathcal{H}\bar{\boldsymbol{H}}_e : \boldsymbol{N}_t - \mu_t\mathcal{H}^2\chi^S - \Delta\eta_t(\theta - \theta_0) - g^t - \mathcal{H}\zeta^t + \zeta^S - \zeta^{MS}$

Martensite reorientation:

$\boldsymbol{D}_N = \dot{\gamma}^{tr}\frac{\boldsymbol{A}_N}{\|\boldsymbol{A}_N\|}$,

where

$\boldsymbol{A}_N = \mathcal{H}\chi^S\left(\mathbb{I} - \boldsymbol{N}_t \otimes \boldsymbol{N}_t\right)\bar{\boldsymbol{M}}_e$

Transformation strain:

$\boldsymbol{D}_t = \mathcal{H}\left[\dot{\gamma}^S\mathcal{S}(A_S)\boldsymbol{N}_t + \dot{\gamma}^{tr}\chi^S\frac{\boldsymbol{A}_N}{\|\boldsymbol{A}_N\|}\right]$

Temperature evolution:

$c_v\dot{\theta} = h_v - \nabla\cdot\boldsymbol{q} + \omega\left(\dot{\gamma}^{tr}\|\boldsymbol{A}_N\| + \dot{\gamma}^M|A_M| + \dot{\gamma}^S|A_S|\right) + \theta\Delta\eta_t\left[\dot{\gamma}^M\mathcal{S}(A_M) + \dot{\gamma}^S\mathcal{S}(A_S)\right]$

Yield functions:

$\mathcal{F}_M = |A_M| - \mathcal{Y}_M, \qquad \mathcal{F}_S = |A_S| - \mathcal{Y}_S, \qquad \mathcal{F}_{tr} = \|\boldsymbol{A}_N\| - (\chi^S)^2 Y_{tr}$

Kuhn-Tucker consistency conditions:

$$\begin{cases} \dot{\gamma}^M \geq 0, & \mathcal{F}_M \leq 0, & \dot{\gamma}^M\mathcal{F}_M = 0; \\ \dot{\gamma}^S \geq 0, & \mathcal{F}_S \leq 0, & \dot{\gamma}^S\mathcal{F}_S = 0; \\ \dot{\gamma}^{tr} \geq 0, & \mathcal{F}_{tr} \leq 0, & \dot{\gamma}^{tr}\mathcal{F}_{tr} = 0. \end{cases}$$

The numerical approximation of the evolution equation (4.81) of transformation strain is based on an exponential integration scheme as

$$\boldsymbol{F}^t = \exp(\boldsymbol{T})\,\boldsymbol{F}_n^t, \tag{4.84}$$

with

$$\boldsymbol{T} = \mathcal{H}\left(\Delta\gamma^S\mathcal{S}(A_S)\boldsymbol{N}_t + \Delta\gamma^{tr}\chi^S\frac{\boldsymbol{A}_N}{\|\boldsymbol{A}_N\|}\right), \tag{4.85}$$

where $\boldsymbol{T}$ is the flow vector of transformation strain, $\Delta\gamma^S$ and $\Delta\gamma^{tr}$ are the multipliers at time t_{n+1}.

Regarding the temperature change in equation (4.82), the following time-discrete temperature evolution equation is given as

$$\theta = \theta_n + \frac{1}{c_v}\left(h_v - \nabla\cdot\boldsymbol{q} + \omega\mathcal{D} + \mathcal{T}\right), \tag{4.86}$$

with

$$\begin{cases} \mathcal{D} = \Delta\gamma^{tr}\|\boldsymbol{A}_N\| + \Delta\gamma^M|A_M| + \Delta\gamma^S|A_S|, \\ \mathcal{T} = \theta_n\Delta\eta_t\left[\Delta\gamma^M\mathcal{S}(A_M) + \Delta\gamma^S\mathcal{S}(A_S)\right]. \end{cases} \tag{4.87}$$

The time-discrete evolution equations (4.83), (4.84) and (4.86), together with the yield functions (4.73) and (4.76), construct the following system of time-discrete constitutive equations:

$$\begin{cases} \mathcal{R}_M = \chi^M - \chi_n^M - \Delta\gamma^M\mathcal{S}(A_M) = 0, \\ \mathcal{R}_t = \boldsymbol{F}^t - \exp(\boldsymbol{T})\,\boldsymbol{F}_n^t = \boldsymbol{0}, \\ \mathcal{R}_\theta = \theta - \theta_n - \frac{1}{c_v}\left(h_v - \nabla\cdot\boldsymbol{q} + \omega\mathcal{D} + \mathcal{T}\right) = 0, \\ \mathcal{F}_M = |A_M| - \mathcal{Y}_M = 0, \\ \mathcal{F}_S = |A_S| - \mathcal{Y}_S = 0, \\ \mathcal{F}_{tr}/\chi^S = \|\boldsymbol{A}_N\|/\chi^S - \chi^S Y_{tr} = 0, \end{cases} \tag{4.88}$$

which is complemented by the following time-discrete Kuhn-Tucker conditions:

$$\begin{cases} \Delta\gamma^M \geq 0, & \mathcal{F}_M \leq 0, & \Delta\gamma^M\mathcal{F}_M = 0; \\ \Delta\gamma^S \geq 0, & \mathcal{F}_S \leq 0, & \Delta\gamma^S\mathcal{F}_S = 0; \\ \Delta\gamma^{tr} \geq 0, & \mathcal{F}_{tr} \leq 0, & \Delta\gamma^{tr}\mathcal{F}_{tr} = 0. \end{cases} \tag{4.89}$$

4.3.2 A Hencky-strain return-mapping algorithm

By using the multiplicative decomposition $\boldsymbol{F}_t = \bar{\boldsymbol{F}}_e^{-1}\bar{\boldsymbol{F}}$ and equation (A.12), the equation (4.84) is equivalently expressed as

$$\bar{\boldsymbol{F}}^e = \bar{\boldsymbol{F}}^{e\ \mathrm{trial}}\exp(-\boldsymbol{T}), \tag{4.90}$$

where $\bar{\boldsymbol{F}}^{e\ \mathrm{trial}} = \bar{\boldsymbol{F}}_\Delta\bar{\boldsymbol{F}}_n^e$ is the elastic trial deformation gradient, $\bar{\boldsymbol{F}}_\Delta$ is the incremental deformation gradient. Then, the post-multiplication of each side of $\bar{\boldsymbol{F}}^e\exp(\boldsymbol{T}) = \bar{\boldsymbol{F}}^{e\ \mathrm{trial}}$ by its transpose, together with the use of equation (A.13), gives

$$\bar{\boldsymbol{V}}^e\exp\left(2\boldsymbol{R}^e\boldsymbol{T}\boldsymbol{R}^{eT}\right)\bar{\boldsymbol{V}}^e = \left(\bar{\boldsymbol{V}}^{e\ \mathrm{trial}}\right)^2. \tag{4.91}$$

In terms of the Eulerian Hencky strains, $\bar{\boldsymbol{h}}^e$ and $\bar{\boldsymbol{h}}^{e\ \mathrm{trial}}$, equation (4.91) can be written

$$\exp\left(\bar{\boldsymbol{h}}^e\right)\exp\left(2\boldsymbol{R}^e\boldsymbol{T}\boldsymbol{R}^{eT}\right)\exp\left(\bar{\boldsymbol{h}}^e\right) = \exp\left(2\bar{\boldsymbol{h}}^{e\ \mathrm{trial}}\right). \tag{4.92}$$

From the series representation of the tensor exponential (equation (A.9)), the term $\exp\left(\bar{\boldsymbol{h}}^e\right)$ in above equation can be expressed as

$$\exp\left(\bar{\boldsymbol{h}}^e\right) = \boldsymbol{1} + \bar{\boldsymbol{h}}^e + \boldsymbol{o}\left(\bar{\boldsymbol{h}}^e\right), \tag{4.93}$$

where $\boldsymbol{o}\left(\bar{\boldsymbol{h}}^{e}\right)$ is a second-order term in the elastic Hencky strain. Therefore, equation (4.92) is written as

$$\exp\left(2\bar{\boldsymbol{h}}^{e\ \mathrm{trial}}\right) = \exp\left(2\boldsymbol{R}^{e}\boldsymbol{T}\boldsymbol{R}^{eT}\right) + \bar{\boldsymbol{h}}^{e}\exp\left(2\boldsymbol{R}^{e}\boldsymbol{T}\boldsymbol{R}^{eT}\right) + \exp\left(2\boldsymbol{R}^{e}\boldsymbol{T}\boldsymbol{R}^{eT}\right)\bar{\boldsymbol{h}}^{e} + \boldsymbol{o}\left(\bar{\boldsymbol{h}}^{e}\right), \tag{4.94}$$

with the following definition of Green-Lagrange-type tensor of incremental transformation strain $\boldsymbol{h}^{t}_{\Delta}$:

$$\boldsymbol{h}^{t}_{\Delta} = \frac{1}{2}\left[\exp\left(2\boldsymbol{R}^{e}\boldsymbol{T}\boldsymbol{R}^{eT}\right) - \boldsymbol{1}\right], \tag{4.95}$$

which can be rewritten equivalently as

$$\exp\left(2\bar{\boldsymbol{h}}^{e\ \mathrm{trial}}\right) = \boldsymbol{1} + 2\left(\boldsymbol{h}^{t}_{\Delta} + \bar{\boldsymbol{h}}^{e} + \bar{\boldsymbol{h}}^{e}\boldsymbol{h}^{t}_{\Delta} + \boldsymbol{h}^{t}_{\Delta}\bar{\boldsymbol{h}}^{e}\right) + \boldsymbol{o}\left(\bar{\boldsymbol{h}}^{e}\right). \tag{4.96}$$

By making use of equation (A.10), the logarithm of both sides of equation (4.96) gives

$$2\bar{\boldsymbol{h}}^{e\ \mathrm{trial}} = \sum_{k=0}^{\infty}\frac{(-1)^{k}}{k+1}\left[2\left(\boldsymbol{h}^{t}_{\Delta} + \bar{\boldsymbol{h}}^{e} + \bar{\boldsymbol{h}}^{e}\boldsymbol{h}^{t}_{\Delta} + \boldsymbol{h}^{t}_{\Delta}\bar{\boldsymbol{h}}^{e}\right) + \boldsymbol{o}\left(\bar{\boldsymbol{h}}^{e}\right)\right]^{k+1}. \tag{4.97}$$

According to the multinomial theorem, equation (4.97) can be approximately expressed as

$$2\bar{\boldsymbol{h}}^{e\ \mathrm{trial}} = \sum_{k=0}^{\infty}\frac{(-1)^{k}}{k+1}\left(2\boldsymbol{h}^{t}_{\Delta}\right)^{k+1} + \sum_{k=0}^{\infty}\frac{(-1)^{k}}{k+1}\left(2\bar{\boldsymbol{h}}^{e}\right)^{k+1} + \boldsymbol{o}\left(\boldsymbol{h}^{t}_{\Delta}\right) + \boldsymbol{o}\left(\bar{\boldsymbol{h}}^{e}\right), \tag{4.98}$$

where $\boldsymbol{o}(\boldsymbol{h}^{t}_{\Delta})$ is the second-order term in the incremental transformation strain. In view of equations (4.93) and (4.95), equation (4.98) then is written as

$$\bar{\boldsymbol{h}}^{e\ \mathrm{trial}} = \bar{\boldsymbol{h}}^{e} + \boldsymbol{R}^{e}\boldsymbol{T}\boldsymbol{R}^{eT} + \boldsymbol{o}\left(\boldsymbol{h}^{t}_{\Delta}\right) + \boldsymbol{o}\left(\bar{\boldsymbol{h}}^{e}\right). \tag{4.99}$$

Since the exponential map integrator (4.91) is first-order accurate and the elastic strain is assumed to be infinitesimal, the second-order terms can be neglected in equation (4.99) leading to the following approximate formula:

$$\mathcal{R}_{t} = \bar{\boldsymbol{h}}^{e\ \mathrm{trial}} - \bar{\boldsymbol{h}}^{e} - \boldsymbol{R}^{e}\boldsymbol{T}\boldsymbol{R}^{eT} = \boldsymbol{0}, \tag{4.100}$$

which is used as a substitute for equation $(4.88)_2$ to improve numerical efficiency. Finally, the system (4.88) is solved using a Newton-Raphson method.

4.3.3 Calibration of the model parameters

In this section, the proposed three-dimensional (3D) model is first reduced to a one-dimensional (1D) version. Then, the 1D model is implemented into MATLAB using an explicit integration scheme to calibrate the model parameters against experimental data.

For the case of uniaxial loading, the Cauchy stress tensor $\boldsymbol{\sigma}$ and the deformation gradient $\boldsymbol{F}$ are given as

$$\boldsymbol{\sigma} = \sigma\, \boldsymbol{e}_1 \otimes \boldsymbol{e}_1 \quad \text{and} \quad \boldsymbol{F} = \lambda\, \boldsymbol{e}_1 \otimes \boldsymbol{e}_1 + \lambda_l\, \boldsymbol{e}_2 \otimes \boldsymbol{e}_2 + \lambda_l\, \boldsymbol{e}_3 \otimes \boldsymbol{e}_3, \tag{4.101}$$

where σ and λ denote the uniaxial stress and stretch, λ_l denotes the lateral contractions. $\boldsymbol{e}_1, \boldsymbol{e}_2, \boldsymbol{e}_3$ are the three orthonormal bases. Since the spherical stress-strain response (4.59) itself is a scalar equation, the reduced 1D equations will not capture it and therefore volume-preserving deformation, *i.e.* $J = \det \boldsymbol{F} = 1$, is assumed. This assumption gives the relation: $\lambda_l = \sqrt{\frac{1}{\lambda}}$. Moreover, the polar decomposition can be written as $\boldsymbol{F} = \boldsymbol{V}\boldsymbol{R} = \boldsymbol{V}$ since $\boldsymbol{R} = \boldsymbol{1}$. The velocity gradient $\boldsymbol{L}$ is then computed as

$$\boldsymbol{L} = \dot{\boldsymbol{F}}\boldsymbol{F}^{-1} = \frac{\dot{\lambda}}{\lambda}\boldsymbol{T} \quad \text{and} \quad \boldsymbol{T} = 1\, \boldsymbol{e}_1 \otimes \boldsymbol{e}_1 - \frac{1}{2}\, \boldsymbol{e}_2 \otimes \boldsymbol{e}_2 - \frac{1}{2}\, \boldsymbol{e}_3 \otimes \boldsymbol{e}_3, \tag{4.102}$$

with the stretching tensor $\boldsymbol{D} = \operatorname{sym}(\boldsymbol{L}) = \boldsymbol{L}$ and spin tensor $\boldsymbol{W} = \operatorname{skew}(\boldsymbol{L}) = \boldsymbol{0}$.

The elastic $\boldsymbol{F}_e$ and the transformation $\boldsymbol{F}_t$ deformation gradients are defined by

$$\boldsymbol{F}_e = \lambda_e\, \boldsymbol{e}_1 \otimes \boldsymbol{e}_1 + \sqrt{\frac{1}{\lambda_e}}\, \boldsymbol{e}_2 \otimes \boldsymbol{e}_2 + \sqrt{\frac{1}{\lambda_e}}\, \boldsymbol{e}_3 \otimes \boldsymbol{e}_3, \tag{4.103}$$

$$\boldsymbol{F}_t = \lambda_t\, \boldsymbol{e}_1 \otimes \boldsymbol{e}_1 + \sqrt{\frac{1}{\lambda_t}}\, \boldsymbol{e}_2 \otimes \boldsymbol{e}_2 + \sqrt{\frac{1}{\lambda_t}}\, \boldsymbol{e}_3 \otimes \boldsymbol{e}_3, \tag{4.104}$$

with

$$\lambda = \lambda_e \lambda_t \quad \text{and} \quad J = J_e J_t = 1. \tag{4.105}$$

Thus, the elastic $\boldsymbol{h}_e$ and transformation $\boldsymbol{h}_t$ Hencky strains in equation (4.14) are written as

$$\boldsymbol{h}_e = \ln \lambda_e \boldsymbol{T} \quad \text{and} \quad \boldsymbol{h}_t = \ln \lambda_t \boldsymbol{T}. \tag{4.106}$$

The deviatoric stress $\boldsymbol{s}$ in equation (4.59) is then written as

$$\boldsymbol{s} = 2\mu \ln \lambda_e \boldsymbol{T} = \frac{2}{3}\sigma \boldsymbol{T}. \tag{4.107}$$

The Mandel stress $\bar{\boldsymbol{M}}_e$ and the direction of transformation strain $\boldsymbol{N}_t$ in equation (4.65) are written as

$$\bar{M}_e = \frac{2}{3}\sigma \boldsymbol{T} \quad \text{and} \quad \boldsymbol{N}_t = \sqrt{\frac{2}{3}}\boldsymbol{T}, \tag{4.108}$$

which indicates that $\bar{\boldsymbol{M}}_e$ and $\boldsymbol{N}_t$ are coaxial for the case of uniaxial loading. Hence, according to equation (4.80), the thermodynamic force of martensitic reorientation A_N is null, *i.e.* $A_N = 0$. Moreover, the thermodynamic forces associated to the multi-variant χ^M and single-variant χ^S martensite phase

transformations are given by

$$\begin{cases} A_M = -\Delta\eta_t(\theta-\theta_0) - g^t + \zeta^M - \zeta^{MS}, \\ A_S = \sqrt{\frac{2}{3}}\mathcal{H}\sigma - \mu_t\mathcal{H}^2\chi^S - \Delta\eta_t(\theta-\theta_0) - g^t - \mathcal{H}\zeta^t + \zeta^S - \zeta^{MS}. \end{cases} \tag{4.109}$$

where the entropy difference $\Delta\eta_t$ takes different quantities $\Delta\eta_f$ for the forward and $\Delta\eta_r$ the reverse phase transformation.

The 1D reduced model is then implemented into MATLAB to calibrate the model parameters from the uniaxial experimental data. The physical interpretation and the graphical illustration of the model parameters are provided in the following.

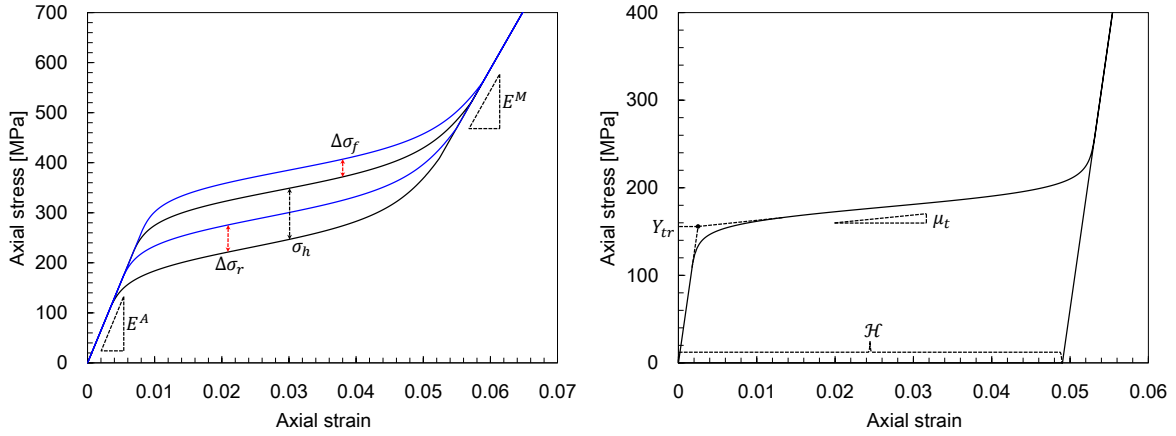

(a) (b)

Figure 4.1 Calibration of the model parameters from the experimental stress-strain curves: (a) identification of E^A, E^M, $\Delta\eta_f$, $\Delta\eta_r$ and $\mathcal{Y}_S$ from the pseudoelastic response, (b) identification of Y_{tr}, μ_t and $\mathcal{H}$ from the martensite orientation response.

- The elastic bulk modulus K and the shear moduli μ^A and μ^M are determined from experimental pseudoelastic stress-strain curve as follows:

$$K = \frac{E^A + E^M}{6(1-2\nu)}, \quad \mu^A = \frac{E^A}{2(1+\nu)} \quad \text{and} \quad \mu^M = \frac{E^M}{2(1+\nu)}, \tag{4.110}$$

  where E^A and E^M are Young's moduli for austenite and martensite as shown in Fig 4.1(a).

- The forward and reverse entropy differences, $\Delta\eta_f$ and $\Delta\eta_r$, govern the variation of transformation stresses with temperature. This influence is demonstrated in Fig 4.1(a) with two stress-strain curves obtained at temperature θ (black) and $\theta + \Delta\theta$ (blue), wherein the temperature increase of $\Delta\theta$ leads to the increase of the forward transformation stress of $\Delta\sigma_f$ and the reverse one of $\Delta\sigma_r$. These two parameters are calculated as follows:

$$\Delta\eta_f = \mathcal{H}\frac{\Delta\sigma_f}{\Delta\theta} \quad \text{and} \quad \Delta\eta_r = \mathcal{H}\frac{\Delta\sigma_r}{\Delta\theta}. \tag{4.111}$$

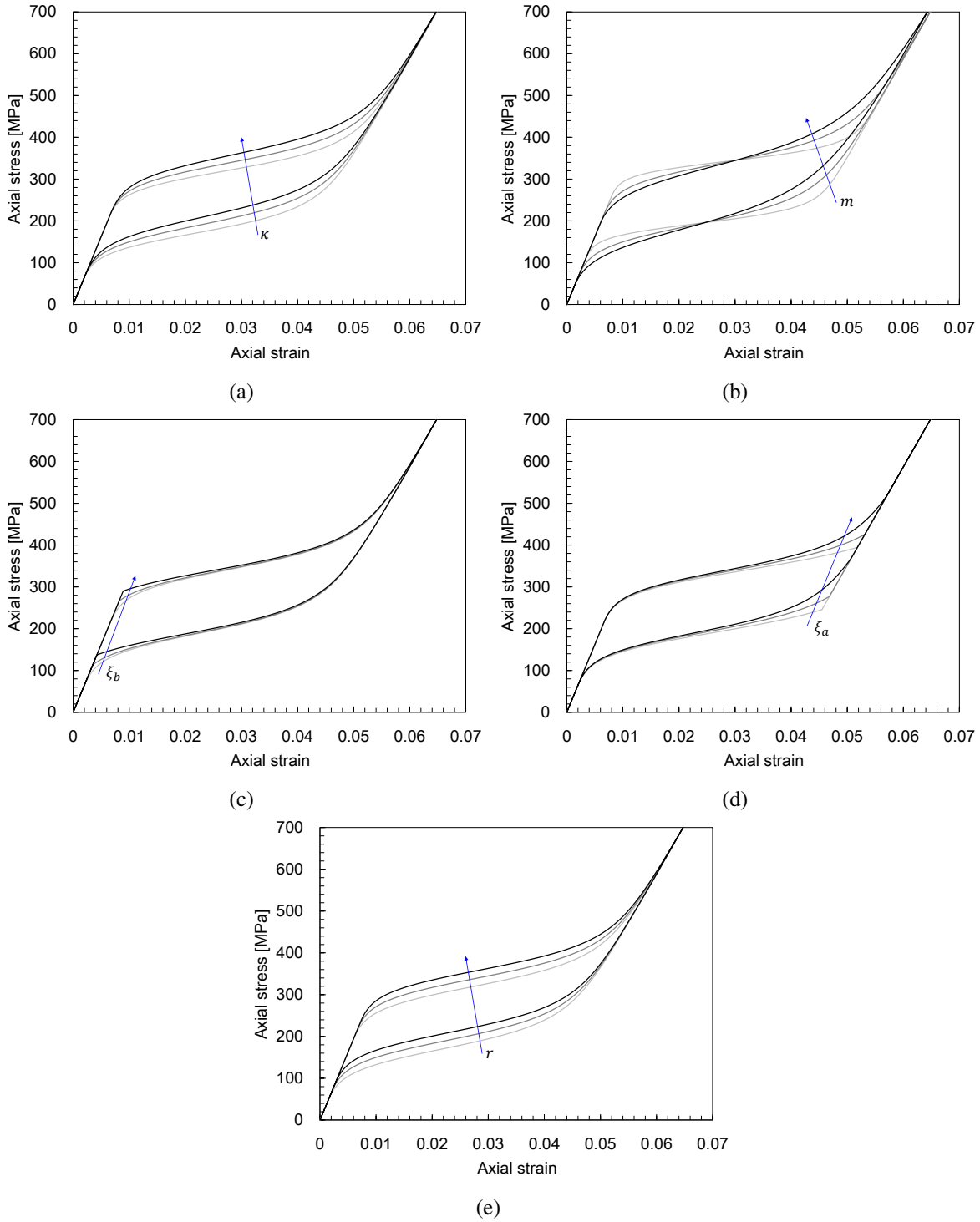

Figure 4.2 Effects of the model parameters κ, m, ξ_b, ξ_a and r in the tangential hardening function on the stress-strain behavior, arrows indicate the value increase of the respective parameters.

- $\mathcal{Y}_S$ and $\mathcal{Y}_M$ control the thresholds of the single-variant and the multi-variant martensite transformations. For the sake of calculus simplicity, it is assumed $\mathcal{Y}_M = \mathcal{Y}_S$. They determine the height of the hysteresis loop σ_h, as shown in Fig 4.1(a). They are computed using the following expression:

$$\mathcal{Y}_S = \frac{1}{2}\mathcal{H}\sigma_h. \tag{4.112}$$

- The martensite reorientation threshold Y_{tr}, the reorientation hardening modulus μ_t and the magnitude limit of transformation strain $\mathcal{H}$ are determined from the stress-strain curve of martensite orientation experiment, wherein multi-variant martensite is completely oriented to single-variant martensite under the uniaxial tensile loading. Y_{tr} takes the initial yield stress, μ_t the slope of orientation plateau and $\mathcal{H}$ the magnitude of the residual strain, as shown in Figure 4.1(b).

- The parameters κ, m, ξ_a, ξ_b and r in the tangential hardening function g^t control the smooth transition at the initiation and completion of the phase transformation. Figure 4.2 shows how the parameters κ, m, ξ_a, ξ_b and r affect the pseudoelastic stress-strain behavior.

4.4 Numerical simulations and experimental validations

The proposed model and the corresponding numerical algorithm presented in the previous sections are implemented into the finite element analysis software Abaqus/Explicit by means of a VUMAT subroutine. To demonstrate capabilities of the model, numerical simulations are carried out and compared to the experimental data under a variety of thermomechanical loading conditions. Finite element simulation of a SMA helical spring actuator undergoing large deformations and temperature variation is also performed.

4.4.1 Isothermal pseudoelasticity

The first set of simulations is dedicated to pseudoelasticity under isothermal uniaxial tensile loading at temperatures of 298 K, 303 K and 313 K. Experimental data for a polycrystalline NiTi wire (50.8 at.% Ni, provided by Memry Corporation) reported by Lagoudas et al. (2012) is utilized for validation. The model parameters used for this set of simulations are calibrated from the experimental data and listed in Table 4.2. In the simulations, the applied stress is increased from 0 to the maximum value of 700 MPa then removed, with the temperature maintained at a constant value.

Figure 4.3 shows comparisons between the model predictions and the experimental data reported by (Lagoudas et al., 2012). The pseudoelastic stress-strain responses at constant temperatures of 298 K, 303 K and 313 K are, respectively, plotted in Figure4.3(a), (b) and (c). In addition, the evolution of the single-variant martensite volume fraction χ^S is presented in Figure 4.3(d). From the figures, it is seen that the proposed model captures the pseudoelastic behavior of the considered polycrystalline SMA with good accuracy. In particular, complete shape recovery is achieved upon unloading, a smooth response is

Table 4.2 Model parameters used in isothermal pseudoelastic uniaxial tensile simulations.

Parameter	Value	Unit	Parameter	Value	Unit
K	23400	MPa	μ^A	12500	MPa
μ^{MS}	9038	MPa	μ_t	500	MPa
$\Delta\eta_f$	0.147	MPa/K	$\Delta\eta_r$	0.133	MPa/K
κ	5.6	MPa	m	0.2	-
ξ_a	0.998	-	ξ_b	0.001	-
r	-6.65	MPa	$\mathcal{H}$	0.035	-
θ_0	240	K	$\mathcal{Y}_M$	2.1	MPa
$\mathcal{Y}_S$	2.1	MPa	Y_{tr}	110	MPa

observed at the initiation and completion of phase transformation, and the elastic modulus is found to depend on phase composition.

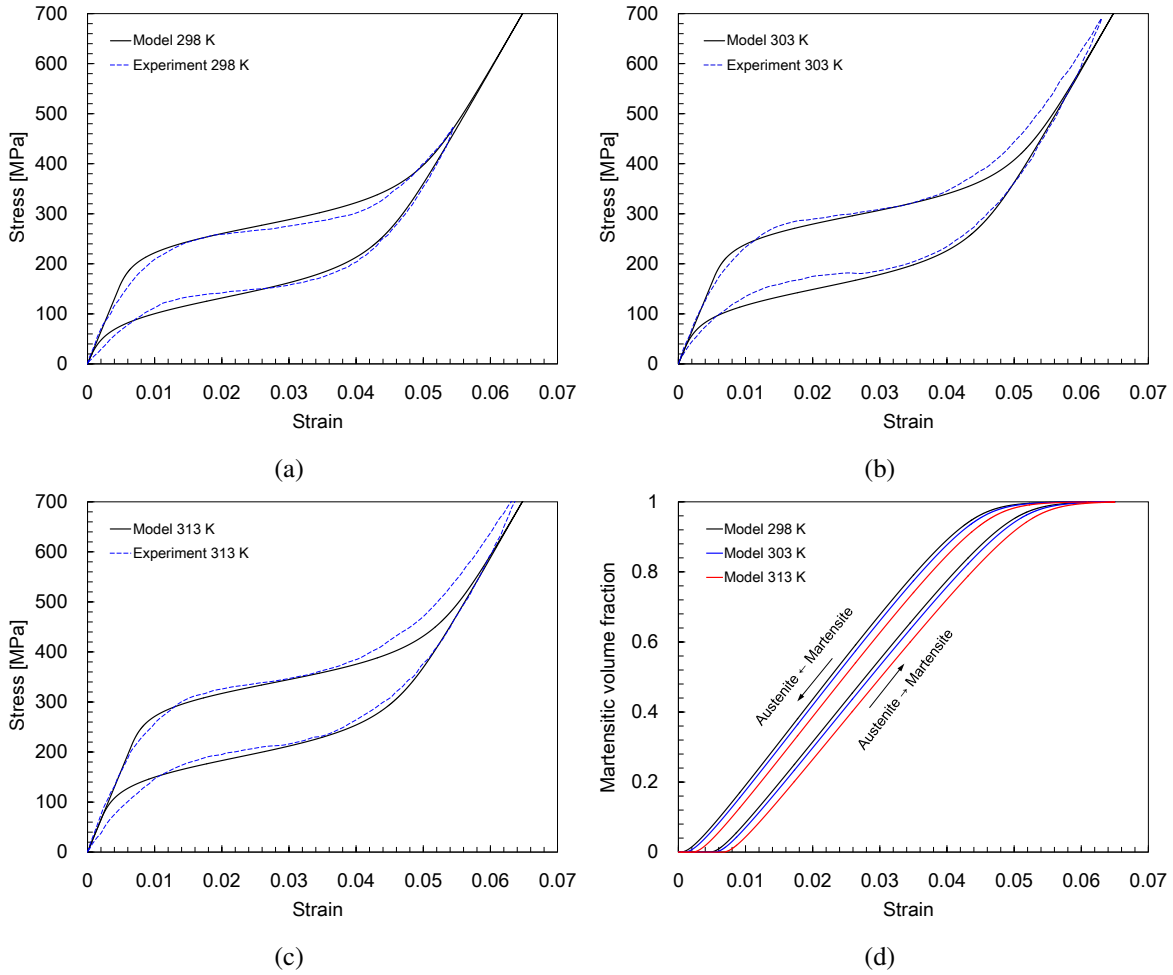

Figure 4.3 Model prediction vs. experimental data under isothermal uniaxial tensile loading: (a) θ = 298 K, (b) θ = 303 K, (c) θ = 313 K, (d) evolution of the single-variant martensite volume fraction.

4.4.2 Thermally-induced phase transformation

This section is devoted to the investigation of SMA response to temperature variation under zero-stress condition. Extensive experimental investigations have shown that phase transformation of SMA is a thermomechanically coupled process. The latent heat and the intrinsic dissipation contribute to heat generation and absorption during phase transformation, which can be measured by Differential Scanning Calorimetry (DSC) thermoanalytical technique. The difference in the amount of heat required to increase the temperature of a SMA sample compared to a reference specimen is measured as a function of temperature in DSC analysis. The thermally-induced phase transformation and the corresponding heat generation/absorption are predicted by the proposed constitutive model. Experimental date reported by Popov and Lagoudas (2007) is utilized for model validation. The model parameters used in the simulation are determined from the uniaxial stress-strain response and the DSC data, listed in Table 4.3. In the simulation, an unconstrained SMA component is first uniformly heated from 273 K to 393 K and then uniformly cooled back to 273 K.

Table 4.3 Model parameters used in unstressed thermally-induced phase transformation simulation.

Parameter	Value	Unit	Parameter	Value	Unit
K	41667	MPa	μ^A	26923	MPa
μ^{MS}	11538	MPa	μ_t	300	MPa
$\Delta\eta_f$	0.588	MPa/K	$\Delta\eta_r$	0.408	MPa/K
κ	9.6	MPa	m	0.2	-
ξ_a	0.998	-	ξ_b	0.001	-
r	10.2	MPa	$\mathcal{H}$	0.06	-
θ_0	313	K	$\mathcal{Y}_M$	8.1	MPa
$\mathcal{Y}_S$	8.1	MPa	Y_{tr}	110	MPa

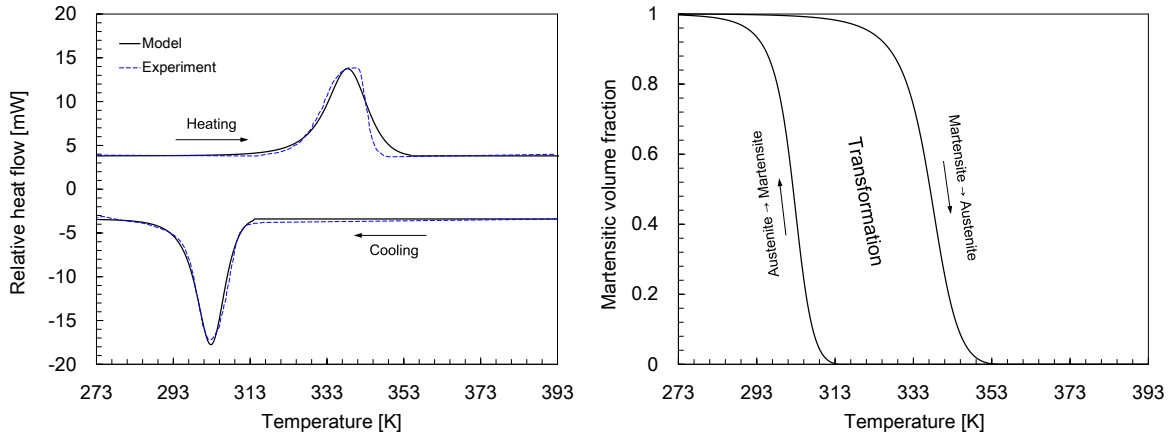

(a) (b)

Figure 4.4 Unstressed thermally-induced phase transformation: (a) heat generation and absorption (latent heat), (b) evolution of the multi-variant martensite volume fraction.

Figure 4.4(a) shows a comparison between the model predictions and the experimental DSC data reported by Popov and Lagoudas (2007), wherein the relative heat flow is plotted as a function of temperature. Heat absorption from martensite to austenite phase transformation results in a ridge along the heating part of the curve, while heat generation from austenite to martensite phase transformation results in a valley along the cooling part. The bottom and peak points on the cooling and heating parts, corresponding to temperatures $\theta_{MA} = 303$ K and $\theta_{AM} = 339$, denote average temperatures for forward and reverse phase transformation, respectively. It is worth noting that the ridge is short and wide, while the valley is deep and narrow. This is because the area under the curve in each case, representing phase transformation latent heat, is assumed to be the same. In this particular case, the temperature range of reverse transformation is larger than that of forward transformation, resulting in a low and wide ridge versus a deep and narrow valley. Overall, the heat absorption/generation during thermally-induced phase transformation is well described by the proposed model despite a small deviation at completion of the reverse phase transformation. Thanks to the tangential hardening function g^t defined in equation (4.62), the smooth experimental DSC curves are simulated with good accuracy. In addition to simulating the heat exchange during phase transformation, the evolution of multi-variant martensite volume fraction is simulated and shown in Figure 4.4(b). According to the simulation, the reverse phase transformation of martensite to austenite is found to initiate at temperature 305 K and complete at temperature 353 K, while the forward phase transformation of austenite to martensite initiates at temperature 313 K and completes at temperature 300 K.

4.4.3 Isobaric thermal cycling tests

In isobaric thermal cycling tests, SMA samples are preloaded uniaxially to different constant stress levels, which are maintained while the material undergoes thermally-induced transformation cycles (actuation cycles). The evolution of transformations train with temperature and its dependence on the level of applied stress are predicted by the proposed model. The experimental data reported by Wu et al. (2003) for equiatomic NiTi (50.0 at.% Ni) is utilized to validate the model. The model parameters used in the simulations are calibrated from the experimental data and listed in Table 4.4. Two constant stress levels of 160 MPa and 360 MPa are considered in the simulations, wherein temperature is decreased uniformly from 393 K to 253 K and then increased uniformly back to 393 K.

Figure 4.5 shows comparisons between model predictions and the experimental data reported by Wu et al. (2003) for stress levels of 160 MPa and 360 MPa. Since the elastic SMA response was not addressed in the source work, the comparisons shown in Figure 4.5 is based on the variation of the transformation strain with temperature. At 160 MPa, the yield functions associated with both single-variant martensite transformation and multi-variant martensite transformation are activated. Thus, austenite transforms simultaneously into these two martensite variants, leading to unsaturated transformation strain of 0.021. In contrast, the stress at 360 MPa is too high to activate the yield function associated with multi-variant martensite transformation. In this case, austenite transforms entirely into single-variant martensite and the maximum transformation strain reaches the saturated value $\mathcal{H} = 0.047$, shown as Table 4.4.

Table 4.4 Model parameters used in the simulations of isobaric thermal cycling tests.

Parameter	Value	Unit	Parameter	Value	Unit
K	50000	MPa	μ^A	23077	MPa
μ^{MS}	23077	MPa	μ_t	300	MPa
$\Delta\eta_f$	0.2585	MPa/K	$\Delta\eta_r$	0.282	MPa/K
κ	7.52	MPa	m	0.08	-
ξ_a	0.998	-	ξ_b	0.001	-
r	-2.585	MPa	$\mathcal{H}$	0.047	-
θ_0	297	K	$\mathcal{Y}_M$	5.64	MPa
$\mathcal{Y}_S$	5.64	MPa	Y_{tr}	110	MPa

It is worth noting that the material response shows abrupt transitions at the completion of forward transformation and at the initiation of reverse transformation at 160 MPa. This phenomenon is due to an assumption in the proposed model that the activation of the yield function associated with multi-variant martensite transformation will shut down the transformation to single-variant martensite. This deficiency can be addressed by considering the coupling effect between these two types of martensite transformation. Overall, the evolution of transformation strain with temperature and the variation of the maximum transformation strain with the applied stress are successfully predicted by the proposed model.

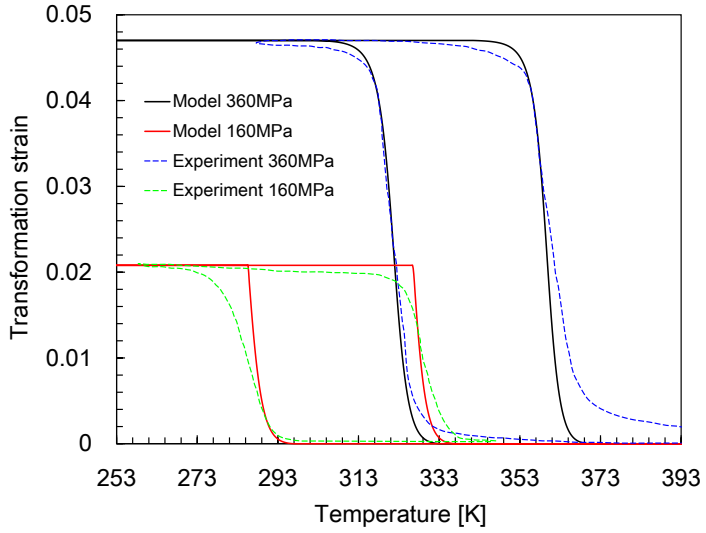

Figure 4.5 Comparisons between the model predictions and the experimental data reported by Wu et al. (2003): transformation strain vs. temperature at constant stress levels 160 MPa and 360 MPa.

4.4.4 Multiaxial non-proportional loading tests

In this section, a biaxial strain-controlled butterfly-shaped loading test is investigated to demonstrate the reliability of the model in presence of multiaxial non-proportional loading conditions. Experimental

data reported by Grabe and Bruhns (2009) is utilized as references. The model parameters used in the simulation are calibrated from the experimental data and listed in Table 4.5. In the source work, $\gamma' = \gamma/\sqrt{3}$ and $\tau' = \sqrt{3}\tau$ are used as shear strain and stress measures for simplicity of a von Mises-type equivalence.

Table 4.5 Model parameters used in butterfly-shaped non-proportional simulation.

Parameter	Value	Unit	Parameter	Value	Unit
K	52083	MPa	μ^A	24038	MPa
μ^{MS}	24038	MPa	μ_t	100	MPa
$\Delta\eta_f$	0.198	MPa/K	$\Delta\eta_r$	0.198	MPa/K
κ	6	MPa	m	0.2	-
ξ_a	0.98	-	ξ_b	0.01	-
r	-4.8	MPa	$\mathcal{H}$	0.03	-
θ_0	288	K	$\mathcal{Y}_M$	2.4	MPa
$\mathcal{Y}_S$	2.4	MPa	Y_{tr}	110	MPa

Figure 4.6 shows the butterfly-shaped strain input and the stress output in both axial and shear directions. The maximum axial and shear strain magnitudes reached in each case are $\varepsilon = \gamma/\sqrt{3} = 0.015$, as shown in Figure 4.6(a). The results of numerical simulation are compared to the reference experimental data in Figure 4.6(b-d). Specifically, Figure 4.6(b) shows the scaled shear stress $\sqrt{3}\tau$ versus axial stress σ, Figure 4.6(c) shows axial stress σ versus axial strain ε and Figure 4.6(d) shows $\sqrt{3}\tau$ versus the scaled shear strain $\gamma/\sqrt{3}$. The overall agreement with the experimental data is satisfactory despite small deviation in presence of dominant shear and compression loadings. This is because the yield criteria for phase transformation and martensite reorientation of the von Mises type, which dose not account for the experimentally observed asymmetry in NiTi behavior in tension, compression and shear. A better simultaneous fit to tension, compression and shear data is achievable by means of more sophisticated criteria.

4.4.5 Pseudoelasticity under non-isothermal conditions

To demonstrate the influence of thermomechanical coupling on SMA behavior, simulations of pseudoelastic uniaxial tensile tests under non-isothermal boundary conditions are carried out. Experimental data reported by Shaw and Kyriakides (1995) is used to validate the model. In the referenced work, pseudoelastic uniaxial tensile tests were performed on polycrystalline NiTi specimens (50.1 at.% Ni) at three different strain rates of $0.0004s^{-1}$, $0.004s^{-1}$ and $0.04s^{-1}$. In each case, heat exchange with the surrounding takes place by means of natural air convection with the external temperature maintained at 343 K. The model parameters used in the simulations are calibrated from the experimental data and listed in Table 4.6. In the simulations, the applied stress is increased from zero to the maximum of 1000 MPa then decreased to zero for each strain rate. The finite element model is defined with a uniform initial temperature field of 343 K and natural convection at the boundary with a convection heat transfer coefficient $h = 50\ Wm^{-2}K^{-1}$.

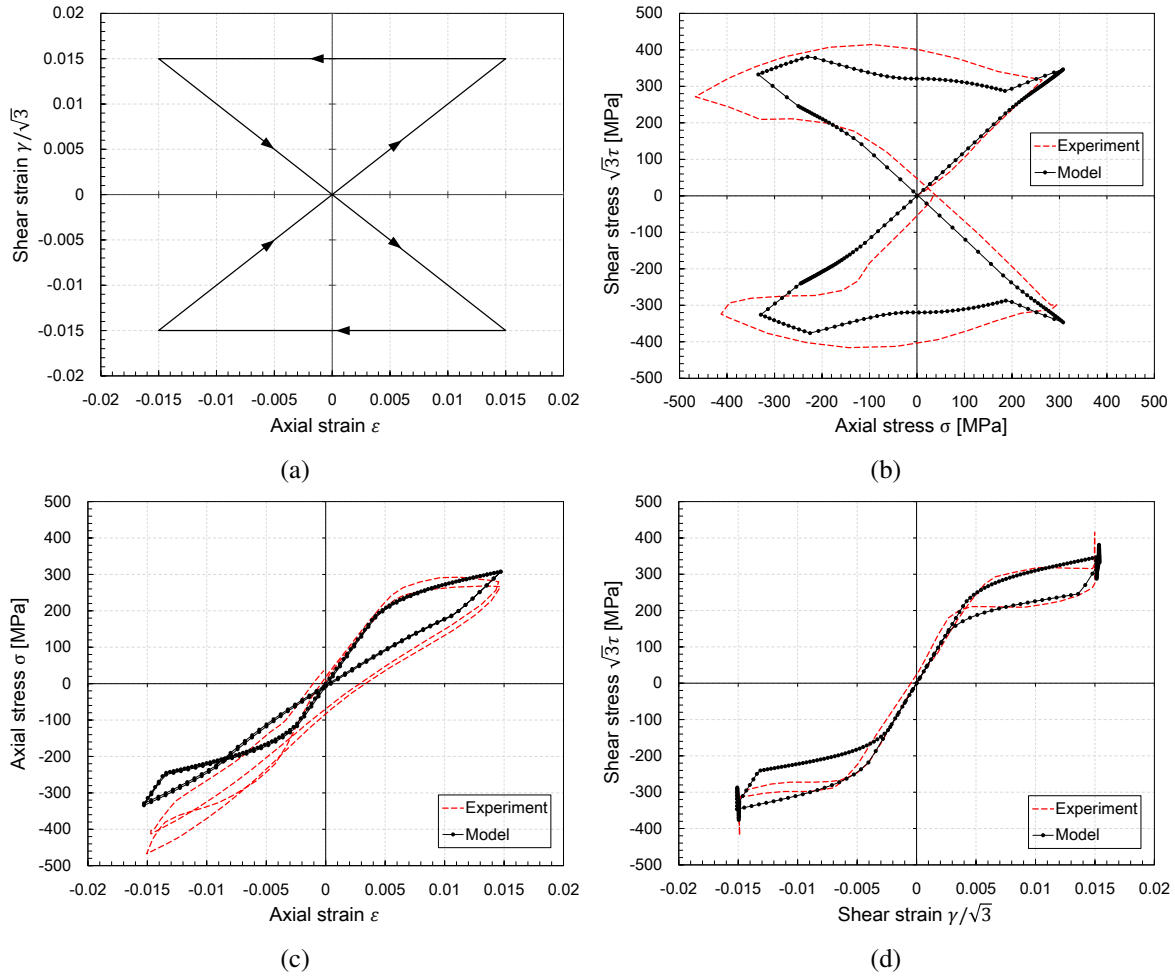

Figure 4.6 Comparisons between the model predictions and the experimental data reported by Grabe and Bruhns (2009): (a) butterfly-shaped axial-shear loading path, (b) shear stress vs. axial stress, (c) axial stress-strain response, (d) shear stress-strain response.

Table 4.6 Model parameters used in non-isothermal simulations at different loading rates.

Parameter	Value	Unit	Parameter	Value	Unit
K	52083	MPa	μ^A	24038	MPa
μ^{MS}	24038	MPa	μ_t	100	MPa
$\Delta\eta_f$	0.33	MPa/K	$\Delta\eta_r$	0.33	MPa/K
κ	3.92	MPa	m	0.2	-
ξ_a	0.98	-	ξ_b	0.01	-
r	1.96	MPa	$\mathcal{H}$	0.049	-
θ_0	288	K	$\mathcal{Y}_M$	7.84	MPa
$\mathcal{Y}_S$	7.84	MPa	Y_{tr}	110	MPa
k	18	W/m/K	c_v	440	J/kg/K
ω	0.86	-	h	50	W/m^2/K

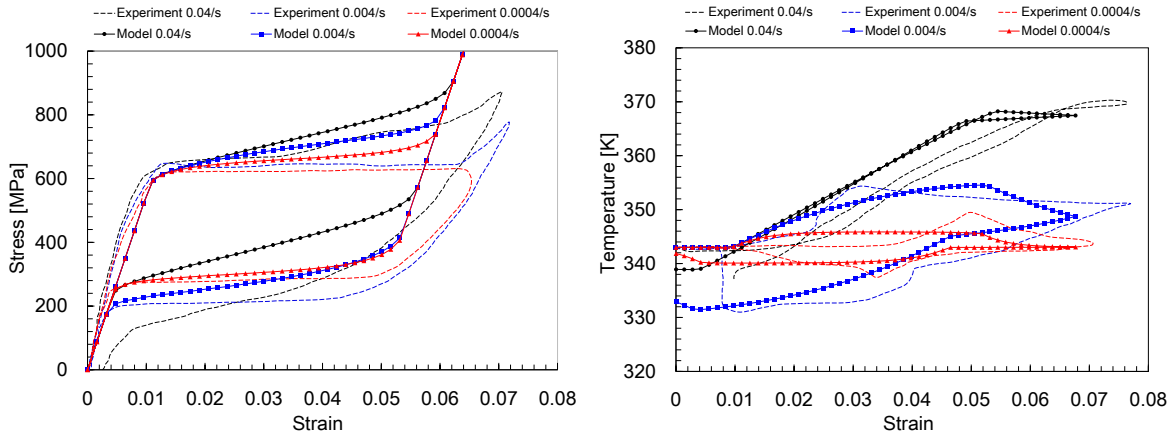

(a) (b)

Figure 4.7 Comparisons between model predictions and the experimental data reported by Shaw and Kyriakides (1995) at different loading rates: (a) stress-strain response, (b) temperature variation.

Figure 4.7 compares the model predictions with the experimental data reported by Shaw and Kyriakides (1995) at three different strain rates of $0.0004s^{-1}$, $0.004s^{-1}$ and $0.04s^{-1}$. In particular, Figure 4.7(a) illustrates the pseudoelastic stress-strain response and Figure 4.7(b) the variation of temperature with the strain. The pseudoelastic stress-strain response significantly depends on temperature and therefore is conjointly determined by the energy released or absorbed due to latent heat and intrinsic dissipation as well as the heat transfer by convection into surrounding medium. At low strain rate ($0.0004s^{-1}$), the rate of heat transfer by convection into the surrounding medium is sufficient to evacuate dissipative and latent phase transformation heat resulting in minor variation in temperature. This variation increases at moderate strain rate ($0.004s^{-1}$) for which the released heat is not convected into the surrounding medium timely, resulting in increased hysteresis. In this particular case, the finish temperature for forward phase transformation increased by 7 K and for reverse phase transformation decreased by 12 K with respect to the initial temperature of 343 K. Finally, at high strain rate ($0.04s^{-1}$), the material behavior approaches approximately adiabatic conditions, with temperature increasing to 368 K upon loading then decreasing to 340 K after unloading. The rate of the released energy becomes dominant in this case, resulting in increased temperature and therefore higher thermodynamic stability of the austenite phase. As a result, it becomes increasingly difficult for forward transformation to proceed whereas the reverse transformation becomes easier. A manifestation of this effect is the increased slope of the stress-strain plateaus corresponding to forward and reverse transformations.

4.4.6 Simulation of a SMA helical spring actuator

To demonstrate the usefulness of the proposed model in analyzing complex structural SMA components subjected to non-trivial thermomechanical loading conditions, a SMA helical spring actuator is simulated in this section. The simulation is carried out considering separate loading cases to illustrate stress-induced pseudoelasticity and temperature-induced actuation. Previous work on the simulation of SMA

actuators can be found in literature (Toi et al., 2004; Hartl et al., 2010; Lagoudas et al., 2012; Saleeb et al., 2013; Auricchio et al., 2014).

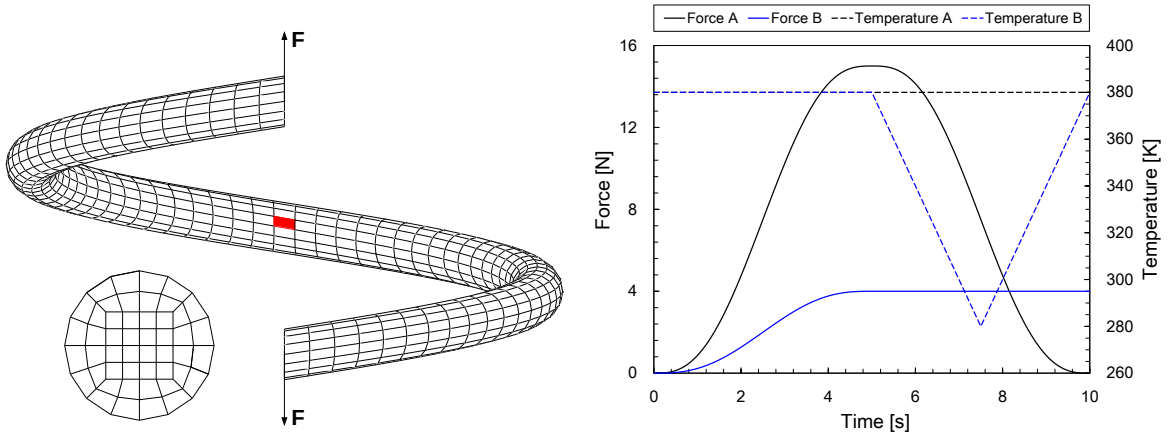

(a) (b)

Figure 4.8 Simulation of a SMA helical spring actuator: (a) geometry and mesh, (b) force and temperature loading paths.

The SMA helical spring actuator adopted in the simulation has a coil diameter of 20 mm, a wire diameter of 2 mm and a spring pitch of 10 mm. Figure 4.8(a) shows the initial geometry, meshed using 3312 coupled temperature-displacement reduced integration hexahedral elements (Abaqus/Explicit C3D8RT). The element highlighted in red is chosen for studying the local material response, *i.e.* stress-strain behavior and phase transformation. The mesh of the cross-section adjacent to the red element is shown in the figure. Loading is applied at the nodes on end surfaces of the spring. The thermomechanical loading cases considered in the simulations are shown in Figure 4.8(b).

In the first simulation, the applied forces are increased from zero to the maximum value of 15 N at the time of 5 seconds and then removed at the time of 10 seconds, with a prescribed temperature 380 K (black lines in Figure 4.8(b)). It is worth noting that the force is applied in a smooth manner to eliminate dynamic effect for quasi-static analysis in Abaqus/Explicit. Figure 4.9 shows the contour plots of the von Mises stress and the martensite volume fraction χ in the spring at the maximum force magnitude of 15 N. The maximum von Mises stress is achieved in central part of the spring, shown as Figure 4.9(a). Regarding its distribution through the cross-section, the von Mises stress is greater towards the outside compared to the core. In Figure 4.9(b), the martensite volume fraction is highest on the inner surface of the central segment of the spring. The local stress response and the phase transformation in the chosen element (red in Figure 4.8(a)) are shown in Figure 4.10(a). With increasing applied force, the von Mises stress on the element increases as well. Phase transformation from austenite to martensite then takes place when the von Mises stress exceeds 670 MPa. When the load is removed, martensite transforms back to austenite. The global force-displacement curve at the point of application of the load on the end surface is plotted in Figure 4.10(b). The figure shows complete recovery of inelastic strain upon removal of the load.

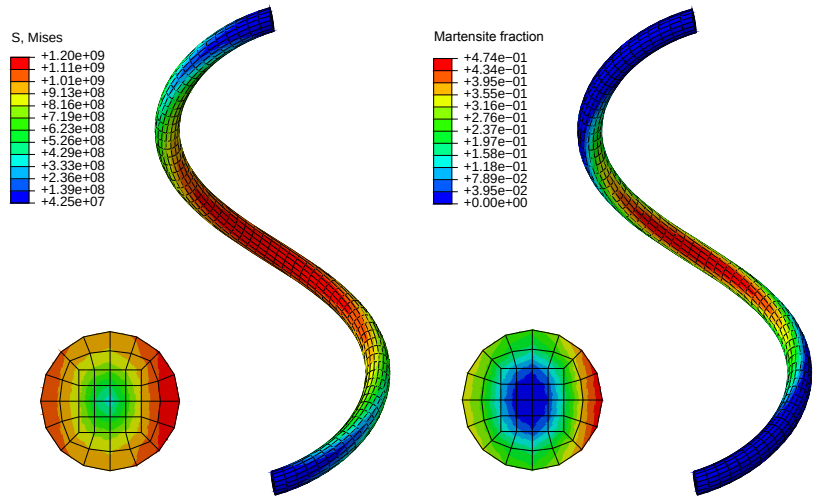

(a) (b)

Figure 4.9 SMA helical spring actuator at maximum loading: (a) von Mises stress contour plot, (b) martensite volume fraction contour plot.

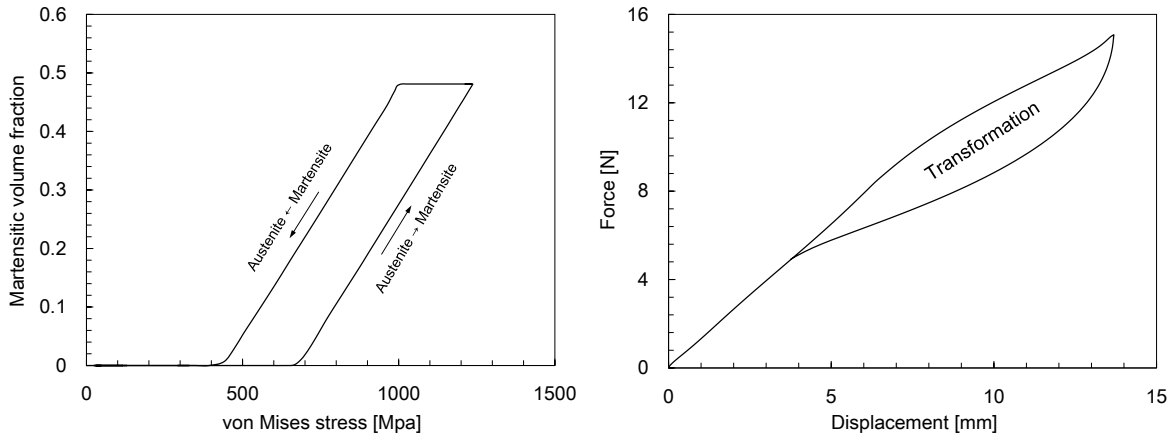

(a) (b)

Figure 4.10 Stress-induced pseudoelasticity of the SMA helical spring actuator: (a) martensite volume fraction vs. von Mises stress curve for the selected element, (b) force vs. displacement curve at the point of application of the load on the end surface.

In the second simulation, the spring is first preloaded with a force of magnitude 4 N in a smooth manner over a time period of 5 seconds at a constant temperature of 380 K. It is then cooled uniformly to 280 K before being uniformly heated back to 380 K over another time period of 5 seconds (blue lines in Figure 4.8(b)). Figure 4.11 shows contour plots of the von Mises stress and the martensite volume fraction χ in the spring at 280 K. The von Mises stress is maximum near the inner surface of the central portion of the spring as shown in Figure 4.11(a). In the same portion, the martensite volume fraction reaches its maximum value of magnitude 1 along toward the outside of the section, indicating complete

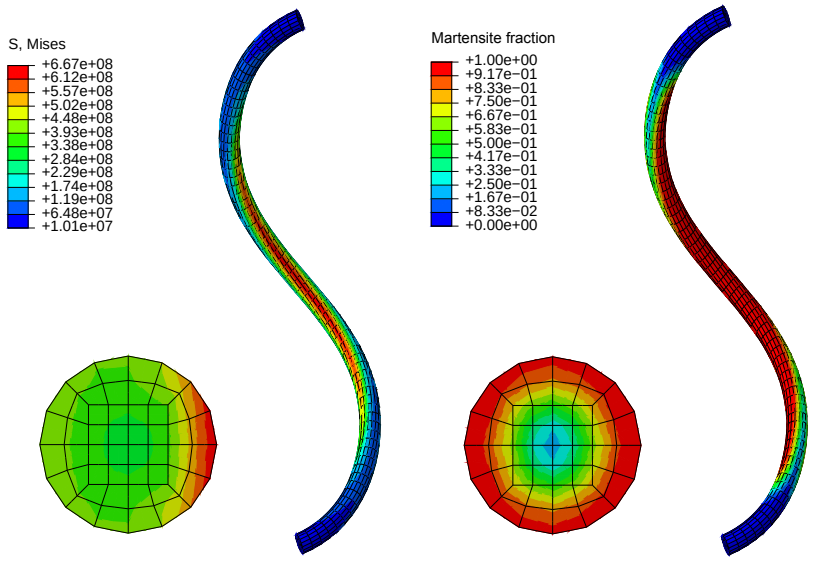

(a) (b)

Figure 4.11 SMA helical spring actuator at temperature 280 K: (a) von Mises stress contour plot, (b) martensite volume fraction contour plot.

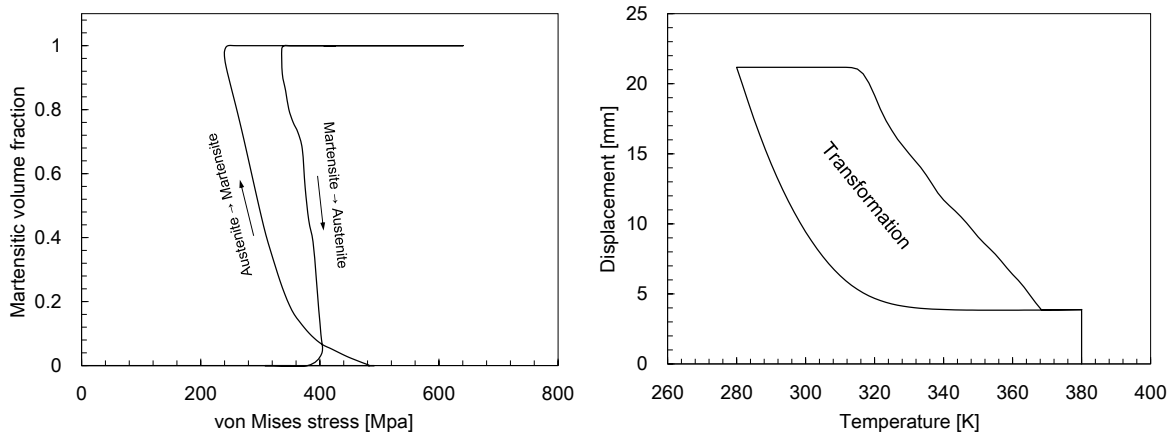

(a) (b)

Figure 4.12 Temperature-induced actuation of the SMA helical spring actuator: (a) martensite volume fraction vs. von Mises stress curve for the selected element, (b) displacement vs. temperature curve at the point of application of the load on the end surface.

transformation of austenite to martensite. The local stress response and phase transformation in the highlighted element (red in Figure 4.8(a)) are shown in Figure 4.12(a). In the first half of the loading sequence, the von Mises stress increases with increased applied force to nearly 480 MPa. However, as the temperature is decreased from 380 K to 280 K at constant applied force, the von Mises stress decreases to 230 MPa and austenite completely transforms to martensite. When temperature is increased again to 380 K, the martensite finally transforms back to austenite. The displacement of the point of

application of the load on the end surface is plotted versus temperature in Figure 4.12(b). At 380 K, the applied force of 4 N generates approximately 4 mm of elastic displacement. when temperature is decreased to 320 K, the formation of single-variant martensite results in significant transformation strain. The spring retrieves its original shape as the temperature is increased back to 380 K. The complete actuation cycle of the SMA helical spring actuator is shown in the figure.

4.5 Conclusion

A thermomechanically coupled, Hencky-strain based constitutive model for SMAs has been proposed in this chapter. The formulation of the model is based on a multi-tier decomposition of deformation kinematics comprising: (i) a multiplicative decomposition of the deformation gradient into elastic, transformation and thermal parts, (ii) an additive decomposition of the Hencky strain into spherical and deviatoric parts, (iii) an additive decomposition of the transformation stretching tensor into phase transformation and martensite reorientation components. A thermodynamically consistent framework was developed, and a Helmholtz free energy function including elastic, thermal, interaction and constraint components was introduced. Constitutive and heat equations were derived from the established thermodynamic framework and Helmholtz free energy.

Three important characteristics of SMA response are considered in formulating the model. First, the effect of phase coexistence between austenite and two martensite variants is accounted for by deriving separate evolution laws of volume fractions for single-variant χ^S and multi-variant χ^M martensites, which can be active simultaneously. Then, the variation of the hysteresis size with temperature is characterized by means of the forward entropy difference $\Delta\eta_f$ and reverse difference $\Delta\eta_r$. Finally, the smooth transition at initiation and completion of phase transformation is accounted for using a unique tangential transformation hardening function g^t.

Time-discrete formulation of the constitutive equations were derived and integrated using a Hencky-strain return-mapping algorithm. Whilst the proposed three-dimensional model was reduced to a one-dimensional form to perform the calibration of the model parameters. The model was then implemented into Abaqus/Explicit using a VUMAT subroutine. Numerical simulations are carried out and validated against experimental data under various loading cases, including proportional, non-proportional, isothermal, non-isothermal conditions. Finally, a simulation example is proposed in which a SMA helical spring is first subjected to mechanical loading resulting in a pseudoelastic response then to thermal loading resulting in a temperature-induced actuation. The simulation results illustrate the ability of the proposed model to describe the behavior of SMA devices subjected to complex thermomechanical loadings.

The proposed thermomechanically coupled finite-strain model has capabilities of capturing the non-isothermal material behavior of SMAs under complex thermomechanical boundaries and loadings. However, it can not predict the characteristics related to the cyclic behavior of SMA, such as the accumulation of residual strain, the degeneration of pseudoelasticity and dissipated energy, and the

evolution of the phase transformation from abrupt to smooth transition. In the next chapter, these cyclic behavior will be addressed by generalizing the model developed in this step.

Chapter 5

Finite-strain cyclic behavior of SMAs

5.1 Introduction

This chapter introduces the third step of the comprehensive constitutive modeling approach to investigate thermomechanical and cyclic behavior of SMAs in finite deformation. The chapter deals with the development of a thermomechanical finite-strain constitutive model capable of predicting cyclic behavior of polycrystalline SMAs. The model can be used for fatigue analysis of SMA structures if a proper fatigue criterion is introduced.

As presented in 2.2.3, in order to predict the cyclic behavior of SMAs, a number of constitutive models have been proposed with different degrees of sophistication. However, these models suffer from the following limitations: (i) all these models were developed under assumption of small strain, though most of the strain levels in cyclic experiments have entered finite strain regime; (ii) most of them are not able to capture the rate dependence; (iii) none of them considered the abrupt to smooth transition during training process.

To this end, this chapter is dedicated to developing a 3D thermomechanical finite-strain constitutive model for cyclic pseudoelasticity of polycrystalline SMAs. The model is able to describe the four fundamental characteristics related to the cyclic behavior of SMA that have not been integrally addressed within the finite-strain framework: (i) large accumulated residual strain that results from the residual martensite and the dislocations slipping during cycling; (ii) degeneration of pseudoelasticity and hysteresis loop due to the increase of dislocation density and internal stresses with the number of cycles; (iii) rate dependence that can be attributed to the thermomechanical coupling effect; (iv) evolution of the phase transformation from abrupt to smooth manner, as a consequence of the diversified crystallographic orientations of the grains, the heterogeneity of internal stresses, and the presence of non-transforming precipitates during cycling. Based on the decomposition of finite Hencky strain into elastic, transformation, residual and thermal parts, the model is constructed within a thermodynamically consistent framework. Evolution equations associated with the internal variables are derived from the reduced form of energy balance, the Clausius-Duhem form of entropy inequality, and a Helmholtz free energy function that includes elastic, thermal, interaction and constraint energies. The residual

strain evolves with the cumulated martensite volume fraction and stabilizes with a saturated value. The evolutions of the internal variables and the model parameters control the degenerations of the pseudoelasticity and the hysteresis loop with the number of cycles. The rate dependence is physically interpreted as the consequence of the competition between internal heat production and external heat transfer, and thereby is formulated by means of the temperature evolution and heat transfer equations. In addition, a tangential transformation hardening function g^t is introduced to describe the evolution of phase transformation from abrupt to smooth manner during cycling. Finally, the model is used to simulate the cyclic tensile experiments on NiTi wire at different loading rates. The good agreement of the model predictions against the experimental data demonstrates the capabilities of the proposed model to well describe cyclic pseudoelasticity of polycrystalline SMAs, and to capture the aforementioned characteristics.

5.2 Constitutive model

5.2.1 Kinematics

The present work aims to develop a comprehensive constitutive model that simultaneously accounts for cyclic effect, finite strain, thermomechanical coupling, martensitic transformation and reorientation. To this end, the deformation gradient $\boldsymbol{F}$ is multiplicatively decomposed into elastic $\boldsymbol{F}_e$, transformation $\boldsymbol{F}_t$, residual $\boldsymbol{F}_r$ and thermal $\boldsymbol{F}_\theta$ parts, such that

$$\boldsymbol{F} = \boldsymbol{F}_e \boldsymbol{F}_t \boldsymbol{F}_r \boldsymbol{F}_\theta, \tag{5.1}$$

where $\boldsymbol{F}_e$ is defined with respect to a local unstressed intermediate configuration, $\boldsymbol{F}_t$ is defined with respect to a zero-transformation intermediate configuration, $\boldsymbol{F}_r$ is defined with respect to a thermally expanded intermediate configuration and $\boldsymbol{F}_\theta$ is defined with respect to the reference configuration. It should be noted that the irreversible deformation $\boldsymbol{F}_r$ stems from two physical mechanisms: residual martensite and dislocations slipping. However, the present work takes no account of this distinction, and therefore $\boldsymbol{F}_r$ is not further split.

To simplify the following formulation, the transformation and residual deformation gradients, $\boldsymbol{F}_t$ and $\boldsymbol{F}_r$, are grouped into a new component as

$$\boldsymbol{F}_* = \boldsymbol{F}_t \boldsymbol{F}_r \quad \text{and} \quad \boldsymbol{F} = \boldsymbol{F}_e \boldsymbol{F}_* \boldsymbol{F}_\theta. \tag{5.2}$$

With regard to transformation, residual and thermal deformations, the following three kinematic assumptions are made:

1. First, the thermal deformation is assumed to be an isotropic thermal expansion, so that

$$\boldsymbol{F}_\theta = J_\theta^{\frac{1}{3}} \mathbf{1}. \tag{5.3}$$

2. Second, transformation and residual deformations are assumed incompressible, that is

$$J_t = \det \boldsymbol{F}_t = 1, \quad J_r = \det \boldsymbol{F}_r = 1 \quad \text{and} \quad J_* = J_t J_r = 1. \tag{5.4}$$

3. Last, for isotropic materials, the assumption of the irrotationality of inelastic flow is widely used in modern elasto-viscoplastic constitutive theories (Dafalias, 1984; Gurtin and Anand, 2005; Anand et al., 2009). Therefore, the transformation and residual flows are assumed irrotational (zero transformation spin)

$$\boldsymbol{W}_t = \boldsymbol{0}, \quad \boldsymbol{W}_r = \boldsymbol{0} \quad \text{and} \quad \boldsymbol{W}_* = \boldsymbol{0}, \tag{5.5}$$

where $\boldsymbol{W}_t$, $\boldsymbol{W}_r$ and $\boldsymbol{W}_*$ denote transformation, residual and total inelastic spin tensors.

Using the above kinematic assumptions (5.3), (5.4) and (5.5) and equations $(3.12)_1$ and (4.13), the elastic, transformation, residual and thermal Lagrangian and Eulerian Hencky strain tensors are written as

$$\begin{aligned} &\boldsymbol{H}_e = \ln \boldsymbol{U}_e = \bar{\boldsymbol{H}}_e + \frac{1}{3}\delta_e \boldsymbol{1}, \quad \boldsymbol{h}_e = \ln \boldsymbol{V}_e = \bar{\boldsymbol{h}}_e + \frac{1}{3}\delta_e \boldsymbol{1}, \\ &\boldsymbol{H}_t = \ln \boldsymbol{U}_t, \quad \boldsymbol{h}_t = \ln \boldsymbol{V}_t, \quad \boldsymbol{H}_r = \ln \boldsymbol{U}_r, \quad \boldsymbol{h}_r = \ln \boldsymbol{V}_r, \quad \boldsymbol{H}_\theta = \boldsymbol{h}_\theta = \frac{1}{3}\delta_\theta \boldsymbol{1}, \end{aligned} \tag{5.6}$$

where $\bar{\boldsymbol{H}}_e = \ln \bar{\boldsymbol{U}}_e$ and $\bar{\boldsymbol{h}}_e = \ln \bar{\boldsymbol{V}}_e$ are deviatoric components, $\delta_e = \ln J_e$ and $\delta_\theta = \ln J_\theta$ are spherical components.

The velocity gradient $\boldsymbol{L}$ in equation $(3.12)_3$ is additively decomposed as

$$\boldsymbol{L} = \bar{\boldsymbol{L}}_e + \bar{\boldsymbol{F}}_e \boldsymbol{L}_* \bar{\boldsymbol{F}}_e^{-1} + \frac{1}{3}\left(\dot{\delta}_e + \dot{\delta}_\theta\right)\boldsymbol{1}, \tag{5.7}$$

where $\bar{\boldsymbol{L}}_e = \dot{\bar{\boldsymbol{F}}}_e \bar{\boldsymbol{F}}_e^{-1}$ and $\boldsymbol{L}_* = \dot{\boldsymbol{F}}_* \boldsymbol{F}_*^{-1}$ are the isochoric elastic and inelastic velocity gradients, $\dot{\delta}_e = \dot{J}_e / J_e$ and $\dot{\delta}_\theta = \dot{J}_\theta / J_\theta$ are the volumetric elastic and thermal velocity gradients. Then the stretching and spin tensors, $\boldsymbol{D}$ and $\boldsymbol{W}$, in equation $(3.15)_1$ is written as

$$\boldsymbol{D} = \bar{\boldsymbol{D}}_e + \operatorname{sym}(\bar{\boldsymbol{F}}_e \boldsymbol{D}_* \bar{\boldsymbol{F}}_e^{-1}) + \frac{1}{3}\left(\dot{\delta}_e + \dot{\delta}_\theta\right)\boldsymbol{1} \quad \text{and} \quad \boldsymbol{W} = \boldsymbol{W}_e + \operatorname{skew}\left(\bar{\boldsymbol{F}}_e \boldsymbol{D}_* \bar{\boldsymbol{F}}_e^{-1}\right), \tag{5.8}$$

where $\bar{\boldsymbol{D}}_e$ and $\boldsymbol{W}_e$ are the stretching and spin tensors of isochoric elastic deformation, $\boldsymbol{D}_*$ is the inelastic stretching tensor.

5.2.2 Thermodynamic framework

The global reduced form of energy balance and Clausius-Duhem form of entropy inequality can be expressed as

$$\overline{\int_{\mathcal{B}} e_v \, \mathrm{d}V}^{\cdot} - \int_{\mathcal{B}} J\boldsymbol{\sigma} : \boldsymbol{D} \, \mathrm{d}V + \int_{\partial\mathcal{B}} \boldsymbol{q} \cdot \boldsymbol{n} \, \mathrm{d}S - \int_{\mathcal{B}} h_v \, \mathrm{d}V = 0, \tag{5.9}$$

$$\overline{\int_{\mathcal{B}} \eta_v \, \mathrm{d}V}^{\cdot} \geq \int_{\mathcal{B}} \frac{1}{\theta} h_v \, \mathrm{d}V - \int_{\partial\mathcal{B}} \frac{1}{\theta} \boldsymbol{q} \cdot \boldsymbol{n} \, \mathrm{d}S, \tag{5.10}$$

where e_v and η_v are the internal energy and the entropy per unit volume, $\boldsymbol{q}$ is the heat flux vector per unit area and $\boldsymbol{n}$ is the outward unit vector normal to the boundary of the body $\partial\mathcal{B}$, h_v is the heat source per unit volume. These state variables are defined in the spatial configuration.

Considering the irrotationality of the transformation and residual flows in equation (5.5), the inelastic stretching tensor is additively split into transformation and residual parts, *i.e.*, $\boldsymbol{D}_* = \boldsymbol{D}_t + \boldsymbol{D}_r$. Subsequently substituting this relation and equation (5.8) into the internal stress power in equation (5.9) gives

$$J\boldsymbol{\sigma} : \boldsymbol{D} = p\dot{\delta}_e + p\dot{\delta}_\theta + \boldsymbol{s} : \bar{\boldsymbol{D}}_e + \bar{\boldsymbol{F}}_e^T \boldsymbol{s} \bar{\boldsymbol{F}}_e^{-T} : (\boldsymbol{D}_t + \boldsymbol{D}_r), \tag{5.11}$$

where p and $\boldsymbol{s}$ are the spherical and deviatoric components of the Kirchhoff stress tensor, *i.e.*, $\boldsymbol{\tau} = J\boldsymbol{\sigma} = p\mathbf{1} + \boldsymbol{s}$. $\boldsymbol{D}_t$ and $\boldsymbol{D}_r$ are the transformation and residual stretching tensors.

Substituting equations (5.11) into equation (5.9) and localizing the integral equations (5.9) and (5.10) gives the following local forms of the energy balance and entropy inequality:

$$\dot{e}_v - p\dot{\delta}_e - p\dot{\delta}_\theta - \boldsymbol{s} : \bar{\boldsymbol{D}}_e - \bar{\boldsymbol{F}}_e^T \boldsymbol{s} \bar{\boldsymbol{F}}_e^{-T} : (\boldsymbol{D}_t + \boldsymbol{D}_r) - h_v + \nabla \cdot \boldsymbol{q} = 0, \tag{5.12}$$

$$\dot{\eta}_v \theta - h_v + \nabla \cdot \boldsymbol{q} - \frac{1}{\theta} \boldsymbol{q} \cdot \nabla\theta \geq 0. \tag{5.13}$$

The Helmholtz free energy ψ per unit volume in the spatial configuration and its time derivative $\dot{\psi}$ are given by

$$\psi = e_v - \eta_v \theta \qquad \text{and} \qquad \dot{\psi} = \dot{e}_v - \dot{\eta}_v \theta - \eta_v \dot{\theta}. \tag{5.14}$$

Combining equations (5.12), (5.13) and $(5.14)_2$ gives the following entropy inequality:

$$p\left(\dot{\delta}_e + \dot{\delta}_\theta\right) + \boldsymbol{s} : \bar{\boldsymbol{D}}_e + \bar{\boldsymbol{F}}_e^T \boldsymbol{s} \bar{\boldsymbol{F}}_e^{-T} : (\boldsymbol{D}_t + \boldsymbol{D}_r) - \left(\dot{\psi} + \eta_v \dot{\theta}\right) - \frac{1}{\theta} \boldsymbol{q} \cdot \nabla\theta \geq 0. \tag{5.15}$$

In order to satisfy the principle of material objectivity, the Helmholtz free energy density ψ in the present work depends on the elastic deformation gradient $\boldsymbol{F}_e$ through the elastic Lagrangian Hencky strain $\boldsymbol{H}_e$, on the transformation deformation gradient $\boldsymbol{F}_t$ through the transformation Lagrangian Hencky strain $\boldsymbol{H}_t$, on the residual deformation gradient $\boldsymbol{F}_r$ through the residual Lagrangian Hencky strain $\boldsymbol{H}_r$,

on the thermal deformation gradient $\boldsymbol{F}_\theta$ through the thermal Lagrangian Hencky strain $\boldsymbol{H}_\theta$, on scalar internal variables χ, χ_c, and on temperature θ as

$$\psi = \psi\left(\boldsymbol{H}_e, \boldsymbol{H}_t, \boldsymbol{H}_r, \boldsymbol{H}_\theta, \chi, \chi_c, \theta\right), \tag{5.16}$$

where χ denotes the volume fraction of martensite, $\chi_c = \int_0^t |\dot{\chi}| \mathrm{d}\tau$ denotes the cumulated volume fraction of martensite. The free energy density ψ is assumed to be an isotropic function of $\boldsymbol{H}_e$, $\boldsymbol{H}_t$, $\boldsymbol{H}_r$ and $\boldsymbol{H}_\theta$, which allows ψ to be expressed as the function of their argument invariants. As the Lagrangian and Eulerian Hencky strains share the same invariants, ψ can be written in terms of Eulerian Hencky strains as

$$\psi\left(\boldsymbol{H}_e, \boldsymbol{H}_t, \boldsymbol{H}_r, \boldsymbol{H}_\theta, \chi, \chi_c, \theta\right) = \psi\left(\delta_e, \bar{\boldsymbol{h}}_e, \boldsymbol{h}_t, \boldsymbol{h}_r, \delta_\theta, \chi, \chi_c, \theta\right). \tag{5.17}$$

Hence, the time derivative of ψ gives

$$\dot{\psi} = \frac{\partial \psi}{\partial \delta_e}\dot{\delta}_e + \frac{\partial \psi}{\partial \bar{\boldsymbol{h}}_e} : \dot{\bar{\boldsymbol{h}}}_e + \frac{\partial \psi}{\partial \boldsymbol{h}_t} : \dot{\boldsymbol{h}}_t + \frac{\partial \psi}{\partial \boldsymbol{h}_r} : \dot{\boldsymbol{h}}_r + \frac{\partial \psi}{\partial \delta_\theta}\dot{\delta}_\theta + \frac{\partial \psi}{\partial \chi}\dot{\chi} + \frac{\partial \psi}{\partial \chi_c}\dot{\chi}_c + \frac{\partial \psi}{\partial \theta}\dot{\theta}. \tag{5.18}$$

Because of isotropy, the derivatives of the isotropic functions $\frac{\partial \psi}{\partial \bar{\boldsymbol{h}}_e}$, $\frac{\partial \psi}{\partial \boldsymbol{h}_t}$ and $\frac{\partial \psi}{\partial \boldsymbol{h}_r}$ are symmetric and, respectively, coaxial with $\bar{\boldsymbol{h}}_e$, $\boldsymbol{h}_t$ and $\boldsymbol{h}_r$. Using equations (A.4) and (A.8),

$$\begin{aligned}
\frac{\partial \psi}{\partial \bar{\boldsymbol{h}}_e} : \dot{\bar{\boldsymbol{h}}}_e &= \frac{\partial \psi}{\partial \bar{\boldsymbol{h}}_e} : \overset{\circ}{\bar{\boldsymbol{h}}}{}_e^L = \frac{\partial \psi}{\partial \bar{\boldsymbol{h}}_e} : \bar{\boldsymbol{D}}_e, \\
\frac{\partial \psi}{\partial \boldsymbol{h}_t} : \dot{\boldsymbol{h}}_t &= \frac{\partial \psi}{\partial \boldsymbol{h}_t} : \mathring{\boldsymbol{h}}_t^L = \frac{\partial \psi}{\partial \boldsymbol{h}_t} : \boldsymbol{D}_t, \\
\frac{\partial \psi}{\partial \boldsymbol{h}_r} : \dot{\boldsymbol{h}}_r &= \frac{\partial \psi}{\partial \boldsymbol{h}_r} : \mathring{\boldsymbol{h}}_r^L = \frac{\partial \psi}{\partial \boldsymbol{h}_r} : \boldsymbol{D}_r,
\end{aligned} \tag{5.19}$$

where $\overset{\circ}{\bar{\boldsymbol{h}}}{}_e^L$, $\mathring{\boldsymbol{h}}_t^L$ and $\mathring{\boldsymbol{h}}_r^L$ are, respectively, the logarithmic corotational rates of elastic, transformation and residual Eulerian Hencky strains.

Substituting equations (5.18) and (5.19) into the entropy inequality (5.15) gives

$$\begin{aligned}
&\left(p - \frac{\partial \psi}{\partial \delta_e}\right)\dot{\delta}_e + \left(p - \frac{\partial \psi}{\partial \delta_\theta}\right)\dot{\delta}_\theta + \left(\boldsymbol{s} - \frac{\partial \psi}{\partial \bar{\boldsymbol{h}}_e}\right) : \bar{\boldsymbol{D}}_e + \left(\bar{\boldsymbol{F}}_e^T \boldsymbol{s} \bar{\boldsymbol{F}}_e^{-T} - \frac{\partial \psi}{\partial \boldsymbol{h}_t}\right) : \boldsymbol{D}_t + \\
&\left(\bar{\boldsymbol{F}}_e^T \boldsymbol{s} \bar{\boldsymbol{F}}_e^{-T} - \frac{\partial \psi}{\partial \boldsymbol{h}_r}\right) : \boldsymbol{D}_r - \frac{\partial \psi}{\partial \chi}\dot{\chi} - \frac{\partial \psi}{\partial \chi_c}\dot{\chi}_c - \left(\frac{\partial \psi}{\partial \theta} + \eta_v\right)\dot{\theta} - \frac{1}{\theta}\boldsymbol{q} \cdot \nabla\theta \geq 0.
\end{aligned} \tag{5.20}$$

For arbitrary thermodynamic processes, inequality (5.20) is guaranteed by the following choice of the constitutive laws with respect to the hydrostatic stress p, the deviatoric stress $\boldsymbol{s}$ and the entropy η_v:

$$p = \frac{\partial \psi}{\partial \delta_e} = \frac{\partial \psi}{\partial \delta_\theta}, \quad \boldsymbol{s} = \frac{\partial \psi}{\partial \bar{\boldsymbol{h}}_e} \quad \text{and} \quad \eta_v = -\frac{\partial \psi}{\partial \theta}, \tag{5.21}$$

and by the following inequalities, which ensure nonnegative intrinsic dissipation in arbitrary evolutions of the internal state variables $\boldsymbol{D}_t$, $\boldsymbol{D}_r$, χ and χ_c, so that

$$\left(\bar{\boldsymbol{M}}_e - \boldsymbol{X}_t\right) : \boldsymbol{D}_t + \left(\bar{\boldsymbol{M}}_e - \boldsymbol{X}_r\right) : \boldsymbol{D}_r - \frac{\partial \psi}{\partial \chi}\dot{\chi} - \frac{\partial \psi}{\partial \chi_c}\dot{\chi}_c \geq 0, \tag{5.22}$$

with

$$\bar{\boldsymbol{M}}_e = \bar{\boldsymbol{F}}_e^T \boldsymbol{s} \bar{\boldsymbol{F}}_e^{-T}, \quad \boldsymbol{X}_t = \frac{\partial \psi}{\partial \boldsymbol{h}_t} \quad \text{and} \quad \boldsymbol{X}_r = \frac{\partial \psi}{\partial \boldsymbol{h}_r}, \tag{5.23}$$

as well as nonnegative dissipation due to heat conduction, so that

$$-\frac{1}{\theta}\boldsymbol{q} \cdot \nabla\theta \geq 0, \tag{5.24}$$

where $\bar{\boldsymbol{M}}_e$ is a symmetric and traceless Mandel stress tensor by rotating the deviatoric Kirchhoff stress $\boldsymbol{s}$ back into the intermediate unstressed configuration, $\boldsymbol{X}_t$ and $\boldsymbol{X}_r$ are symmetric stress-like tensors.

Combining equations $(5.14)_2$, (5.18) and (5.21) gives the following Gibbs relation between internal energy and entropy:

$$\dot{e}_v = \theta\dot{\eta}_v + p\left(\dot{\delta}_e + \dot{\delta}_\theta\right) + \boldsymbol{s} : \dot{\bar{\boldsymbol{h}}}_e + \boldsymbol{X}_t : \dot{\boldsymbol{h}}_t + \boldsymbol{X}_r : \dot{\boldsymbol{h}}_r + \frac{\partial \psi}{\partial \chi}\dot{\chi} + \frac{\partial \psi}{\partial \chi_c}\dot{\chi}_c, \tag{5.25}$$

which, with the energy balance equation (5.12), yields the following entropy evolution:

$$\theta\dot{\eta}_v = h_v - \nabla \cdot \boldsymbol{q} + \left(\bar{\boldsymbol{M}}_e - \boldsymbol{X}_t\right) : \boldsymbol{D}_t - \left(\bar{\boldsymbol{M}}_e - \boldsymbol{X}_r\right) : \boldsymbol{D}_r - \frac{\partial \psi}{\partial \chi}\dot{\chi} - \frac{\partial \psi}{\partial \chi_c}\dot{\chi}_c. \tag{5.26}$$

The internal energy and the entropy densities are assumed to depend on the same state variables as the Helmholtz free energy:

$$e_v = e\left(\delta_e, \bar{\boldsymbol{h}}_e, \boldsymbol{h}_t, \boldsymbol{h}_r, \delta_\theta, \chi, \chi_c, \theta\right), \quad \eta_v = \eta\left(\delta_e, \bar{\boldsymbol{h}}_e, \boldsymbol{h}_t, \boldsymbol{h}_r, \delta_\theta, \chi, \chi_c, \theta\right). \tag{5.27}$$

The specific heat capacity is defined as

$$c_v \overset{\text{def}}{=} \frac{\partial e\left(\delta_e, \bar{\boldsymbol{h}}_e, \boldsymbol{h}_t, \boldsymbol{h}_r, \delta_\theta, \chi, \chi_c, \theta\right)}{\partial \theta}, \tag{5.28}$$

which, with equations (5.14) and $(5.21)_3$, can be written as

$$c_v = \theta\frac{\partial \eta\left(\delta_e, \bar{\boldsymbol{h}}_e, \boldsymbol{h}_t, \boldsymbol{h}_r, \delta_\theta, \chi, \chi_c, \theta\right)}{\partial \theta} = -\theta\frac{\partial^2 \psi\left(\delta_e, \bar{\boldsymbol{h}}_e, \boldsymbol{h}_t, \boldsymbol{h}_r, \delta_\theta, \chi, \chi_c, \theta\right)}{\partial \theta^2}. \tag{5.29}$$

Hence, from equations (5.21)$_3$, (5.27) and (5.29),

$$\begin{aligned}\theta\dot{\eta}_v =&\theta\left(\frac{\partial\eta}{\partial\delta_e}\dot{\delta}_e+\frac{\partial\eta}{\partial\bar{\boldsymbol{h}}_e}:\dot{\bar{\boldsymbol{h}}}_e+\frac{\partial\eta}{\partial\boldsymbol{h}_t}:\dot{\boldsymbol{h}}_t+\frac{\partial\eta}{\partial\boldsymbol{h}_r}:\dot{\boldsymbol{h}}_r+\frac{\partial\eta}{\partial\delta_\theta}\dot{\delta}_\theta+\frac{\partial\eta}{\partial\chi}\dot{\chi}+\frac{\partial\eta}{\partial\chi_c}\dot{\chi}_c\right)+c_v\dot{\theta}\\ =&c_v\dot{\theta}-\theta\left(\frac{\partial^2\psi}{\partial\theta\partial\delta_e}\dot{\delta}_e+\frac{\partial^2\psi}{\partial\theta\partial\bar{\boldsymbol{h}}_e}:\dot{\bar{\boldsymbol{h}}}_e+\frac{\partial^2\psi}{\partial\theta\partial\delta_\theta}\dot{\delta}_\theta\right)-\\ &\theta\left(\frac{\partial^2\psi}{\partial\theta\partial\boldsymbol{h}_t}:\dot{\boldsymbol{h}}_t+\frac{\partial^2\psi}{\partial\theta\partial\boldsymbol{h}_r}:\dot{\boldsymbol{h}}_r+\frac{\partial^2\psi}{\partial\theta\partial\chi}\dot{\chi}+\frac{\partial^2\psi}{\partial\theta\partial\chi_c}\dot{\chi}_c\right).\end{aligned}\tag{5.30}$$

Then, combining equations (5.26) and (5.30) gives the following partial differential equation for the temperature θ:

$$\begin{aligned}c_v\dot{\theta} =&h_v-\nabla\cdot\boldsymbol{q}+\underbrace{\left(\bar{\boldsymbol{M}}_e-\boldsymbol{X}_t\right):\boldsymbol{D}_t+\left(\bar{\boldsymbol{M}}_e-\boldsymbol{X}_r\right):\boldsymbol{D}_r-\frac{\partial\psi}{\partial\chi}\dot{\chi}-\frac{\partial\psi}{\partial\chi_c}\dot{\chi}_c}_{\mathcal{D}=\text{intrinsic dissipation}}\\ &+\underbrace{\theta\left(\frac{\partial^2\psi}{\partial\theta\partial\boldsymbol{h}_t}:\boldsymbol{D}_t+\frac{\partial^2\psi}{\partial\theta\partial\boldsymbol{h}_r}:\boldsymbol{D}_r+\frac{\partial^2\psi}{\partial\theta\partial\chi}\dot{\chi}+\frac{\partial^2\psi}{\partial\theta\partial\chi_c}\dot{\chi}_c\right)}_{\mathcal{T}=\text{thermoplastic + thermo-transformation coupling}}\\ &+\underbrace{\theta\left(\frac{\partial^2\psi}{\partial\theta\partial\delta_e}\dot{\delta}_e+\frac{\partial^2\psi}{\partial\theta\partial\bar{\boldsymbol{h}}_e}:\bar{\boldsymbol{D}}_e+\frac{\partial^2\psi}{\partial\theta\partial\delta_\theta}\dot{\delta}_\theta\right)}_{\mathcal{X}=\text{thermoelastic coupling}},\end{aligned}\tag{5.31}$$

wherein, the term $\mathcal{D}$ represents the intrinsic dissipations associated to plastic deformation, martensitic transformation and reorientation; the term $\mathcal{T}$ represents the entropy change due to plastic and transformation deformations as well as the latent heat during phase transformation; the term $\mathcal{X}$ represents the entropy change due to thermoelastic deformation; the heat flux $\boldsymbol{q}$ is taken to be governed by Fourier's law

$$\boldsymbol{q}=-k\nabla\theta,\tag{5.32}$$

where k is the nonnegative thermal conductivity.

5.2.3 Helmholtz free energy function

The Helmholtz free energy function ψ in equation (5.17) is additively decomposed as follows:

$$\psi=\psi^e+\psi^\theta+\psi^{int}+\psi^{cst},\tag{5.33}$$

where ψ^e is the elastic energy, ψ^θ is the thermal contribution to free energy (Morin et al., 2011a; Lagoudas et al., 2012), ψ^{int} is the interaction energy between martensite and austenite phases (Moumni et al., 2008), ψ^{cst} is the potential energy due to the internal constraints.

By employing the the rule of mixtures (Lagoudas et al., 2006; Moumni et al., 2008; Auricchio et al., 2014), the elastic energy ψ^e and the thermal energy ψ^θ in equation (5.33) can be expressed in the

following form:

$$\psi^{*} = (1-\chi)\,\psi^{*,A} + \chi\psi^{*,M}, \tag{5.34}$$

where $* \in \{e, \theta\}$, $\psi^{*,A}$ and $\psi^{*,M}$ denote the free energies of austenite and martensite phases, respectively.

By assuming isotropic and homogeneous elasticity in austenite and martensite, a Reuss rheological model (Moumni et al., 2008; Auricchio et al., 2014) is considered to formulate the elastic energy ψ^{e} for the phase mixture:

$$\psi^{e} = \frac{1}{2}K\delta^{2} + \mu\|\bar{\boldsymbol{h}}_{e}\|^{2} - 3\alpha K\delta(\theta-\theta_{0}), \tag{5.35}$$

where $\delta = \mathrm{tr}(\boldsymbol{h}) = \delta_{e} + \delta_{\theta}$ is the volumetric component of $\boldsymbol{h}$, θ_{0} is the reference temperature, α is the thermal expansion coefficient. The bulk modulus K is assumed to be equal for the two phases and the shear modulus μ is determined from the Reuss model (Wagner and Windl, 2008; Auricchio et al., 2014) as follows:

$$K = K^{A} = K^{M} \quad \text{and} \quad \frac{1}{\mu} = (1-\chi)\,\frac{1}{\mu^{A}} + \chi\frac{1}{\mu^{M}}. \tag{5.36}$$

The thermal energy ψ^{θ} is sometimes referred to as chemical energy (Sedlák et al., 2012; Auricchio et al., 2014), which is related to the changes in internal energy and entropy. The thermal energies in equation $(5.34)_2$ for the two different phases, $\psi^{\theta,*}$, are defined as

$$\psi^{\theta,*} = e_{0}^{*} - \eta_{0}^{*}\theta + c_{v}^{*}\left[(\theta-\theta_{0}) - \theta\ln\left(\frac{\theta}{\theta_{0}}\right)\right], \tag{5.37}$$

where $*$ denotes either of the phases A and M, e_{0} and η_{0} are reference internal energy and entropy at reference temperature θ_{0}, c_{v} is the specific heat capacity. Substituting equation (5.37) into equation $(5.34)_2$ gives the following thermal energy:

$$\psi^{\theta} = e_{0}^{A} - \eta_{0}^{A}\theta + \chi\Delta\eta_{t}\,(\theta-\theta_{0}) + \left(c_{v}^{A} - \chi\Delta c_{v}^{t}\right)\left[(\theta-\theta_{0}) - \theta\ln\left(\frac{\theta}{\theta_{0}}\right)\right], \tag{5.38}$$

where $\Delta\eta_{t} = \eta_{0}^{A} - \eta_{0}^{M}$ and $\Delta c_{v}^{t} = c_{v}^{A} - c_{v}^{M}$ are the differences of entropy and heat capacity between austenite and martensite.

The interaction energy ψ^{int} represents the crystal boundary energy between austenite and martensite phases, which is often derived from micro-mechanical or crystallographic considerations and finally expressed as a function of internal state variables (Zaki and Moumni, 2007b; Auricchio et al., 2014). In the present work, the interaction energy ψ^{int} is assumed to depend on the volume fraction of martensite χ, transformation strain $\boldsymbol{h}_{t}$ and residual strain $\boldsymbol{h}_{r}$ as

$$\psi^{int} = \psi^{int}(\chi, \chi_{c}, \boldsymbol{h}_{t}, \boldsymbol{h}_{r}) = \mathcal{G}^{t}(\chi, \chi_{c}) + \frac{1}{2}\mu_{t}\|\boldsymbol{h}_{t}\|^{2} + \frac{1}{2}\mu_{r}\|\boldsymbol{h}_{r}\|^{2}, \tag{5.39}$$

where μ_{t} and μ_{r} are transformation and residual hardening moduli. The first term $\mathcal{G}^{t}$ on the right-hand side of equation (5.39) represents the interaction energy due to the coexistence of austenite and martensite

phases, the second term $\frac{1}{2}\mu_t\|\boldsymbol{h}_t\|^2$ represents increase in interaction due to orientation/reorientation of martensite variants, and the last term $\frac{1}{2}\mu_r\|\boldsymbol{h}_r\|^2$ represents increase in interaction due to dislocation slipping.

Finally, the following Lagrangian potential is defined as the constraint energy ψ^{cst} to guarantee the physical constraints on χ and $\boldsymbol{h}_t$:

$$\psi^{cst} = -\zeta^t\left(\mathcal{H} - \|\boldsymbol{h}_t\|\right) - \zeta^f(1-\chi) - \zeta^r\chi, \tag{5.40}$$

where $\mathcal{H}$ is the fully oriented strain magnitude of martensite variants, ζ^t is a nonnegative Lagrange multiplier associated with the unilateral constraint $\mathcal{H} - \|\boldsymbol{h}_t\| \geq 0$; ζ^f and ζ^r are nonnegative Lagrange multipliers associated with the bilateral constraints $0 \geq \chi \geq 1$. The constraint energy (5.40) is complemented by the following classical Kuhn-Tucker conditions:

$$\begin{cases} \mathcal{H} - \|\boldsymbol{h}_t\| \geq 0, & \zeta^t \geq 0, & \zeta^t\left(\mathcal{H} - \|\boldsymbol{h}_t\|\right) = 0; \\ 1-\chi \geq 0, & \zeta^f \geq 0, & \zeta^f(1-\chi) = 0; \\ \chi \geq 0, & \zeta^r \geq 0, & \zeta^r\chi = 0. \end{cases} \tag{5.41}$$

In conclusion, the Helmholtz free energy function ψ is constructed as

$$\begin{aligned} \psi =& \frac{1}{2}K\delta^2 + \mu\|\bar{\boldsymbol{h}}_e\|^2 - 3\alpha K\delta(\theta-\theta_0) + e_0^A - \eta_0^A\theta + \left(c_v^A - \chi\Delta c_v^t\right)\left[(\theta-\theta_0) - \theta\ln\left(\frac{\theta}{\theta_0}\right)\right] + \\ & \chi\Delta\eta_t(\theta-\theta_0) + \mathcal{G}^t + \frac{1}{2}\mu_t\|\boldsymbol{h}_t\|^2 + \frac{1}{2}\mu_r\|\boldsymbol{h}_r\|^2 - \zeta^t\left(\mathcal{H} - \|\boldsymbol{h}_t\|\right) - \zeta^f(1-\chi) - \zeta^r\chi. \end{aligned} \tag{5.42}$$

5.2.4 Constitutive equations

Substituting the Helmholtz free energy function ψ in equation (5.42) into the established thermodynamic framework, specifically, equations (5.21) and (5.23), gives the volumetric and the deviatoric stresses, p and $\boldsymbol{s}$, and the entropy η_v as follows:

$$\begin{cases} p = \frac{\partial\Psi}{\partial\delta} = K\left[\delta - 3\alpha(\theta-\theta_0)\right], \\ \boldsymbol{s} = \frac{\partial\Psi}{\partial\bar{\boldsymbol{h}}_e} = 2\mu\bar{\boldsymbol{h}}_e, \\ \eta_v = -\frac{\partial\Psi}{\partial\theta} = 3\alpha K\delta + \eta_0^A + \left(c_v^A - \chi\Delta c_v^t\right)\ln\left(\frac{\theta}{\theta_0}\right) - \Delta\eta_t\chi, \end{cases} \tag{5.43}$$

as well as the following Mandel stress $\bar{\boldsymbol{M}}_e$ and state quantities $\boldsymbol{X}_t$ and $\boldsymbol{X}_r$:

$$\bar{\boldsymbol{M}}_e = 2\mu\bar{\boldsymbol{H}}_e, \quad \boldsymbol{X}_t = \mu_t\boldsymbol{h}_t + \zeta^t\boldsymbol{N}_t \quad \text{and} \quad \boldsymbol{X}_r = \mu_r\boldsymbol{h}_r, \tag{5.44}$$

where $\boldsymbol{N}_t = \frac{\boldsymbol{h}_t}{\|\boldsymbol{h}_t\|}$ denotes the direction of the transformation strain. Moreover, the partial derivative of ψ with respect to χ is given by

$$\frac{\partial\psi}{\partial\chi} = \Delta\eta_t(\theta-\theta_0) - \Delta c_v^t\left[(\theta-\theta_0) - \theta\ln\left(\frac{\theta}{\theta_0}\right)\right] + g^t + \zeta^f - \zeta^r, \tag{5.45}$$

where $g^t = \partial \mathcal{G}^t / \partial \chi$ is the phase transformation hardening function. In order to capture the abrupt to smooth transition during cycling at the initiation and completion of phase transformation, as experimentally demonstrated in the literature for polycrystalline SMAs (Lagoudas et al., 2006; Hartl et al., 2010; Morin et al., 2011b), a tangential transformation hardening function g^t is considered as

$$g^t = \kappa \tan^m \left[\frac{1}{2}(\xi_a \chi + \xi_b)\pi \right] + r, \tag{5.46}$$

where π is the circular constant, κ, m, ξ_a, ξ_b and r are model parameters. To account for the degeneration of the pseudoelasticity and dissipated energy during the cyclic deformation, these model parameters are considered to be functions of the cumulated martensite volume fraction χ_c:

$$f = f^0 + (f^{sat} - f^0)\left[1 - \exp\left(-\frac{\chi_c}{\tau}\right)\right], \tag{5.47}$$

where $f = \{\kappa, m, \xi_a, \xi_b, r\}$, f^0 and f^{sat} correspond, respectively, to untrained and completely trained SMA, τ is a dimensionless time constant. Additionally, the model parameters $\Delta\eta_t$ and $\mathcal{H}$ also depend on χ_c according to equation (5.47).

The martensite volume fraction χ, according to the literature (Reese and Christ, 2008; Moumni et al., 2008; Lagoudas et al., 2012), can be expressed in terms of the transformation strain, *i.e.*, $\chi = \|\boldsymbol{h}_t\|/\mathcal{H}$. Thus, using this relation, the time derivative of deformation strain is additively split as follows:

$$\dot{\boldsymbol{h}}_t = \mathcal{H}\left(\boldsymbol{N}_t \dot{\chi} + \chi \dot{\boldsymbol{N}}_t\right), \tag{5.48}$$

where the first term represents phase transformation between austenite and martensite, while the second term represents martensitic reorientation. Substituting equation (5.48) into equation (A.4) gives the following split of the transformation stretching $\boldsymbol{D}_t$:

$$\boldsymbol{D}_t = \mathring{\boldsymbol{h}}_t^L = \mathcal{H}\left(\dot{\chi}\boldsymbol{N}_t + \chi \boldsymbol{D}_N\right), \tag{5.49}$$

where $\boldsymbol{D}_N = \mathring{\boldsymbol{N}}_t^L = \dot{\boldsymbol{N}}_t - \boldsymbol{\Omega}_t^L \boldsymbol{N}_t + \boldsymbol{N}_t \boldsymbol{\Omega}_t^L$ is the stretching tensor associated with martensitic reorientation.

Substituting equation (5.49) into inequality (5.22) gives

$$\mathcal{H}\chi\left(\bar{\boldsymbol{M}}_e - \boldsymbol{X}_t\right) : \boldsymbol{D}_N + \left(\bar{\boldsymbol{M}}_e - \boldsymbol{X}_r\right) : \boldsymbol{D}_r + \left[\mathcal{H}\left(\bar{\boldsymbol{M}}_e - \boldsymbol{X}_t\right) : \boldsymbol{N}_t - \frac{\partial \psi}{\partial \chi}\right]\dot{\chi} - \frac{\partial \psi}{\partial \chi_c}\dot{\chi}_c \geq 0. \tag{5.50}$$

The nonnegative dissipation of equation (5.50) is guaranteed by the following choice of the evolution equations:

$$\boldsymbol{D}_N = \dot{\gamma}^N \frac{\boldsymbol{A}_N}{\|\boldsymbol{A}_N\|}, \quad \boldsymbol{D}_r = \dot{\gamma}^r \frac{\boldsymbol{A}_r}{\|\boldsymbol{A}_r\|} \quad \text{and} \quad \dot{\chi} = \dot{\gamma}^t \mathcal{S}(A_\chi), \tag{5.51}$$

with

$$\begin{cases} \boldsymbol{A}_N = 2\mu\bar{\boldsymbol{H}}_e - \mu_t \boldsymbol{h}_t - \zeta^t \boldsymbol{N}_t, \\ \boldsymbol{A}_r = 2\mu\bar{\boldsymbol{H}}_e - \mu_t \boldsymbol{h}_r, \\ A_\chi = \mathcal{H}\left(2\mu\bar{\boldsymbol{H}}_e : \boldsymbol{N}_t - \mu_t \mathcal{H}\chi - \zeta^t\right) + \left(\Delta c_v^t - \Delta\eta_t\right)(\theta - \theta_0) - \Delta c_v^t \theta \ln\left(\frac{\theta}{\theta_0}\right) - g^t - \zeta^f + \zeta^r, \end{cases} \tag{5.52}$$

where $\dot{\gamma}^N$, $\dot{\gamma}^r$ and $\dot{\gamma}^t$ are nonnegative multipliers, the sign function $\mathcal{S}(\cdot)$ is used to extract the sign of A_χ. The rate of residual deformation $\dot{\gamma}^r$ is determined by the rate of cumulated martensite volume fraction $\dot{\chi}_c$ as

$$\dot{\gamma}^r = \frac{R^{sat}}{\tau} \exp\left(-\frac{\chi_c}{\tau}\right) \dot{\chi}_c, \tag{5.53}$$

where R^{sat} denotes the saturated residual strain in the stabilized hysteresis loop. According to the experimental data reported by (Kan et al., 2016), R^{sat} has an approximately linear relation with logarithmic strain rate, and therefore is defined in present work as

$$R^{sat} = \begin{cases} R_c \log \dot{h}_{eq} + R_0 & \text{if } \dot{h}_{eq} \geq \dot{h}_{th}, \\ R_s & \text{otherwise}, \end{cases} \tag{5.54}$$

where $\dot{h}_{eq} = \sqrt{\frac{2}{3}\dot{\boldsymbol{h}} : \dot{\boldsymbol{h}}}$ is the equivalent strain rate and $\log \dot{h}_{eq}$ denotes the logarithmic strain rate; R_c, R_0 and R_s are model parameters that control the change of R^{sat} with strain rate when $\dot{h}_{eq}$ is greater than the threshold value $\dot{h}_{th}$.

Moreover, using equations $(5.51)_1$ and (A.8), with the relation $\overline{\|\boldsymbol{N}_t\|} = 0$, allows writing the Lagrangian multiplier ζ^t as

$$\zeta^t = \bar{\boldsymbol{M}}_e : \boldsymbol{N}_t - \mu_t \mathcal{H}\chi. \tag{5.55}$$

Substituting equation (5.55) into equation $(5.52)_1$, $\boldsymbol{A}_N$ is written as

$$\boldsymbol{A}_N = \bar{\boldsymbol{M}}_e - \left(\bar{\boldsymbol{M}}_e : \boldsymbol{N}_t\right) \boldsymbol{N}_t = \left(\mathbb{I} - \boldsymbol{N}_t \otimes \boldsymbol{N}_t\right) \bar{\boldsymbol{M}}_e, \tag{5.56}$$

where $\mathbb{I}$ is the fourth-order identity tensor, and $\boldsymbol{A}_N$ represents the component normal to $\boldsymbol{N}_t$ of the Mandel stress $\bar{\boldsymbol{M}}_e$.

Then, the associated yield functions to describe phase transformation and martensitic reorientation evolutions are given by

$$\mathcal{F}_\chi = |A_\chi| - Y_\chi \qquad \text{and} \qquad \mathcal{F}_N = \|\boldsymbol{A}_N\| - \chi Y_N, \tag{5.57}$$

where Y_χ and Y_N control the thresholds of the phase transformation and the martensitic reorientation. $\dot{\gamma}^t$, $\dot{\gamma}^N$, $\mathcal{F}_\chi$ and $\mathcal{F}_N$ are subjected to the following Kuhn-Tucker consistency conditions:

$$\begin{cases} \dot{\gamma}^t \geq 0, & \mathcal{F}_\chi \leq 0, & \dot{\gamma}^t \mathcal{F}_\chi = 0; \\ \dot{\gamma}^N \geq 0, & \mathcal{F}_N \leq 0, & \dot{\gamma}^N \mathcal{F}_N = 0. \end{cases} \tag{5.58}$$

Finally, using equations (5.43), (5.51) and (5.31), the temperature evolution equation is written as

$$c_v \dot{\theta} = h_v - \nabla \cdot \boldsymbol{q} + \dot{\gamma}^N \|\boldsymbol{A}_N\| + \dot{\gamma}^r \|\boldsymbol{A}_r\| + \dot{\gamma}^t |A_\chi| + \dot{\gamma}^t \mathcal{S}(A_\chi)\theta \left[\Delta\eta_t + \Delta c_v^t \ln\left(\frac{\theta}{\theta_0}\right)\right] - 3\alpha\theta K\dot{\delta}. \tag{5.59}$$

A review of the constitutive equations derived in this section is presented in Table 5.1.

Table 5.1 Summary of the model accounting for cyclic effect.

State and internal variables: $\delta_e, \bar{\boldsymbol{h}}_e, \boldsymbol{h}_t, \boldsymbol{h}_r, \delta_\theta, \chi, \chi_c, \theta$

Thermoelasticity:

$p = K\left[\delta_e + \delta_\theta - 3\alpha(\theta - \theta_0)\right]$ and $\boldsymbol{s} = 2\mu\bar{\boldsymbol{h}}_e$

Phase transformation:

$\boldsymbol{D}_t = \mathring{\boldsymbol{h}}_t^L = \mathcal{H}\left(\dot{\chi}\boldsymbol{N}_t + \chi\boldsymbol{D}_N\right)$, $\boldsymbol{D}_N = \dot{\gamma}^N \frac{\boldsymbol{A}_N}{\|\boldsymbol{A}_N\|}$, $\dot{\chi} = \dot{\gamma}^t \mathcal{S}(A_\chi)$,

where

$\boldsymbol{A}_N = \left(\mathbb{I} - \boldsymbol{N}_t \otimes \boldsymbol{N}_t\right)\bar{\boldsymbol{M}}_e$,

$A_\chi = \mathcal{H}\left(2\mu\bar{\boldsymbol{H}}_e : \boldsymbol{N}_t - \mu_t\mathcal{H}\chi - \zeta^t\right) + \left(\Delta c_v^t - \Delta\eta_t\right)(\theta - \theta_0) - \Delta c_v^t \theta \ln\left(\frac{\theta}{\theta_0}\right) - g^t - \zeta^f + \zeta^r$

Residual deformation:

$\boldsymbol{D}_r = \mathring{\boldsymbol{h}}_r^L = \dot{\gamma}^r \frac{\boldsymbol{A}_r}{\|\boldsymbol{A}_r\|}$,

where

$\boldsymbol{A}_r = 2\mu\bar{\boldsymbol{H}}_e - \mu_t \boldsymbol{h}_r$, $\dot{\gamma}^r = \frac{R^{sat}}{\tau}\exp\left(-\frac{\chi_c}{\tau}\right)\dot{\chi}_c$, $\dot{\chi}_c = |\dot{\chi}|$

Temperature evolution:

$c_v\dot{\theta} = h_v - \nabla\cdot\boldsymbol{q} + \dot{\gamma}^N\|\boldsymbol{A}_N\| + \dot{\gamma}^r\|\boldsymbol{A}_r\| + \dot{\gamma}^t|A_\chi| + \dot{\gamma}^t\mathcal{S}(A_\chi)\theta\left[\Delta\eta_t + \Delta c_v^t\ln\left(\frac{\theta}{\theta_0}\right)\right] - 3\alpha\theta K\dot{\delta}$

Evolution of model parameters:

$f = f^0 + (f^{sat} - f^0)\left[1 - \exp\left(-\frac{\chi_c}{\tau}\right)\right]$, $f \in \{\kappa, m, \xi_a, \xi_b, r, Y_\chi, \Delta\eta_t, \mathcal{H}\}$

Yield functions:

$\mathcal{F}_\chi = |A_\chi| - Y_\chi$ and $\mathcal{F}_N = \|\boldsymbol{A}_N\| - \chi Y_N$

Kuhn-Tucker consistency conditions:

$\begin{cases} \dot{\gamma}^t \geq 0, & \mathcal{F}_\chi \leq 0, & \dot{\gamma}^t\mathcal{F}_\chi = 0 \\ \dot{\gamma}^N \geq 0, & \mathcal{F}_N \leq 0, & \dot{\gamma}^N\mathcal{F}_N = 0 \end{cases}$

5.3 Model parameters calibration

In this section, the 3D constitutive model presented in Section 5.2 is first reduced to a 1D version. Then, the heat transfer conditions in the real experiment is simplified. Finally, the reduced constitutive and heat equations are implemented into MATLAB to calibrate the model parameters against the experimental data.

5.3.1 1D version of the constitutive equations

For the case of uniaxial loading, the Cauchy stress tensor $\boldsymbol{\sigma}$ and the deformation gradient $\boldsymbol{F}$ are given as

$$\boldsymbol{\sigma} = \sigma\, \boldsymbol{e}_1 \otimes \boldsymbol{e}_1 \quad \text{and} \quad \boldsymbol{F} = \lambda\, \boldsymbol{e}_1 \otimes \boldsymbol{e}_1 + \lambda_l\, \boldsymbol{e}_2 \otimes \boldsymbol{e}_2 + \lambda_l\, \boldsymbol{e}_3 \otimes \boldsymbol{e}_3, \tag{5.60}$$

where σ and λ denote the uniaxial stress and stretch, λ_l denotes the lateral contractions. $\boldsymbol{e}_1, \boldsymbol{e}_2, \boldsymbol{e}_3$ are the three orthonormal bases. Since the spherical stress-strain response (5.43) itself is a scalar equation, the reduced 1D equations will not capture it and therefore volume-preserving deformation, *i.e.* $J = \det \boldsymbol{F} = 1$, is assumed. This assumption gives the relation: $\lambda_l = \sqrt{\frac{1}{\lambda}}$. Moreover, the polar decomposition can be written as $\boldsymbol{F} = \boldsymbol{V}\boldsymbol{R} = \boldsymbol{V}$ since $\boldsymbol{R} = \boldsymbol{I}$. The velocity gradient $\boldsymbol{L}$ is then computed as

$$\boldsymbol{L} = \dot{\boldsymbol{F}}\boldsymbol{F}^{-1} = \frac{\dot{\lambda}}{\lambda}\boldsymbol{T} \quad \text{and} \quad \boldsymbol{T} = 1\, \boldsymbol{e}_1 \otimes \boldsymbol{e}_1 - \frac{1}{2}\, \boldsymbol{e}_2 \otimes \boldsymbol{e}_2 - \frac{1}{2}\, \boldsymbol{e}_3 \otimes \boldsymbol{e}_3, \tag{5.61}$$

with the stretching tensor $\boldsymbol{D} = \mathrm{sym}(\boldsymbol{L}) = \boldsymbol{L}$ and spin tensor $\boldsymbol{W} = \mathrm{skew}(\boldsymbol{L}) = \boldsymbol{0}$.

The elastic $\boldsymbol{F}_e$, transformation $\boldsymbol{F}_t$ and residual $\boldsymbol{F}_r$ deformation gradients are defined by

$$\boldsymbol{F}_e = \lambda_e\, \boldsymbol{e}_1 \otimes \boldsymbol{e}_1 + \sqrt{\frac{1}{\lambda_e}}\, \boldsymbol{e}_2 \otimes \boldsymbol{e}_2 + \sqrt{\frac{1}{\lambda_e}}\, \boldsymbol{e}_3 \otimes \boldsymbol{e}_3, \tag{5.62}$$

$$\boldsymbol{F}_t = \lambda_t\, \boldsymbol{e}_1 \otimes \boldsymbol{e}_1 + \sqrt{\frac{1}{\lambda_t}}\, \boldsymbol{e}_2 \otimes \boldsymbol{e}_2 + \sqrt{\frac{1}{\lambda_t}}\, \boldsymbol{e}_3 \otimes \boldsymbol{e}_3, \tag{5.63}$$

$$\boldsymbol{F}_r = \lambda_r\, \boldsymbol{e}_1 \otimes \boldsymbol{e}_1 + \sqrt{\frac{1}{\lambda_r}}\, \boldsymbol{e}_2 \otimes \boldsymbol{e}_2 + \sqrt{\frac{1}{\lambda_r}}\, \boldsymbol{e}_3 \otimes \boldsymbol{e}_3, \tag{5.64}$$

with

$$\lambda = \lambda_e \lambda_t \lambda_r \quad \text{and} \quad J = J_e J_t J_r = 1. \tag{5.65}$$

Thus, the elastic $\boldsymbol{h}_e$, transformation $\boldsymbol{h}_t$ and residual $\boldsymbol{h}_r$ Hencky strains in equation (5.6) are written as

$$\boldsymbol{h}_e = \ln \lambda_e \boldsymbol{T}, \quad \boldsymbol{h}_t = \ln \lambda_t \boldsymbol{T} \quad \text{and} \quad \boldsymbol{h}_r = \ln \lambda_r \boldsymbol{T}. \tag{5.66}$$

The deviatoric stress $\boldsymbol{s}$ in equation (5.43) is then written as

$$\boldsymbol{s} = 2\mu \ln \lambda_e \boldsymbol{T} = \frac{2}{3}\sigma \boldsymbol{T}. \tag{5.67}$$

The Mandel stress $\bar{\boldsymbol{M}}_e$ and the direction of transformation strain $\boldsymbol{N}_t$ in equation (5.44) are written as

$$\bar{\boldsymbol{M}}_e = \frac{2}{3}\sigma \boldsymbol{T} \quad \text{and} \quad \boldsymbol{N}_t = \sqrt{\frac{2}{3}}\boldsymbol{T}, \tag{5.68}$$

which indicates that $\bar{\boldsymbol{M}}_e$ and $\boldsymbol{N}_t$ are coaxial for the case of uniaxial loading. Hence, according to equation (5.56), the thermodynamic force of martensitic reorientation $\boldsymbol{A}_N$ is null, *i.e.* $\boldsymbol{A}_N = 0$. Moreover, the

thermodynamic forces of residual deformation $\boldsymbol{A}_r$ and phase transformation A_χ in equation (5.52), with the assumption of equal heat capacities of austenite and martensite, *i.e.* $\Delta c_v^t = 0$, are written as

$$\boldsymbol{A}_r = \left(\frac{2}{3}\sigma - \mu_t \ln \lambda_r\right)\boldsymbol{T}, \tag{5.69}$$

$$A_\chi = \sqrt{\frac{2}{3}}\mathcal{H}\sigma - \mu_t \mathcal{H}^2 \chi - \mathcal{H}\zeta^t - \Delta\eta_t(\theta - \theta_0) - g^t - \zeta^f + \zeta^r. \tag{5.70}$$

Combining equations (5.51), (5.53) and (5.69) gives the following residual evolution equation:

$$\dot{\boldsymbol{h}}_r = \frac{\dot{\lambda}_r}{\lambda_r} = \frac{R^{sat}}{\tau}\exp\left(-\frac{\chi_c}{\tau}\right)\dot{\chi}_c \boldsymbol{N}_t. \tag{5.71}$$

5.3.2 Simplification of the heat transfer condition

In the present work, the proposed constitutive model is validated against the experimental data reported by Morin et al. (2011b) for polycrystalline NiTi (56.1 at.% Ni) wire. The heat transfer conditions in the source work are shown in Fig. 5.1. According to Yin et al. (2014) and Yu et al. (2015b), the heat flow through the two grips is simplified as heat conduction through the two boundary cross sections of the gauge-length of the wire. A cylindrical coordinate is defined with radius ρ, azimuth φ and altitude z, which is utilized in the following to formulate integral equations of the heat transfer over the NiTi wire.

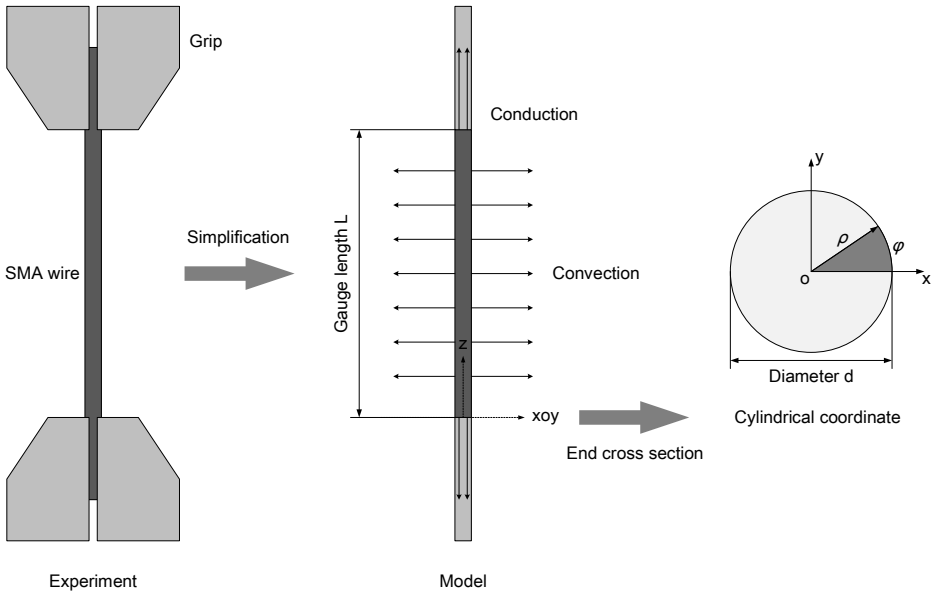

Figure 5.1 Heat transfer conditions in the experiment and simplification in the model.

According to the literature of Morin et al. (2011b), Yin et al. (2014) and Yu et al. (2015b), the initial and boundary conditions of the heat transfer in the experimental NiTi wire are described as:

$$\begin{cases} \boldsymbol{q}\cdot\boldsymbol{n}_c = h\,(\theta-\theta_a) & \text{in } S_c,\\ \boldsymbol{q}\cdot\boldsymbol{n}_l = \frac{\beta k}{L}\,(\theta-\theta_a) & \text{in } S_l,\\ \theta(t=0)=\theta_a & \text{in } \mathcal{B}, \end{cases} \tag{5.72}$$

where $\boldsymbol{n}_c$ and $\boldsymbol{n}_l$ are outward unit vectors, respectively, normal to the cross-section surface S_c and the lateral surface S_l, θ_a is the ambient temperature. The first equation represents the heat convection of the NiTi wire lateral surface to ambient media, and h is the heat convection coefficient. While the second equation represents the heat conduction through the cross-section surface, where k is the thermal conductivity and β is a constant.

Using stokes's theorem, the integral form of the heat transfer $\nabla\cdot\boldsymbol{q}$ in equation (5.31) can be expressed as:

$$\iiint_{\mathcal{B}} \nabla\cdot\boldsymbol{q}\,\mathrm{d}V = \oiint_{\partial\mathcal{B}} \boldsymbol{q}\cdot\boldsymbol{n}_S\,\mathrm{d}S = \oiint_{S_c} \boldsymbol{q}\cdot\boldsymbol{n}_c\,\mathrm{d}\rho\mathrm{d}\varphi + \oiint_{S_l} \boldsymbol{q}\cdot\boldsymbol{n}_l\,\mathrm{d}\varphi\mathrm{d}z, \tag{5.73}$$

where $\boldsymbol{n}_S$ is the outward unit vector normal to the surface of the NiTi wire.

Using the aforementioned 1D constitutive equations, the temperature evolution equation (5.59) is written as

$$\begin{aligned} \iiint_{\mathcal{B}} c_v\dot{\theta}\,\mathrm{d}\rho\mathrm{d}\varphi\mathrm{d}z = \iiint_{\mathcal{B}} h_v\,\mathrm{d}\rho\mathrm{d}\varphi\mathrm{d}z - \oiint_{S_c} \boldsymbol{q}\cdot\boldsymbol{n}_c\,\mathrm{d}\rho\mathrm{d}\varphi - \oiint_{S_l} \boldsymbol{q}\cdot\boldsymbol{n}_l\,\mathrm{d}\varphi\mathrm{d}z\\ + \iiint_{\mathcal{B}} \mathcal{I}_r + |\mathcal{I}_\chi| + \mathcal{L}\,\mathrm{d}\rho\mathrm{d}\varphi\mathrm{d}z, \end{aligned} \tag{5.74}$$

where

$$\begin{cases} \mathcal{I}_r = \frac{R^{sat}}{\tau}\exp\left(-\frac{\chi_c}{\tau}\right)\left(\sqrt{\frac{2}{3}}\sigma - \sqrt{\frac{3}{2}}\mu_t\ln\lambda_r\right)\dot{\chi}_c,\\ \mathcal{I}_\chi = \left[\sqrt{\frac{2}{3}}\mathcal{H}\sigma - \mu_t\mathcal{H}^2\chi - \mathcal{H}\zeta^t - \Delta\eta_t(\theta-\theta_0) - g^t - \zeta^f + \zeta^r\right]\dot{\chi},\\ \mathcal{L} = \theta\left[\Delta\eta_t + \Delta c_v^t\ln\left(\frac{\theta}{\theta_0}\right)\right]\dot{\chi}. \end{cases} \tag{5.75}$$

In equation (5.75), $\mathcal{I}_r$ denotes the intrinsic dissipation due to residual deformation, $\mathcal{I}_\chi$ denotes the intrinsic dissipation due to phase transformation and $\mathcal{L}$ denotes the latent heat during the phase transformation. Using equation (5.72), the second and third terms in the right side of equation (5.75) can be written as

$$\oiint_{S_c} \boldsymbol{q}\cdot\boldsymbol{n}_c\,\mathrm{d}\rho\mathrm{d}\varphi = \oiint_{S_c} h\,(\theta-\theta_a)\,\mathrm{d}\rho\mathrm{d}\varphi = hA_c\left(\theta_m^c-\theta_a\right), \tag{5.76}$$

$$\oiint_{S_l} \boldsymbol{q}\cdot\boldsymbol{n}_l\,\mathrm{d}\varphi\mathrm{d}z = \oiint_{S_l} \frac{\beta k}{L}\,(\theta-\theta_a)\,\mathrm{d}\varphi\mathrm{d}z = \frac{\beta k}{L}A_l\left(\theta_m^l-\theta_a\right), \tag{5.77}$$

where θ_m^c and A_c are mean temperature and area of the cross-section surface, while θ_m^l and A_l are mean temperature and area of the lateral surface, *i.e.*,

$$A_c = \frac{1}{2}\pi d^2 \quad \text{and} \quad \theta_m^c = \frac{1}{A_c}\oiint_{S_c} \theta \, \mathrm{d}\rho\mathrm{d}\varphi, \tag{5.78}$$

$$A_l = \pi d L \quad \text{and} \quad \theta_m^l = \frac{1}{A_l}\oiint_{S_l} \theta \, \mathrm{d}\varphi\mathrm{d}z. \tag{5.79}$$

Then, substituting equations (5.76) and (5.77) into equation (5.74) gives

$$\begin{aligned}\iiint_{\mathcal{B}} c_v\dot{\theta} \, \mathrm{d}\rho\mathrm{d}\varphi\mathrm{d}z = &\iiint_{\mathcal{B}} h_v \, \mathrm{d}\rho\mathrm{d}\varphi\mathrm{d}z - hA_c\left(\theta_m^c - \theta_a\right) - \frac{\beta k}{L}A_l\left(\theta_m^l - \theta_a\right) \\ &+ \iiint_{\mathcal{B}} \mathcal{I}_r + |\mathcal{I}_\chi| + \mathcal{L} \, \mathrm{d}\rho\mathrm{d}\varphi\mathrm{d}z.\end{aligned} \tag{5.80}$$

Considering the NiTi wire used in the experiment is an axisymmetric structure, the temperature field in the azimuthal direction is uniform. Meanwhile, since the diameter of the wire is very small compared to the gauge length, the temperature field in the radial direction is also assumed to be uniform. Moreover, by neglecting the temperature gradient in the altitude direction the temperature field in the NiTi wire can be regarded as uniform. Under this assumption of uniform temperature field, the temperature in the cross-section and lateral surfaces are considered to be the same as the mean temperature in the NiTi wire, *i.e.*,

$$\theta_m^c = \theta_m^l = \theta_m = \frac{4}{\pi d^2 L}\iiint_{\mathcal{B}} \theta(\rho, \varphi, z) \, \mathrm{d}\rho\mathrm{d}\varphi\mathrm{d}z. \tag{5.81}$$

Besides the assumption of uniform temperature field, it should be noted that the NiTi wire subjected to also a uniformly uniaxial stress field. Thus, all the state quantities and internal variables can be regarded as uniform, and therefore equation (5.80) yields

$$c_v\dot{\theta} = h_v - \frac{hd + 2\beta k}{dL}\left(\theta_m - \theta_a\right) + \mathcal{I}_r + |\mathcal{I}_\chi| + \mathcal{L}. \tag{5.82}$$

5.3.3 Model parameters calibration

The 1D constitutive model and the simplified heat transfer condition are implemented into MATLAB to calibrate the model parameters. All the model parameters are classified into four categories: thermoelasticity, phase transformation, cyclic deformation and heat transfer, and listed in Tab. 5.2.

Table 5.2 Model parameters required to be calibrated.

Elasticity: K, μ^A, μ^M, α;
Phase transformation: κ, m, ξ_a, ξ_b, r, Y_χ, $\Delta\eta_t$, $\mathcal{H}$, μ_t, Y_N;
Cyclic deformation: μ_r, R_c, R_0, R_s, τ;
Heat transfer: c_v, Δc_v^t, h, k, β, θ_0, θ_a.

With regard to the model parameters, the following two assumptions are introduced to simplify the calibration: (i) according to the differential scanning calorimetry (DSC) experiments (Qidwai and Lagoudas, 2000), the heat capacities of austenite and martensite are almost equal, *i.e.*, $\Delta c_v^t = 0$; (ii) since the evolution of residual deformation is directly related to the phase transformation (equation (5.53)) and controlled by the loading function $(5.57)_1$, the change of loading surface due to dislocation slipping is therefore neglected, *i.e.*, $\mu_r = 0$. Moreover, it should be noted that the eight parameters $\{\kappa, m, \xi_a, \xi_b, r, Y_\chi, \Delta\eta_t, \mathcal{H}\}$ depend on the cumulated martensite volume fraction χ_c according to equation (5.47). Thus, the parameters in both the first and the stabilized cycles, *i.e.*, $\{\kappa, m, \xi_a, \xi_b, r, Y_\chi, \Delta\eta_t, \mathcal{H}\}^0$ and $\{\kappa, m, \xi_a, \xi_b, r, Y_\chi, \Delta\eta_t, \mathcal{H}\}^{sat}$, are required to be calibrated.

The elastic bulk modulus K and the shear moduli μ^A and μ^M are determined from experimental pseudoelastic stress-strain curve as follows:

$$K = \frac{E^A + E^M}{6(1-2\nu)}, \quad \mu^A = \frac{E^A}{2(1+\nu)} \quad \text{and} \quad \mu^M = \frac{E^M}{2(1+\nu)}, \tag{5.83}$$

where E^A and E^M are Young's moduli for austenite and martensite as shown in Fig 5.2(a). The thermal expansion coefficient α is obtained from the literature of Yu et al. (2015b).

The entropy difference $\Delta\eta_t$ governs the variation of transformation stress with temperature. This influence is demonstrated in Fig 5.2(a) with two stress-strain curves obtained at temperature θ (black) and $\theta + \Delta\theta$ (blue), wherein the temperature increase of $\Delta\theta$ results in transformation stress increase of $\Delta\sigma_T$. The yield threshold for phase transformation Y_χ controls the height of the hysteresis loop σ_h as shown in Fig 5.2(a). These two parameters are calculated as follows:

$$\Delta\eta_t = \mathcal{H}\frac{\Delta\sigma_T}{\Delta\theta} \quad \text{and} \quad Y_\chi = \frac{1}{2}\mathcal{H}\sigma_h. \tag{5.84}$$

The martensitic reorientation threshold Y_N, the reorientation hardening modulus μ_t and the magnitude limit of transformation strain $\mathcal{H}$ are determined from the stress-strain curve of martensitic orientation experiment, wherein self-accommodation martensite is completely oriented under the uniaxial tensile loading. Y_N takes the initial yield stress, μ_t the slope of orientation plateau and $\mathcal{H}$ the magnitude of the residual strain, as shown in Figure 5.2(b). It is noteworthy that the parameters $\Delta\eta_t^0$, Y_χ^0 and $\mathcal{H}^0$ are determined from the experimental curves of the first cycle, while $\Delta\eta_t^{sat}$, Y_χ^{sat} and $\mathcal{H}^{sat}$ from the stabilized cycle.

The parameters κ, m, ξ_a, ξ_b and r in the tangential hardening function g^t control the abrupt to smooth transition during the cyclic deformation, especially at initiation and completion of phase transformation. Figure 4.2 shows how the parameters κ, m, ξ_a, ξ_b and r affect the pseudoelastic stress-strain behavior of SMAs. Likewise, κ^0, m^0, ξ_a^0, ξ_b^0 and r^0 are determined from the experimental curves of the first cycle, while κ^{sat}, m^{sat}, ξ_a^{sat}, ξ_b^{sat} and r^{sat} from the stabilized cycle.

The parameters R_c, R_0 and R_s are determined from the experimental curve of the saturated residual strain R^{sat} versus the logarithmic strain rate $\log \dot{h}_{eq}$ (referring to Kan et al. (2016)) according to equation (5.54). The dimensionless time constant τ in function f (equation (5.47)) controls the evolution rate of

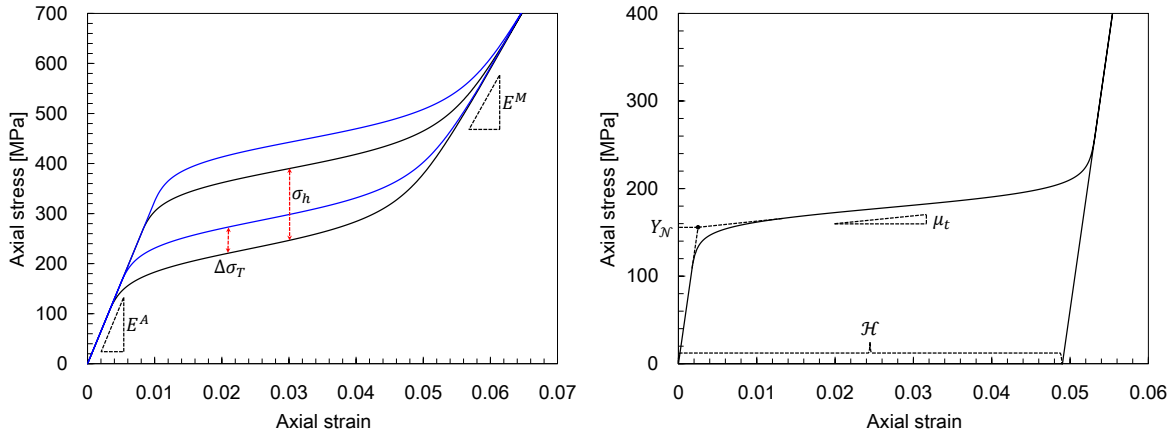

(a) (b)

Figure 5.2 Calibration of the model parameters from the experimental stress-strain curves: (a) identification of K, μ^A, μ^M, $\Delta\eta_t$ and Y_χ from the pseudoelastic stress-strain curve, (b) identification of Y_N, μ_t and $\mathcal{H}$ from the stress-strain curve of martensitic orientation.

the parameters, which can be obtained from the curve of the transformation strain magnitude $\mathcal{H}$ versus the cumulated martensite volume fraction χ_c (referring to Fig. 2.1(b)). Here, data points in the 1st, 5th, 10th, 20th and last cycles are used to calibrate τ.

The heat capacity c_v is obtained from the literature of Morin et al. (2011b). The reference temperature θ_0 takes the equilibrium temperature of the phase transformation, *i.e.*,

$$\theta_0 = \frac{1}{4}\left(A_s + A_f + M_s + M_f\right), \tag{5.85}$$

where A_s and A_f are austenite start and finish temperatures, M_s and M_f are martensite start and finish temperatures. They are determined by DSC tests.

The heat convection coefficient h, the thermal conductivity k and the constant β, together with geometrical parameters of the NiTi wire L and d, constitute a new model parameter ω as

$$\omega = \frac{hd + 2\beta k}{dL}. \tag{5.86}$$

Thus, equation (5.82), without the external heat source h_v, is written as

$$c_v\dot{\theta} = \mathcal{I}_r + |\mathcal{I}_\chi| + \mathcal{L} - \omega\left(\theta_m - \theta_a\right), \tag{5.87}$$

which is then utilized to determine ω from the pseudoelastic stress-strain curves at different strain rates (referring to Fig. 2.2).

5.4 Numerical simulations and model validations

In this section, the experiments performed by (Morin et al., 2011b) are simulated using the reduced constitutive model and the simplified heat transfer condition presented in Section 5.3. Then, the model predictions are validated against the experimental data. In the source work, the transformation temperatures of the NITi wire were measured using DSC, *i.e.*, martensite start temperature $M_s = 23\ ^\circ C$, martensite finish temperature $M_f = 13\ ^\circ C$, austenite start temperature $A_s = 9\ ^\circ C$ and austenite finish temperature $A_f = 24\ ^\circ C$. The experiments were carried out at constant ambient temperature of $50 \pm 1\ ^\circ C$, which is higher than the austenite finish temperature $A_f = 24$. Thus, the initial phase of the NiTi wire is austenite and exhibits pseudoelasticity under applied stress. The NiTi wire is subjected to 50 cycles of quasi-static tensile loading at six different loading rates of $1 \times 10^{-4} s^{-1}$, $2.5 \times 10^{-4} s^{-1}$, $5 \times 10^{-4} s^{-1}$, $1 \times 10^{-3} s^{-1}$, $2.5 \times 10^{-3} s^{-1}$ and $5 \times 10^{-3} s^{-1}$. The maximum applied stress is about 800 MPa, which is higher than the martensite finish stress σ_{mf}, allowing austenite to completely transform to martensite. The model parameters used in the simulation are determined following the calibration procedure described in Section 5.3.3 from the experimental data. They are listed in Tab. 5.3.

Table 5.3 Model parameters used in the simulation of cyclic tests.

Parameter	Value	Unit	Parameter	Value	Unit
K	41557	Mpa	α	22×10^{-6}	K^{-1}
μ^A	26811	Mpa	μ^M	11550	Mpa
κ^0	2	Mpa	κ^{sat}	5	Mpa
m^0	0.1	-	m^{sat}	0.3	-
ξ_a^0	0.899	-	ξ_a^{sat}	0.98	-
ξ_b^0	0.1	-	ξ_b^{sat}	0.001	-
r^0	-0.15	Mpa	r^{sat}	-4.3	Mpa
Y_χ^0	5.8	Mpa	Y_χ^{sat}	2.5	Mpa
$\Delta\eta_t^0$	0.5	MPa/K	$\Delta\eta_t^{sat}$	0.3	MPa/K
$\mathcal{H}^0$	0.044	-	$\mathcal{H}^{sat}$	0.035	-
μ_t	500	Mpa	Y_N	110	Mpa
R_c	0.145	s	R_0	2.345	%
R_s	1.68	%	τ	11	-
c_v	2.86×10^6	$J/m^3/K$	ω	0.55×10^6	$J/m^3/K$
θ_0	290	K	θ_a	323	K

Fig. 5.3 shows the cyclic stress-strain curves at strain rate of $1 \times 10^{-4} s^{-1}$. The two black hysteresis loops denote the simulated stress-strain curves for the first and the stabilized cycles, while the gray curves demonstrate the evolution of stress-strain relation during cycling. As expected, the dissipated energy and the reversible transformation strain degenerate while the residual strain accumulates with the number of cycles. Meanwhile, the martensite start stress σ_{ms} and the austenite finish stress σ_{af} decrease but the transformation hardening modulus increases with the number of cycles. With regard to the initiation and completion of phase transformation on the stress-strain curves, the abrupt transition for the first cycle finally evolves into a smooth manner for the stabilized cycle. Figs. 5.3(b-d) show the

comparisons of the model predictions against the experimental data and numerical results reported by (Morin et al., 2011b) for the 1st, 10th and stabilized cycles, respectively. In the experimental curve for the 1st cycle, instabilities appear at the initiations of phase transformations due to the propagation of the phase transformation front (Li and Sun, 2002). However, both Morin's and the present models do not capture this phenomenon. This localization phenomenon is specialized in some other literature (Favier et al., 2002; Shaw, 2002). The experimental stress-strain curves for the 10th and the stabilized cycles show a smooth manner compared to the 1st cycle one. The proposed model captures this characteristic with a high degree of accuracy thanks to the introduction of the tangential transformation hardening function g^t. This is an important improvement compared to Morin's model, in which the initiation and completion of phase transformation is abrupt and the transformation hardening is linear, as shown in Figs. 5.3(c,d).

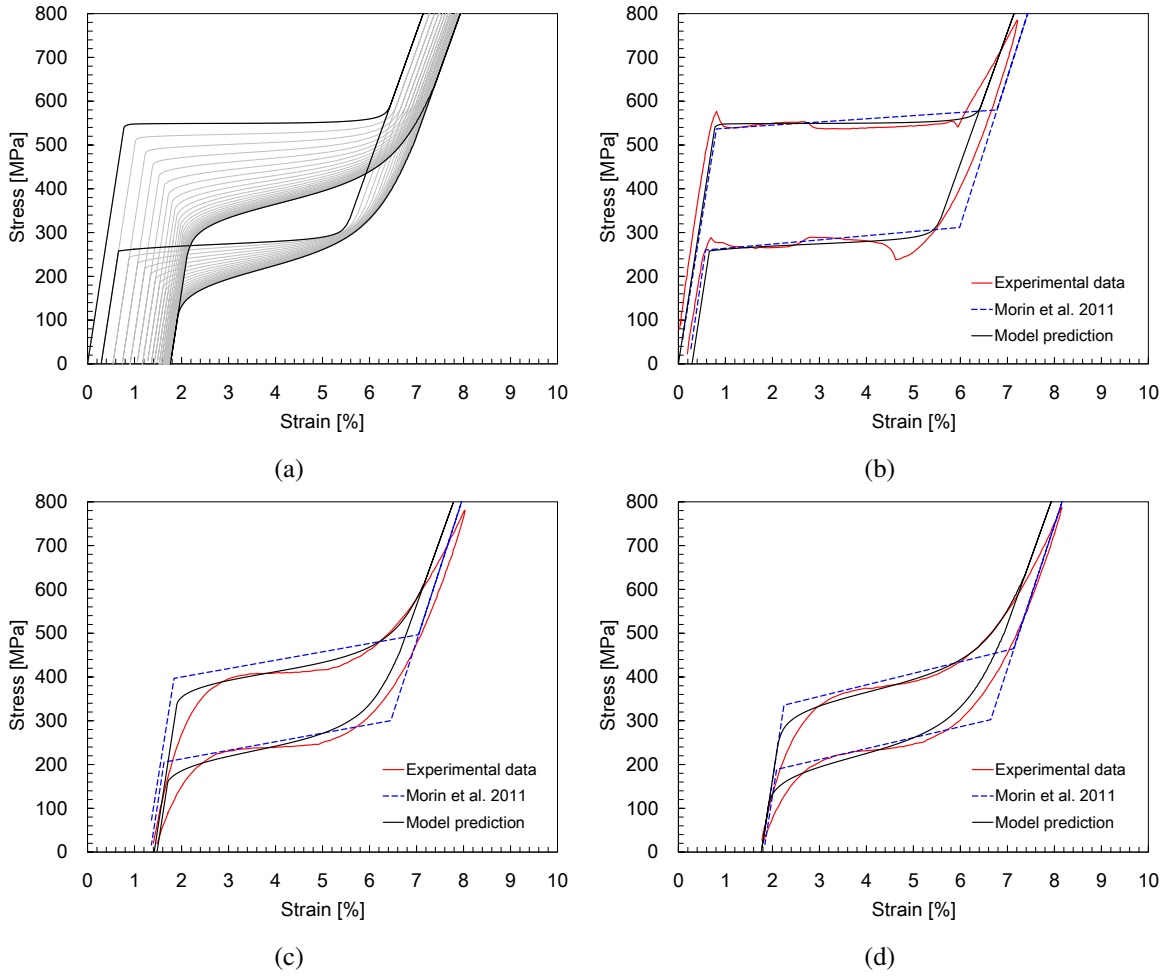

Figure 5.3 Cyclic stress-strain behavior of NiTi SMA at strain rate of $1 \times 10^{-4} s^{-1}$: (a) evolution of stress-strain curves with the number of cycles, (b) comparison for the 1st cycle, (c) comparison for the 10th cycle, (d) comparison for the stabilized cycle.

Figs. 5.4–5.8 present the cyclic stress-strain curves at strain rates of $2.5 \times 10^{-4} s^{-1}$, $5 \times 10^{-4} s^{-1}$, $1 \times 10^{-3} s^{-1}$, $2.5 \times 10^{-3} s^{-1}$ and $5 \times 10^{-3} s^{-1}$, respectively. From these figures, it can be seen that the cyclic deformation of SMA strongly depends on the strain rate. The transformation hardening modulus, the martensite finish stress σ_{mf}, the austenite start stress σ_{as} and the saturated residual strain increase, but the reversible transformation strain decreases with the increasing strain rate. The underlying cause for this rate dependence lies in four aspects: (i) phase transformation takes place with internal heat production due to the intrinsic dissipation and the latent heat; (ii) external heat transfer depends on the testing duration and therefore the loading rate; (iii) competition of the internal heat production against the external heat transfer determines the temperature on NiTi wire; (iv) the transformation stress of SMA is strongly influenced by temperature. The proposed model accounts for fully thermomechanical coupling and therefore describes the rate dependence reasonably well.

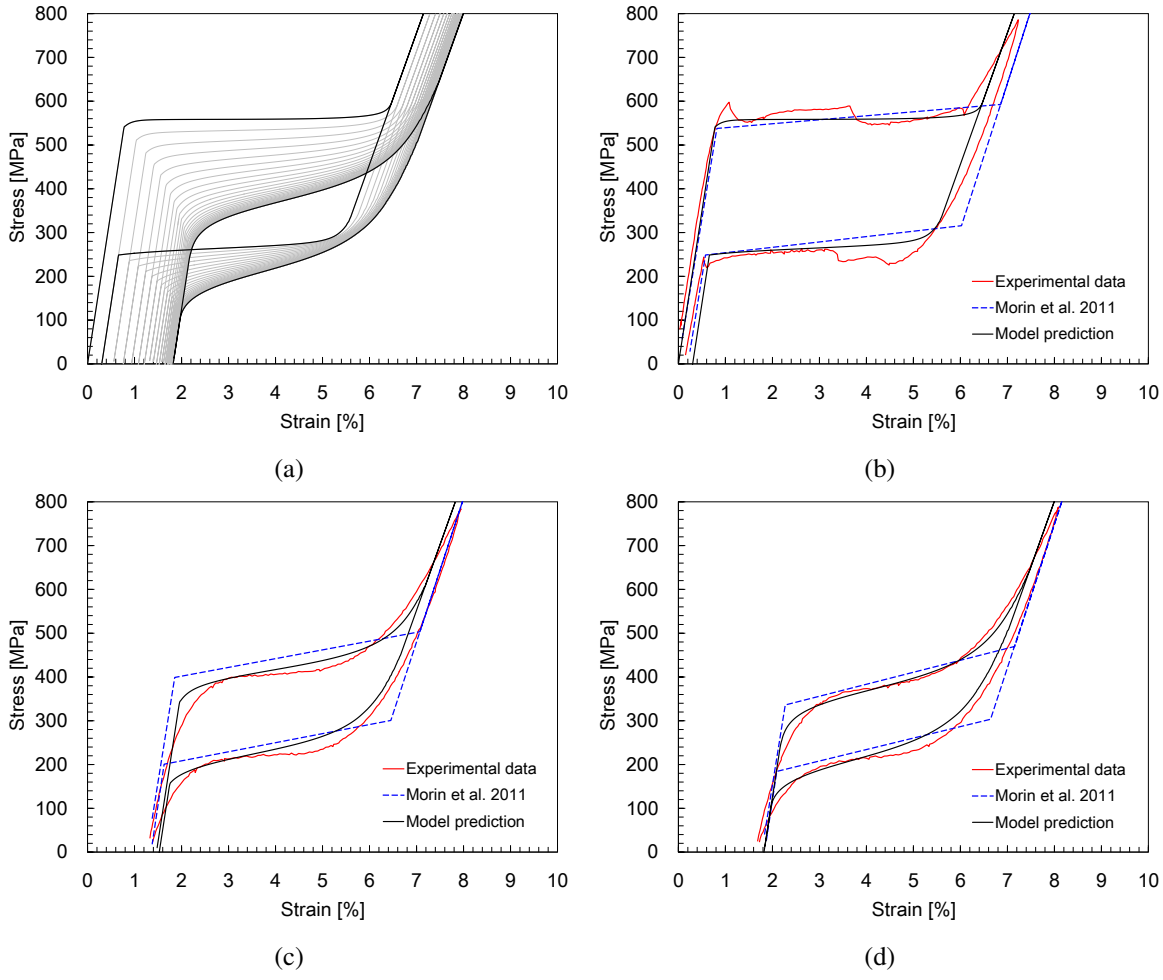

Figure 5.4 Cyclic stress-strain behavior of NiTi SMA at strain rate of $2.5 \times 10^{-4} s^{-1}$: (a) evolution of stress-strain curves with the number of cycles, (b) comparison for the 1st cycle, (c) comparison for the 10th cycle, (d) comparison for the stabilized cycle.

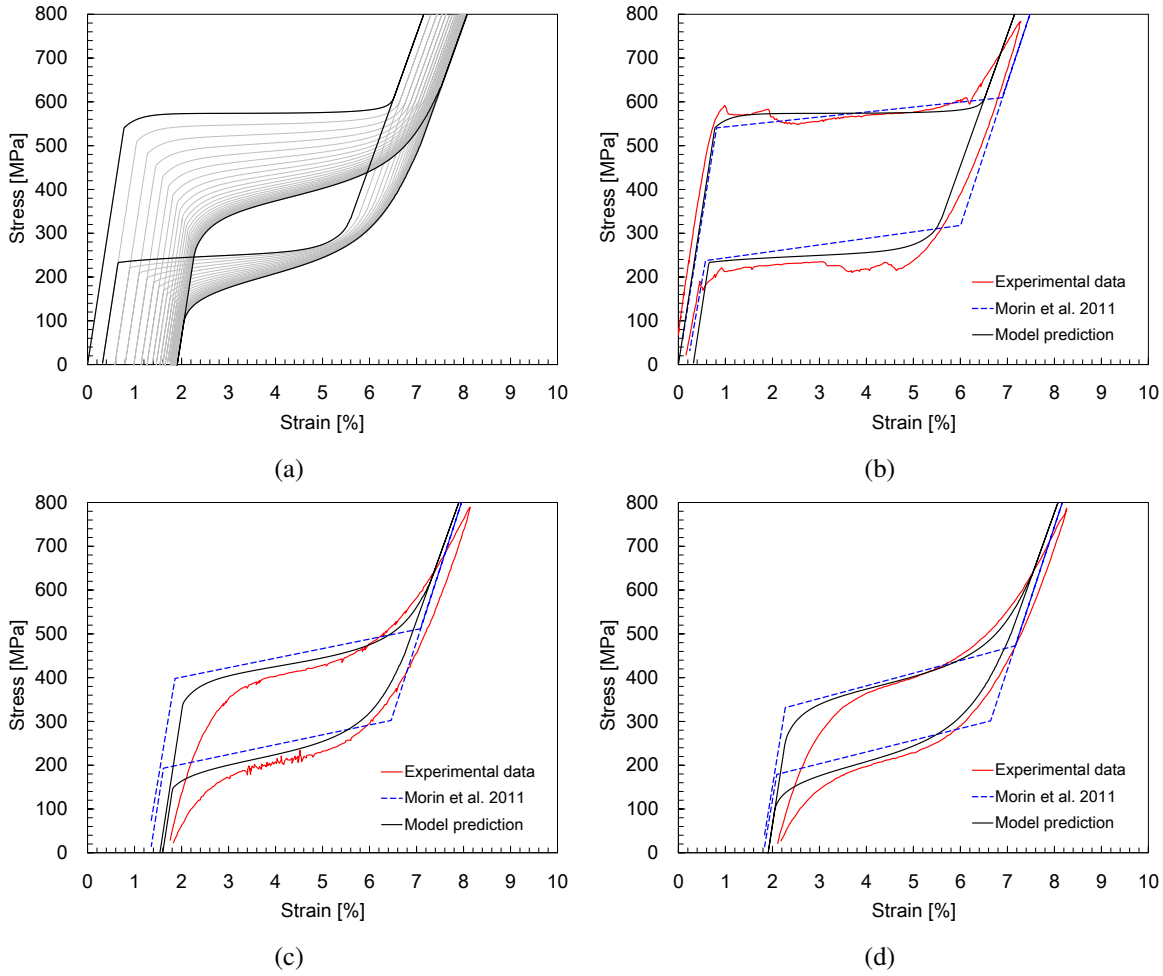

Figure 5.5 Cyclic stress-strain behavior of NiTi SMA at strain rate of $5 \times 10^{-4} s^{-1}$: (a) evolution of stress-strain curves with the number of cycles, (b) comparison for the 1st cycle, (c) comparison for the 10th cycle, (d) comparison for the stabilized cycle.

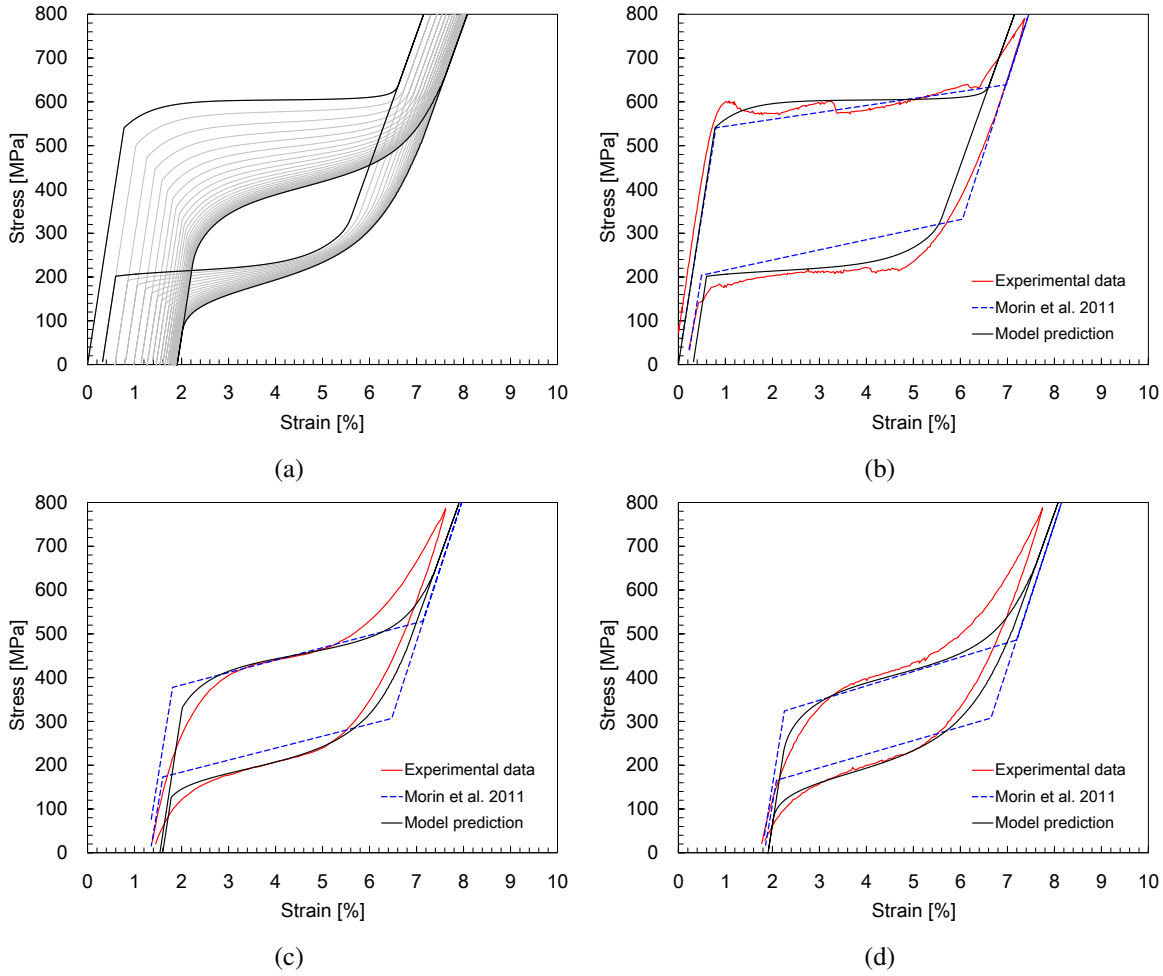

Figure 5.6 Cyclic stress-strain behavior of NiTi SMA at strain rate of $1 \times 10^{-3} s^{-1}$: (a) evolution of stress-strain curves with the number of cycles, (b) comparison for the 1st cycle, (c) comparison for the 10th cycle, (d) comparison for the stabilized cycle.

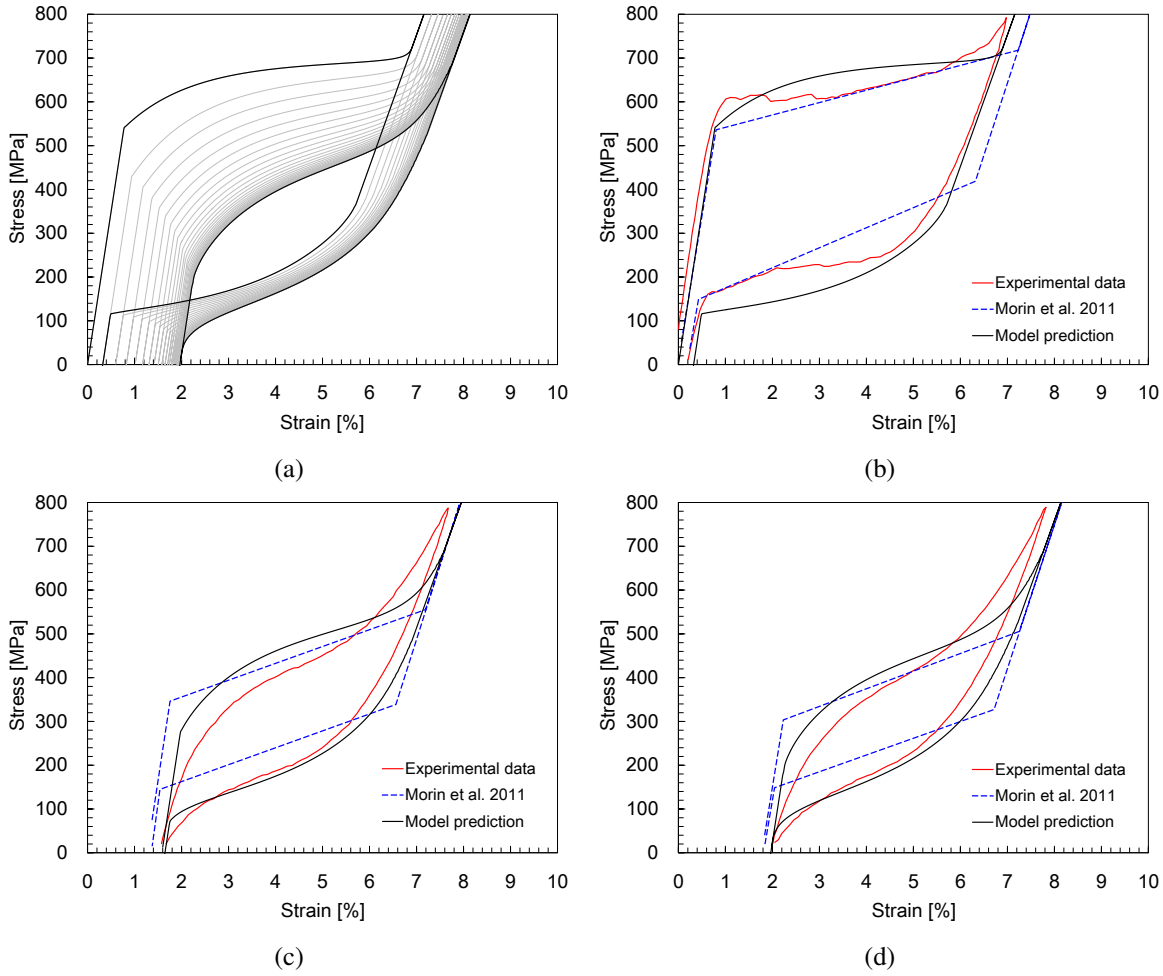

Figure 5.7 Cyclic stress-strain behavior of NiTi SMA at strain rate of $2.5 \times 10^{-3} s^{-1}$: (a) evolution of stress-strain curves with the number of cycles, (b) comparison for the 1st cycle, (c) comparison for the 10th cycle, (d) comparison for the stabilized cycle.

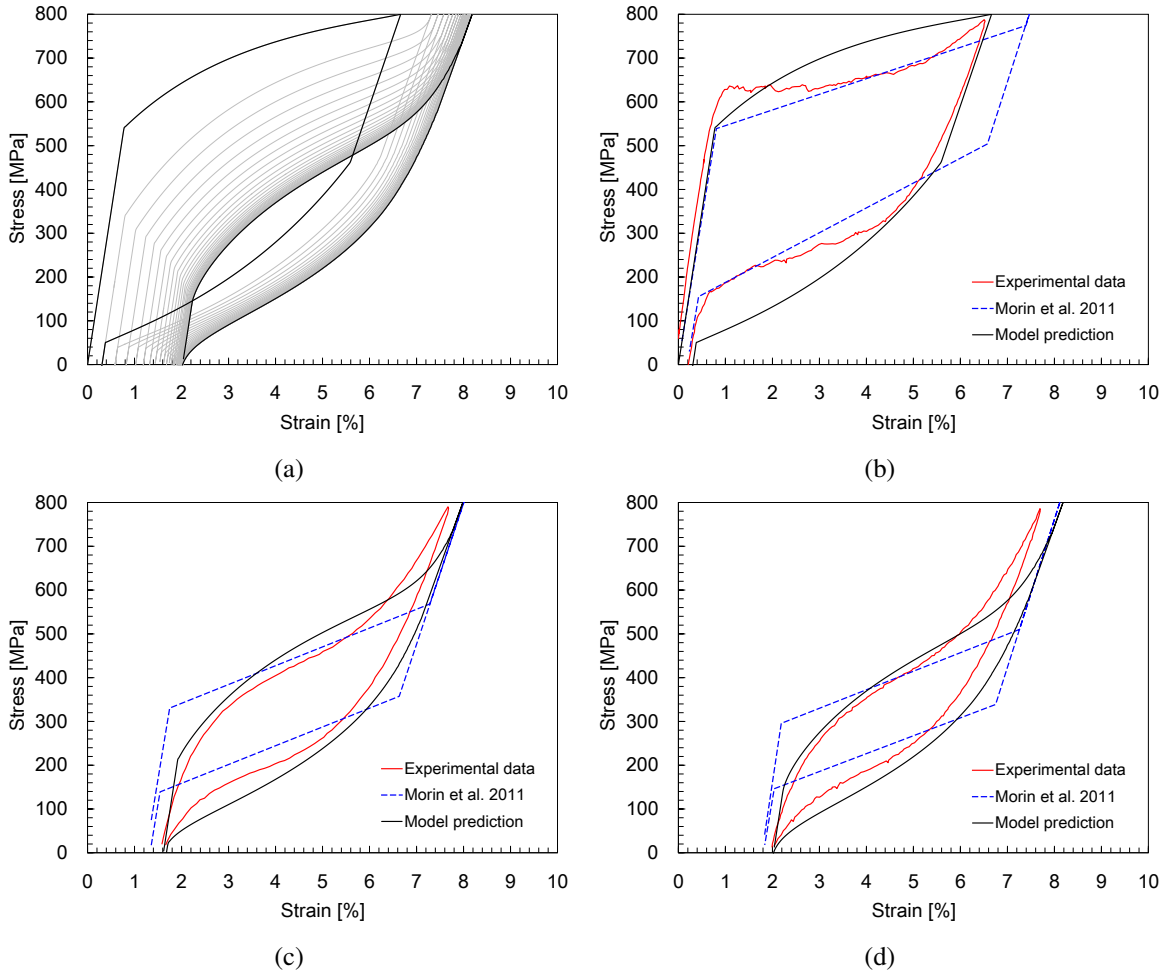

Figure 5.8 Cyclic stress-strain behavior of NiTi SMA at strain rate of $5 \times 10^{-3} s^{-1}$: (a) evolution of stress-strain curves with the number of cycles, (b) comparison for the 1st cycle, (c) comparison for the 10th cycle, (d) comparison for the stabilized cycle.

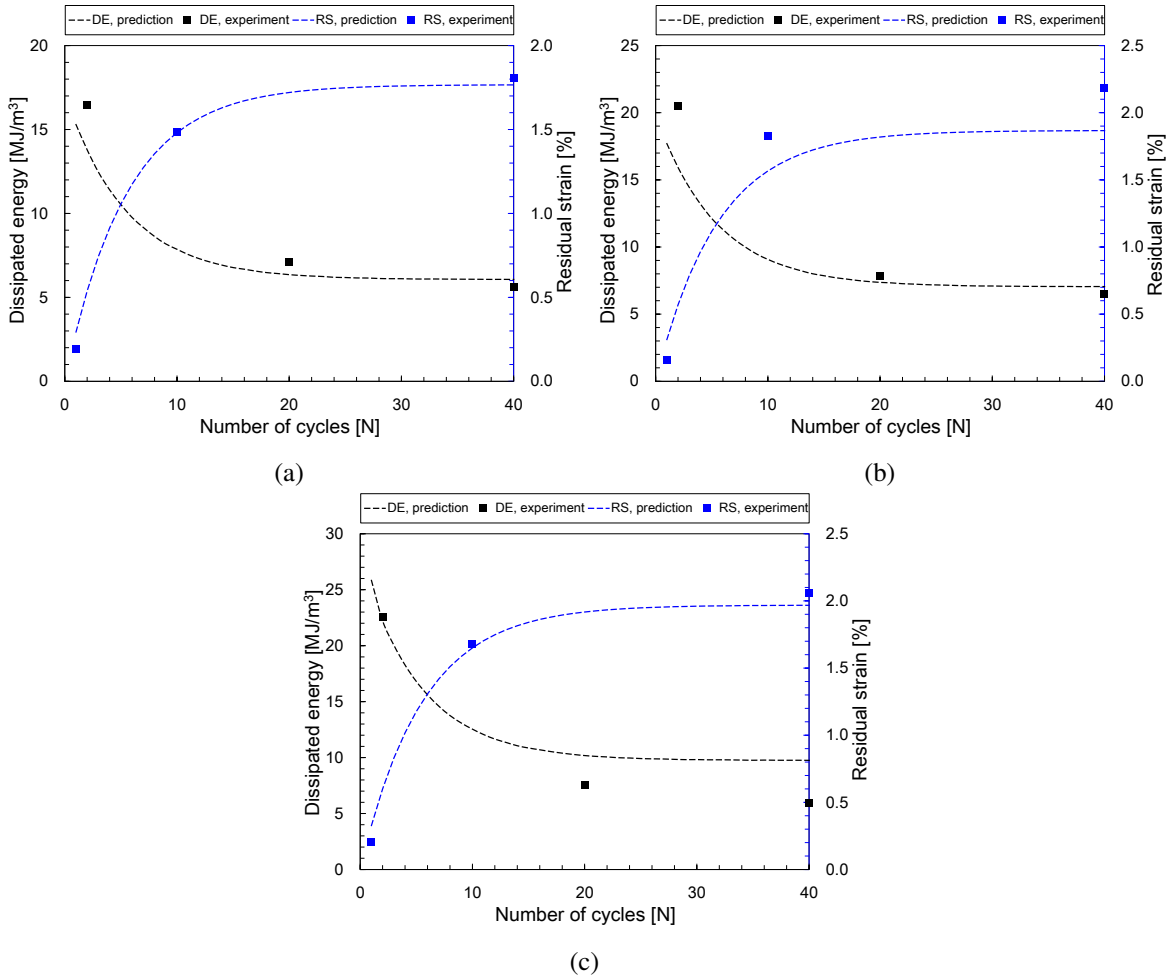

Figure 5.9 Evolutions of the dissipated energy and the residual strain with the number of cycles: (a) strain rate of $1 \times 10^{-4} s^{-1}$, (b) strain rate of $5 \times 10^{-3} s^{-1}$, (c) strain rate of $2.5 \times 10^{-3} s^{-1}$.

Fig. 5.9 shows the evolutions of the dissipated energy (DE) and the residual strain (RS) with the number of cycles at strain rates of $1 \times 10^{-4} s^{-1}$, $5 \times 10^{-4} s^{-1}$ and $2.5 \times 10^{-3} s^{-1}$. Model predictions are validated against the experimental data reported by (Morin et al., 2011b). In the source work, the experimental values for the 2nd, 20th and 40th cycles of DE and the 1st, 10th and 40th of RS are presented. In Fig. 5.9(a), it can be quantitatively observed the decrease of DE from 16.4 MJ/m^3 for the 2nd cycle to the stabilized value of 5.6 MJ/m^3 for the 40th cycle, while the increase of RS from 0.19% for the 1st cycle to a saturated value of 1.8% for the 40th cycle. The proposed model predicts the evolutions of these two variables in good agreement. In Fig. 5.9(b,c), with the increasing strain rate the stabilized values of DE and RS increase simultaneously. This rate dependence is also reasonably predicted by the proposed model.

Fig. 5.10 shows the temperature evolutions during cycling at strain rates of $2.5 \times 10^{-4} s^{-1}$, $1 \times 10^{-3} s^{-1}$ and $5 \times 10^{-3} s^{-1}$. The experimental curves during the first 20 cycles are presented for the three different strain rates. For the given cycle, the temperature increases during forward transformation (austenite to

martensite) and decreases during reverse transformation (martensite to austenite). This phenomenon is due to the predominance of latent heat with respect to other heat sources during phase transformation. The temperature amplitude decreases with the number of cycles and stabilizes at a certain value. However, with the increasing strain rate it increases dramatically. As a matter of fact, the size of hysteresis loop on stress-strain curve is strongly influenced by the temperature amplitude, as shown in Figs. 5.4, 5.6 and 5.8. At high strain rate, the hysteresis loop is larger. Overall, the temperature evolutions during cycling are reasonably predicted by the proposed model.

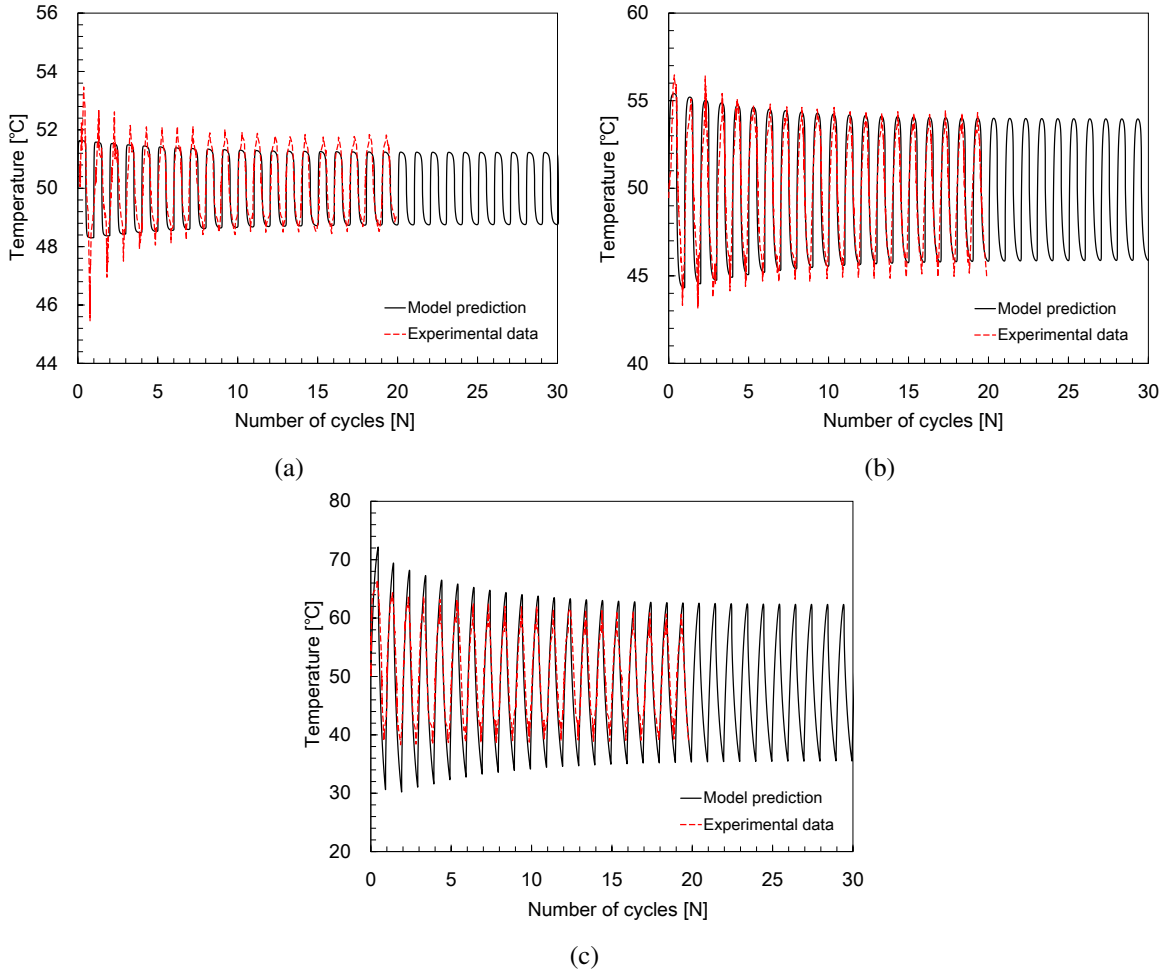

Figure 5.10 Comparisons of the model predictions against the experimental data for the temperature evolution during cycling: (a) strain rate of $2.5 \times 10^{-4} s^{-1}$, (b) strain rate of $1 \times 10^{-3} s^{-1}$, (c) strain rate of $5 \times 10^{-3} s^{-1}$.

5.5 Finite elements simulation of a SMA torsion spring

The proposed model is implemented into finite elements analysis software Abaqus/Explicit by means of a user-defined material subroutine VUMAT. To demonstrate the capabilities of the proposed model in

analyzing complex multi-axial boundary value problems, a SMA torsion spring undergoing large cyclic deformations is simulated in this section. The SMA torsion spring used in the simulation is shown in Fig. 5.11, with 1 mm $\times$ 1 mm rectangle cross-section. Because of symmetry with respect to the horizontal axis, only half of the structure is considered in the simulation. The spring is meshed using 1740 coupled temperature-displacement reduced integration hexahedral elements (Abaqus/Explicit C3D8RT). In the simulation, the pressure is repeatedly increased from zero to the maximum value 5.5×10^5 Pa then removed for 20 cycles during the time period of 20 s.

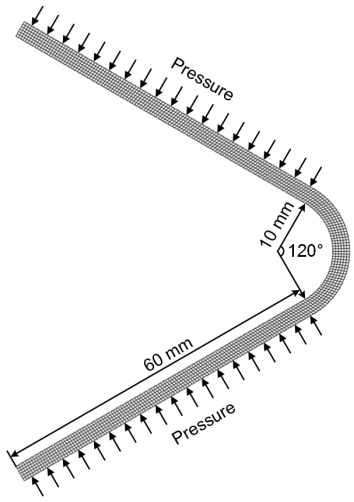

Figure 5.11 Finite elements model of the SMA torsion spring: geometry, mesh and loadings.

Fig. 5.12 shows the martensite volume fraction contour plots at the maximum loading for cycles of 1st, 5th, 10th and 20th. In order to highlight the evolution of phase transformation zone, the simulation result around the corner is magnified. From the figures, it is noted, with the number of cycles, the maximum value of the martensite volume fraction increases and the transformation zone dramatically expands. These results can be explained by the fact that during the cyclic deformations transformation stress gradually decreases with the number of cycles, as shown in Figs. 5.3-5.8. Thereby, austenite transforms to martensite more easily under the same applied loadings.

Fig. 5.13 shows the residual deformation on the torsion spring. Specifically, Fig. 5.13(a) shows the deformation of the inside edge on the torsion spring in absence of loading for cycles of 1st, 5th, 10th and 20th. It is clearly observed the residual deformation increases with the number of cycles. Thereby, the torsion spring deviates increasingly from its initial configuration (reference in the figure). Furthermore, Fig. 5.13(b) shows the residual strain contour plot on the deformed torsion spring after undergoing 20 loading-unloading cycles. The residual strain mainly distributes at the round corner on the torsion spring, and the maximum value is approximate 1.5%. The global residual deformation on the torsion spring is also well shown by comparing the current torsion spring with its initial mesh.

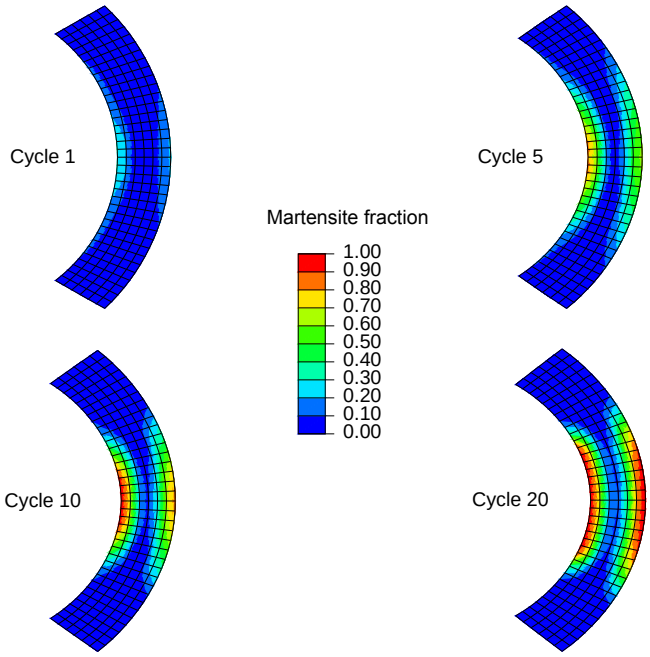

Figure 5.12 Evolution of the martensite volume fraction contour plot at the maximum loading with the number of cycles.

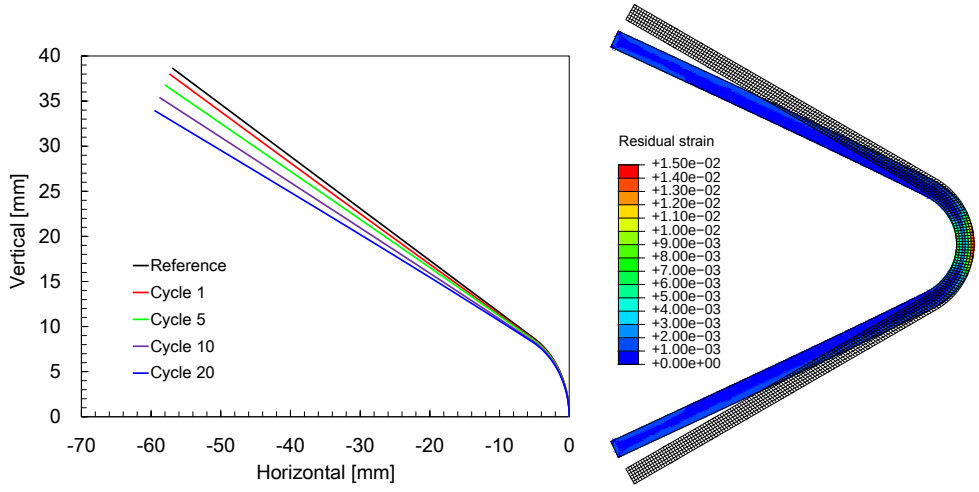

(a) (b)

Figure 5.13 Residual deformation on the torsion spring: (a) deformation of the inside edge in absence of loading for different cycles, (b)initial mesh and residual strain contour plot for the 20th cycle.

5.6 Conclusion

In this chapter, a 3D thermomechanically coupled, finite-strain constitutive model is developed for cyclic pseudoelasticity of polycrystalline SMAs. The proposed model captures several fundamental characteristics deduced from the experimental observations, such as accumulated residual strain, degeneration of

pseudoelasticity and dissipated energy, rate dependence, and evolution of the phase transformation from abrupt to smooth transition. The formulation of the model is based on the decomposition of the finite Hencky strain into elastic, transformation, residual and thermal components. A thermodynamically consistent framework and a Helmholtz free energy function including elastic, thermal, interaction, and constraint energies are constructed to derive the constitutive equations, *i.e.*, thermoelasticity, evolution of martensite volume fraction, flow rule of residual strain, martensite reorientation, heat production, and temperature evolution. Then, the 3D model is reduced to a 1D version, also the heat transfer condition of the cyclic tensile experiment on NiTi wire is simplified under the assumption of uniform temperature field. Model parameters are calibrated from the experimental data. Numerical simulations of the cyclic experiments at different strain rates are carried out to validate the model. The good agreement between the model predictions and the experimental data well demonstrates the model capabilities to capture the fundamental characteristics related to the cyclic pseudoelasticity of polycrystalline SMAs. Finally, an application example involving a SMA torsion spring undergoing large cyclic deformations is presented.

The future direction of this step is to predict fatigue life of SMA structures. Indeed, according to Moumni et al. (2005), the number of cycles to failure depends on the hysteresis area at the stabilized cycle. Thus, if a proper fatigue criterion is introduced, the model will be useful to predict fatigue life of SMA structures subjected to finite cyclic deformations.

Chapter 6

Conclusion and future work

6.1 Conclusion

Shape Memory Alloys exhibit many interesting properties when undergoing large deformations, thermomechanical or cyclic loading conditions. With the increasing industrial applications of these SMAs properties, a comprehensive and in-depth understanding of constitutive behavior became indispensable. To this end, this work developed a comprehensive constitutive modeling approach to investigate thermomechanical and cyclic behavior of SMAs in finite deformation. Moreover, the proposed models are implemented into finite element software as computational tools for the analysis, design and optimization of SMA structures. The whole work is accomplished by the following three steps.

The first step, detailed in Chapter 3, is the finite-strain extension of the ZM model proposed by Zaki and Moumni (2007b). This step aims at the constitutive modeling and numerical implementation of SMAs undergoing large strains and rotations. The finite-strain formulation is based on a two tier decomposition of the deformation gradient into elastic and transformation parts, where the transformation deformation is further decomposed into phase transformation and martensite reorientation components. Constitutive equations are derived within a finite-strain thermomechanical framework. Numerical implementation of the model features the symmetrization of evolution equation to improve efficiency and robustness, and the material and spatial tangent operators involving the objective stress rates. The numerical algorithm is programmed into Abaqus/Standard by means of UMAT subroutine. Simulation results using the proposed finite-strain model demonstrate superiorities of the model dealing with SMA problems with large strains and rotations.

The second step, detailed in Chapter 4, takes into account thermomechanical coupling effect in addition to finite deformation. The Hencky strain is used, due to its remarkable properties in large deformations, to provide a more straightforward finite-strain formulation. The model incorporates three important characteristics of SMA response. First, the effect of phase coexistence between austenite and two martensite variants is accounted for by introducing two distinct internal variable, representing the volume fractions for single-variant χ^S and multi-variant χ^M martensites. Then, the variation of the hysteresis size with temperature is characterized by means of the forward entropy difference $\Delta\eta_f$

and the reverse difference $\Delta\eta_r$. Finally, the smooth material behavior at initiation and completion of phase transformation is accounted for using a unique tangential transformation hardening function g^t. Time-discrete formulation of the constitutive equations were derived and integrated using a Hencky-strain return-mapping algorithm. Whilst the proposed three-dimensional model was reduced to a one-dimensional version to perform the model parameters calibration. The model was then implemented into Abaqus/Explicit using VUMAT subroutine. Numerical simulations are carried out and validated against experimental data for a variety of loading cases, including proportional, non-proportional, isothermal, non-isothermal conditions. Finally, a simulation example is presented in which a SMA helical spring is first subjected to mechanical loading resulting in a pseudoelastic response then to thermal loading resulting in a temperature-induced actuation. The simulation results show the ability of the proposed model to describe the behavior of SMA structures subjected to complex thermomechanical loadings.

The last step, detailed in Chapter 5, deals with cyclic pseudoelasticity of polycrystalline SMAs by generalizing the second-step model. This model captures several fundamental characteristics related to cyclic behavior of SMAs, *i.e.*, large accumulated residual strain, degeneration of superelasticity and hysteresis loop, rate dependence, and evolution of phase transformation from abrupt to smooth transition. The formulation of the model is based on the decomposition of finite Hencky strain into elastic, transformation, residual and thermal components. A thermodynamically consistent framework is established in compliance with the reduced form of energy balance and the Clausius-Duhem form of entropy inequality, while a Helmholtz free energy function including elastic, thermal, interaction and constraint parts is constructed. Constitutive equations, *i.e.*, thermoelasticity, evolution of martensite volume fraction, flow rule of residual strain, martensite reorientation and heat production are then derived from them. The 3D model is reduced to a 1D version and the heat transfer condition of the cyclic tensile experiment on NiTi wire is simplified. Model parameters are calibrated from the experimental data. Finally, numerical simulations of the cyclic experiments at different strain rates are carried out to validate the model. The model is able to capture the rate dependence, the temperature variation, the abrupt to smooth transition, and the evolutions of the dissipated energy, the reversible transformation strain, the residual strain, the transformation stresses and the transformation hardening modulus during cyclic deformations. Finite element simulation of a torsion spring shows the potential of the proposed model for fatigue analysis of SMA structures.

6.2 Future work

Though the present work has developed a relatively comprehensive approach to investigate the thermo-mechanical and cyclic behavior of SMAs in finite deformations, there are several improvements that would be the made for future work. Examples of them are plasticity and fatigue analysis.

- In general, the strain in pseudoelasticity of SMA is within 10%. This strain level is insufficient to demonstrate the advantages of the finite-strain models. Hence, the models might be extended to

account for large irreversible plastic deformations that occur when SMA is subjected to severe mechanical loading. Moreover, plasticity, also as a failure mechanism, compromises the integrity of SMA devices under certain service loading. Material behavior after the plastic yield point could be described by introducing a plastic deformation $\boldsymbol{F}_p$ and its corresponding evolution law and yield criterion.

- The fatigue analysis of SMA structures requires two fundamental aspects: a reliable constitutive model capable of capturing thermomechanical characteristics related to the cyclic behavior of SMAs, as well as a proper fatigue criterion predicting the number of cycles to failure of the structures. Since the present model has shown the capabilities of well describing degeneration and transformation shakedown state in SMAs, if proper fatigue criterion is introduced, the model can be utilized to carry out the fatigue analysis of complex SMA structures.

- The internal loops in partially loaded and unloaded condition is a complex and tricky issue but is central to applications of SMAs since in most cases, due to the considerations of fatigue, the strains are severely restricted. If the relevant internal variables are introduced, the model can be generalized to address this phenomenon.

- Nowadays, the 3D printing technology is widely used to manufacture complex SMA structures. Thus, the model can be used to predict thermomechanical behavior of 3D printed SMAs, and therefore to study its difference from the classical SMAs.

Appendix A

Mathematical supplementation

Corotational rates

The corotational rate of a symmetric Eulerian tensor $\boldsymbol{A}$ is defined by

$$\mathring{\boldsymbol{A}} = \boldsymbol{Q}\left(\overline{\boldsymbol{Q}^T\boldsymbol{A}\boldsymbol{Q}}\right)\boldsymbol{Q}^T = \dot{\boldsymbol{A}} - \boldsymbol{\Omega}\boldsymbol{A} + \boldsymbol{A}\boldsymbol{\Omega}, \tag{A.1}$$

where $\boldsymbol{Q}$ is a time dependent orthogonal tensor denoting the rotation of the frame, $\dot{\boldsymbol{A}}$ is the material time derivative and $\boldsymbol{\Omega} = \dot{\boldsymbol{Q}}\boldsymbol{Q}^T$ is an antisymmetric tensor denoting the frame-spin.

Xiao et al. (1998) showed that the spin tensor $\boldsymbol{\Omega}$ in equation (A.1) can be written in the following general form:

$$\boldsymbol{\Omega} = \boldsymbol{W} + \sum_{i,j=1,i\neq j}^{n} h\left(\frac{\lambda_i}{I}, \frac{\lambda_i}{I}\right)\boldsymbol{P}_i\boldsymbol{D}\boldsymbol{P}_j, \tag{A.2}$$

where λ_i and $\boldsymbol{P}_i$ are the distinct eigenvalues and eigenprojections and $I = \mathrm{tr}\boldsymbol{b}$ the first invariant of the left Cauchy-Green deformation tensor $\boldsymbol{b}$, $I = \mathrm{tr}\boldsymbol{b}$, h is a continuous antisymmetric function denoting the particular corotational objective rate. Moreover, for the Eulerian Hencky strain measure $\boldsymbol{h}$, a logarithmic spin tensor is considered that has the following expression:

$$\boldsymbol{\Omega}^L = \boldsymbol{W} + \sum_{i,j=1,i\neq j}^{n}\left(\frac{\lambda_i + \lambda_j}{\lambda_i - \lambda_j} + \frac{2}{\ln\lambda_i - \ln\lambda_j}\right)\boldsymbol{P}_i\boldsymbol{D}\boldsymbol{P}_j, \tag{A.3}$$

which yields the following relation between the logarithmic corotational rate of Eulerian Hencky strain $\mathring{\boldsymbol{h}}^L$ and the rate of deformation tensor $\boldsymbol{D}$:

$$\mathring{\boldsymbol{h}}^L = \dot{\boldsymbol{h}} - \boldsymbol{\Omega}^L\boldsymbol{h} + \boldsymbol{h}\boldsymbol{\Omega}^L = \boldsymbol{D}. \tag{A.4}$$

Khan and Huang (1995) proposed that the corotational integration for any spatial tensor $\boldsymbol{A}$ can, in general, be written

$$\int_C \boldsymbol{A}\mathrm{d}t = \boldsymbol{Q}\left[\int_m \boldsymbol{Q}^T\boldsymbol{A}\boldsymbol{Q}\mathrm{d}t\right]\boldsymbol{Q}^T, \tag{A.5}$$

where $\int_C$ and $\int_m$ denote, respectively, the corotational integration and the material integration. When the spatial tensor $\boldsymbol{A}$ itself is a corotational rate, *i.e.*, the logarithmic corotational rate $\mathring{\boldsymbol{h}}^L$, substituting equation (A.4) into equation (A.5) gives

$$\boldsymbol{h} = \int_{LC} \mathring{\boldsymbol{h}}^L\mathrm{d}t = \int_{LC} \boldsymbol{D}\mathrm{d}t = \boldsymbol{Q}^L\left[\int_m \left(\boldsymbol{Q}^L\right)^T\boldsymbol{D}\boldsymbol{Q}^L\mathrm{d}t\right]\left(\boldsymbol{Q}^L\right)^T, \tag{A.6}$$

where $\int_{LC}$ denotes the logarithmic corotational integration. The integration scheme (A.6) indicates that the logarithmic corotational integration of the rate of deformation tensor $\boldsymbol{D}$ is the Eulerian Hencky strain $\boldsymbol{h}$.

By using the property of the skew symmetric tensor $\boldsymbol{\Omega} = -\boldsymbol{\Omega}^T$, the inner product of $\mathring{\boldsymbol{A}}$ and an arbitrary second-order symmetric tensor $\boldsymbol{B}$ is written

$$\mathring{\boldsymbol{A}} : \boldsymbol{B} = \dot{\boldsymbol{A}} : \boldsymbol{B} + 2\boldsymbol{\Omega} : \boldsymbol{A}\boldsymbol{B}. \tag{A.7}$$

If $\boldsymbol{A}$ and $\boldsymbol{B}$ are coaxial, $\boldsymbol{A}\boldsymbol{B}$ is also symmetric, indicating that the inner product of the symmetric tensor $\boldsymbol{A}\boldsymbol{B}$ and the skew tensor $\boldsymbol{\Omega}$ becomes null. Therefore, the following identity is obtained:

$$\mathring{\boldsymbol{A}} : \boldsymbol{B} = \dot{\boldsymbol{A}} : \boldsymbol{B}, \tag{A.8}$$

when the symmetric tensors $\boldsymbol{A}$ and $\boldsymbol{B}$ are coaxial for any arbitrary choice of the spin tensor $\boldsymbol{\Omega}$.

Tensor exponential and logarithm

For a generic tensor $\boldsymbol{X}$, the tensor exponential function can be explicitly expressed by means of its series expansion as

$$\exp(\boldsymbol{X}) = \sum_{n=0}^{\infty} \frac{1}{n!}\boldsymbol{X}^n. \tag{A.9}$$

Moreover, the series representation of the tensor logarithm function is written

$$\ln(\boldsymbol{I} + \boldsymbol{X}) = \sum_{n=0}^{\infty} \frac{(-1)^n}{n+1}\boldsymbol{X}^{n+1}. \tag{A.10}$$

The tensor exponential function possesses the following important properties:

1. The determinant of the tensor exponential satisfies

$$\det[\exp(\boldsymbol{X})] = \exp[\mathrm{tr}(\boldsymbol{X})]. \tag{A.11}$$

2. The inverse of the tensor exponential satisfies

$$[\exp(\boldsymbol{X})]^{-1} = \exp(-\boldsymbol{X}). \tag{A.12}$$

3. For any invertible tensor $\boldsymbol{B}$, the tensor exponential satisfies

$$\exp\left(\boldsymbol{B}\boldsymbol{X}\boldsymbol{B}^{-1}\right) = \boldsymbol{B}\exp\left(\boldsymbol{X}\right)\boldsymbol{B}^{-1}. \tag{A.13}$$

Bibliography

Abeyaratne, R. and Kim, S.-J. (1997). Cyclic effects in shape-memory alloys: a one-dimensional continuum model. *International Journal of Solids and Structures*, 34(25):3273–3289.

Alder, B. J. and Wainwright, T. E. (1959). Studies in molecular dynamics. I. General method. *The Journal of Chemical Physics*, 31(2):459–466.

Ali, M. S. M. and Takahata, K. (2010). Frequency-controlled wireless shape-memory-alloy microactuators integrated using an electroplating bonding process. *Sensors and Actuators A: Physical*, 163(1):363–372.

Ames, N. M., Srivastava, V., Chester, S. A., and Anand, L. (2009). A thermo-mechanically coupled theory for large deformations of amorphous polymers. Part II: Applications. *International Journal of Plasticity*, 25(8):1495–1539.

Anand, L., Ames, N. M., Srivastava, V., and Chester, S. A. (2009). A thermo-mechanically coupled theory for large deformations of amorphous polymers. Part I: Formulation. *International Journal of Plasticity*, 25(8):1474–1494.

Anand, L. and Gurtin, M. E. (2003). Thermal effects in the superelasticity of crystalline shape-memory materials. *Journal of the Mechanics and Physics of Solids*, 51:1015–1058.

Andani, M. T. and Elahinia, M. (2014). A rate dependent tension-torsion constitutive model for superelastic nitinol under non-proportional loading; a departure from von Mises equivalency. *Smart Materials and Structures*, 23(1):15012.

Andreasen, G. F. and Hilleman, T. B. (1971). An evaluation of 55 cobalt substituted Nitinol wire for use in orthodontics. *The Journal of the American Dental Association*, 82(6):1373–1375.

Arghavani, J. (2010). *Thermo-mechanical behavior of shape memory alloys under multiaxial loading: constitutive modeling and numerical implementation at small and finite strains*. PhD thesis, Sharif University of Technology.

Arghavani, J., Auricchio, F., and Naghdabadi, R. (2011). A finite strain kinematic hardening constitutive model based on Hencky strain: General framework, solution algorithm and application to shape memory alloys. *International Journal of Plasticity*, 27(6):940–961.

Arghavani, J., Auricchio, F., Naghdabadi, R., Reali, A., and Sohrabpour, S. (2010). A 3-D phenomenological constitutive model for shape memory alloys under multiaxial loadings. *International Journal of Plasticity*, 26(7):976–991.

Auricchio, F. (2001). A robust integration-algorithm for a finite-strain shape-memory-alloy superelastic model. *International Journal of Plasticity*, 17(7):971–990.

Auricchio, F., Bonetti, E., Scalet, G., and Ubertini, F. (2014). Theoretical and numerical modeling of shape memory alloys accounting for multiple phase transformations and martensite reorientation. *International Journal of Plasticity*, 59:30–54.

Auricchio, F. and Petrini, L. (2002). Improvements and algorithmical considerations on a recent three-dimensional model describing stress-induced solid phase transformations. *International Journal for numerical methods in engineering*, 55(11):1255–1284.

Auricchio, F., Reali, A., and Stefanelli, U. (2007). A three-dimensional model describing stress-induced solid phase transformation with permanent inelasticity. *International Journal of Plasticity*, 23(2):207–226.

Auricchio, F., Reali, A., and Tardugno, A. (2010). Shape-memory alloys: effective 3D modelling, computational aspects and design of devices. *International Journal of Computational Materials Science and Surface Engineering*, 3(2-3):199–223.

Auricchio, F. and Taylor, R. L. (1997). Shape-memory alloys: modelling and numerical simulations of the finite-strain superelastic behavior. *Computer methods in applied mechanics and engineering*, 143(1-2):175–194.

Ball, J. M. and James, R. D. (1987). Fine phase mixtures as minimizers of energy. *Archive for Rational Mechanics and Analysis*, 100(1):13–52.

Barnes, B., Brei, D., Luntz, J., Browne, A., and Strom, K. (2006). Panel deployment using ultrafast SMA latches. In *ASME 2006 International Mechanical Engineering Congress and Exposition*, pages 273–280. American Society of Mechanical Engineers.

Baxevanis, T., Parrinello, A., and Lagoudas, D. (2015). On the driving force for crack growth during thermal actuation of shape memory alloys. *Journal of the Mechanics and Physics of Solids*, 89:255–271.

Bažant, Z. P., Caner, F. C., Carol, I., Adley, M. D., and Akers, S. A. (2000). Microplane model M4 for concrete. I: Formulation with work-conjugate deviatoric stress. *Journal of Engineering Mechanics*, 126(9):944–953.

Bechle, N. J. and Kyriakides, S. (2016). Evolution of localization in pseudoelastic NiTi tubes under biaxial stress states. *International Journal of Plasticity*, 82:1–31.

Bekker, A. and Brinson, L. C. (1998). Phase diagram based description of the hysteresis behavior of shape memory alloys. *Acta materialia*, 46(10):3649–3665.

Bellini, A., Colli, M., and Dragoni, E. (2009). Mechatronic design of a shape memory alloy actuator for automotive tumble flaps: a case study. *IEEE Transactions on Industrial Electronics*, 56(7):2644–2656.

Berry, M. and Garcia, E. (2008). Bio-inspired shape memory alloy actuated hexapod robot. In *The 15th International Symposium on: Smart Structures and Materials & Nondestructive Evaluation and Health Monitoring*, pages 69281M–69281M. International Society for Optics and Photonics.

Bhattacharyya, A., Lagoudas, D. C., Wang, Y., and Kinra, V. K. (1995). On the role of thermoelectric heat transfer in the design of SMA actuators: theoretical modeling and experiment. *Smart Materials and Structures*, 4(4):252.

Birman, V. (1997). Review of mechanics of shape memory alloy structures. *Applied Mechanics Reviews*, 50:629–646.

Blanc, P. and Lexcellent, C. (2004). Micromechanical modelling of a CuAlNi shape memory alloy behaviour. *Materials Science and Engineering: A*, 378(1-2):465–469.

Bo, Z. and Lagoudas, D. C. (1999). Thermomechanical modeling of polycristaline SMAs under cyclic loading, Part I: theroretical derivations. *International Journal of Engineering Science*, 37(March 1997):1089–1140.

Bouvard, J. L., Francis, D. K., Tschopp, M. A., Marin, E. B., Bammann, D. J., and Horstemeyer, M. F. (2013). An internal state variable material model for predicting the time, thermomechanical, and stress state dependence of amorphous glassy polymers under large deformation. *International Journal of Plasticity*, 42:168–193.

Bouvet, C., Calloch, S., and Lexcellent, C. (2004). A phenomenological model for pseudoelasticity of shape memory alloys under multiaxial proportional and nonproportional loadings. *European Journal of Mechanics-A/Solids*, 23(1):37–61.

Bowles, J. S. and Mackenzie, J. K. (1954). The crystallography of martensite transformations I. *Acta metallurgica*, 2(1):129–137.

Boyd, J. and Lagoudas, D. (1996). A thermodynamical constitutive model for shape memory materials. Part I. The monolithic shape memory alloy. *International Journal of Plasticity*, 12(6):805–842.

Brassart, L., Inglis, H., Delannay, L., Doghri, I., and Geubelle, P. (2009). An extended Mori–Tanaka homogenization scheme for finite strain modeling of debonding in particle-reinforced elastomers. *Computational Materials Science*, 45(3):611–616.

Brugger, D., Kohl, M., Hollenbach, U., Kapp, A., and Stiller, C. (2006). Ferromagnetic shape memory microscanner system for automotive applications. *International Journal of Applied Electromagnetics and Mechanics*, 23(1, 2):107–112.

Bundhoo, V., Haslam, E., Birch, B., and Park, E. J. (2009). A shape memory alloy-based tendon-driven actuation system for biomimetic artificial fingers, part I: design and evaluation. *Robotica*, 27(01):131–146.

Caldwell, N., Gutmark, E., and Ruggeri, R. (2007). Heat transfer model for blade twist actuator system. *Journal of thermophysics and heat transfer*, 21(2):352–360.

Calkins, F. T. and Mabe, J. H. (2010). Shape memory alloy based morphing aerostructures. *Journal of Mechanical Design*, 132(11):111012.

Carlo, M. and Metin, S. (2006). A biomimetic climbing robot based on the gecko. *Journal of Bionic Engineering*, 3(3):115–125.

Carpenter, B. and Lyons, J. (2001). EO-1 technology validation report: lightweight flexible solar array experiment. *NASA/GSFC. Last updated: August*, 8.

Chan, K. C., Godman, M. J., Walsh, K., Wilson, N., Redington, A., and Gibbs, J. L. (1999). Transcatheter closure of atrial septal defect and interatrial communications with a new self expanding nitinol double disc device (Amplatzer septal occluder): multicentre UK experience. *Heart*, 82(3):300–306.

Chatziathanasiou, D., Chemisky, Y., Chatzigeorgiou, G., and Meraghni, F. (2016). Modeling of coupled phase transformation and reorientation in shape memory alloys under non-proportional thermomechanical loading. *International Journal of Plasticity*, 82:192–224.

Chemisky, Y., Chatzigeorgiou, G., Kumar, P., and Lagoudas, D. C. (2014). A constitutive model for cyclic actuation of high-temperature shape memory alloys. *Mechanics of Materials*, 68:120–136.

Cheung, G. S. P. and Darvell, B. W. (2007). Fatigue testing of a NiTi rotary instrument. Part 1: strain–life relationship. *International endodontic journal*, 40(8):612–618.

Cho, K.-J., Hawkes, E., Quinn, C., and Wood, R. J. (2008). Design, fabrication and analysis of a body-caudal fin propulsion system for a microrobotic fish. In *Robotics and Automation, 2008. ICRA 2008. IEEE International Conference*, pages 706–711. IEEE.

Christ, D. and Reese, S. (2008). Finite-element modelling of shape memory alloys-A comparison between small-strain and large-strain formulations. *Materials Science and Engineering A*, 481-482(1-2 C):343–346.

Christ, D. and Reese, S. (2009). A finite element model for shape memory alloys considering thermomechanical couplings at large strains. *International Journal of Solids and Structures*, 46(20):3694–3709.

Cisse, C., Zaki, W., and Ben Zineb, T. (2016a). A review of constitutive models and modeling techniques for shape memory alloys. *International Journal of Plasticity*, 76:244–284.

Cisse, C., Zaki, W., and Zineb, T. B. (2016b). A review of modeling techniques for advanced effects in shape memory alloy behavior. *Smart Materials and Structures*, 25(10):103001.

Cleveland, M. A. (2008). Apparatus and method for releaseably joining elements. *U.S. Patent*, 7,367,738.

Colorado, J., Barrientos, A., Rossi, C., and Breuer, K. S. (2012). Biomechanics of smart wings in a bat robot: morphing wings using SMA actuators. *Bioinspiration & Biomimetics*, 7(3):36006.

Cwikiel, W., Willen, R., Stridbeck, H., Lillo-Gil, R., and von Holstein, C. S. (1993). Self-expanding stent in the treatment of benign esophageal strictures: experimental study in pigs and presentation of clinical cases. *Radiology*, 187(3):667–671.

Dafalias, Y. F. (1984). The plastic spin concept and a simple illustration of its role in finite plastic transformations. *Mechanics of Materials*, 3(4):361.

Daw, M. S. and Baskes, M. I. (1984). Embedded-atom method: Derivation and application to impurities, surfaces, and other defects in metals. *Physical Review B*, 29(12):6443.

Deng, J., Ding, X., Lookman, T., Suzuki, T., Saxena, A., Otsuka, K., Sun, J., and Ren, X. (2010). Origin of ultrafast annihilation effect of martensite aging: Atomistic simulations. *Physical Review B*, 82(18):184101.

Dimitrienko, Y. I. (2011). *Nonlinear continuum mechanics and large inelastic deformations*, volume 174. Springer Science & Business Media.

Dotter, C. T., Buschmann, R. W., McKinney, M. K., and Rösch, J. (1983). Transluminal expandable nitinol coil stent grafting: preliminary report. *Radiology*, 147(1):259–260.

Duerig, T. W., Pelton, A. R., and Stöckel, D. (1997). Superelastic nitinol for medical devices. *MEDICAL PLASTIC AND BIOMATERIALS*, 4:30–43.

Engmann, E. and Asch, M. R. (1998). Clinical experience with the antecubital Simon nitinol IVC filter. *Journal of vascular and interventional radiology*, 9(5):774–778.

Evangelista, V., Marfia, S., and Sacco, E. (2010). A 3D SMA constitutive model in the framework of finite strain. *International Journal for Numerical Methods in Engineering*, 81(6):761–785.

Falk, F. (1980). Model free energy, mechanics, and thermodynamics of shape memory alloys. *Acta Metallurgica*, 28(c):1773–1780.

Falk, F. (1983). Ginzburg-Landau theory of static domain walls in shape-memory alloys. *Zeitschrift fur Physik B Condensed Matter*, 51(2):177–185.

Favier, D., Liu, Y., Orgeas, L., and Rio, G. (2002). Mechanical instability of NiTi in tension, compression and shear. In *IUTAM Symposium on Mechanics of Martensitic Phase Transformation in Solids*, pages 205–212. Springer.

Furst, S. J., Bunget, G., and Seelecke, S. (2012). Design and fabrication of a bat-inspired flapping-flight platform using shape memory alloy muscles and joints. *Smart Materials and Structures*, 22(1):14011.

Gall, K. and Sehitoglu, H. (1999). The role of texture in tension–compression asymmetry in polycrystalline NiTi. *International Journal of Plasticity*, 15(1):69–92.

Giacomel, J. A. (1998). Shape memory alloy actuator. *U.S. Patent*, 5,816,306.

Govindjee, S. and Hall, G. J. (2000). A computational model for shape memory alloys. *International Journal of Solids and Structures*, 37(5):735–760.

Grabe, C. and Bruhns, O. T. (2008). On the viscous and strain rate dependent behavior of polycrystalline NiTi. *International Journal of Solids and Structures*, 45(7-8):1876–1895.

Grabe, C. and Bruhns, O. T. (2009). Path dependence and multiaxial behavior of a polycrystalline NiTi alloy within the pseudoelastic and pseudoplastic temperature regimes. *International Journal of Plasticity*, 25(3):513–545.

Grange, R. A. and Stewart, H. M. (1946). The temperature range of martensite formation. *Trans. AIME*, 167:467–501.

Greninger, A. B. and Troiano, A. R. (1938). Orientation Habit of Martensite. *Nature*, 141:38.

Greninger, A. B. and Troiano, A. R. (1949). The mechanism of martensite formation. *trans. AIME*, 185(9):590–598.

Gu, X., Zaki, W., Morin, C., Moumni, Z., and Zhang, W. (2015). Time integration and assessment of a model for shape memory alloys considering multiaxial nonproportional loading cases. *International Journal of Solids and Structures*, 54:82–99.

Gurtin, M. E. and Anand, L. (2005). The decomposition F= F e F p, material symmetry, and plastic irrotationality for solids that are isotropic-viscoplastic or amorphous. *International Journal of Plasticity*, 21(9):1686–1719.

Guthikonda, V. S. and Elliott, R. S. (2013). Modeling martensitic phase transformations in shape memory alloys with the self-consistent lattice dynamics approach. *Journal of the Mechanics and Physics of Solids*, 61(4):1010–1026.

Hackl, K. and Heinen, R. (2008). A micromechanical model for pretextured polycrystalline shape-memory alloys including elastic anisotropy. *Continuum Mechanics and Thermodynamics*, pages 499–510.

Halphen, B. and quoc Son, N. (1974). Plastic and visco-plastic materials with generalized potential. *Mechanics Research Communications*, 1(1):43–47.

Hartl, D. J., Chatzigeorgiou, G., and Lagoudas, D. C. (2010). Three-dimensional modeling and numerical analysis of rate-dependent irrecoverable deformation in shape memory alloys. *International Journal of Plasticity*, 26(10):1485–1507.

Hartl, D. J. and Lagoudas, D. C. (2007). Aerospace applications of shape memory alloys. *Proceedings of the Institution of Mechanical Engineers, Part G: Journal of Aerospace Engineering*, 221(4):535–552.

Hartl, D. J., Lagoudas, D. C., Calkins, F. T., and Mabe, J. H. (2009a). Use of a Ni60Ti shape memory alloy for active jet engine chevron application: I. Thermomechanical characterization. *Smart Materials and Structures*, 19(1):15020.

Hartl, D. J., Mabe, J. H., Benafan, O., Coda, a., Conduit, B., Padan, R., and Doren, B. V. (2015). Standardization of shape memory alloy test methods toward certification of aerospace applications. *Smart Materials and Structures*, 24(8):082001.

Hartl, D. J., Mooney, J. T., Lagoudas, D. C., Calkins, F. T., and Mabe, J. H. (2009b). Use of a Ni60Ti shape memory alloy for active jet engine chevron application: II. Experimentally validated numerical analysis. *Smart Materials and Structures*, 19(1):15021.

Hazar, S., Zaki, W., Moumni, Z., and Anlas, G. (2015). Modeling of steady-state crack growth in shape memory alloys using a stationary method. *International Journal of Plasticity*, 67:26–38.

Helm, D. and Haupt, P. (2003). Shape memory behaviour: modelling within continuum thermomechanics. *International Journal of Solids and Structures*, 40(4):827–849.

Huang, W. and Toh, W. (2000). Training two-way shape memory alloy by reheat treatment. *Journal of materials science letters*, 19(17):1549–1550.

Huett, B. and Willey, C. (2000). Design and development of miniature mechanisms for small spacecraft. In *14th AIAA/USU Conference on Small Satellites*.

Idesman, A. V., Levitas, V. I., Preston, D. L., and Cho, J. Y. (2005). Finite element simulations of martensitic phase transitions and microstructures based on a strain softening model. *Journal of the Mechanics and Physics of Solids*, 53(3):495–523.

Itzhak'Vinograd, M. D., Klin, B., and Brosh, T. (1994). A new intratracheal stent made from nitinol, an alloy with" shape memory effect. *Cardiovascular Surgery*.

Ivshin, Y. and Pence, T. J. (1994). A constitutive model for hysteretic phase transition behavior. *International Journal of Engineering Science*, 32(4):681–704.

James, R. D. and Zhang, Z. (2005). A way to search for multiferroic materials with "unlikely" combinations of physical properties. In *Magnetism and structure in functional materials*, pages 159–175. Springer.

Johnson, A. D. (1992). Non-explosive separation device. *U.S. Patent*, 5,119,555.

Junker, P. and Hackl, K. (2011). Finite element simulations of poly-crystalline shape memory alloys based on a micromechanical model. *Computational Mechanics*, pages 505–517.

Kan, Q. and Kang, G. (2010). Constitutive model for uniaxial transformation ratchetting of super-elastic NiTi shape memory alloy at room temperature. *International Journal of Plasticity*, 26(3):441–465.

Kan, Q., Yu, C., Kang, G., Li, J., and Yan, W. (2016). Experimental observations on rate-dependent cyclic deformation of super-elastic NiTi shape memory alloy. *Mechanics of Materials*, 97:48–58.

Kauffman, G. and Mayo, I. (1993). Memory metal. *Chem Matters*, 11:4.

Kennedy, D. K., Straub, F. K., Schetky, L. M., Chaudhry, Z., and Roznoy, R. (2004). Development of an SMA actuator for in-flight rotor blade tracking. *Journal of intelligent material systems and structures*, 15(4):235–248.

Khan, A. S. and Huang, S. (1995). *Continuum theory of plasticity*. John Wiley & Sons.

Khandelwal, A. and Buravalla, V. (2009). Models for Shape Memory Alloy Behavior: An overview of modeling approaches. *The International Journal of Structural Changes in Solids*, 1(1):111–148.

Khater, H. A., Monnet, G., Terentyev, D., and Serra, A. (2014). Dislocation glide in Fe-carbon solid solution: From atomistic to continuum level description. *International Journal of Plasticity*, 62:34–49.

Kheirikhah, M., Rabiee, S., and Edalat, M. (2011). A Review of Shape Memory Alloy Actuators in Robotics. *RoboCup 2010: Robot Soccer World Cup XIV*, pages 206–217.

Kimiecik, M., Jones, J. W., and Daly, S. (2016). The effect of microstructure on stress-induced martensitic transformation under cyclic loading in the SMA Nickel-Titanium. *Journal of the Mechanics and Physics of Solids*, 89:16–30.

Knowles, G. and Bird, R. W. (2004). Telescopic wing system. *U.S. Patent*, 6,834,835.

Kockar, B., Karaman, I., Kim, J. I., Chumlyakov, Y. I., Sharp, J., and Yu, C. J. M. (2008). Thermomechanical cyclic response of an ultrafine-grained NiTi shape memory alloy. *Acta Materialia*, 56(14):3630–3646.

Krone, L., Mentz, J., Bram, M., Buchkremer, H., Stöver, D., Wagner, M., Eggeler, G., Christ, D., Reese, S., and Bogdanski, D. (2005). The Potential of Powder Metallurgy for the Fabrication of Biomaterials on the Basis of Nickel-Titanium: A Case Study with a Staple Showing Shape Memory Behaviour. *Advanced Engineering Materials*, 7(7):613–619.

Kudoh, Y., Tokonami, M., Miyazaki, S., and Otsuka, K. (1985). Crystal structure of the martensite in Ti-49.2 at.% Ni alloy analyzed by the single crystal X-ray diffraction method. *Acta Metallurgica*, 33(11):2049–2056.

Kudva, J. N. (2004). Overview of the DARPA smart wing project. *Journal of intelligent material systems and structures*, 15(4):261–267.

Kutlucinar, I. (2005). Aircraft with shape memory alloys for retractable landing gear. *U.S. Patent*, 6,938,416.

Lagoudas, D., Hartl, D., Chemisky, Y., Machado, L., and Popov, P. (2012). Constitutive model for the numerical analysis of phase transformation in polycrystalline shape memory alloys. *International Journal of Plasticity*, 32-33:155–183.

Lagoudas, D. C. (2008). *Shape Memory Alloys: Modeling and Engineering Applications*. Springer Science & Business Media.

Lagoudas, D. C., Bo, Z., and Qidwai, M. A. (1996). A unified thermodynamic constitutive model for SMA and finite element analysis of active metal matrix composites. *Mechanics of Composite Materials and Structures*, 3(2):153–179.

Lagoudas, D. C., Entchev, P. B., Popov, P., Patoor, E., Brinson, L. C., and Gao, X. (2006). Shape memory alloys, Part II: Modeling of polycrystals. *Mechanics of Materials*, 38(5-6):430–462.

Lagoudas, D. C. and Vandygriff, E. L. (2002). Processing and characterization of NiTi porous SMA by elevated pressure sintering. *Journal of Intelligent Material Systems and Structures*, 13(12):837–850.

Lai, W. S. and Liu, B. X. (2000). Lattice stability of some Ni-Ti alloy phases versus their chemical composition and disordering. *Journal of Physics: Condensed Matter*, 12(5):L53.

Larssen, J. V. and Calkins, F. T. (2013). Deployable flap edge fence. *U.S. Patent*, 7,753,316.

Laster, Z., MacBean, A. D., Ayliffe, P. R., and Newlands, L. C. (2001). Fixation of a frontozygomatic fracture with a shape-memory staple. *British Journal of Oral and Maxillofacial Surgery*, 39(4):324–325.

Leclercq, S. and Lexcellent, C. (1996). A general macroscopic description of the thermomechanical behavior of shape memory alloys. *Journal of the Mechanics and Physics of Solids*, 44(6):953–980.

León Baldelli, A., Maurini, C., and Pham, K. (2015). A gradient approach for the macroscopic modeling of superelasticity in softening shape memory alloys. *International Journal of Solids and Structures*, 52:45–55.

Levitas, V. I. and Ozsoy, I. B. (2009). Micromechanical modeling of stress-induced phase transformations. Part 1. Thermodynamics and kinetics of coupled interface propagation and reorientation. *International Journal of Plasticity*, 25(2):239–280.

Levitas, V. I. and Preston, D. L. (2002). Three-dimensional Landau theory for multivariant stress-induced martensitic phase transformations. I. Austenite-martensite. *Physical review B*, 66(13):134206.

Lexcellent, C. (2013). *Shape-memory alloys handbook*. John Wiley & Sons.

Lexcellent, C., Blanc, P., and Creton, N. (2008). Two ways for predicting the hysteresis minimisation for shape memory alloys. *Materials Science and Engineering A*, 481-482(1-2 C):334–338.

Lexcellent, C., Boubakar, M., Bouvet, C., and Calloch, S. (2006). About modelling the shape memory alloy behaviour based on the phase transformation surface identification under proportional loading and anisothermal conditions. *International Journal of Solids and Structures*, 43(3-4):613–626.

Lexcellent, C. and Bourbon, G. (1996). Thermodynamical model of cyclic behaviour of Ti-Ni and Cu-Zn-Al shape memory alloys under isothermal undulated tensile tests. *Mechanics of Materials*, 24(1):59–73.

Li, Z. Q. and Sun, Q. P. (2002). The initiation and growth of macroscopic martensite band in nano-grained NiTi microtube under tension. *International Journal of Plasticity*, 18(11):1481–1498.

Liang, C. and Rogers, C. A. (1990). One-dimensional thermomechanical constitutive relations for shape memory materials. *Journal of intelligent material systems and structures*, 1(2):207–234.

Lim, G., Park, K., Sugihara, M., Minami, K., and Esashi, M. (1996). Future of active catheters. *Sensors and Actuators A: Physical*, 56(1-2):113–121.

Lim, T. J. and McDowell, D. L. (2002). Cyclic thermomechanical behavior of a polycrystalline pseudoelastic shape memory alloy. *Journal of the Mechanics and Physics of Solids*, 50(3):651–676.

Liu, Y. and McCormick, P. G. (1990). Factors influencing the development of two-way shape memory in NiTi. *Acta Metallurgica et Materialia*, 38(7):1321–1326.

Loewy, R. G. (1997). Recent developments in smart structures with aeronautical applications. *Smart Materials and Structures*, 6(5):R11.

Lovey, F. C., Rodriguez, P. L., Malarria, J., Sade, M., and Torra, V. (1995). On the origin of the two way shape memory effect in Cu-Zn-Al alloys. *Le Journal de Physique IV*, 5(C2):C2–287.

Lubliner, J. and Auricchio, F. (1996). Generalized plasticity and shape-memory alloys. *International Journal of Solids and Structures*, 33(7):991–1003.

Ma, J., Karaman, I., and Noebe, R. D. (2010). High temperature shape memory alloys. *International Materials Reviews*, 55(5):257–315.

Machado, G., Louche, H., Alonso, T., and Favier, D. (2015). Superelastic cellular NiTi tube-based materials: Fabrication, experiments and modeling. *Materials and Design*, 65:212–220.

Machado, L. G. and Savi, M. A. (2003). Medical applications of shape memory alloys. *Brazilian journal of medical and biological research*, 36(6):683–691.

Masud, A., Panahandeh, M., and Aurrichio, F. (1997). A finite-strain finite element model for the pseudoelastic behavior of shape memory alloys. *Computer Methods in Applied Mechanics and Engineering*, 148(1-2):23–37.

Mehrabi, R., Andani, M. T., Elahinia, M., and Kadkhodaei, M. (2014). Anisotropic behavior of superelastic NiTi shape memory alloys; An experimental investigation and constitutive modeling. *Mechanics of Materials*, 77:110–124.

Miyazaki, S., Otsuka, K., and Suzuki, Y. (1981). Transformation pseudoelasticity and deformation behavior in a Ti-50.6 at% Ni alloy. *Scripta Metallurgica*, 15(3):287–292.

Mohd Jani, J., Leary, M., Subic, A., and Gibson, M. A. (2014). A review of shape memory alloy research, applications and opportunities. *Materials and Design*, 56:1078–1113.

Mori, T. and Tanaka, K. (1973). Average stress in matrix and average elastic energy of materials with misfitting inclusions. *Acta Metallurgica*, 21(5):571–574.

Morin, C., Moumni, Z., and Zaki, W. (2011a). A constitutive model for shape memory alloys accounting for thermomechanical coupling. *International Journal of Plasticity*, 27(5):748–767.

Morin, C., Moumni, Z., and Zaki, W. (2011b). Thermomechanical coupling in shape memory alloys under cyclic loadings: Experimental analysis and constitutive modeling. *International Journal of Plasticity*, 27(12):1959–1980.

Moumni, Z. (1995). *Sur la modélisation du changement de phase solide: application aux matériaux à mémoire de forme et à l'endommagement fragile partiel*. PhD thesis, Ecole Nationale des Ponts et Chaussées.

Moumni, Z., Herpen, A. V., and Riberty, P. (2005). Fatigue analysis of shape memory alloys: energy approach. *Smart Materials and Structures*, 14(5):S287–S292.

Moumni, Z., Zaki, W., and Maitournam, H. (2009). Cyclic behavior and energy approach to the fatigue of shape memory alloys. *Journal of Mechanics of Materials and Structures*, 4(2):395–411.

Moumni, Z., Zaki, W., and Nguyen, Q. S. (2008). Theoretical and numerical modeling of solid–solid phase change: Application to the description of the thermomechanical behavior of shape memory alloys. *International Journal of Plasticity*, 24(4):614–645.

Müller, C. and Bruhns, O. T. (2006). A thermodynamic finite-strain model for pseudoelastic shape memory alloys. *International Journal of Plasticity*, 22(9):1658–1682.

Mutter, D. and Nielaba, P. (2013). Simulation of the shape memory effect in a NiTi nano model system. *Journal of Alloys and Compounds*, 577:S83–S87.

Neugebauer, R., Bucht, A., Pagel, K., and Jung, J. (2010). Numerical simulation of the activation behavior of thermal shape memory alloys. In *SPIE Smart Structures and Materials+ Nondestructive Evaluation and Health Monitoring*, pages 76450J–76450J. International Society for Optics and Photonics.

Nishida, M., Tanaka, K., and Wang, H. O. (2006). Development and control of a micro biped walking robot using shape memory alloys. In *Robotics and Automation, 2006. ICRA 2006. Proceedings 2006 IEEE International Conference on*, pages 1604–1609. IEEE.

Oehler, S. D., Hartl, D. J., Lopez, R., Malak, R. J., and Lagoudas, D. C. (2012). Design optimization and uncertainty analysis of SMA morphing structures. *Smart Materials and Structures*, 21(9):94016.

Ölander, A. (1932). An electrochemical investigation of solid cadmium-gold alloys. *Journal of the American Chemical Society*, 54(10):3819–3833.

Ortin, J. (1992). Preisach modeling of hysteresis for a pseudoelastic Cu-Zn-Al single crystal. *Journal of applied physics*, 71(3):1454–1461.

Ortin, J. and Delaey, L. (2002). Hysteresis in shape-memory alloys. *International Journal of Non-Linear Mechanics*, 37(8):1275–1281.

Ostwald, R., Bartel, T., and Menzel, A. (2010a). A computational micro-sphere model applied to the simulation of phase-transformations. *Journal of Applied Mathematics and Mechanics/Zeitschrift für Angewandte Mathematik und Mechanik*, 90(7-8):605–622.

Ostwald, R., Bartel, T., and Menzel, A. (2010b). A micro-sphere approach applied to the modelling of phase-transformations. *PAMM*, 10(1):315–316.

Ostwald, R., Bartel, T., and Menzel, A. (2014). A Gibbs-energy-barrier-based computational micro-sphere model for the simulation of martensitic phase-transformations. *International Journal for Numerical Methods in Engineering*, 97(12):851–877.

Ostwald, R., Bartel, T., and Menzel, A. (2015). An energy-barrier-based computational micro-sphere model for phase-transformations interacting with plasticity. *Computer Methods in Applied Mechanics and Engineering*, 293:232–265.

Otsuka, K. and Wayman, C. M. (1999). *Shape memory materials*. Cambridge university press.

Paine, J. and Rogers, C. (1995). High velocity impact response of composites with surface bonded nitinol-SMA hybrid layers. In *36th Structures, Structural Dynamics and Materials Conference*, page 1409.

Panoskaltsis, V. P., Polymenakos, L. C., and Soldatos, D. (2014). Large deformation constitutive theory for a two-phase shape memory alloy. *Engineering Transactions*, 62(4):355–380.

Paranjape, H. M., Manchiraju, S., and Anderson, P. M. (2016). A phase field - Finite element approach to model the interaction between phase transformations and plasticity in shape memory alloys. *International Journal of Plasticity*, 80:1–18.

Patoor, E., Eberhardt, A., and Berveiller, M. (1989). Thermomechanical behavior of shape memory alloys. In *European Symposium on Martensitic Transformations*, pages 133–140. EDP Sciences.

Patoor, E., Lagoudas, D. C., Entchev, P. B., Brinson, L. C., and Gao, X. (2006). Shape memory alloys, Part I: General properties and modeling of single crystals. *Mechanics of Materials*, 38(5-6):391–429.

Pelton, A. R., Schroeder, V., Mitchell, M. R., Gong, X.-Y., Barney, M., and Robertson, S. W. (2008). Fatigue and durability of Nitinol stents. *Journal of the mechanical behavior of biomedical materials*, 1(2):153–164.

Perkins, J. (1974). Residual stresses and the origin of reversible (two-way) shape memory effects. *Scripta Metallurgica*, 8(12):1469–1476.

Perkins, J. and Sponholz, R. O. (1984). Stress-induced martensitic transformation cycling and two-way shape memory training in Cu-Zn-Al alloys. *Metallurgical transactions A*, 15(2):313–321.

Peultier, B., Ben Zineb, T., and Patoor, E. (2006). Macroscopic constitutive law of shape memory alloy thermomechanical behaviour. Application to structure computation by FEM. *Mechanics of Materials*, 38(5-6):510–524.

Peyroux, R., Chrysochoos, A., Licht, C., and Löbel, M. (1998). Thermomechanical Couplings and Pseudoelasticity of Shape Memory Alloys. *International Journal of Engineering Science*, 36(4):489–509.

Pitt, D., Dunne, J., White, E., and Garcia, E. (2001). SAMPSON smart inlet SMA powered adaptive lip design and static test. In *19th AIAA Applied Aerodynamics Conference*, page 1359.

Poletti, P.-A., Becker, C. D., Prina, L., Ruijs, P., Bounameaux, H., Didier, D., Schneider, P. A., and Terrier, F. (1998). Long-term results of the Simon nitinol inferior vena cava filter. *European radiology*, 8(2):289–294.

Popov, P. and Lagoudas, D. C. (2007). A 3-D constitutive model for shape memory alloys incorporating pseudoelasticity and detwinning of self-accommodated martensite. *International Journal of Plasticity*, 23(10-11):1679–1720.

Prahlad, H. and Chopra, I. (2001). Design of a variable twist tilt-rotor blade using shape memory alloy (SMA) actuators. In *SPIE's 8th Annual International Symposium on Smart Structures and Materials*, pages 46–59. International Society for Optics and Photonics.

Qiao, L. and Radovitzky, R. (2015). Computational modeling of size-dependent superelasticity of shape memory alloys. *Journal of the Mechanics and Physics of Solids*, 93:93–117.

Qidwai, M. A. and Lagoudas, D. C. (2000). On thermomechanics and transformation surfaces of polycrystalline NiTi shape memory alloy material. *International journal of plasticity*, 16(10):1309–1343.

Rahman, A. (1964). Correlations in the motion of atoms in liquid argon. *Physical Review*, 136(2A):A405.

Raniecki, B., Lexcellent, C., and Tanaka, K. (1992). Thermodynamic models of pseudoelastic behaviour of shape memory alloys. *Archiv of Mechanics, Archiwum Mechaniki Stosowanej*, 44:261–284.

Reedlunn, B., Churchill, C. B., Nelson, E. E., Shaw, J. A., and Daly, S. H. (2014). Tension, compression, and bending of superelastic shape memory alloy tubes. *Journal of the Mechanics and Physics of Solids*, 63(1):506–537.

Reese, S. and Christ, D. (2008). Finite deformation pseudo-elasticity of shape memory alloys – Constitutive modelling and finite element implementation. *International Journal of Plasticity*, 24(3):455–482.

Reinhardt, W. D. and Dubey, R. N. (1996). Application of objective rates in mechanical modeling of solids. *Journal of applied mechanics*, 63(3):692–698.

Rizzoni, R. and Marfia, S. (2015). A thermodynamical formulation for the constitutive modeling of a shape memory alloy with two martensite phases. *Meccanica*, 50(4):1121–1145.

Saadat, S., Salichs, J., Noori, M., Hou, Z., Davoodi, H., Bar-On, I., Suzuki, Y., and Masuda, A. (2002). An overview of vibration and seismic applications of NiTi shape memory alloy. *Smart materials and structures*, 11(2):218.

Sadjadpour, A. and Bhattacharya, K. (2007). A micromechanics inspired constitutive model for shape-memory alloys: the one-dimensional case. *Smart materials and structures*, 16(1):S51.

Saint-Sulpice, L., Chirani, S. A., and Calloch, S. (2009). A 3D super-elastic model for shape memory alloys taking into account progressive strain under cyclic loadings. *Mechanics of Materials*, 41(1):12–26.

Saleeb, A. F., Dhakal, B., Dilibal, S., Owusu-Danquah, J. S., and Padula, S. A. (2015). On the modeling of the thermo-mechanical responses of four different classes of NiTi-based shape memory materials using a general multi-mechanism framework. *Mechanics of Materials*, 80(Part A):67–86.

Saleeb, A. F., Dhakal, B., Hosseini, M. S., and Padula II, S. A. (2013). Large scale simulation of NiTi helical spring actuators under repeated thermomechanical cycles. *Smart Materials and Structures*, 22(9):94006.

Saleeb, A. F., Padula, S. A., and Kumar, A. (2011). A multi-axial, multimechanism based constitutive model for the comprehensive representation of the evolutionary response of SMAs under general thermomechanical loading conditions. *International Journal of Plasticity*, 27(5):655–687.

Sanders, A. E., Sanders, J. O., and More, R. B. (1994). Nitinol spinal instrumentation and method for surgically treating scoliosis. *U.S. Patent*, 5,290,289.

Schroeder, T. A. and Wayman, C. M. (1977). The two-way shape memory effect and other "training" phenomena in Cu-Zn single crystals. *Scripta metallurgica*, 11(3):225–230.

Sedlák, P., Frost, M., Benešová, B., Ben Zineb, T., and Šittner, P. (2012). Thermomechanical model for NiTi-based shape memory alloys including R-phase and material anisotropy under multi-axial loadings. *International Journal of Plasticity*, 39:132–151.

Sengupta, A., Papadopoulos, P., and Taylor, R. L. (2009). Multiscale finite element modeling of superelasticity in Nitinol polycrystals. *Computational mechanics*, 43(5).

Shaw, J. A. (2002). A thermochemical model for a 1-D shape memory alloy wire with propagating instabilities. *International Journal of Solids and Structures*, 39(5):1275–1305.

Shaw, J. A. and Kyriakides, S. (1995). Thermomechanical aspects of NiTi. *Journal of the Mechanics and Physics of Solids*, 43(8):1243–1281.

Simo, J. C. and Hughes, T. J. R. (2008). *Computational inelasticity*. Springer.

Singh, K. and Chopra, I. (2002). Design of an improved shape memory alloy actuator for rotor blade tracking. In *SPIE's 9th Annual International Symposium on Smart Structures and Materials*, pages 244–266. International Society for Optics and Photonics.

Sittner, P., Hara, Y., and Tokuda, M. (1995). Experimental study on the thermoelastic martensitic transformation in shape memory alloy polycrystal induced by combined external forces. *Metallurgical and Materials Transactions A*, 26(11):2923–2935.

Šittner, P. and Novák, V. (2000). Anisotropy of martensitic transformations in modeling of shape memory alloy polycrystals. *International Journal of Plasticity*, 16(10):1243–1268.

Smith, R. C. (2005). *Smart material systems: model development*. Society for Industrial and Applied Mathematics.

Sofla, A. Y. N., Meguid, S. A., Tan, K. T., and Yeo, W. K. (2010). Shape morphing of aircraft wing: status and challenges. *Materials & Design*, 31(3):1284–1292.

Song, C. (2010). History and current situation of shape memory alloys devices for minimally invasive surgery. *The Open Medical Devices Journal*, 2(1).

Song, D., Kang, G., Kan, Q., Yu, C., and Zhang, C. (2014). Non-proportional multiaxial transformation ratchetting of super-elastic NiTi shape memory alloy: Experimental observations. *Mechanics of Materials*, 70:94–105.

Song, G. and Ma, N. (2009). Shape memory alloy actuated adaptive exhaust nozzle for jet engine. *U.S. Patent*, 7,587,899.

Souza, A. C., Mamiya, E. N., and Zouain, N. (1998). Three-dimensional model for solids undergoing stress-induced phase transformations. *European Journal of Mechanics - A/Solids*, 17(5):789–806.

Souza Neto, E., Peric, D., and Owen, D. (2008). *Computational methods for plasticity: theory and applications*. John Wiley & Sons.

Stebner, A. and Brinson, L. (2013). Explicit finite element implementation of an improved three dimensional constitutive model for shape memory alloys. *Computer Methods in Applied Mechanics and Engineering*, 257:17–35.

Strittmatter, J., Gumpel, P., and Zhigang, H. (2009). Long-time stability of shape memory actuators for pedestrian safety system. *J. Achiev. Mater. Manuf Eng*, 34(1):23–30.

Stupkiewicz, S. and Petryk, H. (2002). Modelling of laminated microstructures in stress-induced martensitic transformations. *Journal of the Mechanics and Physics of Solids*, 50(11):2303–2331.

Stupkiewicz, S. and Petryk, H. (2006). Finite-strain micromechanical model of stress-induced martensitic transformations in shape memory alloys. *Materials Science and Engineering: A*, 438:126–130.

Stupkiewicz, S. and Petryk, H. (2010). Grain-size effect in micromechanical modelling of hysteresis in shape. *ZAMM-Journal of Applied Mathematics and Mechanics/Zeitschrift für Angewandte Mathematik und Mechanik*, 795(10):783–795.

Sun, Q. P. and Hwang, K. C. (1993). Micromechanics modelling for the constitutive behavior of polycrystalline shape memory alloys-I. Derivation of general relations. *Journal of the Mechanics and Physics of Solids*, 41(1):1–17.

Sun, Q.-P. and Hwang, K.-C. (1994). Micromechanics constitutive description of thermoelastic martensitic transformations. *Advances in Applied Mechanics*, 31:249–298.

Suzuki, T. and Shimono, M. (2003). A simple model for martensitic transformation. In *Journal de Physique IV (Proceedings)*, volume 112, pages 129–132. EDP sciences.

Tadaki, T., Otsuka, K., and Shimizu, K. (1988). Shape memory alloys. *Annual Review of Materials Science*, 18(1):25–45.

Tanaka, K., Kobayashi, S., and Sato, Y. (1986). Thermomechanics of transformation pseudoelasticity and shape memory effect in alloys. *International Journal of Plasticity*, 2(1):59–72.

Tao, T., Liang, Y.-C., and Taya, M. (2006). Bio-inspired actuating system for swimming using shape memory alloy composites. *International Journal of Automation and Computing*, 3(4):366–373.

Tawfik, M., Ro, J.-J., and Mei, C. (2002). Thermal post-buckling and aeroelastic behaviour of shape memory alloy reinforced plates. *Smart Materials and Structures*, 11(2):297.

Taylor, G. I. and Quinney, H. (1932). The plastic distortion of metals. *Philosophical Transactions of the Royal Society of London. Series A, Containing Papers of a Mathematical or Physical Character*, 230:323–362.

Teeriaho, J. P. (2013). An extension of a shape memory alloy model for large deformations based on an exactly integrable Eulerian rate formulation with changing elastic properties. *International Journal of Plasticity*, 43:153–176.

Testa, C., Leone, S., and Ameduri, S. (2005). Feasibility study on rotorcraft blade morphing in hovering. In *Smart Structures and Materials*, pages 171–182. International Society for Optics and Photonics.

Thamburaja, P. (2010). A finite-deformation-based phenomenological theory for shape-memory alloys. *International Journal of Plasticity*, 26(8):1195–1219.

Thamburaja, P. and Anand, L. (2001). Polycrystalline shape-memory materials: effect of crystallographic texture. *Journal of the Mechanics and Physics of Solids*, 49(4):709–737.

Thanopoulos, B. V. D., Laskari, C. V., Tsaousis, G. S., Zarayelyan, A., Vekiou, A., and Papadopoulos, G. S. (1998). Closure of atrial septal defects with the Amplatzer occlusion device: preliminary results. *Journal of the American College of Cardiology*, 31(5):1110–1116.

Toi, Y., Lee, J.-B., and Taya, M. (2004). Finite element analysis of superelastic, large deformation behavior of shape memory alloy helical springs. *Computers & Structures*, 82(20-21):1685–1693.

Tuna, C., Solomon, J. H., Jones, D. L., and Hartmann, M. J. Z. (2012). Object shape recognition with artificial whiskers using tomographic reconstruction. In *Acoustics, Speech and Signal Processing (ICASSP), 2012 IEEE International Conference on*, pages 2537–2540. IEEE.

Uehara, T., Asai, C., and Ohno, N. (2009). Molecular dynamics simulation of shape memory behaviour using a multi-grain model. *Modelling and Simulation in Materials Science and Engineering*, 17(3):35011.

Vladimirov, I. N., Pietryga, M. P., and Reese, S. (2010). Anisotropic finite elastoplasticity with nonlinear kinematic and isotropic hardening and application to sheet metal forming. *International Journal of Plasticity*, 26(5):659–687.

Wagner, M.-X. and Windl, W. (2008). Lattice stability, elastic constants and macroscopic moduli of NiTi martensites from first principles. *Acta Materialia*, 56(20):6232–6245.

Wang, J., Sehitoglu, H., and Maier, H. J. (2014). Dislocation slip stress prediction in shape memory alloys. *International Journal of Plasticity*, 54:247–266.

Wang, L. X. and Melnik, R. V. N. (2007). Thermo-mechanical wave propagations in shape memory alloy rod with phase transformations. *Mechanics of Advanced Materials and Structures*, 14(8):665–676.

Wang, X. M., Xu, B. X., and Yue, Z. F. (2008a). Micromechanical modelling of the effect of plastic deformation on the mechanical behaviour in pseudoelastic shape memory alloys. *International Journal of Plasticity*, 24:1307–1332.

Wang, Z., Hang, G., Wang, Y., Li, J., and Du, W. (2008b). Embedded SMA wire actuated biomimetic fin: a module for biomimetic underwater propulsion. *Smart Materials and Structures*, 17(2):25039.

Williams, E. and Elahinia, M. H. (2008). An automotive SMA mirror actuator: modeling, design, and experimental evaluation. *Journal of Intelligent Material Systems and Structures*, 19(12):1425–1434.

Williams, E. A., Shaw, G., and Elahinia, M. (2010). Control of an automotive shape memory alloy mirror actuator. *Mechatronics*, 20(5):527–534.

Wu, X. D., Sun, G. J., and Wu, J. S. (2003). The nonlinear relationship between transformation strain and applied stress for nitinol. *Materials Letters*, 57(7):1334–1338.

Xiao, H. (2014). An explicit, straightforward approach to modeling SMA pseudoelastic hysteresis. *International Journal of Plasticity*, 53:228–240.

Xiao, H., Bruhns, O., and Meyers, a. (2004). Explicit dual stress-strain and strain-stress relations of incompressible isotropic hyperelastic solids via deviatoric Hencky strain and Cauchy stress. *Acta Mechanica*, 168(1-2):21–33.

Xiao, H., Bruhns, O. T., and Meyers, A. (1998). On objective corotational rates and their defining spin tensors. *International journal of solids and structures*, 35(30):4001–4014.

Yanagihara, K., Mizuno, H., Wada, H., and Hitomi, S. (1997). Tracheal stenosis treated with self-expanding nitinol stent. *The Annals of thoracic surgery*, 63(6):1786–1789.

Yin, H., He, Y., and Sun, Q. (2014). Effect of deformation frequency on temperature and stress oscillations in cyclic phase transition of NiTi shape memory alloy. *J. Mech. Phys. Solids*, 67:100–128.

Yu, C., Kang, G., and Kan, Q. (2014). Study on the rate-dependent cyclic deformation of super-elastic NiTi shape memory alloy based on a new crystal plasticity constitutive model. *International Journal of Solids and Structures*, 51(25-26):4386–4405.

Yu, C., Kang, G., and Kan, Q. (2015a). A micromechanical constitutive model for anisotropic cyclic deformation of super-elastic NiTi shape memory alloy single crystals. *Journal of the Mechanics and Physics of Solids*, 82:97–136.

Yu, C., Kang, G., Kan, Q., and Song, D. (2013). A micromechanical constitutive model based on crystal plasticity for thermo-mechanical cyclic deformation of NiTi shape memory alloys. *International Journal of Plasticity*, 44:161–191.

Yu, C., Kang, G., Kan, Q., and Zhu, Y. (2015b). Rate-dependent cyclic deformation of super-elastic NiTi shape memory alloy: Thermo-mechanical coupled and physical mechanism-based constitutive model. *International Journal of Plasticity*, 72:60–90.

Yu, C., Kang, G., Song, D., and Kan, Q. (2012). Micromechanical constitutive model considering plasticity for super-elastic NiTi shape memory alloy. *Computational Materials Science*, 56:1–5.

Zaki, W. (2010). An approach to modeling tensile-compressive asymmetry for martensitic shape memory alloys. *Smart Materials and Structures*, 19(2):25009.

Zaki, W. (2011). Modeling and simulation of the mechanical response of martensitic shape memory alloys. In *ASME 2011 Conference on Smart Materials, Adaptive Structures and Intelligent Systems*, pages 189–193. American Society of Mechanical Engineers.

Zaki, W. (2012). An efficient implementation for a model of martensite reorientation in martensitic shape memory alloys under multiaxial nonproportional loading. *International Journal of Plasticity*, 37:72–94.

Zaki, W., Morin, C., and Moumni, Z. (2010a). A simple 1D model with thermomechanical coupling for superelastic SMAs. In *IOP Conference Series: Materials Science and Engineering*, volume 10, page 12149. IOP Publishing.

Zaki, W. and Moumni, Z. (2007a). A 3D model of the cyclic thermomechanical behavior of shape memory alloys. *Journal of the Mechanics and Physics of Solids*, 55(11):2427–2454.

Zaki, W. and Moumni, Z. (2007b). A three-dimensional model of the thermomechanical behavior of shape memory alloys. *Journal of the Mechanics and Physics of Solids*, 55:2455–2490.

Zaki, W., Zamfir, S., and Moumni, Z. (2010b). An extension of the ZM model for shape memory alloys accounting for plastic deformation. *Mechanics of Materials*, 42(3):266–274.

Zhang, X., Yan, X., Xie, H., and Sun, R. (2014). Modeling evolutions of plastic strain, maximum transformation strain and transformation temperatures in SMA under superelastic cycling. *Computational Materials Science*, 81:113–122.

Zhang, Y., You, Y., Moumni, Z., Anlas, G., Zhu, J., and Zhang, W. (2017). Experimental and theoretical investigation of the frequency effect on low cycle fatigue of shape memory alloys. *International Journal of Plasticity*, 90:1–30.

Zhong, Y. and Zhu, T. (2012). Patterning of martensitic nanotwins. *Scripta Materialia*, 67(11):883–886.

Zhong, Y. and Zhu, T. (2014). Phase-field modeling of martensitic microstructure in NiTi shape memory alloys. *Acta Materialia*, 75:337–347.

Zhou, B. (2012). A macroscopic constitutive model of shape memory alloy considering plasticity. *Mechanics of Materials*, 48:71–81.

Zhu, Y., Kang, G., Kan, Q., and Bruhns, O. T. (2014). Logarithmic stress rate based constitutive model for cyclic loading in finite plasticity. *International Journal of Plasticity*, 54:34–55.

Ziolkowski, A. (2007). Three-dimensional phenomenological thermodynamic model of pseudoelasticity of shape memory alloys at finite strains. *Continuum Mechanics and Thermodynamics*, 19(6):379–398.

Titre : Modélisation du comportement thermomécanique et cyclique des matériaux à mémoire de forme en transformations finies

Résumé : Cette thèse présente une approche globale de la modélisation du comportement thermomécanique et cyclique des alliages à mémoire de forme (AMF) en grandes déformations. Cette approche s'articule en trois étapes :
i) La généralisation du modèle ZM de comportement des AMF en grandes déformations dans le cadre de la thermodynamique des processus irréversibles. Pour ce faire, le gradient de la transformation totale est décomposé sous la forme du produit de trois gradients : le gradient de transformation lié à la déformation élastique, le gradient lié au changement de phase et le gradient de transformation lié à la réorientation de la martensite. Cette décomposition permet ainsi la modélisation de la réponse des structures en AMF dans le cas de chargements multiaxiaux non-proportionnels en transformations finies.
ii) La prise en compte du couplage thermomécanique en transformations finies. Pour ce faire, la déformation de Hencky a été introduite. Le modèle obtenu intègre trois caractéristiques thermomécaniques importantes des AMF, à savoir l'effet de la coexistence de l'austénite et de deux variantes de martensites distinctes, la variation de la taille de la boucle d'hystérésis avec la température et la transition du processus de changement de phase, d'abrupt à doux.
iii) Enfin, en vue de prédire la réponse des structures en AMF sous chargement thermomécanique cyclique, le modèle développé dans la deuxième étape est généralisé pour décrire la pseudoélasticité cyclique des AMF polycristallins. Le modèle obtenu permet la prise en compte de quatre caractéristiques fondamentales liées au comportement cyclique des AMF : la déformation résiduelle accumulée, la dégénérescence de la boucle d'hystérésis, l'évolution de la transformation de phase, d'abrupte à douce. La mise en œuvre numérique de ces modèles s'appuie sur des algorithmes d'intégration appropriés.
Des exemples numériques on été traités pour valider chaque étape.
Mots clés : les alliages à mémoire de forme, modèle constitutif, transformations finies, couplage thermomécanique, comportement cyclique, simulation numérique.

Title: Constitutive modeling of the thermomechanical and cyclic behavior of shape memory alloys in finite deformations

Abstract: Shape Memory Alloys (SMAs) are a class of smart materials that possess two salient features known as pseudoelasticity (PE) and shape memory effect(SME). In industrial applications, SMA structures are typically subjected to complex service conditions, such as large deformations, thermomechanically coupled boundaries and loadings, and cyclic loadings. The reliability and durability analysis of these SMA structures requires a good understanding of constitutive behavior in SMAs. To this end, this work develops a comprehensive constitutive modeling approach to investigate thermomechanical and cyclic behavior of SMAs in finite deformations. The work is generally divided into three steps. First, to improve accuracy of SMA model in finite deformation regime, the ZM model proposed by Zaki and Moumni (2007b) is extended within a finite-strain thermodynamic framework. Moreover, the transformation strain is decomposed into phase transformation and martensite reorientation components to capture multi-axial non-proportional response. Secondly, in addition to the finite deformation, thermomechanical coupling effect is taken into account by developing a new finite-strain thermomechanical constitutive model. A more straightforward approach is obtained by using the finite Hencky strain. This model incorporates three important thermomechanical characteristics, namely the coexistence effect between austenite and two distinct martensite variants, the variation with temperature of hysteresis size, and the smooth transition at initiation and completion of phase transformation. Finally, with a view to studying SMA behavior under cyclic loading, the model developed in the second step is generalized to describe cyclic pseudoelasticity of polycrystalline SMAs. The generalized model captures four fundamental characteristics related to the cyclic behavior of SMAs: large accumulated residual strain, degeneration of pseudoelasticity and hysteresis loop, rate dependence, and evolution of phase transformation from abrupt to smooth transition. Numerical implementation of these models are realized by introducing proper integration algorithms. Finite element simulations, including orthodontic archwire, helical and torsion spring actuators, are carried out using the proposed models. The future directions of this work mainly involve plasticity and fatigue analysis of SMA structures.
Keywords: Shape Memory Alloy; Constitutive model; Finite deformation; Thermomechanical coupling; Cyclic loading; Numerical simulation.

Université Paris-Saclay
Espace Technologique / Immeuble Discovery
Route de l'Orme aux Merisiers RD 128 / 91190 Saint-Aubin, France